

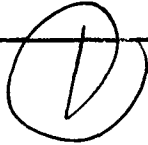
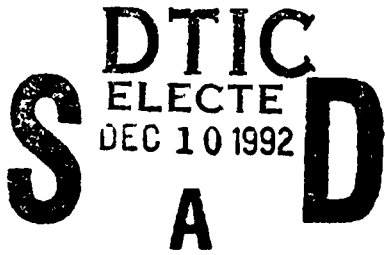
AD-A258 190



IDENTIFICATION PAGE

Form Approved
OMB No. 0704-0188

Estimated to average 1 hour per response, including the time for reviewing instructions, searching existing data sources, gathering and reviewing the collection of information, sending comments regarding this burden estimate or any other aspect of this collection of information, including suggestions for reducing this burden, to Washington Headquarters Services, Directorate for Information Operations and Reports, 1215 Jefferson Davis Highway, Suite 1204, Arlington, VA 22202-4302, and to the Office of Management and Budget, Paperwork Reduction Project (0704-0188), Washington, DC 20503.

1. AGENCY USE ONLY (Leave blank)	2. REPORT DATE 1992	3. REPORT TYPE AND DATES COVERED XXXXXX DISSERTATION		
4. TITLE AND SUBTITLE A Dynamical Theory for Hurricane Spiral Bands		5. FUNDING NUMBERS 		
6. AUTHOR(S) Thomas A. Guinn, Captain				
7. PERFORMING ORGANIZATION NAME(S) AND ADDRESS(ES) AFIT Student Attending: Colorado State University		8. PERFORMING ORGANIZATION REPORT NUMBER AFIT/CI/CIA- 92-020D		
9. SPONSORING/MONITORING AGENCY NAME(S) AND ADDRESS(ES) AFIT/CI Wright-Patterson AFB OH 45433-6583		10. SPONSORING/MONITORING AGENCY REPORT NUMBER		
11. SUPPLEMENTARY NOTES				
12a. DISTRIBUTION/AVAILABILITY STATEMENT Approved for Public Release IAW 190-1 Distributed Unlimited ERNEST A. HAYGOOD, Captain, USAF Executive Officer		12b. DISTRIBUTION CODE		
13. ABSTRACT (Maximum 200 words) <div style="text-align: center;"><p>DTIC ELECTE DEC 10 1992 A</p></div>				
14. SUBJECT TERMS		15. NUMBER OF PAGES 178		16. PRICE CODE
17. SECURITY CLASSIFICATION OF REPORT	18. SECURITY CLASSIFICATION OF THIS PAGE	19. SECURITY CLASSIFICATION OF ABSTRACT	20. LIMITATION OF ABSTRACT	

Author: Captain Thomas A. Guinn, USAF

Title: A dynamical theory for hurricane spiral bands.

Date: 1992

Number of pages: 178

Degree: Ph.D. in Atmospheric Science

University: Colorado State University

Accession For	
NTIS CRA&I DTIC TAB Unannounced Justification	
By _____ Distribution /	
Availability Codes	
Dist	Avail. and/or Special
A-1	

012200

92-31208

192PR

92 12 09 034

DISSERTATION

A DYNAMICAL THEORY FOR HURRICANE SPIRAL BANDS

Submitted by

Thomas A. Guinn

Department of Atmospheric Science

In partial fulfillment of the requirements

for the degree of Doctor of Philosophy

Colorado State University

Fort Collins, Colorado

Summer 1992

COLORADO STATE UNIVERSITY

May 12, 1992

WE HEREBY RECOMMEND THAT THE DISSERTATION PREPARED UNDER OUR SUPERVISION BY THOMAS A. GUINN ENTITLED A DYNAMICAL THEORY FOR HURRICANE SPIRAL BANDS BE ACCEPTED AS FULFILLING IN PART REQUIREMENTS FOR THE DEGREE OF DOCTOR OF PHILOSOPHY.

Committee on Graduate Work

William M. Gray

Daniel C. Randall

Robert N. Mesinger

Wayne Schubert

Adviser

Stephen K. Cox

Department Head

ABSTRACT OF DISSERTATION

A DYNAMICAL THEORY FOR HURRICANE SPIRAL BANDS

A new theory is presented for the formation of two classes of hurricane spiral bands, inner and outer. Inner bands are defined as those which form within 500 km of the hurricane center and owe their existence to asymmetries in the PV field. Outer bands are defined as those which form outside a radius of 500 km from the hurricane center and owe their existence to the breakdown of the intertropical convergence zone (ITCZ). Inner bands are discussed in the context of Rossby wave breaking and vortex merger. A shallow water, normal mode spectral model on an f -plane is used to study the banding process. Inner bands are found to form when the potential vorticity (PV) field is initially asymmetric or when a symmetric vortex moves sufficiently close to another region of high PV air. When the PV field is initially asymmetric, wave breaking occurs and filaments of high PV are ejected out to large radii in the form of spiral bands. When a symmetric vortex moves close to a region high PV air, the vortex can merge with the region of PV and advect the region of PV towards the center of the vortex in the form of a spiral band. Because the basis functions of the model are the normal modes of the system, we can easily partition the the total flow into its rotational and gravitational components. The bands are found to project almost entirely onto the rotational modes. Observations, however, show that spiral bands are also associated with strong convergence, thus suggesting gravitational modes play an important role in the formation of spiral bands. We therefore argue that spiral bands are slow manifold phenomena which project onto both the rotational and gravitational modes in such a way that transient gravity waves are minimized. In addition to the banding process, the PV field was also found to undergo a symmetrization process. Langrangian

studies indicate that the higher PV air is drawn into the center while the lower PV air appears to rotate about the axis, thus making the PV field more symmetric. The wave-activity and its flux are also calculated. These results indicate that the bands are regions of high wave-activity and therefore regions of high wave amplitude. Experiments were also performed in which asymmetric heating was added to the model. When heating was added, bands in the PV field were also formed, but in addition, the bands were associated with deviations in the geopotential.

Outer bands were also studied with the model. The model was initialized with various shaped strips of high PV air. These strips of PV satisfied the necessary condition for barotropic instability. When the strips were perturbed with random noise, the PV began to pool with thin filaments of PV connecting the pools. These filaments represent outer spiral bands which are observed in nature. Results suggest that this process can occur anywhere ITCZ convection is intense.

The stability of spiral bands is also considered using the model. The bands are idealized as annular regions of high PV air. When a vortex of twice the vorticity of the band is introduced, enough adverse shear is provided to stabilize the bands for well over 64 hours. When no adverse shear is present, instabilities in the bands rapidly grow and bands are completely broken by 48 hours. These experiments also suggest that polygonal eyewalls and meso-vortices may be partially understood using barotropic instability arguments.

Thomas A. Guinn
Department of Atmospheric Science
Colorado State University
Fort Collins, Colorado 80523
Summer 1992

ACKNOWLEDGEMENTS

First and foremost, I would like to thank my advisor, Dr. Wayne Schubert, for all of his guidance and patience throughout both my Masters and Ph.D. work. During my time at CSU, I have benefited greatly from his tremendous knowledge and insight in the fields of meteorology and fluid dynamics. I would also like to extend my gratitude to my committee members Drs. Dave Randall, William Gray, and Robert Meroney for their helpful comments and evaluations.

I would also like to thank Paul Ciesielski and Rick Taft for the countless hours of assistance they provided me with my computing needs. Their expert advice aided immeasurably in the successful completion of my dissertation. A special note of thanks goes to Paul Ciesielski and Jim Edwards for the computer drafting of several schematic diagrams used in my dissertation.

I am greatly indebted to my wife, Jolene, for all the support and understanding she has given me not only throughout my graduate studies, but throughout my entire career. I could not have made it without her.

Last, but not least, I would like to thank the United States Air Force and the Air Force Institute of Technology Civilian Institute Program for providing me with the opportunity to complete both my M.S. and Ph.D. degrees. During my studies, I have also received nonsalary support from ONR Grant N000014-88-K-0214 and NSF Grant ATM-8814541. Additional computing support was provided by NCAR.

DEDICATION

To my loving wife, Jolene, for all she's endured.

CONTENTS

1 Introduction	1
1.1 Observed Features of Hurricane Spiral Bands	2
1.2 Theories of Spiral Band Formation	6
1.3 The Scope of the Present Study	9
2 The Normal Mode Spectral Model	12
2.1 The Governing Equations	12
2.2 The Normal Mode Transform	13
2.3 Computational Procedures	16
2.3.1 Computational Aspects of the Horizontal Transforms	16
2.3.2 Calculation of Derivatives	17
2.3.3 Evaluation of Nonlinear Terms Using the Transform Method	18
2.3.4 Discretization in Time	20
2.4 Advantages and Disadvantages of Normal Mode Spectral Models	21
3 Inner Band Formation by Wave Breaking and Vortex Merger	23
3.1 Inner Bands Defined	23
3.2 Potential Vorticity in the Shallow Water Framework	26
3.3 The Concept of Potential Vorticity (Rossby) Waves in Tropical Cyclones	28
3.4 Inner Band Formation by Wave Breaking	31
3.4.1 The Concept of PV Wave Breaking and Surf Zones	32
3.4.2 Wave Breaking Experiments	35
3.4.3 Numerical Results	40
3.5 Wave-Activity and Wave-Activity Flux Diagnostics	64
3.5.1 The Wave-Activity Relation for the Shallow Water Equations	65
3.5.2 Calculation of Wave-Activity and Wave-Activity Flux Vectors	67
3.6 Inner Band Formation by Vortex Merger	68
4 Outer Band Formation through ITCZ Breakdown	83
4.1 Observational Evidence for Outer Bands	83
4.2 A Review of Stability Theory	86
4.2.1 Rayleigh's Theorem	86
4.2.2 Arnol'd's Theorem	88
4.2.3 Ripa's Theorem	91
4.3 Numerical Analyses and Simulations	93
4.3.1 Normal Mode Stability Analysis	94
4.3.2 Numerical Experiments	97

5	On the Stability of Spiral Bands	123
5.1	Normal Mode Stability Analysis	124
5.2	The Stability of Annular Potential Vorticity Regions	125
5.3	The Effect of Adverse Shear on Stability	140
5.3.1	Normal Mode Stability Analysis	140
5.3.2	Numerical Simulation of Adverse Shear	142
6	Summary and Conclusions	147
	References	155
A	The Normal Mode Model in Cylindrical Coordinates	163
A.1	The Governing Equations in Cylindrical Coordinates	163
A.2	The Tangential Transform and Lateral Boundary Condition	164
A.3	The Radial Transform	165
A.4	Computational Procedures	168
A.4.1	The Horizontal Transforms	168
A.4.2	Calculation of Derivatives and Nonlinear Terms	169
B	The Skew-Hermitian Properties of the Linear Operators	171
B.1	The Cartesian Coordinate System	171
B.2	The Cylindrical Coordinate System	172
C	The Orthonormality of the Basis Functions	173
C.1	Orthonormality of Cartesian Coordinate Basis Functions	173
C.2	Orthonormality of Cylindrical Coordinate Basis Functions	173
D	On the Use of Temperton's CFFT Routines	177

LIST OF FIGURES

1.1	Cross-band dynamical fields from Hurricane Josephine (1984).	4
1.2	Cross-band dynamical fields from Tropical Depression Irma (1987).	5
1.3	Wind barbs (knots) and D -value fields for Tropical Depression Irma.	6
1.4	An artist's conception of how clouds associated with tilted troughs in the troposphere might appear from an extra terrestrial viewpoint. (From MacDonald, 1968.)	9
3.1	An example of inner hurricane convective bands.	25
3.2	A wavenumber four perturbation (dashed) of a circular (smooth) PV surface.	30
3.3	An example of fluid dynamical irreversibility	34
3.4	An example of the wave breaking process in the mid-stratosphere.	36
3.5	The profile function, $f_{\kappa}(r')$, as function of r' for two different values of steepness parameters, κ	38
3.6	Examples of wavenumber one and wavenumber two patterns for different values of κ . See text.	41
3.7	Dynamic fields at initial time for experiment one.	43
3.8	Same as Fig. 3.7 but for 6 hours.	44
3.9	Same as Fig. 3.7 but for 12 hours.	45
3.10	Same as Fig. 3.7 but for 18 hours.	46
3.11	Same as Fig. 3.7 but for 24 hours.	47
3.12	Tangentially averaged values of vorticity, normalized PV, and wind speed at 18 hours for experiment one.	48
3.13	Initial fields for experiment two.	50
3.14	Same as Fig. 3.13 but at 6 hours.	51
3.15	Same as Fig. 3.13 but at 12 hours.	52
3.16	Same as Fig. 3.13 but at 18 hours.	53
3.17	Same as Fig. 3.13 but at 24 hours.	54
3.18	The radial wind and PV fields at the initial time for experiment two.	55
3.19	Tangentially averaged vorticity (top), normalized PV (middle) and wind speed at initial time (dotted) and 18 hours (smooth). The normalized PV and vorticity are in units of 10^{-6} s^{-1} and the wind speed is given in ms^{-1}	56
3.20	The evolution of a material tracer field for experiment two	59
3.21	Fast and slow mode contributions to the vorticity field at 12 hours for experiment one.	60
3.22	Fast and slow mode contributions to the wind and mass fields at 12 hours for experiment one.	61
3.23	A schematic diagram of Leith's slow manifold.	62
3.24	The wave-activity and PV flux at 4 hour intervals for experiment two.	69

3.25	Normalized PV fields showing the merger of two equally sized vortices of different intensities.	71
3.26	Normalized PV fields showing the merger of large weak vortex with a small strong vortex.	72
3.27	Normalized PV fields showing the merger of large weak vortex with a small strong vortex.	74
3.28	Normalized PV fields showing the interaction of a vortex with a strip of vorticity.	75
3.29	The time dependent part of the heating function $Q(x, y, t)$	77
3.30	Wind and mass fields for the asymmetrically heated vortex at 24 hrs.	78
3.31	The same as Fig. 3.30 but for 36 hrs.	79
3.32	The same as Fig. 3.30 but for 48 hrs.	80
3.33	The tangential wind along four radial arms extending from the center the diabatic vortex at 48 hrs.	82
4.1	GOES IR images at 1646 UTC on 26 July (top) and 3 August (bottom), 1988. Outer bands are especially noticeable extending from the second vortex from the left in the bottom panel.	84
4.2	Same as Fig. 4.1 but for 12 August 1988.	85
4.3	The change in normalized maximum growth rate and most unstable (nondimensional) wavenumber with increased adverse shear.	98
4.4	Dynamic fields at initial time for experiment one.	100
4.5	Vorticity and PV at day eight for experiment number one.	102
4.6	Same as for Fig. 4.5 but for day ten.	103
4.7	Same as for Fig. 4.5 but for day twelve.	104
4.8	Same as for Fig. 4.5 but for day fourteen.	105
4.9	Same as for Fig. 4.4 but for day fourteen.	106
4.10	Initial vorticity profiles for experiments one through three.	107
4.11	Vorticity and PV for experiment two at 10 days.	108
4.12	Same as Fig. 4.11 but for day fourteen.	109
4.13	Dynamic fields for experiment two at fourteen days.	110
4.14	Vorticity and PV for experiment three at twelve days.	112
4.15	Same as Fig. 4.14 but for day sixteen.	113
4.16	Dynamic fields for experiment three at sixteen days.	114
4.17	Nondimensional growth rate versus nondimensional zonal wavenumber s	115
4.18	PV fields for experiment four at 10 days.	116
4.19	Same as Fig. 4.18 but at fourteen days.	117
4.20	Dynamic fields at initial time for experiment five.	119
4.21	Same as figure 4.20 but for day two.	120
4.22	Same as figure 4.20 but for day three.	121
4.23	Same as figure 4.20 but for day four.	122
5.1	The piecewise continuous mean vorticity distribution as a function of r	124
5.2	The assumed vorticity profile for $J = 2$	126
5.3	The normalized growth rates as a function of the width of the annular region	127
5.4	The amplitude and phase relationship for a wavenumber four disturbance	128
5.5	The initial wind and mass fields for the wavenumber four perturbed pattern.	129
5.6	The same as Fig. 5.5 but for 24 hours.	130
5.7	The same as Fig. 5.5 but for 36 hours.	131

5.8	The same as Fig. 5.5 but for 48 hours.	132
5.9	The wind and mass fields for the wavenumber three perturbed case at 24 hrs.	133
5.10	The same as Fig. 5.9 but for 48 hours.	134
5.11	The wind and mass fields for the wavenumber five perturbed case at 24 hrs.	135
5.12	The same as Fig. 5.11 but for 48 hours.	136
5.13	Two examples of polygonal eyewall features of Hurricane Betsy as seen by WSR-57 radar. (From Lewis and Hawkins, 1982.)	138
5.14	A schematic representation of adverse shear.	140
5.15	An example of the vorticity profile for $J = 3$	141
5.16	The growth rates (ν) of the most unstable modes for wavenumbers $m = 3$ through 9 as a function of ξ_1	142
5.17	The initial wind and mass fields for the wavenumber four perturbed pattern with a main vortex.	143
5.18	The same as Fig. 5.17 but for 64 hours.	144
5.19	The same as Fig. 5.17 but for 120 hours.	145
D.1	The storage of the model spectral coefficients.	178

LIST OF TABLES

4.1 Summary of linear and nonlinear stability theory for various types of dynamical systems. 86

5.1 Summary of tropical cyclone characteristics and features of polygonal eyes. (From Muramatsu, 1986). 139

Chapter 1

INTRODUCTION

One of the most unmistakable features of tropical cyclones is their persistent spiral convective bands. The first known radar depiction of a tropical cyclone was taken at the U.S. Naval Air Station, Lakehurst, New Jersey, in September, 1944, and the first published radar images of spiral bands were presented by Maynard (1945). The curious nature of spiral bands was evidenced in Maynard's paper when he stated,

"The echoes from this type of weather phenomena [tropical cyclones] are very easily identified. The eye of the storm which appears as a dark area is surrounded by curved bands of echoes with feathered edges and trailing wisps. Even if the range is not great enough to encompass the eye of the storm, the definite whorls of the pattern are unmistakable." *Commander R.H. Maynard, USN, 1945.*

The curious nature of spiral bands, however, is not unique to hurricanes. Astrophysicists have also struggled to explain the spiral nature of galaxies, such as that of M51. Numerous theories have been proposed which attempt to explain this phenomena (Toomre, 1977), but a consensus has eluded the science. In a similar fashion, meteorologists have struggled to explain the existence spiral hurricane bands, with no true consensus being established (although the gravity wave theory is conventionally accepted). In this study we propose another theory for hurricane spiral band formation in hopes that a consensus can be obtained.

Numerous meteorological studies of spiral bands, both observational and theoretical, have been accomplished. Some of the significant results of these studies, as well as the scope of the present study, are presented below.

1.1 Observed Features of Hurricane Spiral Bands

The first published paper on the observed structure of hurricane rainbands was presented by Wexler (1947). He noted that the passage of a band was accompanied by heavy rain, a wind shift and increase in wind speed, a large temperature fall, and a temporary dip and recovery in the pressure of about 1 mb. Similar patterns were also found by Ligda (1955). Tatehira (1961), in a study of Typhoon Helen (1958), observed similar trends in the wind and mass fields but found no significant change in the temperature field. Tatehira also made calculations of the horizontal divergence and the vertical component of vorticity. These calculations showed the inner edge (closest the center) of the band was associated with a convergence zone with a strong divergence zone near the rear of the rainband. No systematic distribution of the vertical component of vorticity was found however.

In more recent studies, Powell (1990) and Ryan *et al.* (1992) have been able to obtain more extensive wind data through use of airborne Doppler radar. In both studies, wind vectors were obtained using a pseudo-dual Doppler technique. This technique involves flying the aircraft in zigzag patterns across the bands to obtain radar scans in orthogonal directions. The winds were assumed to be steady for the time required to complete two orthogonal scans, thus allowing two-dimensional wind vectors to be calculated. The use of this technique has allowed for the calculation of reasonably accurate and dense wind fields. The most pertinent results to the present study are the calculations of the relative vorticity and horizontal divergence.

Powell (1990) presented hurricane boundary layer results from two tropical cyclones, Josephine (1984) and Earl (1986). In each of these cases, the bands were stationary with respect to the storm. At the time of Josephine's analysis, the maximum flight level winds were 50 ms^{-1} and the minimum sea-level pressure was 970 mb. At the time of Earl's analysis, the maximum flight level winds were also 50 ms^{-1} and the pressure was 983 mb. Cross-band fields from a relatively narrow band ($\sim 20 \text{ km}$) of Josephine showed a region of high relative vorticity associated with the band with a maximum of $2.5 \times 10^{-3} \text{ s}^{-1}$ at 1500 m. In addition, the inner edge of the band was associated with a maximum in convergence of $2.0 \times 10^{-3} \text{ s}^{-1}$ at 500 m. The band examined in Hurricane Earl, which

was slightly wider (~ 30 km), exhibited the same general characteristics as Josephine but the maximums were slightly lower in magnitude. The high relative vorticity associated with the bands in both cases was due to strong cyclonic shear across the band with a maximum of the along-band wind component near the outer edge of the band. Other dynamical features which were common to both Josephine and Earl were upward vertical velocity and convergence maxima on the inner side of the band axis and D -value minima found at the band axis. The D -value is the difference between the radar altitude and the pressure altitude with reference to the standard atmosphere. It is therefore analogous to the deviation geopotential. In Fig. 1.1, cross-band fields of Hurricane Josephine from Powell (1990) are presented. This figure shows vertical cross sections based on two passes through the band, one at 500 m and one at 1500 m. The dashed box in panel (a) represents a cross section in the x - z plane (i.e. coming out of the page).

Ryan *et al.* (1992) examined a relatively wide band associated with Tropical Cyclone Irma (1987) which formed over the Gulf of Carpentaria. The band examined in their study was relatively wide (~ 80 km). At the time of the analysis, the observations indicated Irma was at least a strong depression. It was declared to be a named tropical storm roughly 15 hours later, achieving a minimum pressure of 978 mb. Although Ryan *et al.* did not explicitly calculate the divergence and vorticity, they did calculate both the along-band and cross-band components of the the wind fields. These calculations are shown in Fig. 1.2 along with a radar composite of the storm. To estimate the vorticity and divergence fields, we used the same calculation as Powell (1990), i.e.

$$\text{div} \approx \frac{\partial V_{\text{cro}}}{\partial x}, \quad (1.1)$$

and

$$\zeta \approx \frac{\partial V_{\text{alo}}}{\partial x}, \quad (1.2)$$

where x is the cross-band distance, and V_{cro} and V_{alo} are the cross-band and along-band components of the wind, respectively. This allowed us to conclude that the band had similar vorticity and divergence patterns to those of Josephine and Earl. They were, however, roughly an order of magnitude weaker. This can be attributed to the fact that

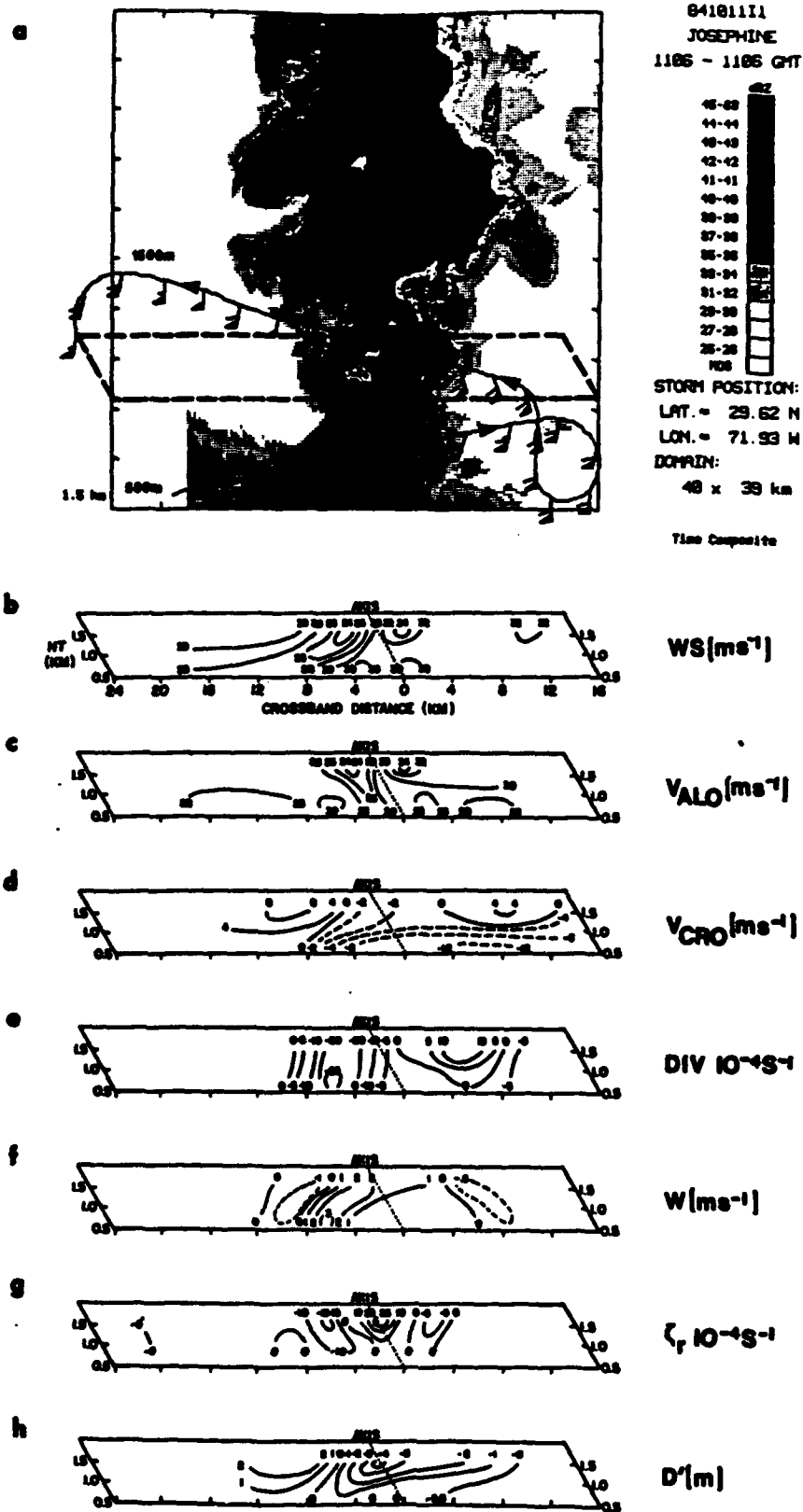


Figure 1.1: Cross-band dynamical fields of Hurricane Josephine (1984). (a) 40x40 km lower fuselage radar composite, (b) band-relative windspeed, (c) along-band wind component, (d) cross-band wind component, (e) divergence, (f) vertical wind, (g) relative vorticity and (h) D -value perturbation. (From Powell, 1990.)

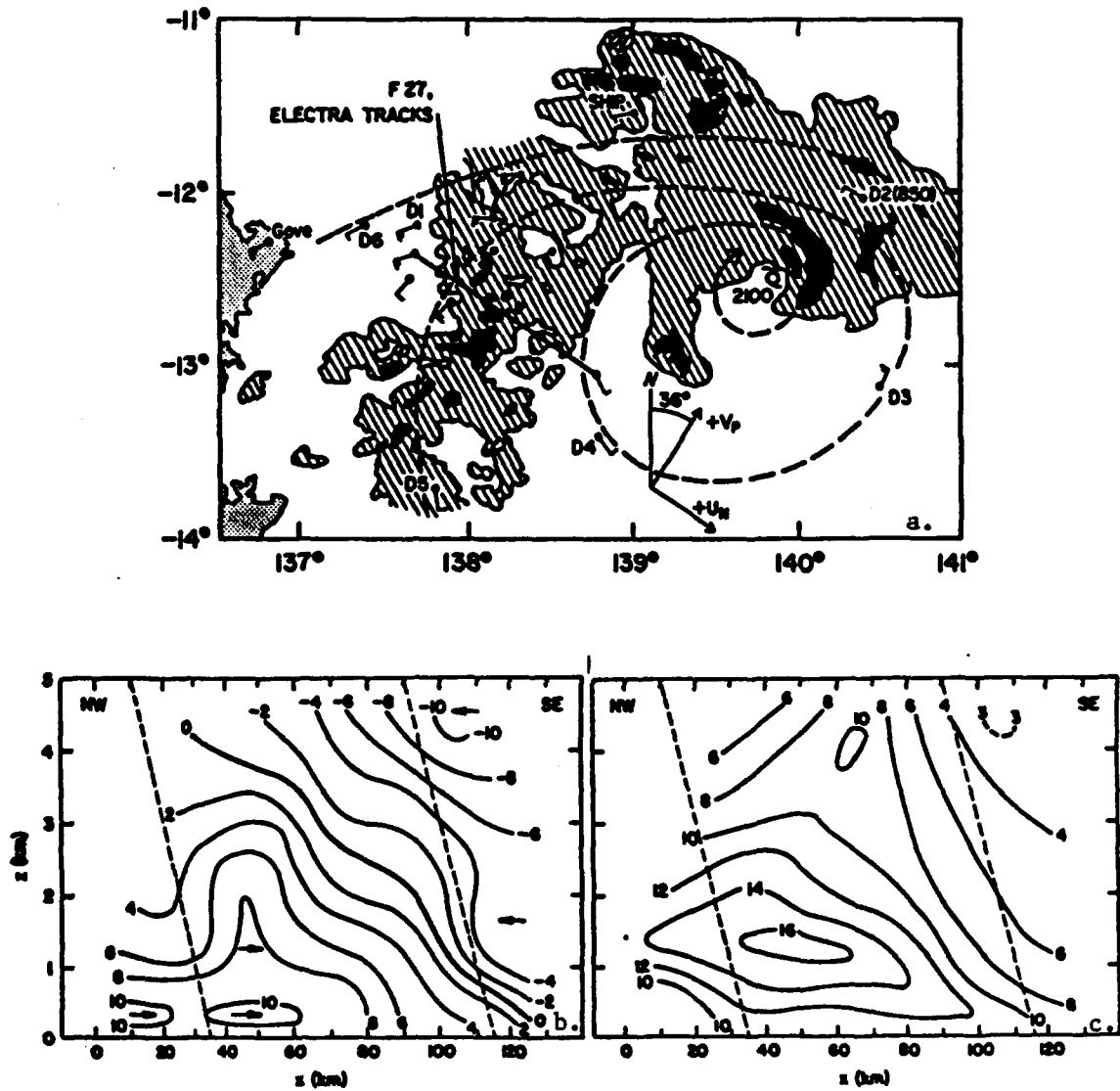


Figure 1.2: Cross-band dynamical fields from Tropical Depression Irma (1987). (a) Reflectivity pattern from Gove and P-3 radars showing the major rainband and its relation to the center of the incipient cyclone. The heavy line locates the aircraft tracks used for cross sections. (b) Composite analysis of the cross-band wind component (ms^{-1}). The rainband center is near 70 km and the dashed lines show the approximate location of the rainband edges. (c) The same as (b) but for the along-band component. (From Ryan et al., 1992.)

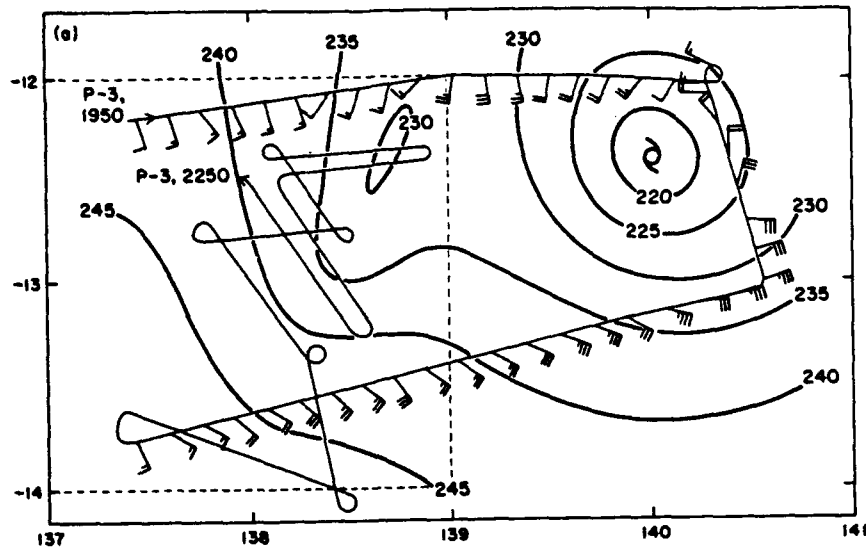


Figure 1.3: Wind (knots) and D -value (geopotential meters) for the 550 mb surface. The trough in D -value is clearly associated with the rainband. (From Ryan *et al.*, 1992.)

Irma was not yet a tropical cyclone at the time of the analysis and that Irma was a much wider band. Even if Irma had achieved the cross-band wind shears of Josephine and Earl, the divergence and vorticity would still be much weaker because of the width over which the shear occurred. Ryan *et al.* also demonstrated that the bands were associated with minima in the D -value. Figure 1.3 shows the D -value field and winds at 550 mb associated with Tropical Depression Irma. Similar to Powell's results, comparisons with Fig. 1.2a show that the trough in D -value also appears to be nearly centered about the band axis in Irma as well. The significance of all these bands displaying relative maxima in both the divergence and vorticity fields will be made clear shortly.

1.2 Theories of Spiral Band Formation

Since the discovery of spiral rainbands, many theories have been presented to explain their existence. Fletcher (1945) first theorized that the spiral bands from tropical cyclones which had formed on the intertropical convergence zone (ITCZ) were produced by "individual convergence lines" which had been coiled in the centers of the storms. Wexler (1947) hypothesized that the phenomena wasn't unique to the ITCZ, but rather bands

could occur any time a vortex came in contact with existing "cloud streets." These cloud streets would then become curved and the convergence associated with the vortex would cause the bands to spiral inward towards the center. The advent of satellite meteorology, however, has negated these theories.

Tepper (1958) later related hurricanes to mid-latitude squall lines. He proposed the bands were gravity waves which propagated out from the center. If there existed a stable layer aloft, and "something" impressed an inflow on the circulation of the vortex, gravity waves would be induced near the center of the vortex and propagate outwards at the interface of the stable layer. Spiral regions of convection could then be generated if the height of the stable layer varied azimuthally or if the tropical cyclone was observed to move rapidly. Abdullah (1966) also related hurricane bands to gravity waves at the upper surface of the lower layer. He suggested that gravity waves were generated by a fresh surge of air at the periphery of the storm that propagated towards the storm center. Upon reaching the eye, the waves would break causing turbulence and the release of latent instability. He argued that this would manifest itself in the form of a squall which could then grow and propagate back outwards, taking on a spiral shape. He presented a simple two layer model to justify his theory. Kurihara (1976) suggested the bands were outward propagating gravity waves which were modified slightly by rotation (i.e. gravity-inertia waves). He also noted that bands could also be produced in his six layer model by two other types of waves which propagated inwards, one of which was simply the inward propagating gravity-inertia wave. The third type of wave, however, was found to have features of a geostrophic mode. He noted, however, that the third type had not been observed in nature. In contrast, Willoughby (1978) suggested the inward propagating gravity-inertia waves were most likely to occur in nature and therefore most likely to be responsible for producing the spiral bands. If spiral bands in nature were due solely to gravity-inertia modes, we could not explain the observed relative vorticity maxima which are associated with observed spiral bands (Powell, 1990; Ryan, 1992). It therefore seems likely that these bands are not strictly gravity waves.

Although the gravity wave theory is presently accepted by convention, other theories have also been presented which attempt to explain the formation of spiral bands. Faller

(1961) suggested that spiral bands were formed as a result of boundary layer instabilities. His argument was based on laboratory experiments of a fluid in a rotating tank. When the Reynold's number of the flow exceeded 145, roll vortices appeared. These roll vortices were observed to have crossing angles similar to those of hurricane spiral bands. Fung (1977) also considered boundary layer instability as a possible mechanism for hurricane band formation. In her study she considered Rayleigh instability as the mechanism responsible for band formation. She noted that Rayleigh instability occurred in flows in which the Reynold's number exceeded 110. The roll vortices formed by Rayleigh instability were calculated to be oriented 14° to the left of the geostrophic wind. The existence of these roll vortices also depended highly on the existence of an inflection point in the radial wind profile, which is easily satisfied since the radial wind is observed to have a maximum in the boundary layer. The results of Fung's stability analysis indicated that the most unstable mode had four radial arms and radial wavelengths of about 20 km near the eyewall and about 50 km at a radius of 300 km. The spiral pattern was observed to be nearly stationary. In the present study, we obtain spiral bands without the presence of a boundary layer. Although there is no direct conflict between the theory presented here and boundary layer instability theories, the theory presented in this study helps explain spiral bands in a much simpler fashion.

The final and most overlooked theory of spiral bands is that of Rossby waves. MacDonald (1968) argued that the spiral bands in hurricanes bore a resemblance to troughs in the general circulation of the atmosphere. The clouds associated with these troughs would appear to spiral outwards when seen from an extra-terrestrial viewpoint. An artists conception of how this might appear is shown in Fig. 1.4. MacDonald's analogy received little attention because at the time of its publication (and well after) there were no observational studies which showed bands to be associated with regions of high relative vorticity as would be expected if they were Rossby waves (e.g., Anthes, 1982). In light of recent observations (e.g., Powell, 1990; Ryan et al., 1992), MacDonald's Rossby wave theory deserves more attention.

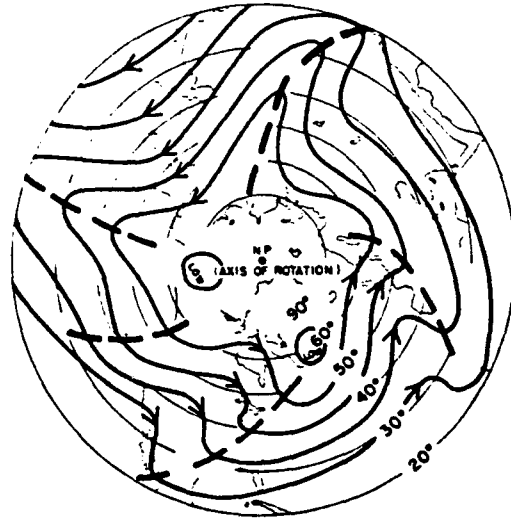


Figure 1.4: An artist's conception of how clouds associated with tilted troughs in the troposphere might appear from an extra terrestrial viewpoint. (From MacDonald, 1968.)

1.3 The Scope of the Present Study

In this study, we propose that spiral bands are neither entirely gravity wave phenomena nor entirely Rossby wave phenomena. Observationally, this seems likely since bands are associated with both horizontal convergence/divergence and relative vorticity. We therefore propose that spiral bands are slow manifold phenomena. That is, they project onto both the gravity-inertia modes as well as the Rossby (rotational) modes in such a way that transient gravity waves are minimized. The formation of these spiral bands can easily be understood through use of wave breaking and vortex merger arguments. Previously, wave breaking arguments have only been used to study stratospheric dynamics, e.g., McIntyre and Palmer (1984), Jukes and McIntyre (1987), and Polvani and Plumb (1992). Several wave breaking studies (e.g., Dritschel, 1989,1992; Polvani and Plumb, 1992) have been accomplished using contour dynamical methods. In contour dynamics, the positions of fluid particles which define a material contour are predicted. This method provides an elegant means by which the morphology of contour shapes can be examined. These methods, however, require the absence of diabatic or frictional effects since these destroy the ability to define a materially conserved variable. In the present model, experiments are performed using a shallow water normal mode, spectral model on an f -plane. Since

the basis functions of a normal mode model are the solutions to the linear system, they provide a natural means with which to partition the gravity-inertia modes from the rotational modes. Because of this feature, we can see directly the part of the solution which is due to the gravity-inertia modes and the part which is due to the rotational modes.

We provide dynamical explanations for two types of hurricane bands, inner and outer. Take note, however, that our definitions of inner and outer bands are *not* those which are conventionally accepted. We define inner bands as those bands which typically form within 500 km of the vortex center and owe their existence to asymmetries in the potential vorticity field. Outer bands, on the other hand, are those which typically form outside of 500 km from the center and owe their existence to the breakdown of the ITCZ. Both wave breaking and vortex merger processes are suggested to be responsible for the formation of inner bands, while barotropic instability is suggested to be primarily responsible for outer bands.

The outline of the study is as follows. In Chapter 2, we present the numerical model which is used for all simulations. We include in this chapter the normal mode transform which allows us to partition the the gravity-inertia modes from the geostrophic (rotational) modes. In Chapter 3, we examine the formation of inner bands by both wave breaking and vortex merger. Wave-activity and flux of wave-activity are calculated to help with diagnostics. Another diagnostic tool used in this chapter is passive tracer experiments. This tool allows us to examine Lagrangian trajectories of the fluid. Also in Chapter 3, we consider the evolution of a vortex which is heated asymmetrically. In Chapter 4, we consider the formation of outer bands by the breakdown of the ITCZ. Several general stability theorems are presented to aid in understanding the instabilities involved. Normal mode stability analysis is also used to gain insight into the unstable patterns and growth rates. Five numerical simulations are presented which demonstrate the breakdown of the ITCZ and the formation of outer bands. In Chapter 5, we consider the stability of spiral bands. Again normal mode stability analysis is used to predict unstable growth rates and patterns. These experiments also lead us to a proposed theory for polygonal eyewalls and meso-vortices. Finally, in Chapter 6, we present a brief summary and some additional conclusions.

It needs to be noted that the terms "hurricane" and "tropical cyclone" are used interchangeably throughout the text. "Hurricane" never refers specifically to those tropical cyclones which form east of the dateline, unless we refer to a specific named storm.

Chapter 2

THE NORMAL MODE SPECTRAL MODEL

In this chapter, we present the normal mode shallow water spectral model which is used in all the numerical simulations. Included are discussions of the normal mode transform, the calculation of the nonlinear terms by the transform method, the time discretization, and the calculation of derivatives. In the final section we discuss some of the advantages and disadvantages of normal mode spectral models as compared with finite difference models and other spectral models.

2.1 The Governing Equations

Using Cartesian coordinates, the shallow water equations on an f -plane can be written in rotational form as

$$\frac{\partial u}{\partial t} - v(f + \zeta) + \frac{\partial}{\partial x} \left[\phi + \frac{1}{2}(u^2 + v^2) \right] = F \quad (2.1)$$

$$\frac{\partial v}{\partial t} + u(f + \zeta) + \frac{\partial}{\partial y} \left[\phi + \frac{1}{2}(u^2 + v^2) \right] = G \quad (2.2)$$

$$\frac{\partial \phi}{\partial t} + c^2 \left(\frac{\partial u}{\partial x} + \frac{\partial v}{\partial y} \right) + \frac{\partial(u\phi)}{\partial x} + \frac{\partial(v\phi)}{\partial y} = S. \quad (2.3)$$

where u and v are, respectively, the east-west and north-south components of the wind field. It should be noted, however, that their orientation is completely arbitrary on an f -plane. The geopotential, ϕ , is defined as gh with g and h being, respectively, gravity and the deviation of the fluid depth from its mean value, H . The variable, c , is defined as \sqrt{gH} . Frictional effects are represented by F and G while diabatic effects are represented by S . Lastly, the variable ζ represents the relative vorticity which is given as $(\partial v/\partial x - \partial u/\partial y)$.

A more convenient way to write (2.1)–(2.3) is in vector form. This is done by defining $\mathbf{W} = [u, v, \phi/c]^T$ and rewriting (2.1)–(2.3) as

$$\frac{\partial \mathbf{W}}{\partial t} + \mathcal{L}\mathbf{W} = \mathbf{F} + \mathbf{N}, \quad (2.4)$$

where the linear operator \mathcal{L} is defined as

$$\mathcal{L} = \begin{pmatrix} 0 & -f & c \frac{\partial}{\partial x} \\ f & 0 & c \frac{\partial}{\partial y} \\ c \frac{\partial}{\partial x} & c \frac{\partial}{\partial y} & 0 \end{pmatrix}, \quad (2.5)$$

nonlinear and forcing terms are written as

$$\mathbf{N} = \left[\zeta v - \frac{\partial}{\partial x} \left(\frac{u^2 + v^2}{2} \right), -\zeta u - \frac{\partial}{\partial y} \left(\frac{u^2 + v^2}{2} \right), -\frac{1}{c} \left(\frac{\partial(u\phi)}{\partial x} + \frac{\partial(v\phi)}{\partial y} \right) \right]^T \quad (2.6)$$

and

$$\mathbf{F} = (F, G, S/c)^T, \quad (2.7)$$

respectively. With the governing equations written in this form, we can now begin the normal mode transform.

2.2 The Normal Mode Transform

We begin the normal mode transform by first defining an appropriate inner product. If we consider our model domain to be periodic in both the x and y directions with periods L_x and L_y respectively, we can define our complex inner product to be

$$(\psi, \xi) = \frac{1}{L_x L_y} \int_0^{L_y} \int_0^{L_x} (\psi_0 \xi_0^* + \psi_1 \xi_1^* + \psi_2 \xi_2^*) dx dy \quad (2.8)$$

where ψ and ξ are three-component complex vectors which are periodic in x and y with periods L_x and L_y respectively and the asterisk denotes the complex conjugate. As discussed in Appendix B, \mathcal{L} is skew-Hermetian with respect to the inner product (2.8). By noting that the eigenvalues of skew-Hermetian operators are pure imaginary, we can write

$$\mathcal{L}\mathbf{K}_{klq} = i\nu_{klq}\mathbf{K}_{klq}, \quad (2.9)$$

where ν_{klq} are the eigenvalues of the matrix operator \mathcal{L} and \mathbf{K}_{klq} are the corresponding vector eigenfunctions or transformation kernels. The subscripts k , l , and q are presently undefined. They will become clear once (2.9) is solved.

Equation (2.9) can easily be solved in the usual manner by first assuming that the three components of \mathbf{K}_{klq} are proportional to $e^{i(kx+ly)}$, where $i \equiv \sqrt{-1}$. By assuming this, all x derivatives are replaced by ik and all y derivatives are replaced by il . The matrix operator \mathcal{L} is then reduced to a simple coefficient matrix. In order for a non-trivial solution to exist, the determinant of this coefficient matrix must vanish. We find that the determinant will vanish provided the following dispersion relation holds,

$$\nu_{klq}[\nu_{klq}^2 - (\mu^2 + f^2)] = 0, \quad (2.10)$$

where

$$\mu^2 \equiv c^2(k^2 + l^2). \quad (2.11)$$

Thus, our eigenvalues are

$$\nu_{klq} = \begin{cases} 0 & q = 0 \quad (\text{geostrophic modes}) \\ -(f^2 + \mu^2)^{\frac{1}{2}} & q = 1 \quad (\text{gravity - inertia mode}) \\ (f^2 + \mu^2)^{\frac{1}{2}} & q = 2 \quad (\text{gravity - inertia mode}) \end{cases}. \quad (2.12)$$

With the use of (2.12), the transformation kernels, which are simply the eigenvectors of \mathcal{L} , can easily be determined. They are

$$\mathbf{K}_{klq} = \begin{cases} \frac{1}{\nu} \begin{pmatrix} -icl \\ ick \\ f \end{pmatrix} e^{i(kx+ly)} & q = 0 \\ \frac{1}{\sqrt{2}\mu\nu} \begin{pmatrix} c(ifl - \nu k) \\ -c(\nu l + ifk) \\ \mu^2 \end{pmatrix} e^{i(kx+ly)} & q = 1 \\ \frac{1}{\sqrt{2}\mu\nu} \begin{pmatrix} c(\nu k + ifl) \\ c(\nu l - ifk) \\ \mu^2 \end{pmatrix} e^{i(kx+ly)} & q = 2 \end{cases}, \quad (2.13)$$

where $\nu \equiv [\mu^2 + f^2]^{\frac{1}{2}}$.

The definitions of the subscripts should now be clear. The subscripts k and l represent wave numbers in the x and y directions respectively, while the subscript q refers to a particular root of (2.10). Physically, q distinguishes between the fast and slow modes. That is, $q = 0$ denotes the geostrophic (slow) modes while $q = 1$ or 2 denotes the east and west propagating gravity-inertia (fast) modes, respectively.

As discussed in Appendix C, the transformation kernels in (2.13) are orthonormal with respect to the complex inner product (2.8), that is

$$(\mathbf{K}_{klq}, \mathbf{K}_{k'l'q'}) = \begin{cases} 1 & k = k', l' = l \text{ and } q' = q \\ 0 & \text{otherwise} \end{cases}. \quad (2.14)$$

Using this orthonormality, we can define our transform pair as

$$\mathbf{W}(x, y, t) = \sum_{l=-\infty}^{\infty} \sum_{k=-\infty}^{\infty} \sum_{q=0}^2 W_{klq}(t) \mathbf{K}_{klq}(x, y) \quad (2.15)$$

$$W_{klq}(t) = (\mathbf{W}(x, y, t), \mathbf{K}_{klq}(x, y)), \quad (2.16)$$

where $W_{klq}(t)$ is a scalar, complex function of time having units of ms^{-1} . Equation (2.15) can then be thought of as the transformation which takes the dependent variables from physical space to spectral space, and (2.16) is the inverse transformation back to physical space.

Finally, we use our spectral transforms (2.15) and (2.16) to reduce our original system of equations to one set of ordinary differential equations for each mode. We accomplished this by taking the inner product (as defined by Eq. 2.8) of (2.4) with the transformation kernel $\mathbf{K}_{klq}(x, y)$ to obtain

$$\frac{\partial}{\partial t}(\mathbf{W}, \mathbf{K}_{klq}) + (\mathcal{L}\mathbf{W}, \mathbf{K}_{klq}) = (\mathbf{F}, \mathbf{K}_{klq}) + (\mathbf{N}, \mathbf{K}_{klq}). \quad (2.17)$$

Because \mathcal{L} is skew-Hermitian with respect to our inner product, we can shift \mathcal{L} off of \mathbf{W} and onto the transformation kernel (see Appendix B). Using (2.9), we can then eliminate \mathcal{L} from the problem which allows us to write (2.17) in final form as

$$\frac{dW_{klq}}{dt} + i\nu_{klq}W_{klq} = F_{klq} + N_{klq}. \quad (2.18)$$

Equation (2.18) is the normal mode oscillation equation. In the absence of external forcings or nonlinear terms, each mode would simply oscillate at its own frequency. It is interesting to note that all normal mode models can be reduced to this one equation regardless of geometry. In Appendix A, we demonstrate this by deriving the normal mode oscillation equation in cylindrical coordinates.

2.3 Computational Procedures

In this section, we discuss the computational procedures involved in numerically integrating the above system of equations. These procedures include the numerical calculation of the finite Fourier and normal mode transforms. We also discuss the calculation of derivatives as well as nonlinear terms. Lastly, we discuss the time differencing scheme which was used.

2.3.1 Computational Aspects of the Horizontal Transforms

In the preceding section, the normal mode transform was described as a single operation. While this is a convenient way to express the transform on paper, it is not convenient for computational purposes. Computationally, it is much easier to perform the same normal mode transform as two separate operations. In addition, we must truncate our transforms in order to compute them numerically.

The first operation consists of transforming the wind and geopotential fields to Fourier spectral space. We define our truncated Fourier transform pair as

$$\psi_{kl} = \frac{1}{IJ} \sum_{j=0}^{J-1} \sum_{i=0}^{I-1} \psi(x_i, y_j) \exp \left[-2\pi i \left(\frac{\hat{k}\hat{i}}{I} + \frac{\hat{l}\hat{j}}{J} \right) \right] \quad (2.19)$$

$$\psi(x_i, y_j) = \sum_{\hat{l}=-L}^L \sum_{\hat{k}=-K}^K \psi_{kl} \exp \left[2\pi i \left(\frac{\hat{k}\hat{i}}{I} + \frac{\hat{l}\hat{j}}{J} \right) \right], \quad (2.20)$$

where the continuous variables have been discretized as

$$k_{\hat{k}} = \frac{2\pi}{L_x} \hat{k}, \quad \text{for } \hat{k} = -K, \dots, K \quad (2.21)$$

$$l_{\hat{l}} = \frac{2\pi}{L_y} \hat{l}, \quad \text{for } \hat{l} = -L, \dots, L \quad (2.22)$$

$$x_{\hat{i}} = \frac{L_x}{I} \hat{i} \quad \text{for } \hat{i} = 0, \dots, I-1 \quad (2.23)$$

$$y_{\hat{j}} = \frac{L_y}{J} \hat{j} \quad \text{for } \hat{j} = 0, \dots, J-1 \quad (2.24)$$

with I and J representing the maximum number of grid points on the transform grid in the x and y directions respectively, and K and L represent the maximum number of discrete wave numbers in the x and y directions respectively. Equation (2.19) is the transform

from physical to Fourier spectral space and (2.20) is its inverse. In order to speed the model computations, fast Fourier transforms (FFTs) are used to evaluate (2.19–2.20) (see Appendix D). If the number of gridpoints used in both model directions, I and J , are both powers of two, FFTs reduce the number of operations needed to evaluate either (2.19) or (2.20) from order $I^2 \times J^2$ to order $I \log_2 I \times J \log_2 J$ (Conte and de Boor, 1980). As an example, if 128×128 gridpoints are used to represent the physical fields, FFTs reduce the number of operations needed to transform these fields to or from Fourier spectral space from order 10^8 to order 10^6 . This is an improvement of roughly two orders of magnitude.

Once the fields have been transformed to Fourier spectral space, the second operation, which can be thought of as the true normal mode transform, reduces to a simple vector multiplication of the Fourier spectral coefficients with the complex conjugate of the x and y independent part of the transformation kernel (2.13) for each mode type q .

The inverse transformation is the summation of the spectral coefficients, W_{klq} with the x and y independent parts of the transformation kernel for each q . Once this is done, the inverse Fourier transform is again performed via FFTs.

2.3.2 Calculation of Derivatives

An advantage of working with a doubly periodic domain is that the transformation kernels are eigenfunctions of the linear operators; that is, derivatives of the transformation kernels are simply scalar multiples of the transformation kernels themselves. We can use this property to show that the spectral coefficients of derivatives of our fields are simply scalar multiples of the spectral coefficients of our fields themselves. To show this, consider the one dimensional finite Fourier transform of the periodic function, $\partial\psi(x)/\partial x$. We write this as

$$\frac{1}{L_x} \int_0^{L_x} \frac{\partial\psi(x)}{\partial x} e^{-ikx} dx. \quad (2.25)$$

If we integrate (2.25) by parts, we can shift the derivative operator off $\psi(x)$ to obtain

$$\frac{1}{L_x} \int_0^{L_x} ik\psi(x)e^{-ikx} dx + [\psi(x)e^{-ikx}]_0^{L_x}. \quad (2.26)$$

Because ψ is periodic in x the rightmost term in (2.26) is identically zero. This implies that

$$\frac{1}{L_x} \int_0^{L_x} \frac{\partial \psi(x)}{\partial x} e^{-ikx} dx = ik\psi_k, \quad (2.27)$$

where ψ_k is the k^{th} Fourier spectral coefficient of $\psi(x)$. Although this proof is only in one dimension, it can easily be generalized to two dimensional transforms and therefore our inner product (2.8). We can therefore write

$$\left(\frac{\partial \mathbf{W}(x, y, t)}{\partial x}, \mathbf{K}_{klq}(x, y) \right) = ik(\mathbf{W}(x, y, t), \mathbf{K}_{klq}(x, y)). \quad (2.28)$$

This is not only true for x derivatives but similar relations also hold true for all linear operators, e.g. second order derivatives, Laplacians, etc. This is useful because it requires us to store only one transformation kernel. All necessary derivatives can then be obtained through scalar multiplications of this single kernel given in (2.13).

2.3.3 Evaluation of Nonlinear Terms Using the Transform Method

Evaluation of the nonlinear terms of the model is the most expensive computation of the model. The reason being that nonlinear products cannot be computed in spectral space simply by multiplying the appropriate Fourier coefficients. In this model we use the transform method as described by Orzag (1970) and Eliassen *et al.* (1970) to calculate the nonlinear terms. The transform method predicts the linear terms and calculates their derivatives in spectral space while the nonlinear terms are computed in physical space. To demonstrate this, consider the normal mode oscillation equation (2.18). The nonlinear terms, N_{klq} , are necessary to predict the dependent variables, W_{klq} , however the calculation of N_{klq} depends on W_{klq} itself. To calculate N_{klq} at a given timestep, we perform the inverse normal transform of W_{klq} at the corresponding time step to obtain the Fourier coefficients. While in Fourier spectral space, all appropriate derivatives are calculated. We next transform the fields and their derivatives to physical space and compute the nonlinear products. The nonlinear products are then transformed back to normal mode spectral space to obtain N_{klq} . The forcing terms, F_{klq} are calculated in a similar fashion. Using N_{klq} and F_{klq} , a new W_{klq} can be predicted from (2.18) and the

whole process repeats itself. It should now be easy to see why the nonlinear and forcing terms use such a large portion of the total computing time. For each time step, a complete transform to and from spectral space is required.

It is important to note that because our basis functions are periodic, the Fourier transforms can be computed exactly if enough grid points are used to discretize the fields in physical space. This holds true even for quadratically nonlinear terms. To demonstrate this, recall Krylov (1962) where it is shown that any periodic function of period L_x with degree no greater than K can be integrated over L_x exactly by trapezoidal quadrature if at least $K + 1$ grid points are used to discretize the function. Now consider any quadratically nonlinear term. Each function which comprises the nonlinear term is of degree of less than or equal to K and L ; that is, each function can be Fourier decomposed to include only terms of the form $e^{i(kx+ly)}$ where $k \leq K$ and $l \leq L$. Since the integral transform itself (2.8) also includes the term $e^{i(kx+ly)}$ for $k \leq K$ and $l \leq L$, the highest degree of the resulting function must be $3K$ and $3L$, i.e. the resulting function takes the form $e^{i(3kx+3ly)}$. This means we can evaluate the integral in (2.8) exactly for up to and including quadratically nonlinear terms if we use at least $3K + 1$ and $3L + 1$ points in the x and y directions respectively. As an example, if we choose a 128×128 point grid, we can resolve roughly 42 waves.

If all terms in the model were strictly linear or quadratically nonlinear, all transformations could be done exactly. As a result, no aliasing error would occur; that is, no information from higher order Fourier modes would be falsely projected onto the lower order Fourier modes. If this were true, non-linear computational instability arising from this false projection as described by Phillips (1959) would be eliminated. However, not all terms in the model, such as the forcing terms, are strictly linear or quadratically nonlinear. As a result, some aliasing can occur in the model, although results indicate that a $(3K + 1) \times (3L + 1)$ grid is large enough to make the non-linear computational instability negligible.

2.3.4 Discretization in Time

The final step in integrating the model is the time discretization of (2.18). In the present model, the second order Adams-Bashforth scheme is used. We use this particular scheme because it damps the computational mode for the oscillation equation. This property was shown by Randall (1989) and can be proved as follows. Consider the linear, frictionless form of (2.18), i.e.

$$\frac{dW_{klq}}{dt} + i\nu_{klq}W_{klq} = 0. \quad (2.32)$$

If we discretize (2.32) using the Adams-Bashforth scheme, we can rewrite (2.32) as

$$W_{klq}^{(n+1)} = W_{klq}^{(n)} + i\Omega \left(\frac{3}{2}W_{klq}^{(n)} - \frac{1}{2}W_{klq}^{(n-1)} \right), \quad (2.33)$$

where $\Omega \equiv i\nu_{klq}\Delta t$ and n represents the time step. If we assume (2.33) has solutions of the form $W_{klq}^{(n+1)} = \lambda W_{klq}^{(n)}$ then (2.33) can be written as

$$\lambda^2 - \lambda \left(1 + \frac{3}{2}i\Omega \right) + i\frac{1}{2}\Omega = 0. \quad (2.34)$$

Equation (2.35) has two possible modes which can be found through use of the quadratic formula. These modes are

$$\lambda_1 = \frac{1}{2} \left(1 + \frac{3}{2}i\Omega + \sqrt{1 - \frac{9}{4}\Omega^2 + i\Omega} \right) \quad (2.35)$$

and

$$\lambda_2 = \frac{1}{2} \left(1 + \frac{3}{2}i\Omega - \sqrt{1 - \frac{9}{4}\Omega^2 + i\Omega} \right). \quad (2.36)$$

Since $\lambda_1 \rightarrow 1$ as $\Omega \rightarrow 0$, this corresponds to the physical mode. The other mode, λ_2 , approaches zero as $\Omega \rightarrow 0$ and is therefore the computational mode. This is an important result because it states that the computational mode damps as Δt becomes smaller.

In order to examine the behavior of the physical mode, it is useful to simplify (2.35). We do this by expanding the radical (while treating the terms containing Ω within the radical as a single variable) using a Taylor series centered about the point zero and keeping the first two terms in the series. We are able to do this since Ω is typically much less than one. The resulting expression can be written as

$$\lambda_1 \cong 1 + i\Omega - \frac{\Omega^2}{2}. \quad (2.37)$$

The modulus of (2.37) is then

$$|\lambda_1| \cong \left(1 + \frac{\Omega^4}{4}\right)^{\frac{1}{2}}. \quad (2.38)$$

From (2.38) it is apparent that the price paid for having a damped computational mode is the weak instability of the physical mode. Because Ω is raised to the fourth power in (2.38), the instability of the physical mode appears to be negligible if Δt is sufficiently small. This assumption was verified through numerous model integrations.

Before integrating (2.18) it proves useful to multiply through by the integrating factor $\exp(i\nu_{klq}t)$. In doing so (2.18) can be rewritten as

$$\frac{d}{dt} [W_{klq} e^{i\nu_{klq}t}] = e^{i\nu_{klq}t} (F_{klq} + N_{klq}). \quad (2.39)$$

Equation (2.39) has the property that all linear terms may be treated exactly while only the nonlinear and forcing terms need to be treated explicitly. Using this "semi-exact" form, we are able to choose a time step roughly two and a half times greater than its purely explicit counter part (DeMaria and Schubert, 1984). If we let $t = n\Delta t$ and use a forward time step for the initial time step and the Adams-Bashforth scheme for all subsequent time steps, (2.39) can be discretized as

$$W_{klq}^{(1)} = [W_{klq}^{(0)} + \Delta t(N_{klq}^{(0)} + F_{klq}^{(0)})] e^{i\nu_{klq}\Delta t} \quad (2.40)$$

and

$$W_{klq}^{(n+1)} = W_{klq}^{(n)} e^{-i\nu_{klq}\Delta t} + \Delta t \left\{ \frac{3}{2} [N_{klq}^{(n)} + F_{klq}^{(n)}] e^{-i\nu_{klq}\Delta t} - \frac{1}{2} [N_{klq}^{(n-1)} + F_{klq}^{(n-1)}] e^{-i\nu_{klq}2\Delta t} \right\}. \quad (2.41)$$

This is the form of (2.18) used in the model integrations.

2.4 Advantages and Disadvantages of Normal Mode Spectral Models

Perhaps the greatest advantage of normal mode spectral models is their ability to partition the contribution to the total flow by the rotational (slow) and gravitational (fast) modes. For the f -plane model discussed above, this means we can see directly that part of the solution which is due to gravity-inertia modes and that which is due to

geostrophic or balanced modes. No other type of model can partition these modes so precisely. In Chapters 3-5, we will demonstrate the usefulness of this feature. Another advantage of normal mode spectral models is the ease with which nonlinear normal mode initialization can be implemented. This results from the models direct calculation of the normal modes. Although this feature is not used in our simple model, it would prove quite useful for more complicated normal mode models. The final advantage of normal mode spectral models is the simplicity with which the time discretization can be performed. As mentioned previously, the discretization in time reduces to a set of ordinary differential equations for each normal mode which can be integrated "semi-exactly."

Unfortunately, the disadvantages associated with normal mode spectral models are equal to, if not greater, than the advantages. Perhaps the greatest disadvantage is the relatively slow convergence rates of the basis functions which must be used. This is especially true for the cylindrical coordinate model discussed in Appendix A. In addition, derivatives of the basis functions are not guaranteed to be eigenfunctions of the linear operators (as is the case with the Cartesian coordinate model), although they are usually known analytically. This makes it necessary to store large arrays containing these derivatives for each mode and at each point on the transform grid (see Appendix A). One more disadvantage is that gravity waves are not allowed to simply radiate out the boundaries of the model. They must either be perfectly reflected or, as in the Cartesian coordinate model, exit one end of the domain and enter the opposing end. Unless gravity waves are treated properly, they will quickly fill the model domain with noise.

For the Cartesian coordinate model which is used in the following chapters, most problems are associated with the use of a doubly periodic domain. Special care must be taken to avoid the false interaction of a disturbance with the same disturbance which exists implicitly in the adjacent domain. To help limit this problem, the model domains are kept larger than one Rossby radius. In linear dynamics, this ensures that the final adjusted geopotential, associated with an initial potential vorticity (PV) disturbance, will e-fold at least once before interacting with the center of itself in the adjacent domain. Model results indicate that this is sufficient to limit any unfavorable interactions.

Chapter 3

INNER BAND FORMATION BY WAVE BREAKING AND VORTEX MERGER

The concepts of potential vorticity (PV) waves and wave breaking have recently served as useful tools in stratospheric dynamics (McIntyre and Palmer, 1983, 1984; Jukes and McIntyre, 1987; Polvani and Plumb, 1992). Until now, however, these conceptual tools have not spread to other areas of meteorology. In this chapter, we show that these same concepts also prove useful in understanding the formation of a class of hurricane convective bands which we will refer to as "inner" bands. We begin by defining the term "inner" bands and presenting observational evidence of their existence. We next review the concept of potential vorticity and mathematically demonstrate the existence of PV waves in tropical cyclones. These concepts are then used to understand the formation of hurricane bands by the wave breaking process through numerical simulations. In addition, we analyze the wave breaking process using the diagnostic tools of wave-activity and wave-activity flux vectors as derived by Haynes (1988). In the final section, we discuss vortex merger and the symmetrization of PV anomalies produced by convective heating.

3.1 Inner Bands Defined

In the present study, we consider two types of hurricane convective bands - "inner" and "outer". The latter will be discussed in the following chapter. We define inner bands to be those convective bands which are located typically less than 500 km from the storm center and owe their existence to asymmetries in the PV field. These asymmetries can be generated through several processes. Three such processes are the advection of the earth's background PV, tropical cyclone motion, and convection.

The earth's background PV field generally increases monotonically with latitude. This is due largely to the earth's rotation. When the cyclonic circulation associated with a tropical cyclone is superimposed on the earth's natural PV field, the right side of the tropical cyclone advects relatively low PV air northward while the left side of the tropical cyclone advects relatively high PV air southward. The end result is a positive PV anomaly on the southern side of the tropical cyclone and a negative PV anomaly on the northern side of the tropical cyclone. This produces a wavenumber one asymmetry in the PV field. Numerical simulations of this effect have recently been presented by Shapiro (1992).

In a similar fashion, tropical cyclone motion can also induce a wavenumber one asymmetry in the PV field. As a tropical cyclone moves westward (in the northern hemisphere), the motion of the cyclone adds to the wind speed on the northern side of the vortex and subtracts from the wind speed on the southern side of the vortex. The vorticity would therefore be expected to be slightly greater on the northern side than on the southern side. Since PV is closely related to vorticity, we would again expect a wavenumber one asymmetry in the PV field.

In addition to advection of the earth's background PV, and tropical cyclone motion, asymmetries in the PV field of a tropical cyclone can also be generated by convection. If we accept that regions of convection are also regions of high PV (as will be discussed in the following section), then any asymmetries in the convection of a tropical cyclone will yield asymmetries in the PV field. An important difference between this mechanism and the previous two is that convection is not limited to wavenumber one asymmetries. All wavenumbers are possible.

Asymmetries in the PV field can lead to PV wave breaking which causes areas of higher PV (more intense convection) to be ejected down gradient in the form of a inner bands. Inner band formation can also be discussed in the context of vortex merger. That is, when a vortex moves sufficiently close to a region of relatively high PV, the vortex will merge with the region of high PV and produce an inner spiral band. An example of inner hurricane bands is presented in Fig. 3.1. The convective bands of Cleo (1958) shown in Fig. 3.1 are well within the 500 km radius required by our definition of inner bands. The

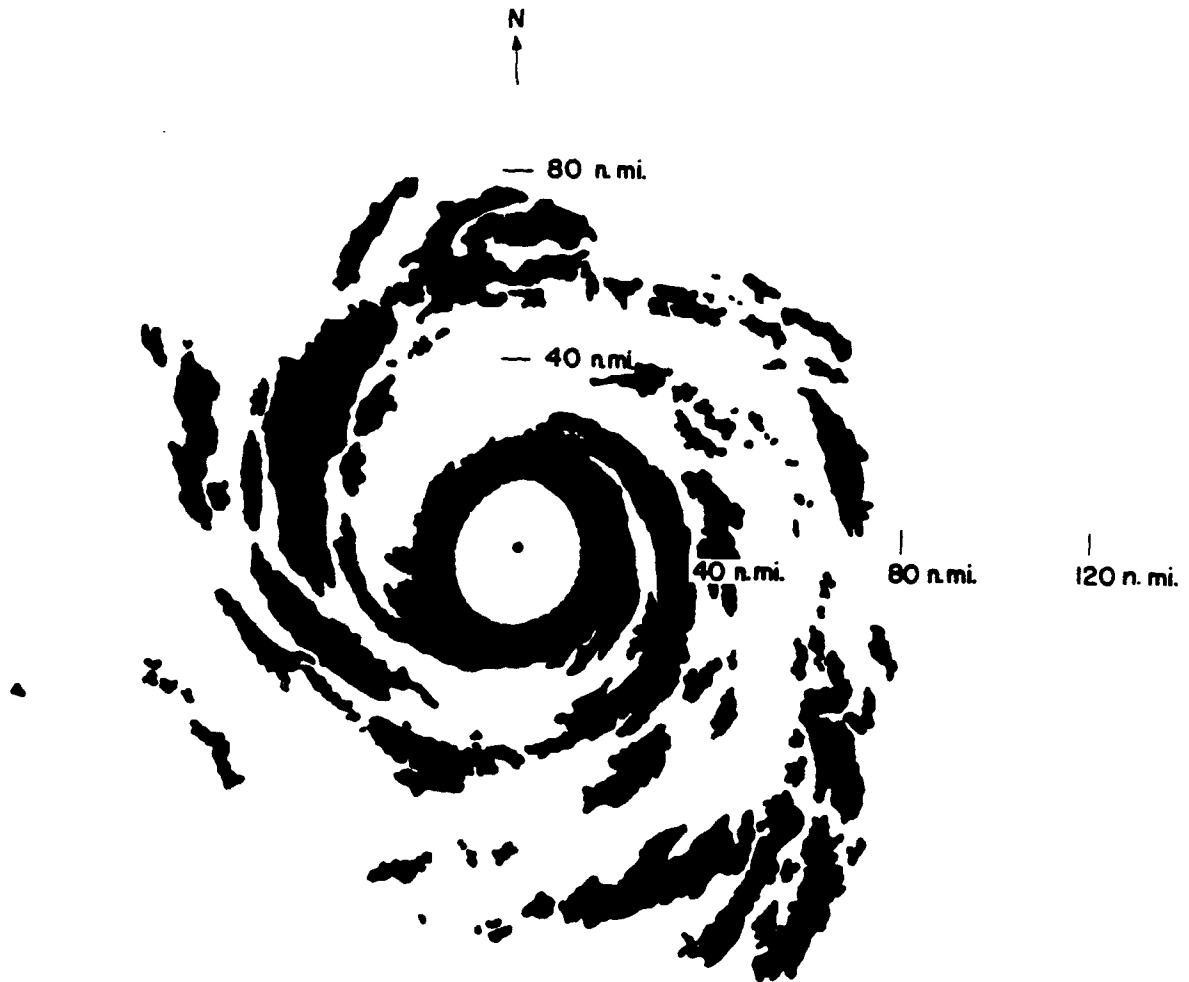


Figure 3.1: An example of inner hurricane convective bands. Hurricane Cleo on 18 August 1958 when it was just east of Bermuda and moving NNE at 7 ms^{-1} . Maximum winds were approximately 47 ms^{-1} and the minimum surface pressure was 970 mb. From Gray, 1964.

processes of wave breaking, vortex merger, and inner band formation will be presented in sections 3.4 and 3.6. We will discuss the relation between regions of high PV and regions of convection in section 3.2.

3.2 Potential Vorticity in the Shallow Water Framework

In tropical cyclone studies, whether observational or numerical, the output is most often examined in terms of the wind and mass fields. In the present study, we wish to examine a field which combines the wind and mass fields to form a single conservative field, i.e. PV. In this section, we derive the PV equation in the shallow water framework and discuss some of its conservative properties.

The derivation of the PV equation for the shallow water system is most easily done when the governing equations are written in advective form. We therefore rewrite (2.1)–(2.3) as

$$\frac{\partial u}{\partial t} + u \frac{\partial u}{\partial x} + v \frac{\partial u}{\partial y} - fv + \frac{\partial \phi}{\partial x} = F \quad (3.1)$$

$$\frac{\partial v}{\partial t} + u \frac{\partial v}{\partial x} + v \frac{\partial v}{\partial y} + fu + \frac{\partial \phi}{\partial y} = G \quad (3.2)$$

$$\frac{d(H+h)}{dt} + (H+h) \left(\frac{\partial u}{\partial x} + \frac{\partial v}{\partial y} \right) = \frac{S}{g}, \quad (3.3)$$

where $d/dt \equiv \partial/\partial t + u\partial/\partial x + v\partial/\partial y$. Using (3.1)–(3.2), we first derive an equation for the vorticity of the fluid. This is done taking $\partial/\partial x(3.2) - \partial/\partial y(3.1)$. After rearranging terms, the vorticity equation can be written as

$$\frac{d\zeta}{dt} + (f + \zeta) \left(\frac{\partial u}{\partial x} + \frac{\partial v}{\partial y} \right) = \frac{\partial G}{\partial x} - \frac{\partial F}{\partial y}. \quad (3.4)$$

The PV equation can now easily be obtained by combining (3.3) and (3.4) to eliminate the divergence terms. We do this by taking $(H+h)(3.4) - (\zeta + f)(3.3)$. After rearrangement of terms, the PV equation can be written as

$$\frac{dP}{dt} = (H+h)^{-1} \left(\frac{\partial G}{\partial x} - \frac{\partial F}{\partial y} - \frac{PS}{g} \right). \quad (3.5)$$

where PV is represented by the variable P which is given as

$$P \equiv \frac{\zeta + f}{H + h}. \quad (3.6)$$

We see from (3.5) that PV is materially conserved for adiabatic and frictionless flow, i.e. $F = G = S = 0$.

Another useful feature of PV is that small amplitude gravity waves are invisible on PV-maps. To show this, we first linearize (3.1)–(3.2) about a basic state of rest and derive a PV equation in much the same manner as we did above. That is, we first derive a linear vorticity equation and eliminate the divergence between it and the continuity equation. The resulting equation will be a conservation equation for the perturbation PV which is defined as

$$P' = c^2 \zeta' - f \phi'. \quad (3.7)$$

One can also show that (3.7) can be obtained (within a constant) by linearizing (3.6) about a basic state of rest.

We can now easily show that the gravity wave contribution to P' is identically zero. The first step is to transform (3.7) to Fourier spectral space to obtain

$$P'_{kl} = c^2 (ikv'_{kl} - ilu'_{kl}) - f\phi'_{kl}, \quad (3.8)$$

where k , and l again represent wavenumbers in the x and y directions respectively. The second and final step is to refer back to the transformation kernel (2.13) and replace u'_{kl} , v'_{kl} and ϕ'_{kl} in (3.8) with the first, second, and third components of \mathbf{K}_{klq} for $q = 1, 2$ respectively. In doing so, P' will sum identically to zero. We therefore conclude that small amplitude gravity waves are invisible on PV maps.

The PV discussed above is the shallow water version of the true Rossby-Ertel PV which is defined as $(1/\rho)\vec{\zeta}_a \cdot \nabla\theta$ where ρ is the density, $\vec{\zeta}_a$ is the absolute vorticity vector and θ is the potential temperature. In regions of intense convection, where both $\vec{\zeta}_a$ and $\nabla\theta$ tend to be large (especially their vertical components), the PV should also be expected to be large. Since the shallow water PV is mathematically and physically analogous to the Rossby-Ertel PV, we conclude that it too must be large where the convection is intense. Because of this, we expect the shallow water PV to not only be a materially conservative variable, but also an indicator of past convection. It must be mentioned however, that no computations of PV in hurricanes based on observed data have been made (that the

author is aware of). This can be explained by both the lack of dense enough observational data to compute PV accurately and the lack of appreciation for PV in tropical dynamics.

3.3 The Concept of Potential Vorticity (Rossby) Waves in Tropical Cyclones

The most elementary treatment of Rossby waves (Platzman, 1968) begins with the linearized (about a resting basic state) nondivergent, barotropic, β -plane model in which the northward gradient of basic state absolute vorticity is the constant β . Under conservation of absolute vorticity, a sinusoidal disturbance causes fluid particles which are displaced northward to acquire a clockwise spin. A fluid particle which has not been displaced and which lies between northward displaced particles to its west and southward displaced particles to its east, will be induced to move southward by the clockwise turning particles to the west and the counterclockwise turning particles to the east. Thus, the whole pattern will propagate to the west, creating what is commonly referred to as a Rossby wave. The mechanism by which Rossby waves are generated is referred to as the β -effect.

A more general treatment of Rossby waves (Hoskins *et al.*, 1985, section 6) begins with consideration of the Rossby-Ertel potential vorticity field displayed on an isentropic surface. A reasonable basic state is one in which the isolines of PV are oriented in the east-west direction with higher values to the north, which yields a generalized β -effect. If the PV contours (which are also material contours) are perturbed in a sinusoidal fashion, a row of alternating positive and negative PV anomalies is produced. By the invertibility principle (which can take on a variety of forms depending on the balance approximation being used) these PV anomalies induce a flow. Just as in the elementary treatment discussed in the previous paragraph, the induced flow makes the PV anomalies propagate westward relative to the basic flow.

In all but the very upper tropospheric part of an axisymmetric tropical cyclone the isolines of PV are circles with the highest values of PV found in the center of the cyclone (Schubert and Alworth, 1987). According to the general argument given in the previous paragraph, this axisymmetric PV field provides a basic state with a monotonic inward

increase of PV on which Rossby waves can propagate. If the PV pattern is only slightly disturbed from circular isolines, there is a restoring effect and Rossby wave propagation—the PV contours simply undulate for long periods of time. In certain circumstances, the positive PV anomalies quickly begin to elongate and form spiral tongues of high PV fluid which become longer, thinner and more circular in time.

To better understand PV waves, let us consider a nondivergent, barotropic fluid system in cylindrical coordinates which is linearized about a basic state tangential flow $\bar{v}(r)$. In this system, the vorticity plays the role of PV as the conservative dynamic variable. Following Lamb (1945), the basic state vorticity is assumed to have the top-hat form given below in (3.11). The corresponding basic state streamfunction has the form

$$\bar{\psi}(r) = \begin{cases} \frac{1}{4}\xi(r^2 - r_1^2) & \text{if } 0 \leq r \leq r_1 \\ \frac{1}{2}\xi r_1^2 \ln(r/r_1) & \text{if } r_1 \leq r < \infty \end{cases}, \quad (3.9)$$

where ξ and r_1 are constants. One differentiation of (3.9) yields the basic state (Rankine) tangential flow

$$\bar{v}(r) = \frac{d\bar{\psi}}{dr} = \begin{cases} \frac{1}{2}\xi r & \text{if } 0 \leq r \leq r_1 \\ \frac{1}{2}\xi r_1^2/r & \text{if } r_1 \leq r < \infty \end{cases}, \quad (3.10)$$

while a second differentiation yields the piecewise constant vorticity pattern

$$\bar{\zeta}(r) = \frac{d(r\bar{v})}{rdr} = \frac{d}{rdr} \left(r \frac{d\bar{\psi}}{dr} \right) = \begin{cases} \xi & \text{if } 0 < r < r_1 \\ 0 & \text{if } r_1 < r < \infty \end{cases}. \quad (3.11)$$

Now suppose the interface r_1 is perturbed by an amount $\eta(\varphi, t)$ in the sinusoidal fashion $\eta(\varphi, t) = \hat{\eta}e^{i(m\varphi - \nu t)}$, where $\hat{\eta}$ is a complex constant, m the tangential wavenumber and ν the frequency. The interface perturbation results in a circular chain of vorticity anomalies, as shown in Fig. 3.2 for $m = 4$. Away from the interface the vorticity is unperturbed from its basic state value so that $\nabla^2\psi' = 0$ for $r \neq r_1$, or, assuming $\psi'(r, \varphi, t) = \Psi(r)e^{i(m\varphi - \nu t)}$,

$$r \frac{d}{dr} \left(r \frac{d\Psi}{dr} \right) - m^2\Psi = 0 \quad \text{for } r \neq r_1 + \eta. \quad (3.12)$$

As solutions of (3.12) which are bounded at $r = 0$ and as $r \rightarrow \infty$ we have

$$\Psi(r) = A \begin{cases} (r/r_1)^m & \text{if } 0 \leq r \leq r_1 + \eta, \\ (r_1/r)^m & \text{if } r_1 + \eta \leq r < \infty, \end{cases} \quad (3.13)$$

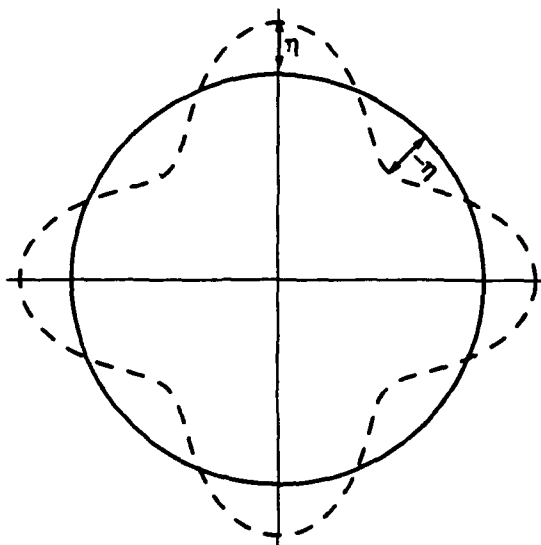


Figure 3.2: A wavenumber four perturbation (dashed) of a circular (smooth) PV surface.

where A is a constant which must now be related to $\hat{\eta}$. Note that $\Psi(r)$ is a continuous function in the small amplitude approximation, i.e. as $\eta \rightarrow 0$. Continuity of v at $r_1 + \eta$ yields

$$\frac{1}{2}\xi r^2 + mA \left(\frac{r}{r_1}\right)^m e^{i(m\varphi - \nu t)} = \frac{1}{2}\xi r_1^2 - mA \left(\frac{r_1}{r}\right)^m e^{i(m\varphi - \nu t)},$$

which, when evaluated at $r_1 + \eta$ and linearized, yields

$$mA = -\frac{1}{2}\xi r_1 \hat{\eta}. \quad (3.14)$$

Since vorticity is conserved, the vorticity discontinuity must move with the fluid. For this reason, the normal component of velocity for a particle on the boundary must be equal to the velocity of the boundary itself. Using this, our equation for the particle displacement can be written

$$\frac{\partial \eta}{\partial t} + \bar{\omega} \frac{\partial \eta}{\partial \varphi} = u' = -\frac{im}{r} \psi', \quad (3.15)$$

where $\bar{\omega} \equiv \bar{v}/r$. When (3.13)–(3.14) are substituted into (3.15) we obtain the dispersion relation

$$\frac{\nu}{m} = \bar{\omega} - \frac{\xi}{2m} = \frac{1}{2}\xi \left(1 - \frac{1}{m}\right). \quad (3.16)$$

From (3.16) we see that like Rossby waves, these PV waves propagate against the mean wind with phase speeds which increase (decrease) with wave length (number). Thus,

wavenumber $m = 1$ is stationary and wavenumbers $m = 2, 3, 4$ move respectively at $\frac{1}{2}$, $\frac{2}{3}$, $\frac{3}{4}$ the speed of the basic state tangential flow. Since the above analysis was first given by William Thomson (Lord Kelvin) in 1880 and was summarized by Lamb (1932, pages 230-231), attributing the origin of this concept to Rossby (1939) is not historically accurate. However, calling the waves obeying the dispersion relation (3.16) Kelvin waves would be confusing for obvious reasons. Here, we shall follow conventional terminology and refer to these waves as Rossby waves, or more generally, PV waves.

3.4 Inner Band Formation by Wave Breaking

The evolution of asymmetric potential vorticity patterns has been studied extensively using contour dynamical methods for the barotropic, nondivergent governing equations (e.g. Dritschel, 1986; Melander *et al.*, 1987b). In contour dynamics, the evolution of a two dimensional area of uniform PV (or vorticity for the case of nondivergent, barotropic flow) is traced by predicting the position of the interface separating distinct areas of PV. This can be done if the flow is adiabatic and frictionless since under these conditions PV is materially conserved and thus the PV boundary represents a material surface. In the above studies, the asymmetric PV patterns undergo a filamentation process which ejects filaments of high PV air into regions of relatively low PV air. This filamentation process can be thought of as an irreversible PV wave breaking process in which the area where the filaments exist is the "surf zone". This terminology was first used by McIntyre and Palmer (1984) to describe the synoptic scale behavior of the winter middle stratosphere.

In this section, we attempt to show that the underlying dynamics of Rossby wave breaking may be used to help understand the the evolution of inner bands in tropical cyclones. We do this by first discussing the concept of Rossby wave breaking and surf zones, and then demonstrating the usefulness of this concept through the integration of the shallow water model. The shallow water model is useful because it allows for maximum resolution in the horizontal and maximum simplification in the vertical while still capturing the fundamental features of vortex dynamics. These features include the necessary mechanisms for PV waves, gravity-inertia waves and two-dimensional turbulence.

Lastly, we demonstrate that filamentation and wave breaking are slow manifold processes, thus suggesting that transient gravity waves play a very minor role in the formation of spiral bands.

3.4.1 The Concept of PV Wave Breaking and Surf Zones

As mentioned previously, the concept of wave breaking was first introduced observationally by McIntyre and Palmer (1983,84) in their analysis of the extratropical middle stratosphere. Numerical studies of this same phenomenon were later presented by Juckes and McIntyre (1987). In these studies, isentropic surfaces in the stratosphere were divided qualitatively into two distinct zonally asymmetric areas. These areas were coined by McIntyre and Palmer as the *main vortex*, described as an area of high PV with sharp PV gradients at its edge and the *surf zone*, described as an area where systematic large scale PV gradients are comparatively weak. The name surf zone was given to represent the region where PV wave breaking occurs.

Having demonstrated the existence of PV waves in tropical cyclones in the previous section, we can now define what is meant by wave breaking. The concept of PV wave breaking bears a conceptual resemblance to waves which break on the shores of large bodies of water, thus prompting the use of the term *surf zone*. If a circular chain of particles all having the same value of PV were perturbed in a sinusoidal fashion, they would simply undulate about their original position and the wave would propagate similar to a gravity wave in a body of water. Under certain conditions, however, the chain of particles does not simply undulate, but rather, some particles are ejected irreversibly away from their original positions similar to waves breaking on the shore of a beach. McIntyre and Palmer (1985) envisaged wave breaking as the rapid, irreversible deformation of material contours. For the adiabatic and frictionless shallow water model, the material contours in question are simply isopleths of PV. Wave breaking in this context is important because it often determines whether PV waves will make quasi-permanent changes to the mean flow in which they are embedded (McIntyre and Palmer, 1985). Before continuing, however, we must first define what is implied by the words "rapid" and "irreversible" in the definition of wave breaking.

The word "rapid," in the context of wave breaking, as defined by McIntyre and Palmer, implies the time scale of the material disturbance should not be much longer than a typical intrinsic wave period in the area of interest but should also be much shorter than dissipative time scales. We will show later in this section that our interpretation of PV wave breaking in tropical cyclones meets both of these criteria. The word "irreversible," as used by McIntyre and Palmer is defined to be conceptually similar to the definition used in statistical mechanics. That is, an irreversible process is one in which small changes in the material contours cannot be made to retrace their path. Unlike in statistical mechanics, however, we concern ourselves only with the bulk properties of the fluid, not the molecular scale properties. As McIntyre and Palmer point out, the irreversibility of the material contours in the fluid dynamical sense would be present regardless of whether or not microscopic dissipative terms such as diffusion were present. As an example of fluid-dynamical irreversibility, consider Fig. 3.3 which was taken from Welander (1955). Figure 3.3 shows the time evolution of a passive material tracer in a laboratory tank containing a rotating fluid. As time moves forward from a-e the material contours undergo an irreversible transformation in the sense that a reverse transformation from e-a is never observed, even though diffusion plays only a very minor role.

It should also be mentioned, as McIntyre and Palmer (1984) point out, that wave breaking does *not* imply instabilities exist in the flow. Although instabilities can be important in certain cases, the irreversible material deformations discussed above can take place in the absence of any recognizable instabilities. As we shall see in chapter five, it is the wave breaking process which causes instabilities and not vice versa.

Finally, it should be remembered that the concept of wave breaking is not an exact diagnostic tool. There are no mathematical derivations or specific patterns which uniquely define wave breaking. The concept is nonetheless useful tool in understanding the complex nature of wave-mean flow interactions. As McIntyre and Palmer best stated,

"In reality we are dealing with complicated kinds of fluid motion to which no analytical theory is likely to be self-consistently applicable over significant spans of time, particularly linear theory. However, the lack of a complete

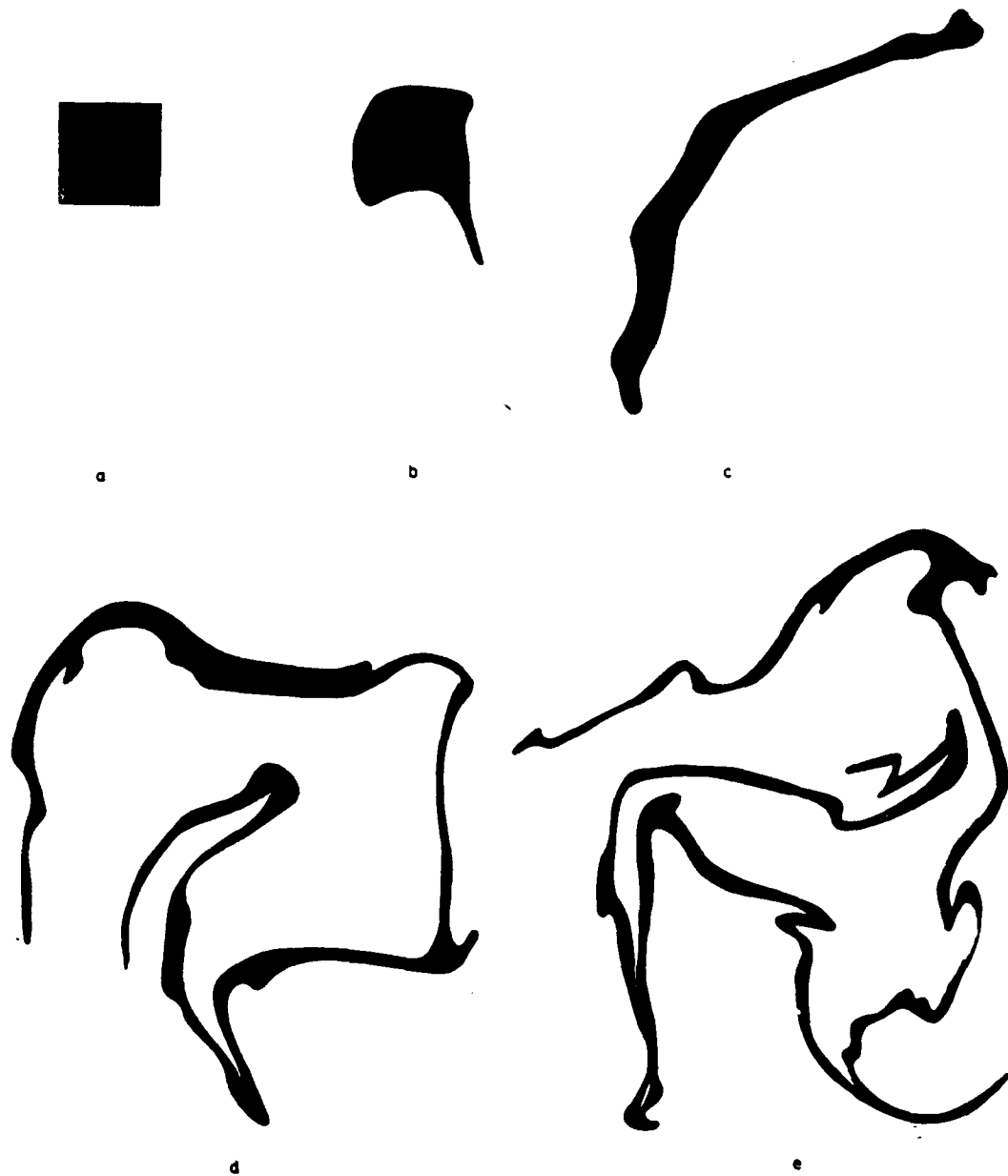


Figure 3.3: An example of fluid-dynamical irreversibility produced by injecting dye into a slowly rotating laboratory tank of water. (From Welander, 1955.)

theory should not deter one from using a concept, especially one which has been found to be useful as a heuristic organizing concept when trying to make sense of very complicated phenomena." *McIntyre and Palmer, 1985*

To demonstrate the concept of wave breaking, we present a model integration taken from Jukes and McIntyre (1987). The model simulation was an integration of the nondivergent barotropic vorticity equation in spherical coordinates with an initial state consisting of a zonally averaged vorticity field which monotonically increased with latitude. The vorticity field was then forced with a time dependent wavenumber one disturbance. The purpose of the experiment was to simulate the effect of a planetary scale Rossby wave incident from below on a layer lying between two isentropic surfaces. Fig. 3.4 shows the results from this integration. By day four of the integration, the wave breaking process has begun to take effect and the material contours have begun a rapid and irreversible deformation. By day 12 the main vortex has eroded considerably and the vorticity (PV) has spread over a larger area, thereby altering the initial mean wind field.

Although tropical cyclones are considerably different in terms of scale and forcing mechanisms from the stratosphere, the concept of wave breaking is also of considerable use in examining the evolution of spiral bands in tropical cyclones. The dynamical similarity lies in the fact that tropical cyclones can also be described by a main vortex surrounded by a surf zone in which the spiral bands are found. In this context, the wave breaking process can be thought of as modifying the mean wind profile by ejecting high PV air down gradient into regions of relative low PV.

3.4.2 Wave Breaking Experiments

The wave breaking experiments presented in this section are accomplished by specifying an asymmetric initial vorticity field which is about to undergo an irreversible material deformation and letting the model evolve unforced. We do this to simulate the effects of PV asymmetries on hurricane band formation. In reality, hurricane banding is a continual process in which asymmetries are constantly being generated. In contrast, the wave breaking experiments in this section consider the evolution of a single asymmetry in the PV field after being formed by convective heating for example.

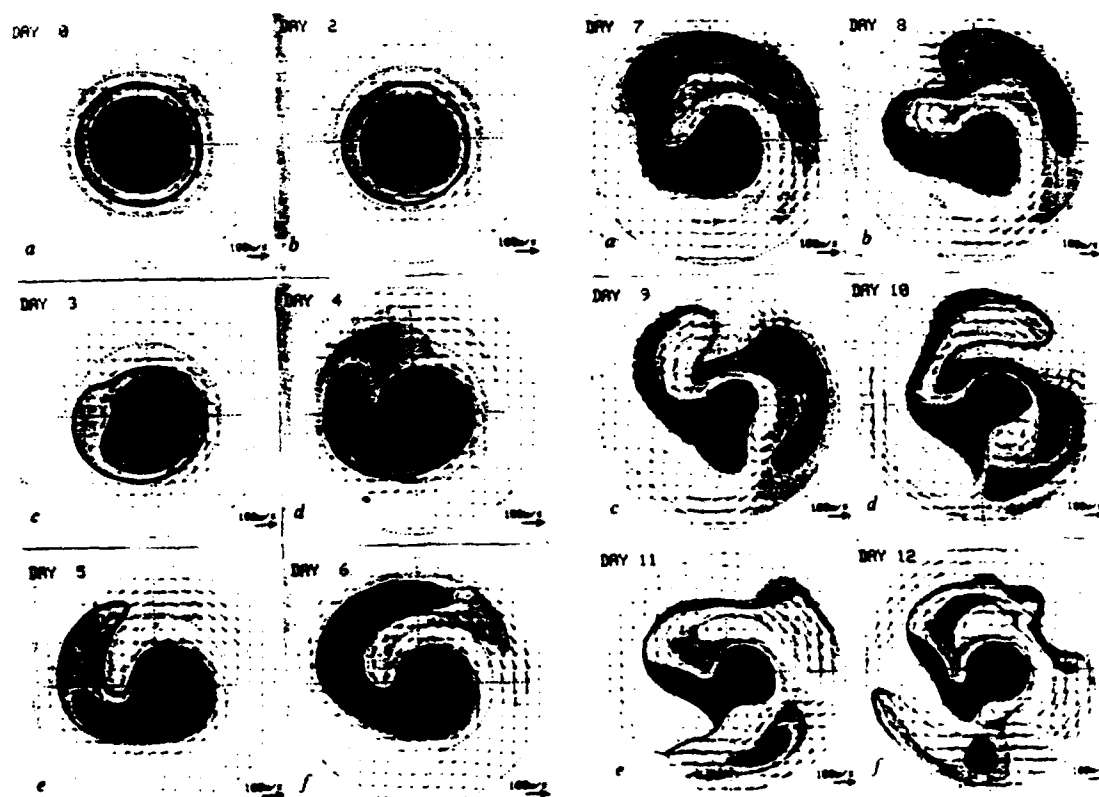


Figure 3.4: An example of the wave breaking process in the mid-stratosphere as simulated with a nondivergent barotropic model. The initially symmetric vortex is forced with a wavenumber one disturbance. Dark shading corresponds to high vorticity (or PV). (From Jukes and McIntyre, 1987.)

The reason we choose to specify the vorticity field rather than the PV is the ease with which it can be inverted to obtain the initially balanced wind and mass fields. Because the PV field closely mirrors the vorticity field, we are indirectly specifying the shape of the initial PV field which, as mentioned previously, is materially conserved for the adiabatic and frictionless flow considered in this section.

The initial vorticity patterns used in these experiments are of two types. The first type of vorticity pattern consists of non-intersecting, non-concentric circles whose radii all fall along the same axis. The second type of vorticity pattern consists of concentric ellipses all sharing similar orientations and aspect ratios. These particular patterns were chosen to represent primarily wavenumber one and wavenumber two PV asymmetries respectively. The methods by which these fields are determined are described below.

To obtain a wavenumber one vorticity pattern, we generate a continuous set of nonconcentric, non-intersecting circles whose centers all fall on the y -axis. This is a wavenumber one pattern in the azimuthal sense; that is, if a compass were positioned at the center of the circle of smallest radius, then as the compass rotated 360° one relative maximum and one relative minimum would be encountered. In the Fourier sense, however, this would only be a primarily wavenumber one pattern. We generate a vorticity field of this type by first defining the function $R(r)$ which specifies how the radius increases as the centers of the circles are moved away from the position (x_0, y_0) in the center of the domain. We define this function as

$$R(r) = \frac{(y_1 - y_0)}{r_1} r + y_0 \quad (3.17)$$

where r is the radius and r_1 is the radius of the circle whose center is located at (x_0, y_1) . It should be noted that if the slope of (3.17) exceeds one, the circles will intersect. With $R(r)$ defined, the field of circles can be defined using the standard equation for a circle in Cartesian coordinates, i.e.

$$(x - x_0)^2 + (y - R(r))^2 = r^2. \quad (3.18)$$

By substituting (3.17) into (3.18) and using the quadratic formula, we can obtain the radius of the circle which satisfies our criteria for any point (x, y) . The next step is to

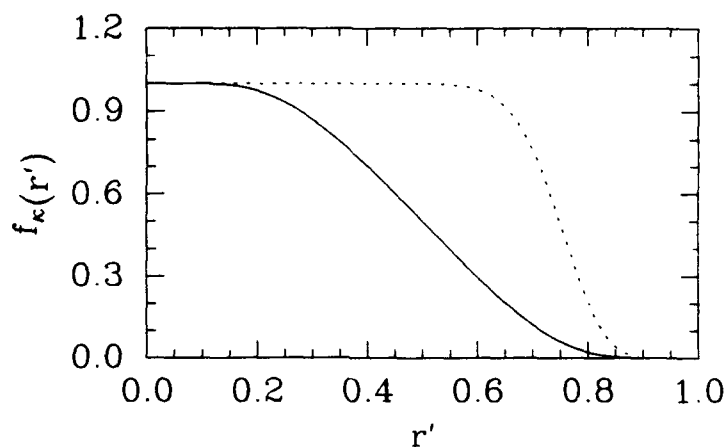


Figure 3.5: The profile function, $f_{\kappa}(r')$, as a function of r' for $\kappa = 2.56$ (smooth curve) and $\kappa = 28.38$ (dotted curve).

specify the vorticity, ζ , as a function of the radius. We follow Melander *et al.*, (1987b) by specifying $\zeta(r)$ as a distribution with a monotone profile function $f_{\kappa}(r)$, $r > 0$. We therefore define the vorticity to be

$$\zeta(r) = \hat{\zeta} \begin{cases} 1 & (r \leq R_i) \\ 1 - f_{\kappa}[(r - R_i)/(R_0 - R_i)] & (R_i < r < R_0) \\ 0 & (R_0 \leq r) \end{cases}, \quad (3.19)$$

where R_i represents the radius at which the vorticity begins to decrease and R_0 is the radius at which the vorticity vanishes. The profile function, $f_{\kappa}(r)$, is chosen from the one-parameter family $\{f_{\kappa}; \kappa > 0\}$ where

$$f_{\kappa}(r') = \exp[-\kappa r'^{-1} \exp(1/(r' - 1))], \quad 0 < r' < 1. \quad (3.20)$$

This function smoothly connects the points R_i and R_0 . The parameter κ is the “steepness parameter” which determines how rapidly the vorticity decreases as the radius increases. If we choose $\kappa = \frac{1}{2}(\exp 2)(\ln 2) \sim 2.56$ then the value of the vorticity will be one half its maximum value when $r' = 0.5$. Likewise, if we chose $\kappa = \frac{3}{4}(\exp 4)(\ln 2) \sim 28.38$ then the vorticity will be one half its maximum value when $r' = 0.75$. These functions are presented in Fig. 3.5 for the above mentioned values of κ . We see from Fig. 3.5 that region of maximum vorticity is much larger for $\kappa = 28.38$ and it decreases to zero at a much faster rate.

Using the specified initial vorticity field, we next determine the initial wind and mass fields which are consistent with this vorticity field. We first obtain the desired wind field by assuming the wind is initially nondivergent. For the shallow water model this is equivalent to assuming that $d\phi/dt = 0$. This assumption allows us to use (3.3) to define a stream function, ψ , such that

$$u = -\frac{\partial\psi}{\partial y}, \quad v = \frac{\partial\psi}{\partial x}, \quad \text{and} \quad \zeta = \nabla^2\psi. \quad (3.21) - (3.23)$$

By transforming ζ to Fourier spectral space the Laplacian operator (3.23) is easily inverted to obtain the spectral coefficients for ψ and its derivatives, i.e. u and v . Obtaining the physical space fields for u and v is then accomplished by simply performing an inverse Fourier transform.

Having found the appropriate wind field, we next determine the appropriate mass field. In order for a unique solution to exist and for transient gravity waves to be minimized, we assume the wind and mass fields are initially in balance. Possibly the simplest method of doing this is through use of the nonlinear balance equation which is obtained by deriving an equation for the local rate of change of the divergence and setting it equal to zero. A better, but more complicated, method of obtaining a balanced mass field is nonlinear normal model initialization. For this method, the time rate of change of the normal mode spectral coefficients for $q = 1, 2$ are initially forced to zero. An excellent comparison of these two methods can be found in DeMaria and Schubert (1984). In the present study we use the nonlinear balance equation method.

The nonlinear balance equation can be derived by first taking $\partial/\partial x(3.1) + \partial/\partial y(3.2)$. By neglecting the local rate of change of the divergence and heating effects from the resulting equation, we obtain an expression relating the wind and mass fields which reduces the amount of transient gravity wave activity initially, i.e.

$$\nabla^2\phi = f\zeta - \frac{\partial}{\partial y}(u\zeta) + \frac{\partial}{\partial x}(v\zeta) - \nabla^2\left(\frac{u^2 + v^2}{2}\right). \quad (3.24)$$

Using (3.24), the ϕ field can easily be found by inverting the Laplacian in Fourier spectral space and returning to physical space.

A wavenumber two vorticity pattern is generated by defining a continuous field of concentric ellipses with identical aspect ratios and orientations. This initial vorticity pattern was studied extensively by Melander *et al.* (1987b) with a nondivergent barotropic model.

We can easily generate an elliptical vorticity field by writing the equation for an ellipse in slightly less familiar form, i.e.

$$x^2 + a_r y^2 = r^2, \quad (3.25)$$

where a_r is the aspect ratio which is defined as length of semi-major axis divided by the length of the semi-minor axis and r is now the length of the semi-major axis. Thus, if we specify an aspect ratio, we can determine the corresponding length of the semi-major axis for each point (x, y) . From this, we can use (3.19)–(3.20) as we did for the wavenumber one case to determine the vorticity field. Once this is done the wind and mass fields can be determined in the same manner as discussed above. Figure 3.6 shows the wavenumber one and wavenumber two type patterns generated by the above formulation for $\kappa = 2.56$ (left) and $\kappa = 28.38$ (right). The minimum contour is 0.2 with a contour interval of 0.2. In all cases, $R_0 = 600$ km and $R_i = 0$ on a 1600×1600 km grid. For the wavenumber one patterns, the variables y_1 and r_1 were chosen to be 1200 km and 600 km respectively.

3.4.3 Numerical Results

The first set of numerical integrations were performed using the primarily wavenumber one pattern described above with no friction or heating. With the absence of friction and heating, PV is materially conserved and the entire process becomes an advective rearrangement of PV. The purpose of this experiment is to simulate the effect of an asymmetric tropical cyclone in which the convection is more intense in the southern half of the domain. It needs to be emphasized that we are in no way assuming that heating and friction are not important aspects of a tropical cyclone; they are indeed critical. We are merely attempting to isolate a particular dynamical aspect of tropical cyclone evolution.

The model domain is 1600 km by 1600 km wide with 256^2 gridpoints on the transform grid. In order to evaluate the quadratically nonlinear terms exactly, 84 waves are kept.

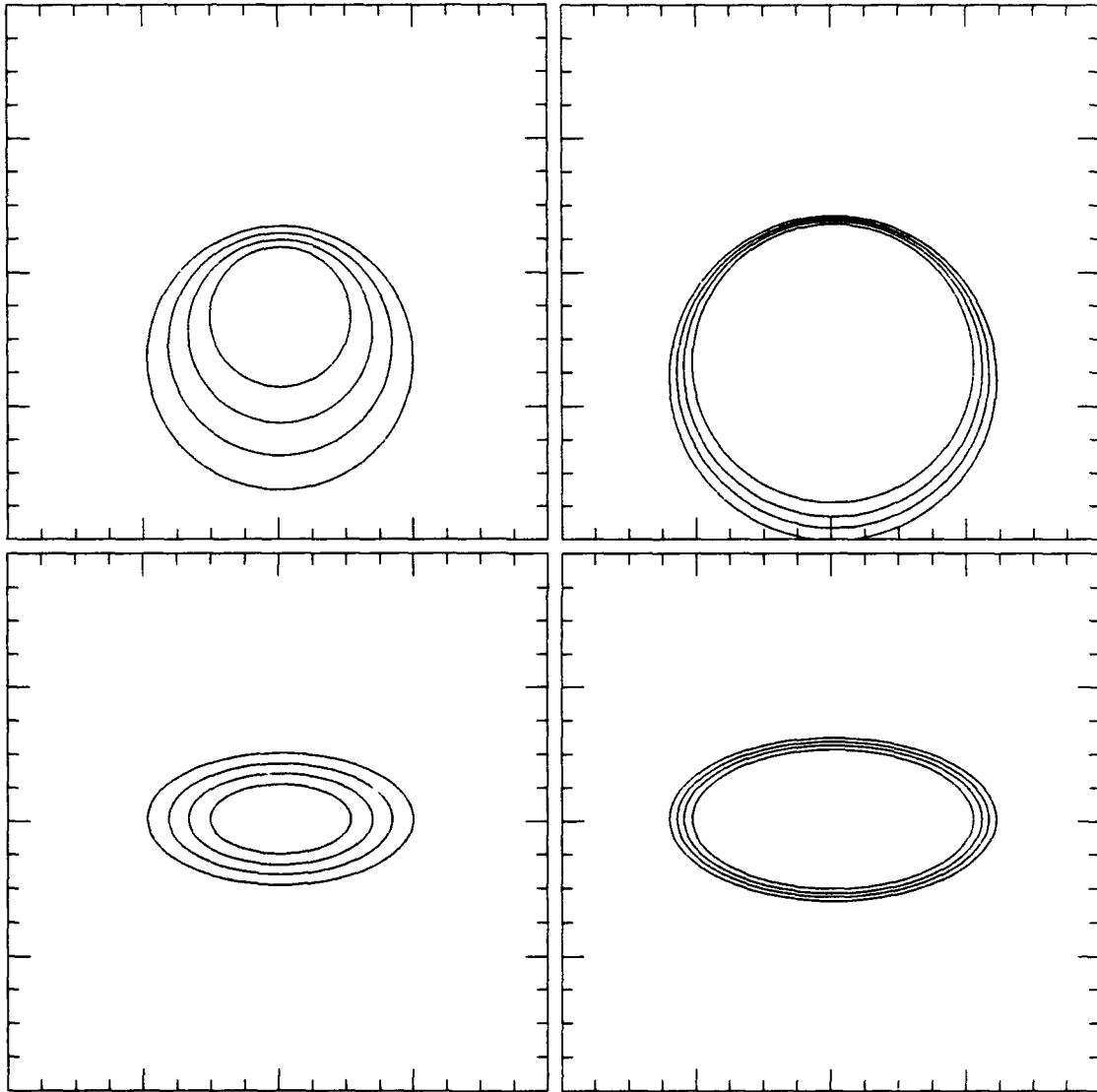


Figure 3.6: Examples of wavenumber one and wavenumber two patterns for different values of κ . See text.

The mean depth, H , of the fluid is 300m giving a gravity wave speed ($c = \sqrt{gH}$) of 54.2 ms^{-1} . The coriolis parameter f is chosen to be $5.0 \times 10^{-5} \text{ s}^{-1}$ which corresponds to roughly 20° latitude. By taking c/f we obtain a Rossby radius of deformation of 1084 km. By choosing these values of H and f we insure that centers of adjacent vortices (which implicitly surround the vortex in question because of the periodic boundary assumption) are at least one Rossby radius away from each other. To avoid resolution problems, the horizontal scales of the initial disturbances are larger than what would be expected for a typical tropical cyclone. The fundamental dynamics, however, are completely general.

Figure 3.7 shows the initial wind and mass fields for the first numerical integration which has a primarily wavenumber one horizontal structure. A maximum value of $5.0 \times 10^{-4} \text{ s}^{-1}$ or $10f$ was chosen for $\hat{\zeta}$ and $R_0 = 300 \text{ km}$ while $R_i = 0$. The steepness parameter, k , was set at 2.56 for this run. Note that only the inner $800 \times 800 \text{ km}$ part of the domain is shown. Figures 3.8–3.11 show the time evolution of the fields at six hour intervals. By six hours, wave breaking has clearly begun. Wave breaking can be most easily understood by noting that the integration of the vorticity field to get the wind field is a smoothing operation. The winds are therefore much more axisymmetric than the corresponding PV field. As a result, cross contour flow distorts the PV contours and wave breaking takes place. As mass is removed from the high PV region, the PV gradient begins to steepen. This is especially noticeable in the lower right quadrant of the domain at 6 hrs. By twelve hours the region of steep PV gradient nearly encircles the main vortex. This process continues with time until 24 hours, at which point, the gradients have become too steep for the model to resolve and the Gibb's phenomenon begins to occur. It is interesting to note the remarkable axisymmetry of the height field at all times. Because of the resolution of most observational data, if a person were to examine a similar tropical cyclone in nature, they would undoubtedly miss the asymmetries of the PV field. This suggests the need for observations at high enough resolution that actual PV values could be accurately measured.

Next we consider the effect of wave breaking on the mean mean wind field. Shown in Fig. 3.12 are the tangentially averaged fields of vorticity, normalized PV, and wind speed

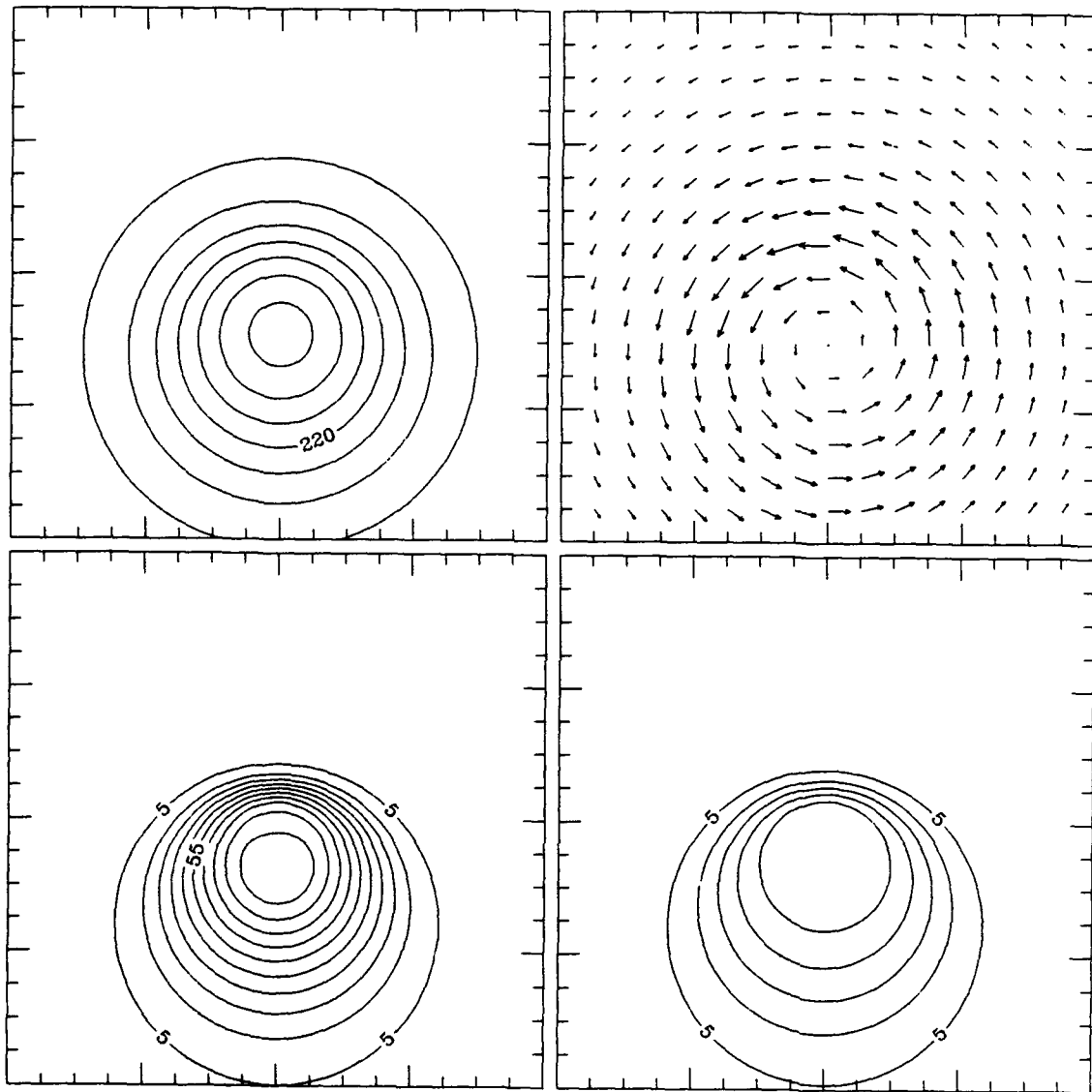


Figure 3.7: Dynamic fields at initial time for experiment one. Upper left panel corresponds to the height field with contour intervals of 20 m. Upper right panel corresponds to winds. The maximum wind vector, which is defined as the distance between two consecutive tick marks, represents 35 ms^{-1} . Lower left panel is the normalized PV (i.e. $P \times H$). Lower right panel is the absolute vorticity field. The normalized PV and absolute vorticity fields are in units of 10^{-5} s^{-1} and have contour intervals of $1.0 \times 10^{-4} \text{ s}^{-1}$.

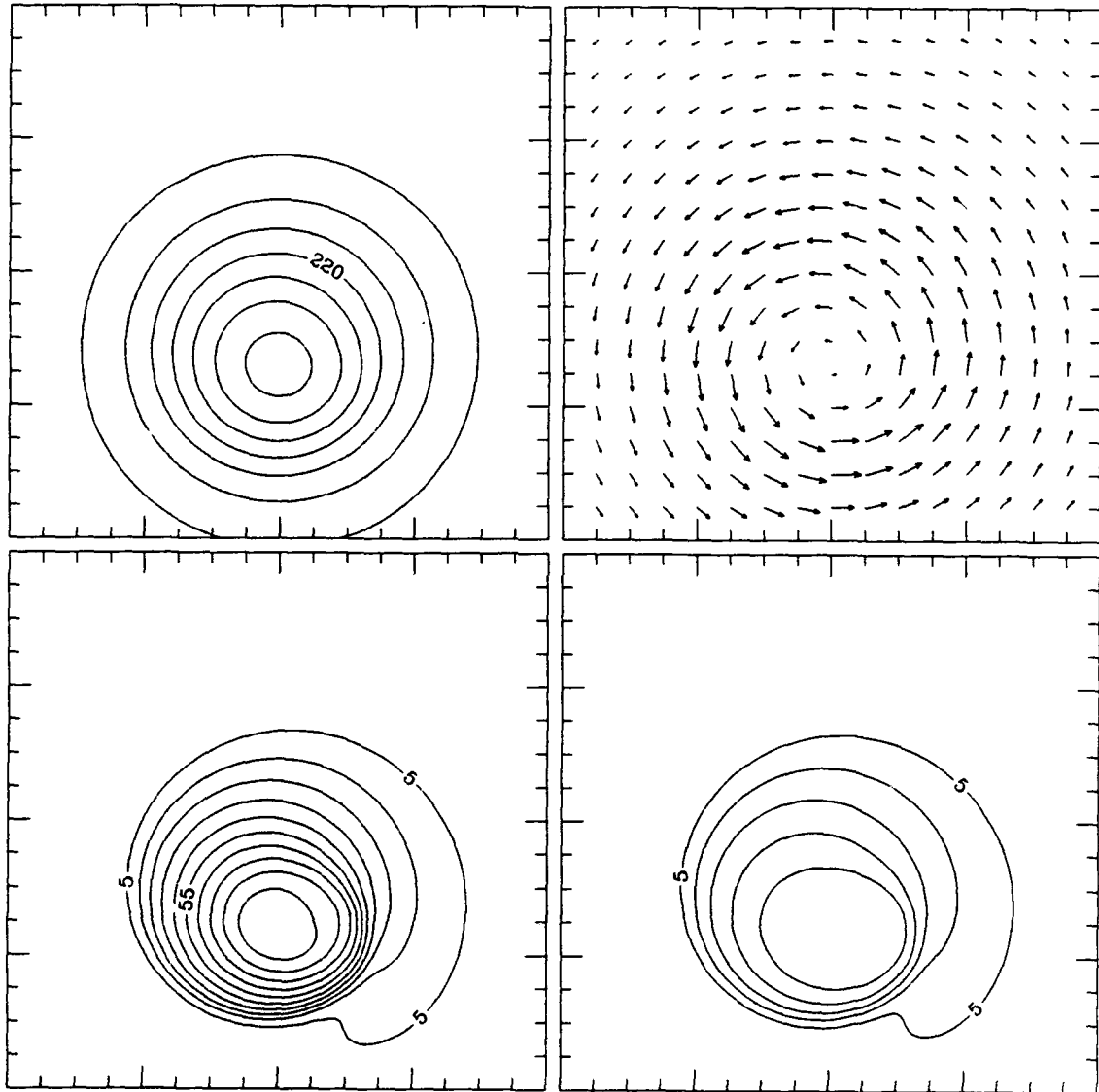


Figure 3.8: Same as Fig. 3.7 but for 6 hours.

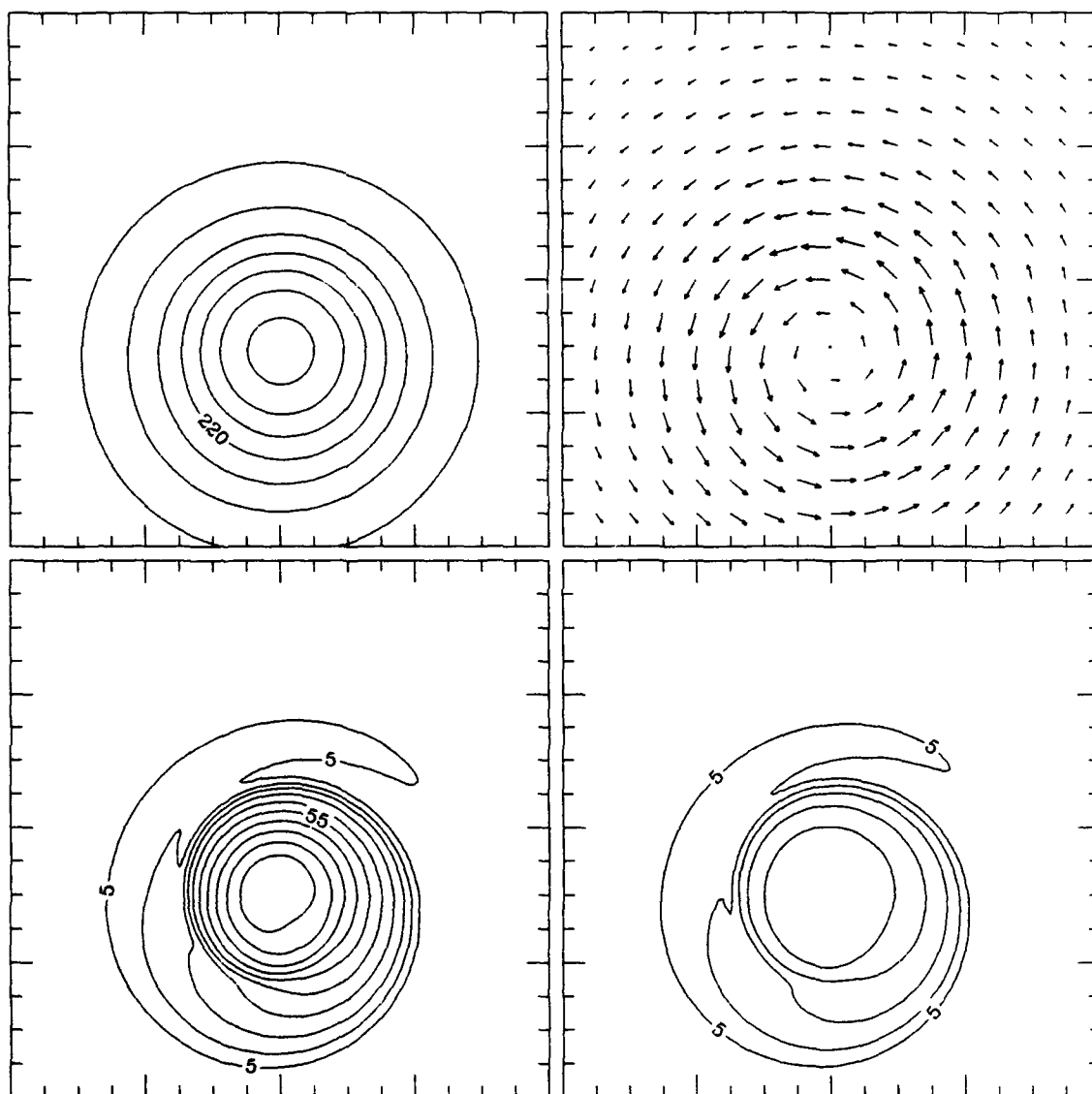


Figure 3.9: Same as Fig. 3.7 but for 12 hours.

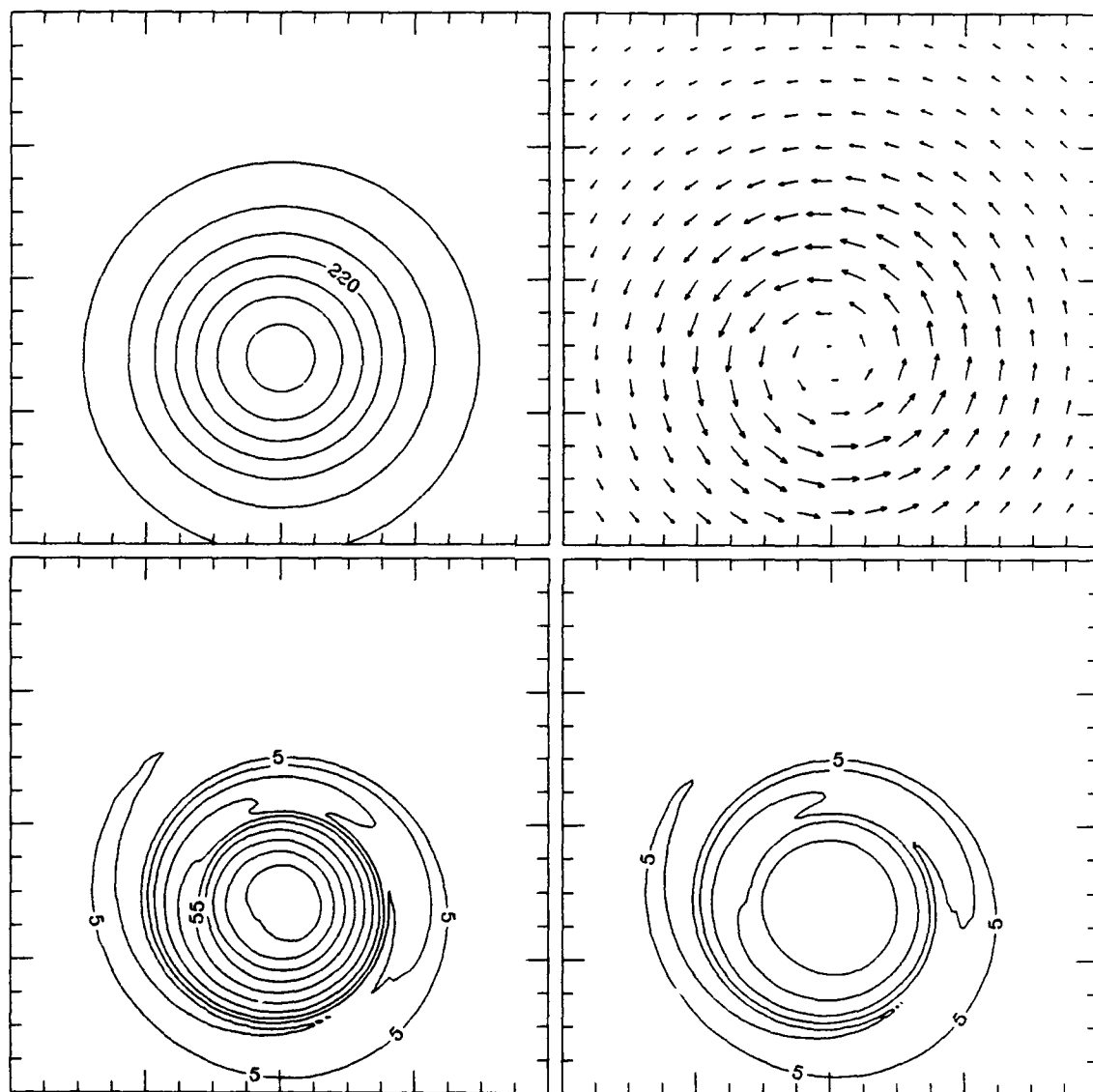


Figure 3.10: Same as Fig. 3.7 but for 18 hours.

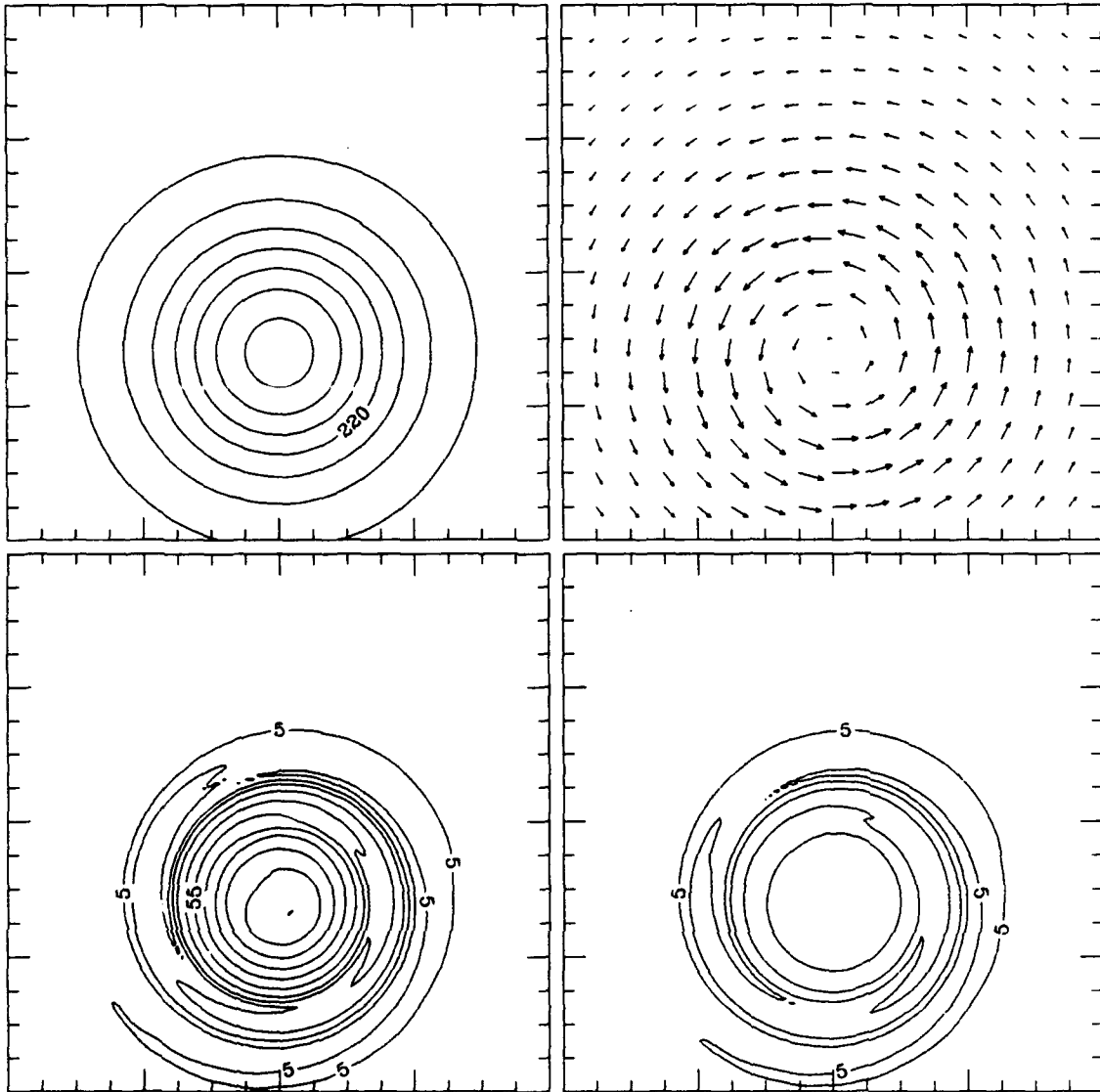


Figure 3.11: Same as Fig. 3.7 but for 24 hours.

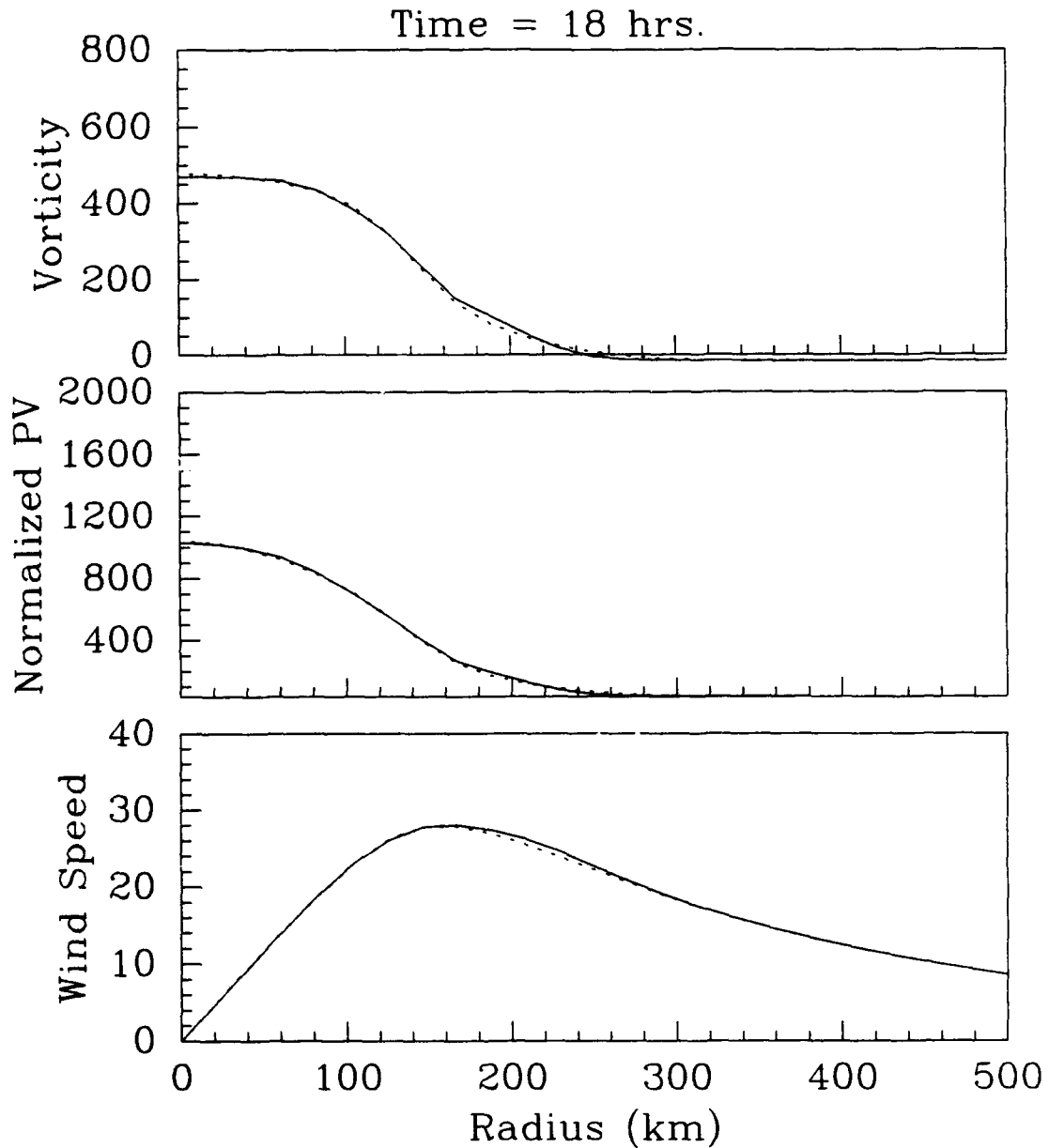


Figure 3.12: Tangentially averaged values of vorticity, normalized PV, and wind speed at 18 hours for experiment one. Dotted curves correspond to initial time and smooth curves correspond to 18 hours. The normalized PV and vorticity are in units of 10^{-6} s^{-1} and the wind speed is in ms^{-1} .

at the initial time (dotted curves) and at 18 hours (smooth curves). Although the PV is redistributed, the effect of wave breaking on the tangential mean is hardly noticeable. This is also true for the tangentially averaged wind and vorticity fields. In the following wave number two experiment, we will see that this is not always the case.

In the second experiment, the model is initialized with a primarily wavenumber two vorticity pattern. As with the previous experiments, the model run is to isolate the fundamental dynamics of a tropical cyclone in which the convective heating has a primarily wavenumber two horizontal structure. The initial vorticity for experiment two has a maximum vorticity, $\hat{\zeta}$, of $6.0 \times 10^{-4} \text{ s}^{-1}$ or $12f$. Other parameter settings include: $a_r = 2.0$, $\kappa = 2.56$, $R_0 = 400\text{km}$, and $R_i = 0$. This vorticity field corresponds to a vortex considerably larger than that expected for a typical hurricane; however, the results are completely general for the simple model we are considering here. The reason for the large vortex is to maximize the horizontal resolution while insuring the domain is at least one Rossby radius in length. The initial fields for experiment two are shown in Fig. 3.13. From Fig. 3.13 we again see that the height field is considerably more symmetric than the PV field. This again sets the stage for wave breaking. Figures 3.14–3.17 show the evolution of the fields for a 24 hour period. By six hours wave breaking has clearly begun. In contrast to experiment one, the wave breaking process causes two tongues of PV to be ejected, one at each end of the semi-major axis. As time proceeds, these tongues elongate forming what we refer to as inner bands. By 18 hours the steepening of the PV gradient by the wave breaking process has caused Gibb's phenomena to again occur. Since no damping terms were included in the integration, the effect of this is to generate spurious noise in the calculations beyond this point. By 24 hours, the bands completely surround the the main vortex.

Another prominent feature of experiment two is the symmetrization of the initially elliptical PV pattern. These results are consistent with the nondivergent results of Melander *et al.* (1987b). Heuristically, the symmetrization process can be understood by examining the radial wind field. Figure 3.18 shows the initial radial wind field superimposed over the initial PV field. As the tangential wind acts to rotate the PV pattern cyclonically, it moves

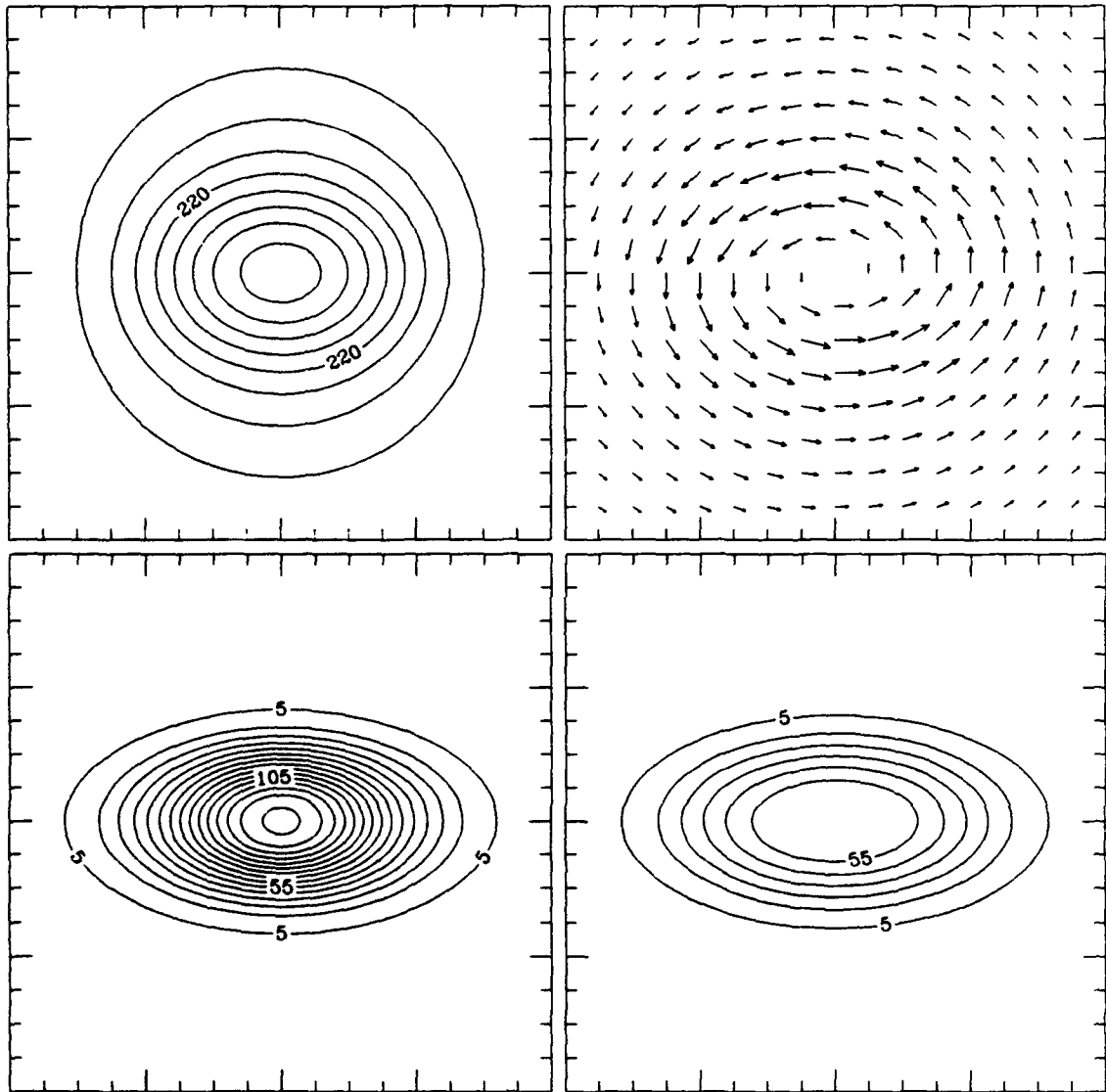


Figure 3.13: Initial fields for experiment two. Panels and contouring are the same as for experiment one.

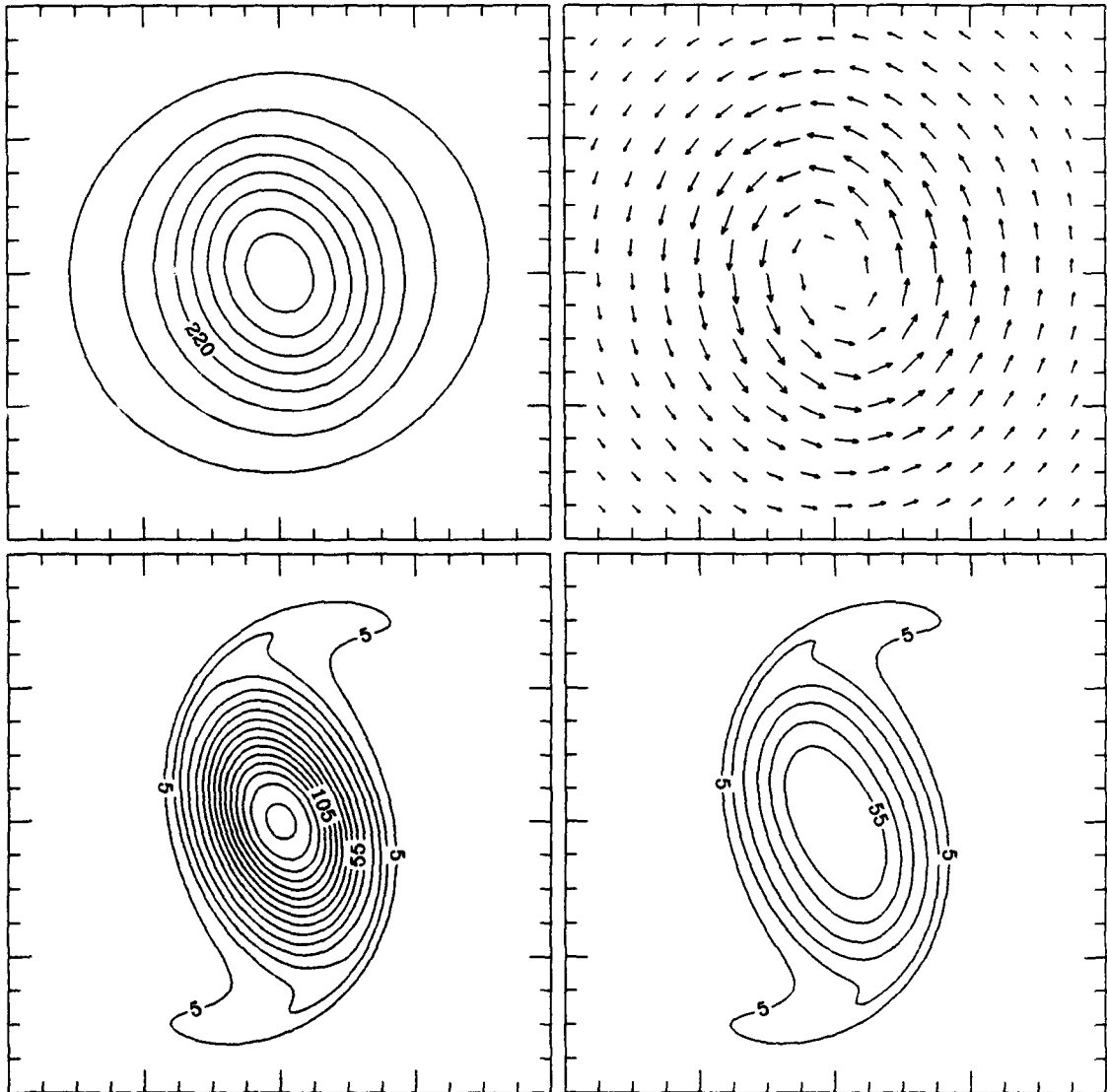


Figure 3.14: Same as Fig. 3.13 but at 6 hours.

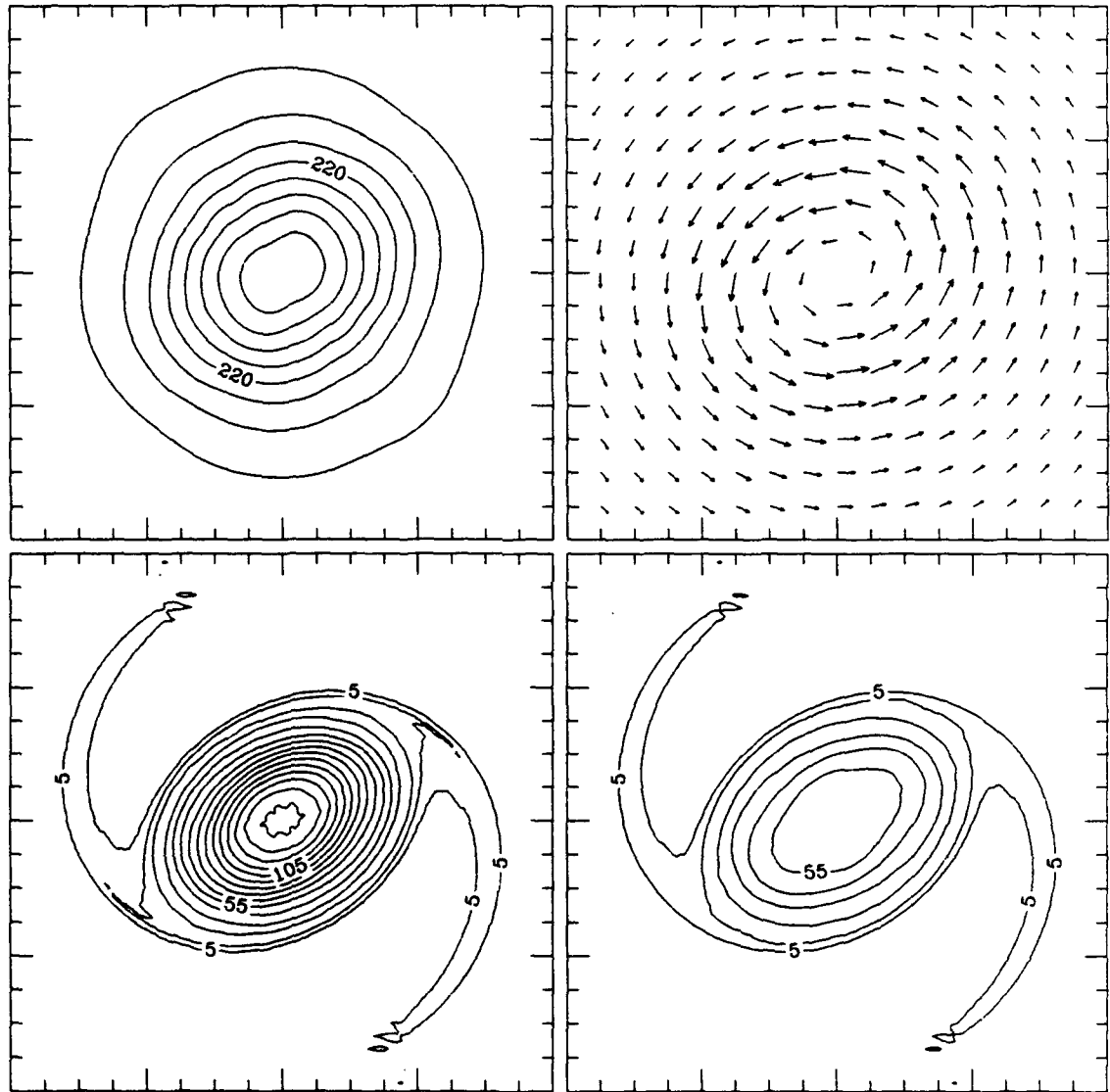


Figure 3.15: Same as Fig. 3.13 but at 12 hours.

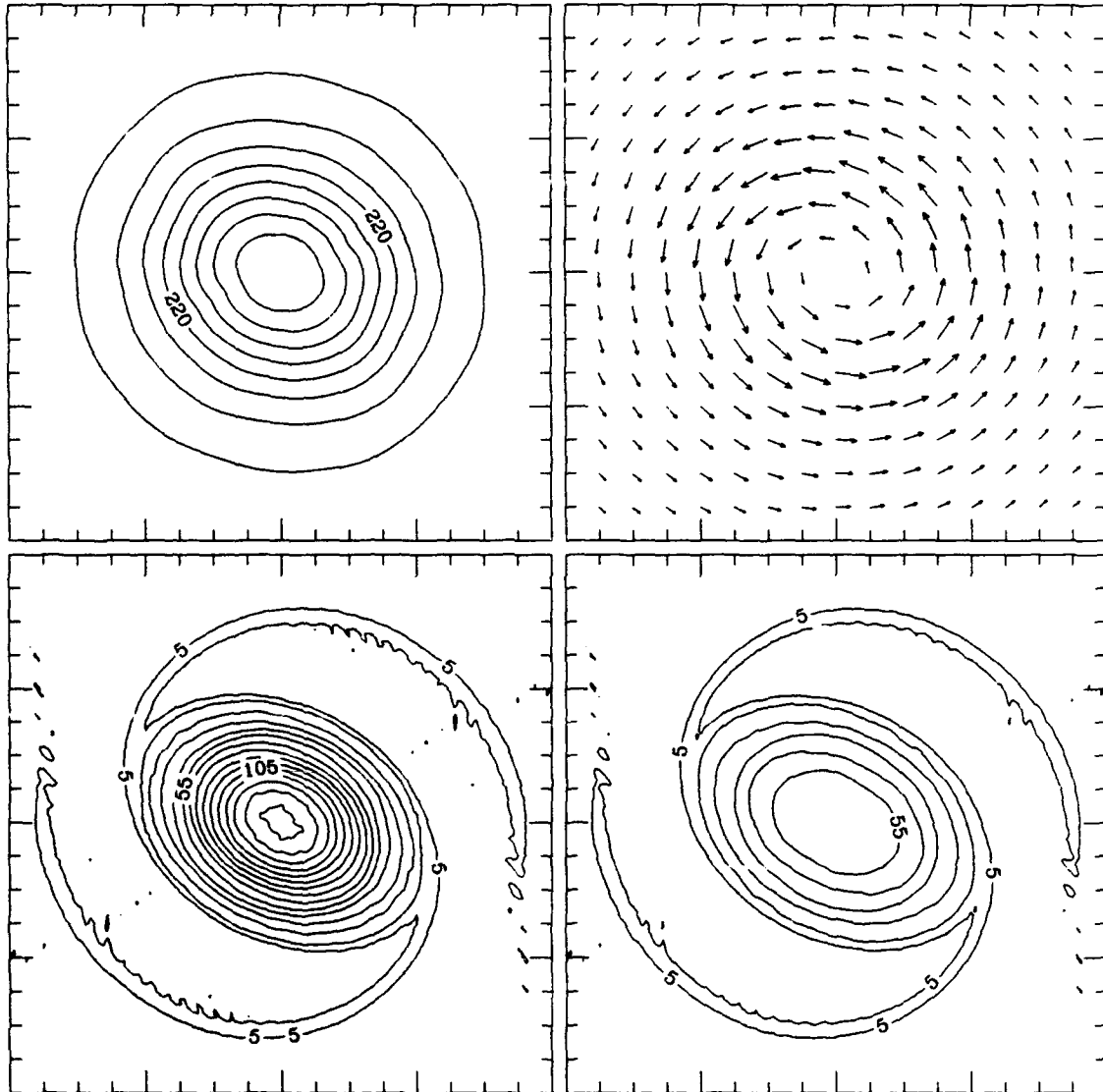


Figure 3.16: Same as Fig. 3.13 but at 18 hours.

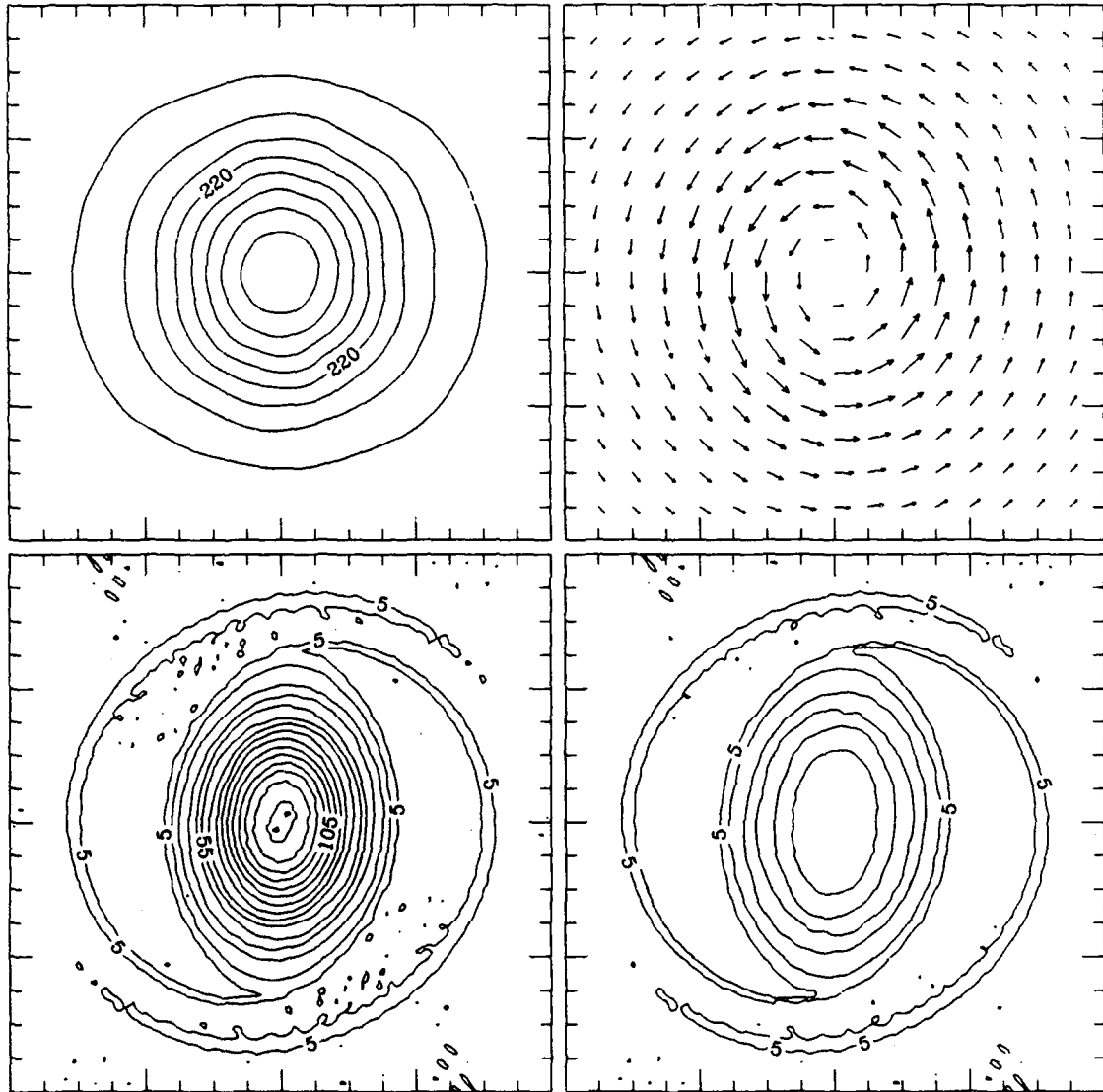


Figure 3.17: Same as Fig. 3.13 but at 24 hours.

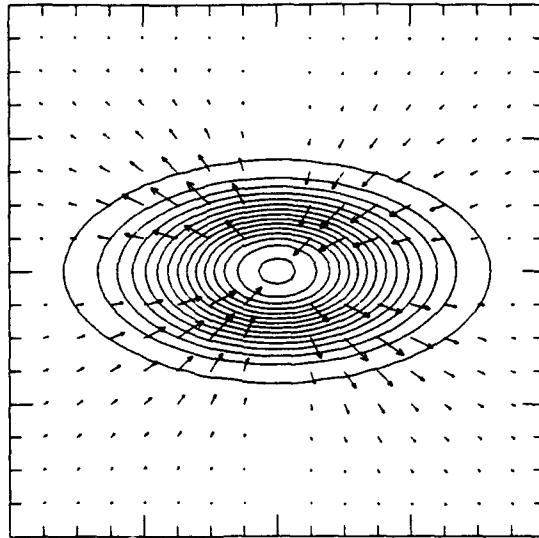


Figure 3.18: The radial wind and PV fields at the initial time for experiment two.

the regions relatively weak PV gradient (either end of the semi-major axis) into areas of inward radial flow. Likewise, regions of relatively sharp PV gradients (either end of the semi-minor axis) are being moved into areas of outward radial flow. The end effect is to tighten the gradient where it is weak and loosen it where its strong, thus symmetrizing the PV pattern.

We now consider the effects of the wave breaking and symmetrization processes on the maintenance of the mean winds. Figure 3.19 shows the tangentially averaged vorticity, normalized PV and wind speed at the initial time (dotted) and at 18 hours (smooth) for experiment two. The symmetrization process has caused the tangentially averaged PV to slightly increase within 180 km of the vortex center. In addition, the symmetrization process has caused the tangentially averaged PV to decrease slightly between 180 km and 300 km radius. Beyond 300 km, although it is not clearly evident from the figure, the tangentially averaged PV has again increased due to ejection of higher PV air to large radii by the wave breaking process. Although there is no direct mathematical correlation between PV and wind speed, the trend in the tangentially averaged PV field closely mirrors the trend in tangentially averaged vorticity (except at small radii) with which there is a direct mathematical correlation, i.e., $\zeta = \partial(rv)/r\partial r$. As the PV and vorticity are shifted outwards, there is both an increase in the maximum wind speed as well as an outward

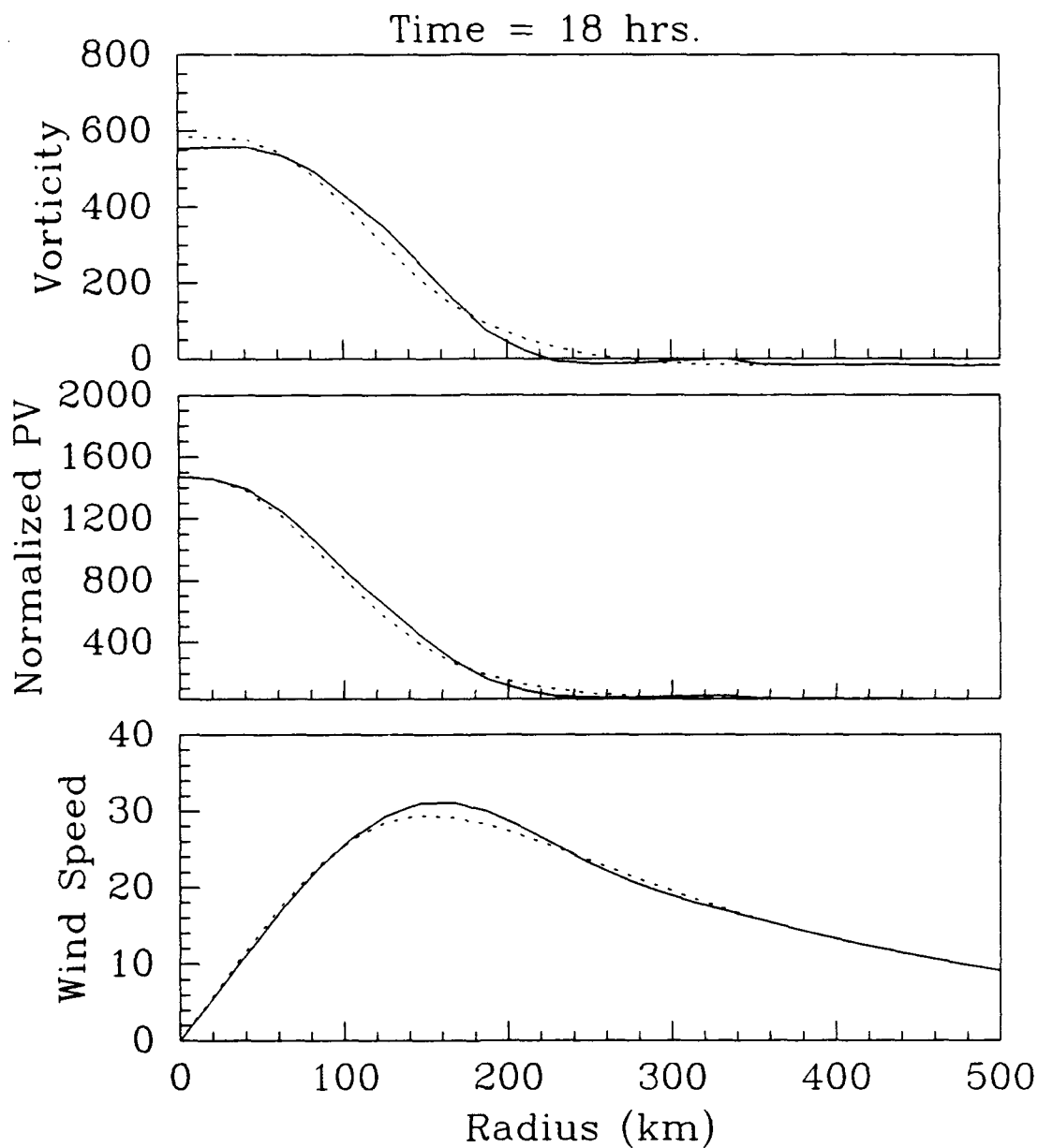


Figure 3.19: Tangentially averaged vorticity (top), normalized PV (middle) and wind speed at initial time (dotted) and 18 hours (smooth). The normalized PV and vorticity are in units of 10^{-6} s^{-1} and the wind speed is given in ms^{-1} .

shift in the radius of maximum winds. Correspondingly, the winds decrease at large radii. Dynamically, we should expect higher tangentially averaged wind speeds when the area under the tangentially averaged vorticity curve is higher. This can easily be understood by integrating the above vorticity relation for Rankine vorticity distributions which are equally wide but differing in maximum vorticity. The vorticity and wind speed curves shown in Fig. 3.18 also demonstrate this relationship. Moving radially outward from the origin, the area under the initial vorticity field is slightly larger than the area under the vorticity curve at 18 hours; correspondingly, the winds are slightly larger initially. However, at ~ 110 km the area under the vorticity curve at 18 hours begins to exceed the area under the initial vorticity curve and the winds at 18 hours are correspondingly larger. At ~ 240 km the pattern is again reversed as the area becomes larger under the initial vorticity curve.

In the above discussions of both wave breaking and axisymmetrization, we treated PV as if it were a passive material tracer. We can easily demonstrate that this is true by *simulating the evolution of a passive material tracer* which has the same initial profile as the PV field. This is accomplished simply by integrating $dT_r/dt = 0$, where T_r is any material tracer, using the model winds to advect the tracer. Results from this test (not shown) show that the tracer evolves in an identical fashion to the PV. This should not be surprising, since PV was shown to be materially conserved in section 3.2. The fact that PV behaves simply as a passive material tracer in the adiabatic, frictionless case, reemphasizes its usefulness as a dynamic variable.

Passive tracer experiments are also useful for viewing the Lagrangian evolution of spiral bands. That is, they allow us to view particle trajectories which in turn allows us to determine where the air in a spiral band originated. We do this by defining two passive tracer fields, one which initially varies as $\sin[(2\pi/L_x)x]$ and one which initially varies as $\sin[(2\pi/L_y)y]$. When displayed graphically, these two tracers create sets of perpendicular lines, respectively, which range from -1 to 1 over our inner 800×800 km display region. Clearly, fields which provide equally spaced contours would be preferred, however, we chose sine functions because they satisfy the models periodic boundary conditions. By displaying

these two fields together, intersecting isopleths uniquely define a single particle which can easily be tracked in time by noting the position of the intersection. The evolution of the passive tracer field is completely decoupled from the dynamics of the system; that is, the model winds are used only to provide the advection. Figure 3.20 shows the deformation of this passive tracer field by the flow field associated with experiment two. In addition to material conservation, the total mass bounded by any four isopleths is also conserved. We have therefore shaded five initial squares, two which are initially located on the lobes of the ellipse (i.e. either end of the semi-major axis), two which are initially located off the ellipse, and one in the center. As time evolves, the passive tracer field is stretched as it wraps around the main vortex. Although the four uncentered regions are initially located equal distances from the center of the vortex, the two which were initially located on the semi-major axis are quickly stretched and wrapped around the main vortex while the two which were initially located off the ellipse are stretched to a much lesser extent and remain separated by nearly equal distances. It appears as if the symmetrization process is accomplished by advecting some of the high PV from the lobes of the ellipse into the center of the vortex. Squares located toward the center of the vortex, however, simply rotate with very little distortion. This is not surprising since the vorticity near the center is very close to that of solid body rotation. It is also interesting to note the evolution of the dot in Fig. 3.20 which represents a single fluid particle. This particle is initially located near the right end of the semi-major axis. By day six, this particle is located near the tip of the incipient band. This allows us to say for certain that the air in both bands originated near the lobes of the ellipse.

Lastly, we consider the contributions to the total solution by the slow and fast modes. This is done simply by summing over either the $q = 0$ coefficients (slow modes) or the $q = 1, 2$ coefficients (fast modes) as mentioned in chapter two. The effect of partitioning the flow is shown in Figs. 3.21–3.22 which give the fast and slow mode contributions to the vorticity field (Fig. 3.21) as well as the wind and mass field (Fig. 3.22). It should be mentioned that the partitioning of nonlinear quantities such as PV is also possible, however, the sum of the slow and fast mode contributions will not give the total solution.

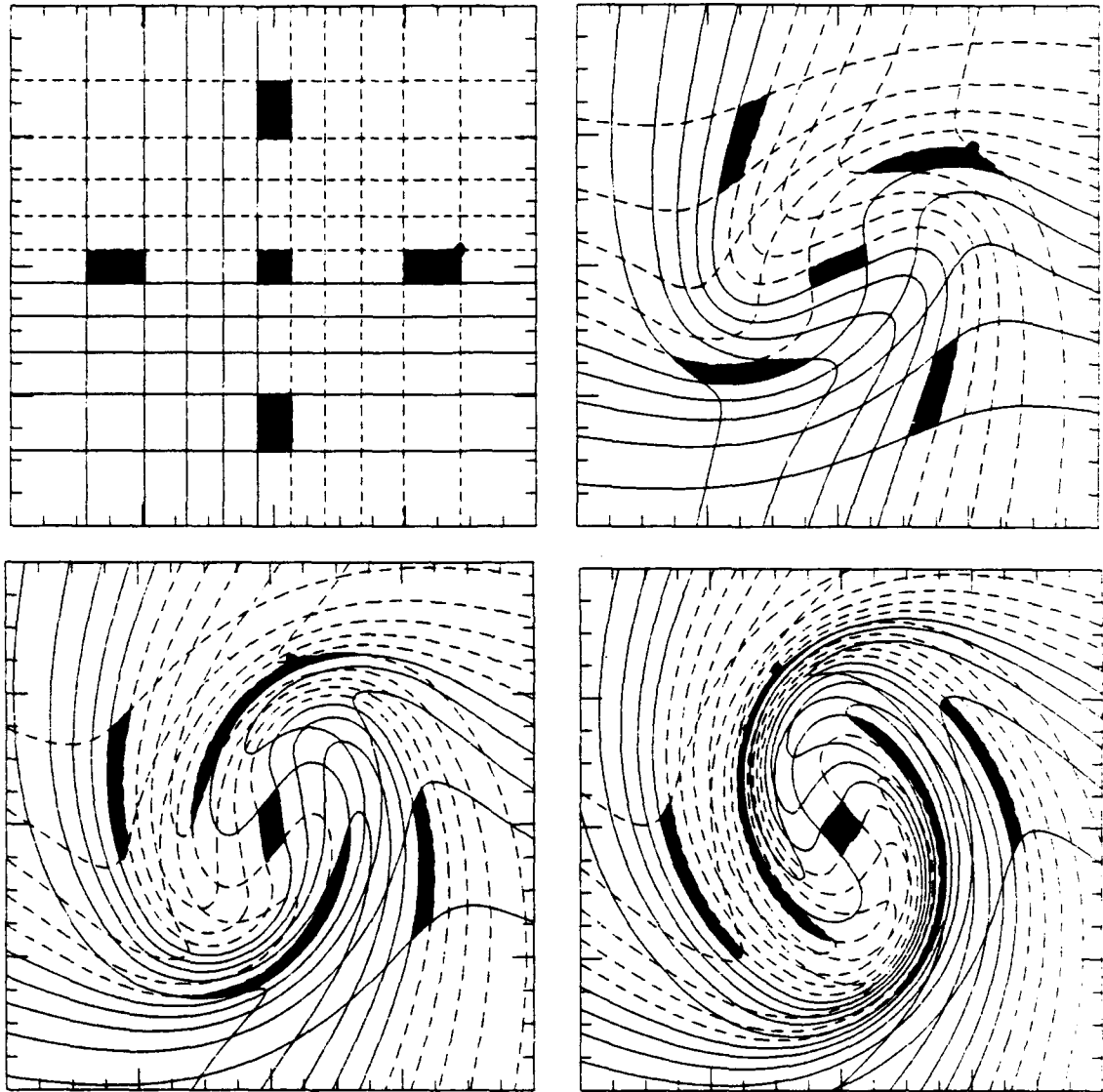


Figure 3.20: The evolution of a material tracer field for experiment two at initial time (upper left), 2 hours (upper right), 4 hours (lower left) and 6 hours (lower right). Contours are from -0.9 to 0.9 by 0.2. Shaded areas are to aid in viewing particle trajectories.

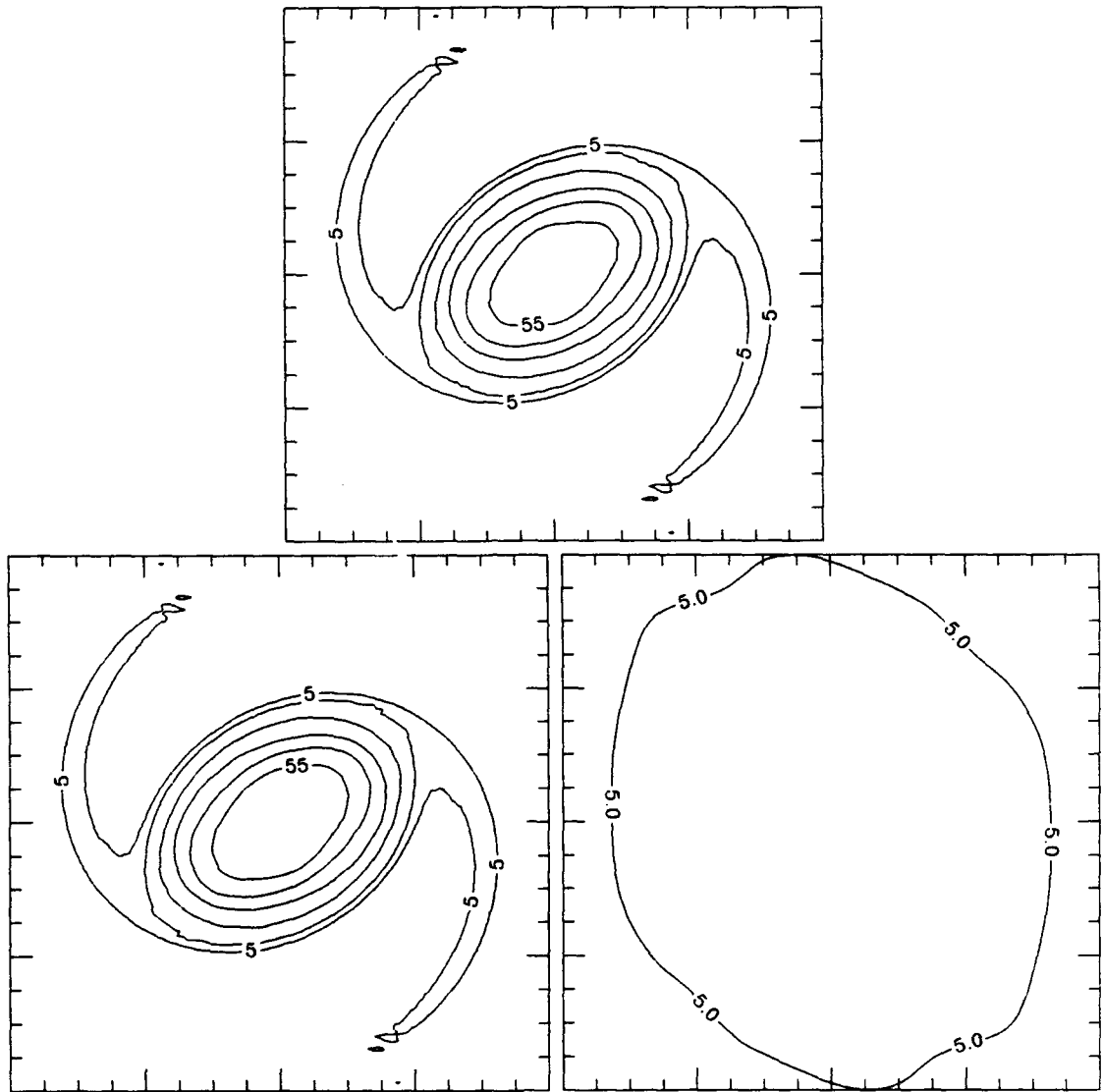


Figure 3.21: Slow and fast mode contributions to the vorticity field at 12 hours for experiment one. Total solution is shown on the top while the slow and fast mode contributions are shown on the lower left and right respectively. Contours are the same as in Fig. 3.7

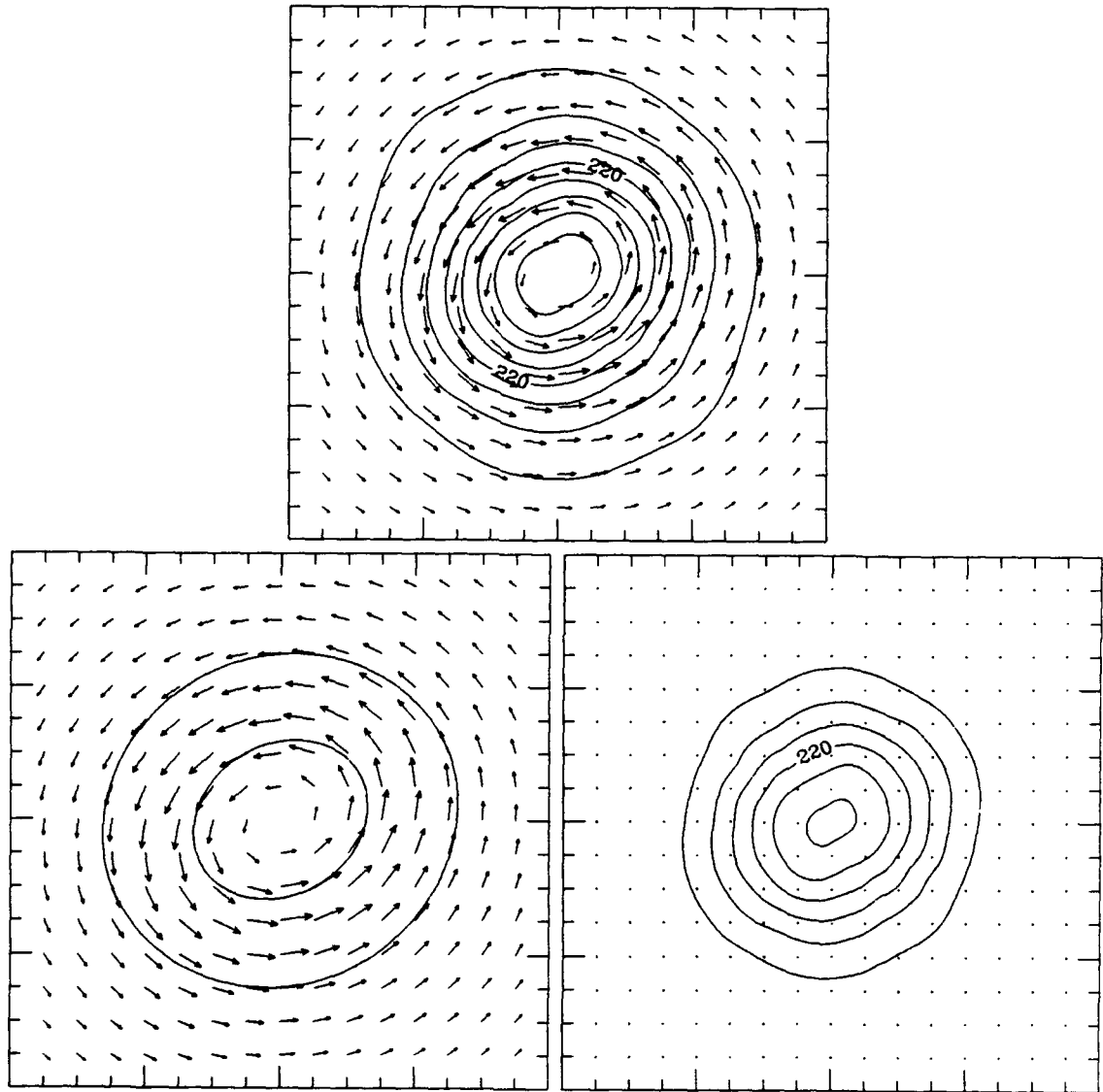


Figure 3.22: Slow and fast mode contributions to the wind and mass fields at 12 hours for experiment one. Total solution is shown on the top while the slow and fast mode contributions are shown on the lower left and right respectively. Contours are the same as in Fig. 3.7

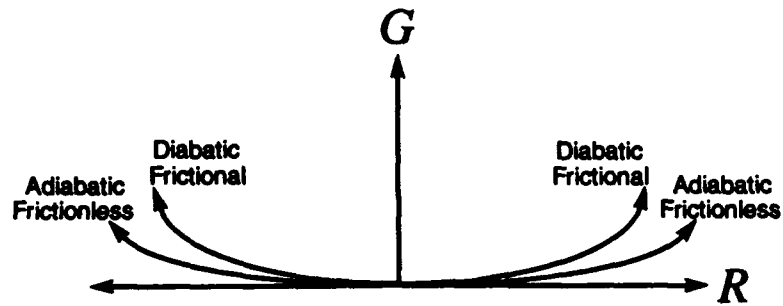


Figure 3.23: A schematic diagram of Leith's slow manifold. See text for explanation.

For this reason, we do not partition nonlinear variables. It clear from Fig. 3.21 that gravity waves play a very minor role in the banding process. This is not to say that hurricane bands are completely balanced phenomena either. This fact is evident from the extensive analysis of Ryan *et al.* (1992) and Powell (1990). In their analysis, Ryan *et al.* found small deviations of the D value associated with the bands. The D value is defined as the difference between the radar altitude and the pressure altitude with reference to the standard atmosphere. It is therefore analogous to the deviation in geopotential from its mean value. The band was found to be an area of increased low level convergence (see Chapter 1). Similar results were also shown by Powell (1990). Both of these findings suggest the presence of gravity wave modes. In addition, Ryan *et al* and Powell both show the bands to be associated with high relative vorticity, just as our model predicted. This is suggestive of rotational modes. It therefore seems inappropriate to classify hurricane bands as either purely rotational or purely gravity wave phenomenon. A more appropriate description is that hurricane bands are slow manifold phenomena, as defined by Leith (1980), which project onto both the slow and fast modes.

The lack of deviations from axisymmetry in the height (or geopotential) field in our model simulations indicates that the bands created in the model are not truly representative of those in nature. One explanation for this difference is that the model evolves near the adiabatic and frictionless slow manifold, whereas in nature, hurricanes evolve along the diabatic and frictional slow manifold. Figure 3.23 shows schematically both the adiabatic and frictionless slow manifold as well as the diabatic and frictional slow manifolds. Drawn on the abscissa is the two dimensional representation of the multi-dimensional ro-

tational manifold (R) which is the set of all linearly independent eigenvectors that can be combined to form any purely rotational field. Likewise, the ordinate is a two-dimensional representation of the multi-dimensional gravitational manifold (G) which is the set of all linearly independent eigenvectors that can be combined to form any purely gravitational field. The slow manifold, whether adiabatic and frictionless or diabatic and frictional, is defined (to a low order approximation) to be the locus of all points such that the total derivative of all gravitational modes is zero. Thus, evolution along the slow manifold is characterized by the absence of transient gravity-wave activity. In this sense, the gravity-wave modes are enslaved to the balanced modes. By using the nonlinear balance equation to initialize our experiments, we are allowing our model to evolve near the adiabatic and frictionless slow manifold. To evolve exactly on the slow manifold would require the use of nonlinear normal mode initialization (Leith, 1980; DeMaria and Schubert, 1984). Nature, however, prefers to evolve near the diabatic and frictional slow manifold in which gravity-wave activity is more prominent. The reason for the increased gravity-wave activity is the addition of frictional convergence and diabatically driven convection. This gravity-wave activity would still be expected to be enslaved by the rotational modes; that is, transient gravity-waves are expected to be minimal. In short, spiral bands project onto both the gravitational and rotational modes, thus pure gravity wave theories are not completely correct. It is likely that evolution along the diabatic frictional slow manifold provides the observed deviations from axisymmetry in the geopotential field. In the final section of this chapter, we will show that the addition of a diabatic heat source produces bands and geopotential fields which are more representative of nature.

Another reason for partitioning the wind and mass fields is to examine roles the slow and fast modes play in providing gradient balance. As pointed out by Schubert and DeMaria (1985) using an axisymmetric model, the gravity wave contribution to the total solution yields $u_r \approx 0$, $v_\varphi \approx 0$, and $\phi \neq 0$ and is responsible for the cyclostrophic part of gradient balance. This is also clearly observed in Fig. 3.22. In terms of the slow manifold diagram (Fig. 3.23), the gravity-wave contribution takes us from a point on the rotational manifold to a point on the adiabatic and frictionless slow manifold. The

addition of diabatic and frictional forcing would then move us to a point on the diabatic and frictional slow manifold.

3.5 Wave-Activity and Wave-Activity Flux Diagnostics

In the previous section, we examined the evolution of inner bands in terms of the dependent variables as well as PV. We now consider the use of wave-activity as a locally conserved variable.

If the atmosphere is partitioned into mean and eddy components, it can often be shown that the eddy quantities will satisfy a local conservation relation of the form

$$\frac{\partial A}{\partial t} + \nabla \cdot \mathbf{F} = S, \quad (3.26)$$

where both A and \mathbf{F} are functions of eddy quantities. The variable A is the wave-activity and \mathbf{F} represents a flux of the wave-activity. The right-hand term, S , is then a source or sink of A . The first to derive an expression similar to (3.26) were Eliassen and Palm (1960) for steady conservative waves (i.e. $\partial A / \partial t = S = 0$) in the quasi-geostrophic framework. It is for this reason that the flux term in (3.26) is commonly referred to as the Eliassen-Palm (EP) flux. To distinguish between the steady conservative waves considered by Eliassen and Palm and more general applications, we will refer to \mathbf{F} simply as the flux of wave-activity. For quasi-geostrophic flows, the flux of wave-activity can be directly related to the zonal wind. It therefore provides an excellent tool for the study of wave-mean flow interactions. Andrews and McIntyre (1978a,b) were able to generalize these concepts to the primitive equations, but their formulation required knowledge of particle displacements, thus making the theory difficult to use in practice. McIntyre and Shepherd (1987) eliminated the need for particle displacements and derived conservation equations above for the nondivergent barotropic equations which were strictly in terms of Eulerian quantities. In a recent work, Haynes (1988) extended the finite amplitude wave-activity conservation laws of McIntyre and Shepard to the hydrostatic primitive equations. The theory is incomplete, however, in the sense that the flux of wave-activity cannot be directly related to changes in the mean flow. It is nonetheless a useful quantity to consider because

of its conservative properties which are directly related to wave amplitude. In addition, this is a first step towards understanding wave-mean flow interactions.

In this section, we simplify Haynes' results to the unforced shallow water equations. These equations are then used to calculate the wave-activity and the associated EP flux vectors. We begin by an in-depth derivation of the wave-activity relation using the momentum Casimir. The derivation is followed by numerical calculations.

3.5.1 The Wave-Activity Relation for the Shallow Water Equations

We consider a shallow water system on an f -plane. Using cylindrical coordinates in the horizontal and denoting the radial wind by u and the tangential wind by v , the governing set takes the form

$$\frac{\partial(hu)}{\partial t} + \frac{\partial(rhuu)}{r\partial r} + \frac{\partial(hvu)}{r\partial\varphi} - \left(f + \frac{v}{r}\right)hv + gh\frac{\partial h}{\partial r} = 0, \quad (3.27)$$

$$\frac{\partial[h(rv + \frac{1}{2}fr^2)]}{\partial t} + \frac{\partial[rhu(rv + \frac{1}{2}fr^2)]}{r\partial r} + \frac{\partial[hv(rv + \frac{1}{2}fr^2)]}{r\partial\varphi} + gh\frac{\partial h}{\partial\varphi} = 0, \quad (3.28)$$

$$\frac{\partial h}{\partial t} + \frac{\partial(rhu)}{r\partial r} + \frac{\partial(hv)}{r\partial\varphi} = 0, \quad (3.29)$$

where h now represents the fluid depth. We regard (3.27)–(3.29) as a closed system in u , v and h . A consequence of (3.27)–(3.29) is the conservation of the potential vorticity $P = (\zeta + f)/h$. Since P is conserved, any function $C(P)$ is also conserved. Thus, the Casimir function $C(P)$ satisfies

$$\frac{\partial(hC)}{\partial t} + \frac{\partial(ruhC)}{r\partial r} + \frac{\partial(vhC)}{r\partial\varphi} = 0. \quad (3.30)$$

Adding (3.28) and (3.29), we obtain

$$\frac{\partial[h(rv + \frac{1}{2}fr^2 + C)]}{\partial t} + \frac{\partial[rhu(rv + \frac{1}{2}fr^2 + C)]}{r\partial r} + \frac{\partial[vh(rv + \frac{1}{2}fr^2 + C) + r\frac{1}{2}gh^2]}{r\partial\varphi} = 0. \quad (3.31)$$

Following McIntyre and Shepherd (1987) and Haynes (1988), we now wish to choose $C(P)$ such that the disturbance part of $h(rv + \frac{1}{2}fr^2 + C)$ can be written as a divergence, plus a term which is explicitly second order in wave amplitude. The disturbance part of $h(rv + \frac{1}{2}fr^2 + C)$ is defined as

$$\left\{ h \left[rv + \frac{1}{2}fr^2 + C(P) \right] \right\}_e = h \left[rv + \frac{1}{2}fr^2 + C(P) \right] - h_0 \left[rv_0 + \frac{1}{2}fr_0^2 + C(P_0) \right].$$

After some manipulation this can be written

$$\begin{aligned} \left\{ h \left[rv + \frac{1}{2} fr^2 + C(P) \right] \right\}_e &= rv_e h_e + h [C(P) - C(P_0) - P_e C'(P_0)] \\ &\quad + \frac{\partial [C'(P_0) rv_e]}{r \partial r} - \frac{\partial [C'(P_0) u_e]}{r \partial \varphi} \\ &\quad + h_e \left[rv_0 + \frac{1}{2} fr^2 + C(P_0) - P_0 C'(P_0) \right] + rv_e \left[h_0 - \frac{\partial C'(P_0)}{r \partial r} \right]. \end{aligned} \quad (3.32)$$

The right hand side of the first line of (3.32) is second order in disturbance amplitude and is defined to be the wave-activity. The second line is the divergence of a flux. We now wish to choose $C(P)$ in such a way that the last line in (3.32) vanishes. The choice

$$C(P) = - \int_P^{P_{max}} m(\bar{P}) d\bar{P}, \quad (3.33)$$

where

$$m(P_0(r)) = \int_0^r h_0(\bar{r}) \bar{r} d\bar{r}, \quad (3.34)$$

makes the last term in the square brackets in (3.32) vanish, as can easily be verified. Since

$$\frac{\partial}{r \partial r} \left[rv_0 + \frac{1}{2} fr^2 + C(P_0) - P_0 C'(P_0) \right] = P_0 \left[h_0 - \frac{\partial C'(P_0)}{r \partial r} \right], \quad (3.35)$$

and since the right hand side of (3.35) vanishes by the previous argument, we conclude that $rv_0 + \frac{1}{2} fr^2 + C(P_0) - P_0 C'(P_0)$ is constant with radius. The constant is zero because the left hand side vanishes at $r = 0$. Thus, the entire third line in (3.32) vanishes and we can write (3.32) as

$$\left\{ h \left[rv + \frac{1}{2} fr^2 + C(P) \right] \right\}_e = A + \frac{\partial [m(P_0) rv_e]}{r \partial r} - \frac{\partial [m(P_0) u_e]}{r \partial \varphi}, \quad (3.36)$$

where

$$A = rv_e h_e + h [C(P) - C(P_0) - P_e m(P_0)]$$

is the wave-activity.

Noting that the basic state is a steady solution of the governing equations and then substituting (3.36) into (3.31) we obtain

$$\frac{\partial A}{\partial t} + \frac{\partial}{r \partial r} \left[h r u (rv + \frac{1}{2} fr^2 + C) + m(P_0) \frac{\partial (rv_e)}{\partial t} \right]$$

$$+\frac{\partial}{r\partial\varphi}\left[hv(rv+\frac{1}{2}fr^2+C)+\frac{1}{2}grh^2-m(P_0)\frac{\partial u_e}{\partial t}\right]=0. \quad (3.37)$$

Using the disturbance momentum equations

$$\frac{\partial u_e}{\partial t}-hPv+h_0P_0v_0+\frac{\partial(g h_e+\frac{1}{2}u_e^2+v_0v_e+\frac{1}{2}v_e^2)}{\partial r}=0, \quad (3.38)$$

$$\frac{\partial(rv_e)}{\partial t}+hPr u+\frac{\partial(g h_e+\frac{1}{2}u_e^2+v_0v_e+\frac{1}{2}v_e^2)}{\partial\varphi}=0 \quad (3.39)$$

in (3.37), we obtain

$$\frac{\partial A}{\partial t}+\frac{\partial[r(uA+h_0ru_e v_e)]}{r\partial r}+\frac{\partial[vA+h_0r\frac{1}{2}(v_e^2-u_e^2)+r\frac{1}{2}gh_e^2]}{r\partial\varphi}=0, \quad (3.40)$$

where the wave-activity can also be written as

$$A=rv_e h_e+h\int_{P_0}^P[m(\bar{P})-m(P_0)]d\bar{P}. \quad (3.41)$$

3.5.2 Calculation of Wave-Activity and Wave-Activity Flux Vectors

Before presenting calculations of wave-activity and its flux, it is important to discuss the usefulness of such quantities. Unlike generalized Lagrangian mean theory, the wave-activity flux cannot be directly correlated to changes in the mean flow, nor can we make statements about the positive definiteness or negative definiteness of A . What we can say, however, is that wave-activity offers a calculable and conservative measure of wave amplitude. In the absence of diabatic or frictional effects, this implies that convergence of the flux vectors cannot occur unless the wave amplitude is building up transiently in the area of convergence. For our present purposes, we should expect banded areas to also be areas of high wave-activity. In addition, convergence of the wave-activity flux vectors should correspond to regions of increasing wave-activity.

To demonstrate the usefulness of wave-activity, we have calculated both A and its flux vectors as defined in (3.40) for the wave-number two experiment discussed previously. Again the model is integrated using 256^2 points on the transform grid and keeping 84 waves. The calculations for A are performed using the definition given in (3.36). The mean state was computed as the tangential average at the initial time. These averages were computed on a cylindrical grid with a maximum radius of 600 km. The fields were

sampled every 12 km in the radial direction (60 grid points) and every 6° in the tangential direction (60 grid points). Since the tangentially averaged initial fields are axisymmetric and in gradient balance, they provide a steady solution of the governing equations. It should be noted that because the calculations are done in cylindrical coordinates, the plotting of data requires the interpolation of the data back to Cartesian coordinates. Because of this, the plots appear to be slightly less smooth than previous figures. Figure 3.24 shows both the wave-activity and the flux vectors for a 12 hour integration. Clearly, the inner bands correspond to regions of high wave-activity.

Initially, the wave-activity is the highest where the deviation of the PV field from axisymmetry is the greatest. From (3.40), we see that A satisfies a local conservation relation. This implies, the area integral of A is constant. An interesting observation of the wave-activity is that not only does it satisfy a local conservation relation, but it also appears to be nearly materially conserved. That is, it appears to follow the same trend as the material tracer trajectories of the previous section.

Since the wave-activity relation used in here is not part of a complete theory, it cannot be said for certain that there is a relationship between the wave-activity flux and wave-mean flow interactions.

3.6 Inner Band Formation by Vortex Merger

In the previous sections we considered the formation and evolution of inner bands through wave breaking processes. We now demonstrate how spiral bands can also be formed when a pre-existing cyclonic vortex merges with a region of relatively high PV. Vortex merger is not a new concept and has been examined in numerous fluid dynamical studies (e.g. McWilliams, 1984; Griffiths and Hopfinger, 1987; Melander *et al.*, 1987a, 1988). The application of vortex merger to tropical cyclones, however, is new. Recent work in this area has been accomplished by Evans and Holland (1991), Holland and Evans (1992), Holland and Lander (1992), Lander and Holland (1992), Ritchie and Holland (1992), and Holland and Dietachmayer (1992). In the present study, we consider the application of vortex merger specifically to the formation of hurricane spiral bands.

When a cyclonic vortex moves sufficiently close to another cyclonic vortex of equal intensity, the two vortices may merge or coalesce to form a larger vortex. Extending from the newly formed vortex will be spiral arms of relatively high vorticity. This process has been shown in laboratory experiments by Griffiths and Hopfinger (1987). If the vortices are not sufficiently close to one another, they may simply rotate around one another without merging. This is sometimes referred to as the Fujiwhara effect (Fujiwhara, 1923). Of greater importance to hurricane spiral bands is the merger of vortices having different intensities. We consider the following five analogies in this section, all of which produce spiral bands in the PV field. The first three simulations are performed using a transform grid with 256^2 points and keeping 108 waves. Although quadratically nonlinear terms are not alias free, results indicate that for relatively short model integrations (~ 1 day), the increased resolution gained outweighs the problem of nonlinear computational instability.

The first simulation involves the interaction of an intense vortex with a weaker vortex of similar size. If we let the PV associated with the weak vortex represent a region of less organized convection, then this case is analogous to a tropical cyclone which encounters an area of convection on the scale of a tropical cloud cluster. We present this simulation in Fig. 3.25. The leftmost vortex is initialized with a maximum vorticity which is three times that of the rightmost. As the vortices evolve, the differential rotation associated with the more intense circulation rapidly acts to deform the weaker vortex, whereas the circulation associated with the weaker vortex has only a slight impact on the more intense vortex. By 24 hours, the weaker vortex has been stretched and advected towards the vortex center yielding a single spiral band of PV.

In our second simulation, we consider a large, strong vortex which encounters a smaller, weaker vortex. This case is analogous to a tropical cyclone which encounters a relatively small region of convection. Figure 3.26 shows the evolution of the PV field for this simulation. The intense circulation of the large vortex rapidly deforms the smaller vortex. By 24 hours, the PV of the smaller vortex has wrapped around the larger vortex again forming a thin spiral band. We should therefore also expect smaller regions of convection in nature to form thinner spiral bands.

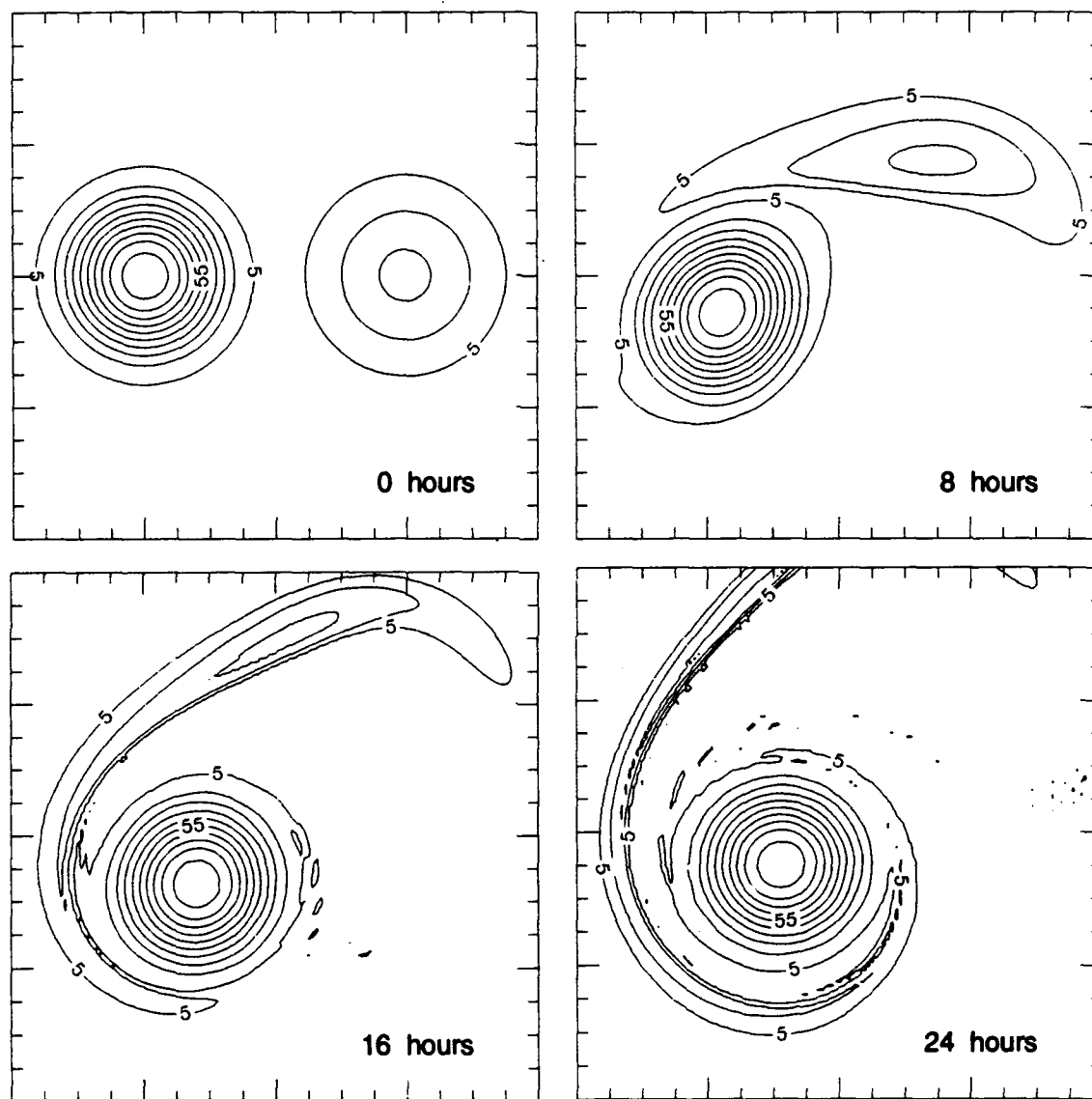


Figure 3.25: The normalized PV field at 0, 8, 16, and 24 hours showing the merger of two initially equally sized vortices having different intensities. The leftmost vortex was initialized with a maximum relative vorticity which was three times that of the rightmost. Units are 10^{-5} s^{-1} with a contour interval of 10^{-4} s^{-1} .

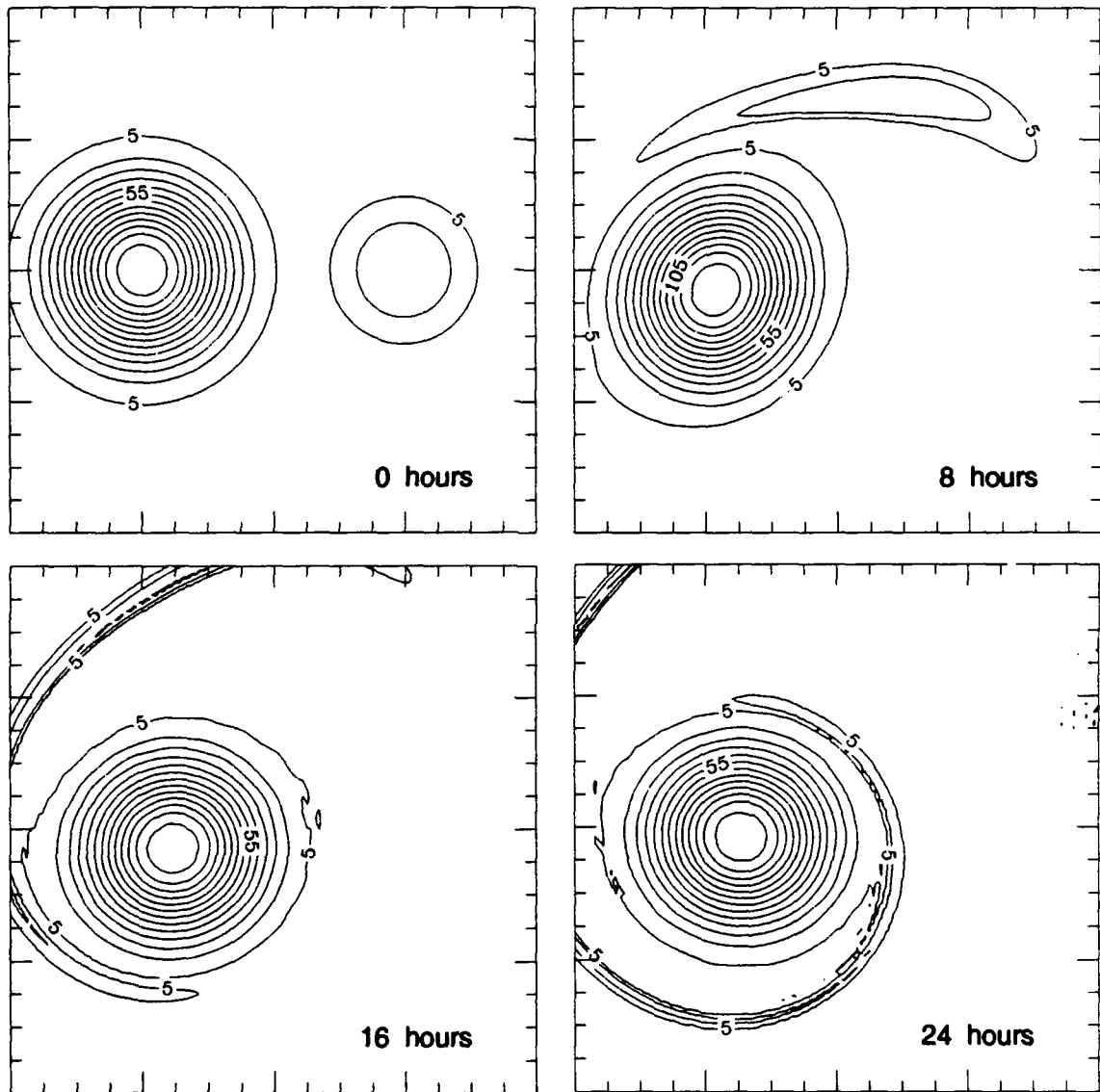


Figure 3.26: The normalized PV field at 0, 8, 16, and 24 hours showing the merger of a large, strong vortex with a small, weak vortex. The large vortex was initialized with a maximum relative vorticity which was three times that of the the small vortex. Units are 10^{-5} s^{-1} with a contour interval of 10^{-4} s^{-1} .

In our third simulation, we consider a strong, small vortex which encounters a larger, weaker vortex. This case is analogous to a hurricane which forms near a monsoon trough which is rather amorphous in appearance. Figure 3.27 shows the evolution of the PV field for this simulation. The initial vorticity of the small vortex has a maximum value which is three times that of the larger vortex. As time evolves, the wind field associated with the small intense vortex stretches the PV field of the large vortex. By 24 hours the PV, which was initially associated with the large vortex, completely surrounds the smaller vortex. In addition, the remainder of the larger vortex appears as a wide spiral band extending from the smaller vortex. The large region of PV therefore allows the smaller intense vortex to grow in size. This may help explain the large variation in size of tropical cyclones (Merrill, 1984). A theory has recently been put forth by G. Holland (personal communication) which suggests that if a tropical cyclone forms near the monsoon trough, it would be provided with a relatively large pool of PV from which to grow; however, if a tropical cyclone forms away from such a PV source, it would be expected to remain much smaller in size. This theory will also be examined in the fourth simulation.

For the fourth simulation, we consider the effect of placing a vortex near a strip of relatively high PV. This experiment is performed using 128^2 points on the transform grid while keeping 42 waves, and is intended to simulate the effect of tropical cyclone forming near the edge of a monsoon trough or ITCZ which is zonal in appearance. Figure 3.28 shows the PV field for this simulation at 0, 16, 32, and 48 hours. The cyclonic circulation associated with the vortex acts to advect relatively high PV air from the strip northward on the right side of the vortex and advect relatively low PV air southward on the left side of the vortex. As time evolves the vortex is made larger by drawing upon the PV of the strip. By 48 hours PV from the strip completely surrounds the original vortex and a large spiral band has formed. This result again supports Holland's idea for the development of large tropical cyclones.

In the previous four simulations we considered the formation of inner bands from initial states which had two pre-existing vortices or regions of PV. For the fifth and final simulation, we consider a single axisymmetric vortex which encounters an area of intense

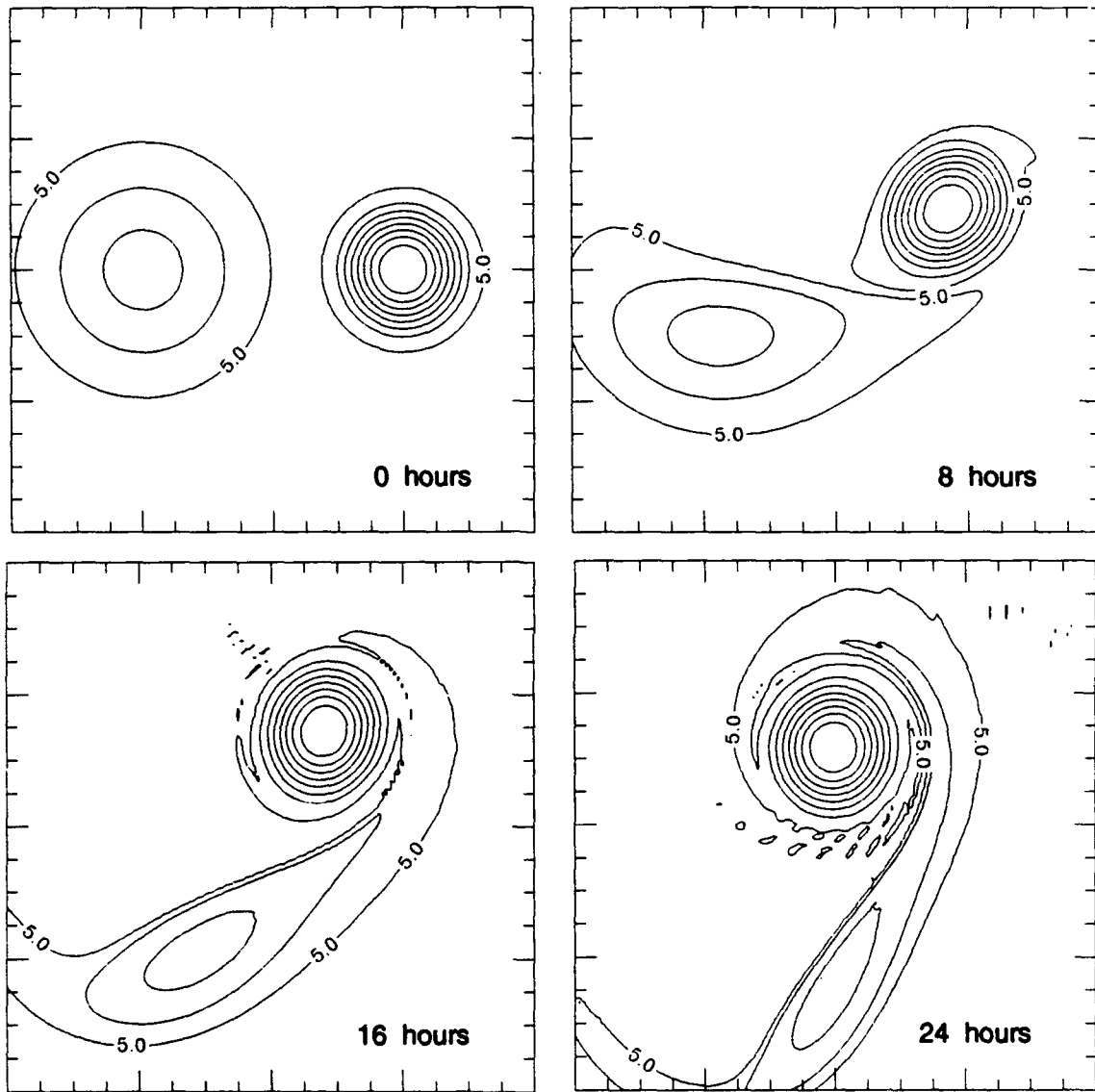


Figure 3.27: The normalized PV field at 0, 8, 16, and 24 hours showing the merger of a large weak vortex with a small strong vortex. The small vortex was initialized with a maximum relative vorticity which was three times that of the large vortex. Units are 10^{-5} s^{-1} with a contour interval of 10^{-4} s^{-1} .

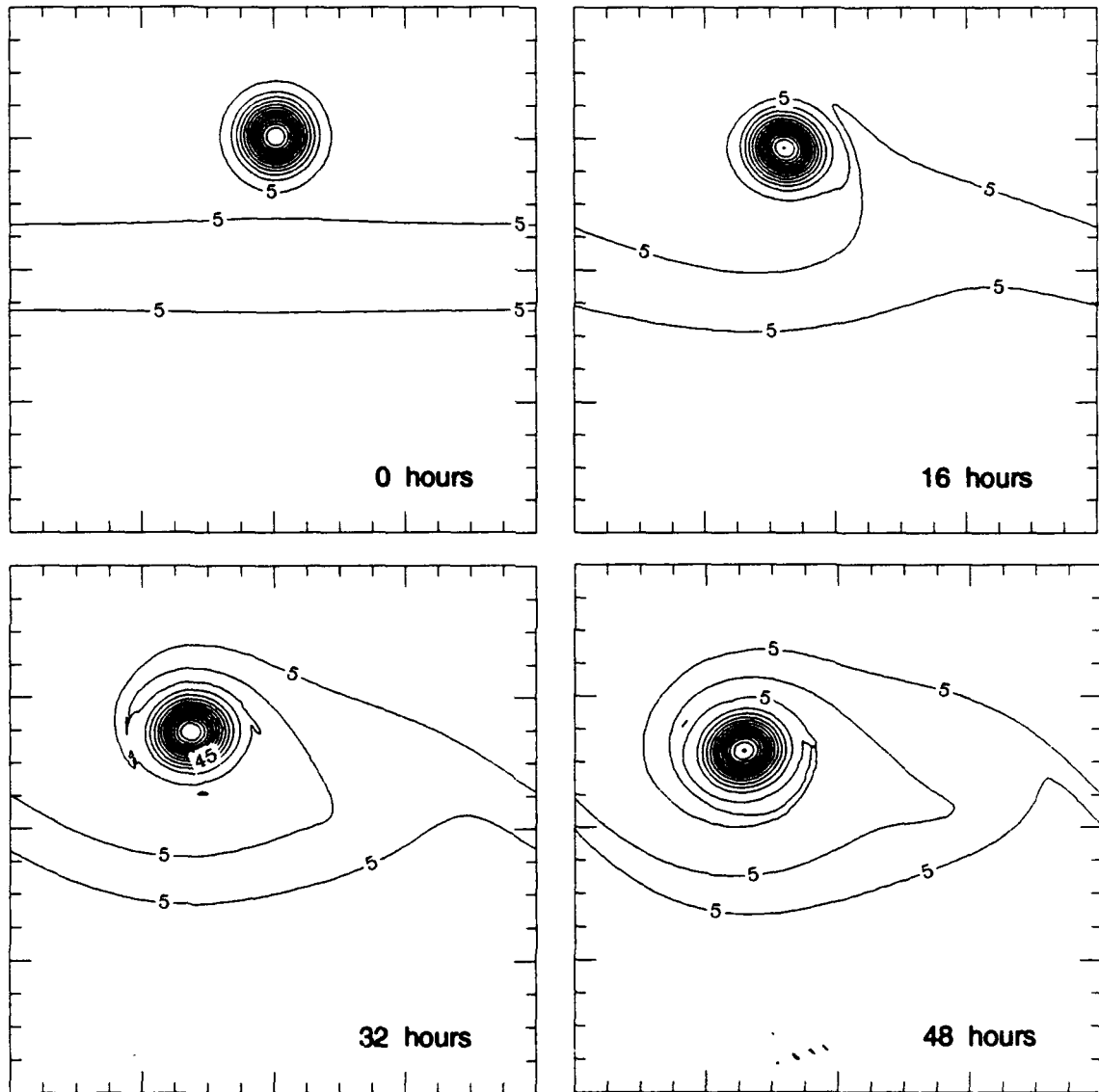


Figure 3.28: The normalized PV field at 0, 16, 32, and 48 hours showing the interaction of a vortex with a strip of PV. The vortex was initialized with a maximum relative vorticity of $4.0 \times 10^{-4} \text{ s}^{-1}$. The strip was initialized with a maximum relative vorticity of $6.25 \times 10^{-5} \text{ s}^{-1}$. Units are 10^{-5} s^{-1} with a contour interval of 10^{-4} s^{-1} .

convection. The goal is to more closely simulate the actual banding process by convective asymmetries in nature.

The generation of PV by convective heating in the model is represented as a mass sink in the continuity equation. This is analogous to an isentropic (layers of constant potential temperature) model in which heating requires mass to leave a layer because the heated air's potential temperature changes, thus simulating a mass transport to another layer. Mathematically, we can see that a mass sink is a source of PV by examining (3.5). Since P is positive for cyclonic circulations in the northern hemisphere, a mass sink (negative S) will produce $dP/dt > 0$ and thus be a source of PV. The conversion between a mass sink in a shallow water model and actual heating, however, is not a precise one. We can estimate an appropriate heating rate by comparing the mass source/sink terms of the continuity equations for both a shallow water system and a stratified fluid in isentropic coordinates. That is, we assume $\rho w \approx \sigma \dot{\theta}$, where $\sigma = -(1/g)(\partial p / \partial \theta)$, w is the vertical velocity, and ρ is the density. If we choose $149 \text{ kg/m}^2\text{K}$ as typical value of σ for a tropical atmosphere (Schubert et al., 1992) we find that a mass sink, w , of 0.017 ms^{-1} corresponds roughly to a heating rate of 10 K/day (for $\rho = 1 \text{ kg/m}^3$).

Because heating is added to the model, the basic state depth of the fluid (H) is increased to 2000 m, which allows the model to evolve without encountering the problems associated with massless layers. By increasing the basic state depth of the fluid, however, we also increase the pure gravity-wave speed and therefore the Rossby radius. Model results indicate that these changes have no adverse effects on the simulations.

Our simulation consists of an axisymmetric vortex which is located north of a large convection area. This area of convection is an ellipse with an aspect ratio of two whose center is initially located 400 km from the center of the vortex. The elliptical region has a maximum semi-major axis length of 300 km and the x and y dependence of the heating uses the Melander profile with a steepness parameter of 2.56, $R_i=100 \text{ km}$ and $R_0=300 \text{ km}$. The heating function is therefore similar in shape (but not size) to the initial vorticity pattern for experiment two in section 3.4. The maximum value of the heating function is 0.08 ms^{-1} which equates to a maximum heating rate of $\sim 40\text{-}50 \text{ K/day}$.

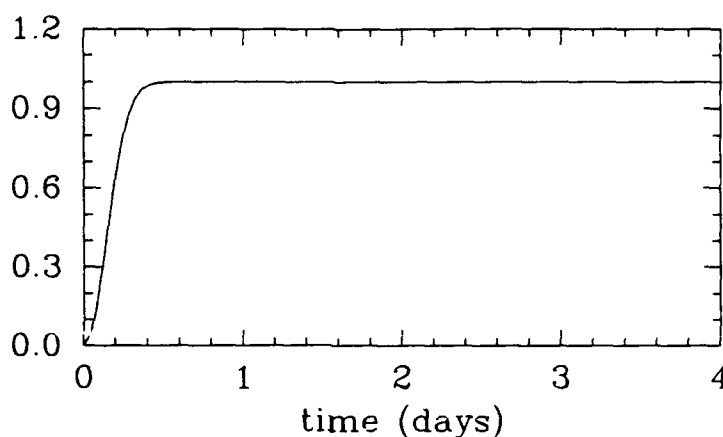


Figure 3.29: The time dependent part of the heating function $Q(x, y, t)$.

To prevent the excitation of transient gravity waves and ensure evolution along the diabatic slow manifold (Schubert *et al.*, 1980), the heating is turned on slowly using a function of the form

$$Q(x, y, t) = \hat{Q}(x, y)[1 - \exp(-at^2)], \quad (3.42)$$

where the constant a is $3.5 \times 10^{-9} \text{s}^{-2}$ and $\hat{Q}(x, y)$ is the elliptical shaped heating pattern described above. The constant a was chosen such that the heating reaches its peak at exactly 12 hrs. The model is integrated using 128^2 points on the transform grid while keeping 42 waves. Fig. 3.29 shows how (3.42) varies with time.

Results from this simulation are shown in Figs. 3.30–3.32. Initially the vortex was located 200 km from the top of the domain and centered in x . The heat source is stationary and located 200 km from the bottom of the domain and also centered in x . By 24 hrs, the presence of the heating anomaly is felt on the entire right edge of the vortex. In addition, the vortex has shifted towards the lower pressure created by the heating, moving almost 200 km. The weak cyclonic circulation created by the heating anomaly has caused the vortex also to move slightly westward. At 36 hrs, the PV anomaly produced by the heating has stretched and shifted to encompass the entire northern half of the vortex. By 48 hrs, the PV field from the vortex and that due to the heating have merged. The result is a large tail of PV extending in a spiral fashion from the southern edge of the vortex. The height field associated with the vortex shows slight asymmetries associated with the spiral

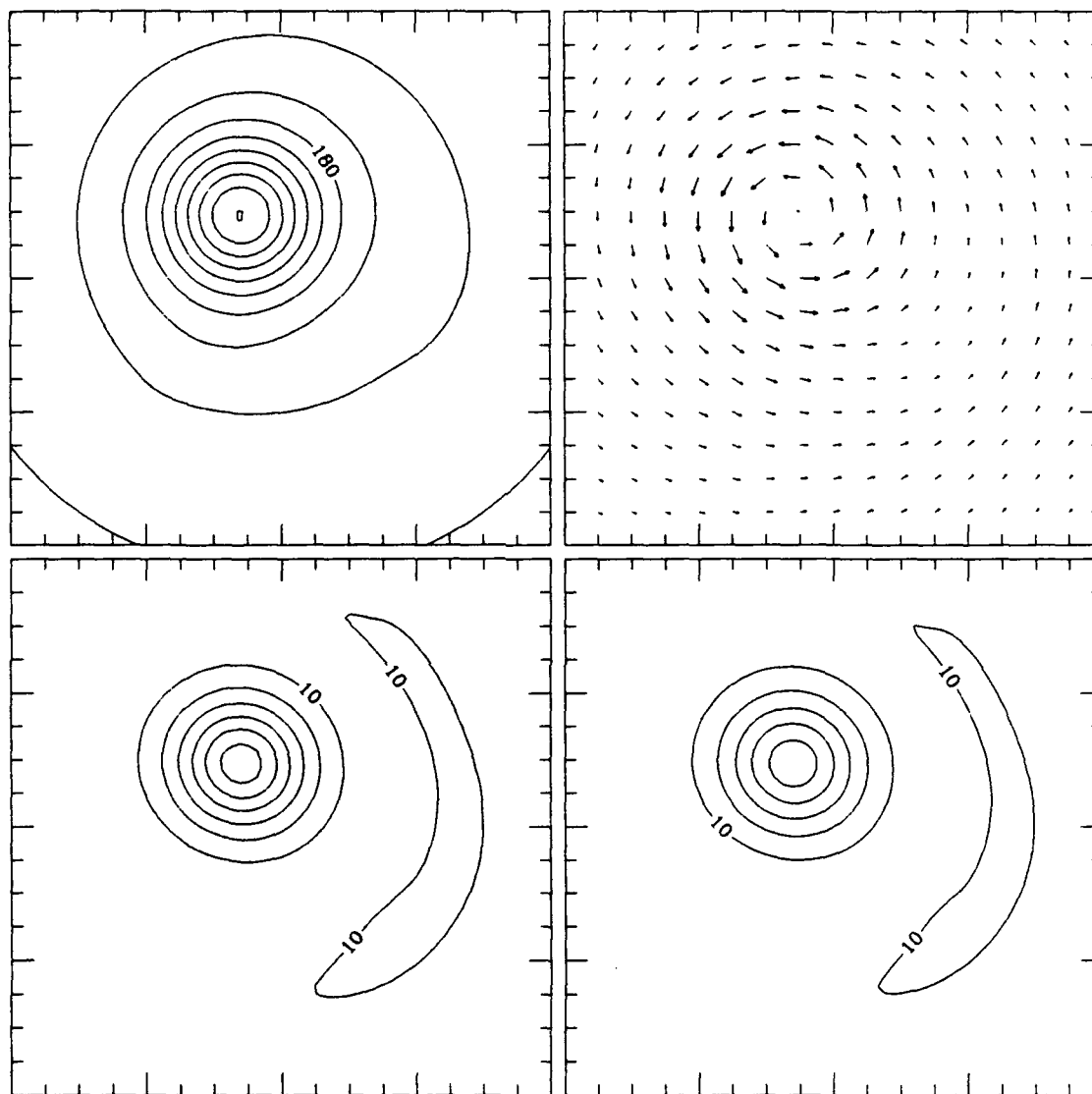


Figure 3.30: The wind and mass fields for the asymmetrically heated vortex at 24 hrs. The height (upper right) is measured in decameters and has a contour interval of 2 decameters. The maximum wind vector, defined as the distance between two consecutive tick marks, is 50 ms^{-1} . The normalized PV (lower left) and absolute vorticity (lower right) are in units of 10^{-5} s^{-1} and have contour intervals of $2.0 \times 10^{-4} \text{ s}^{-1}$. Shown is the inner $800 \times 800 \text{ km}$ domain. Tick marks are every 50 km.

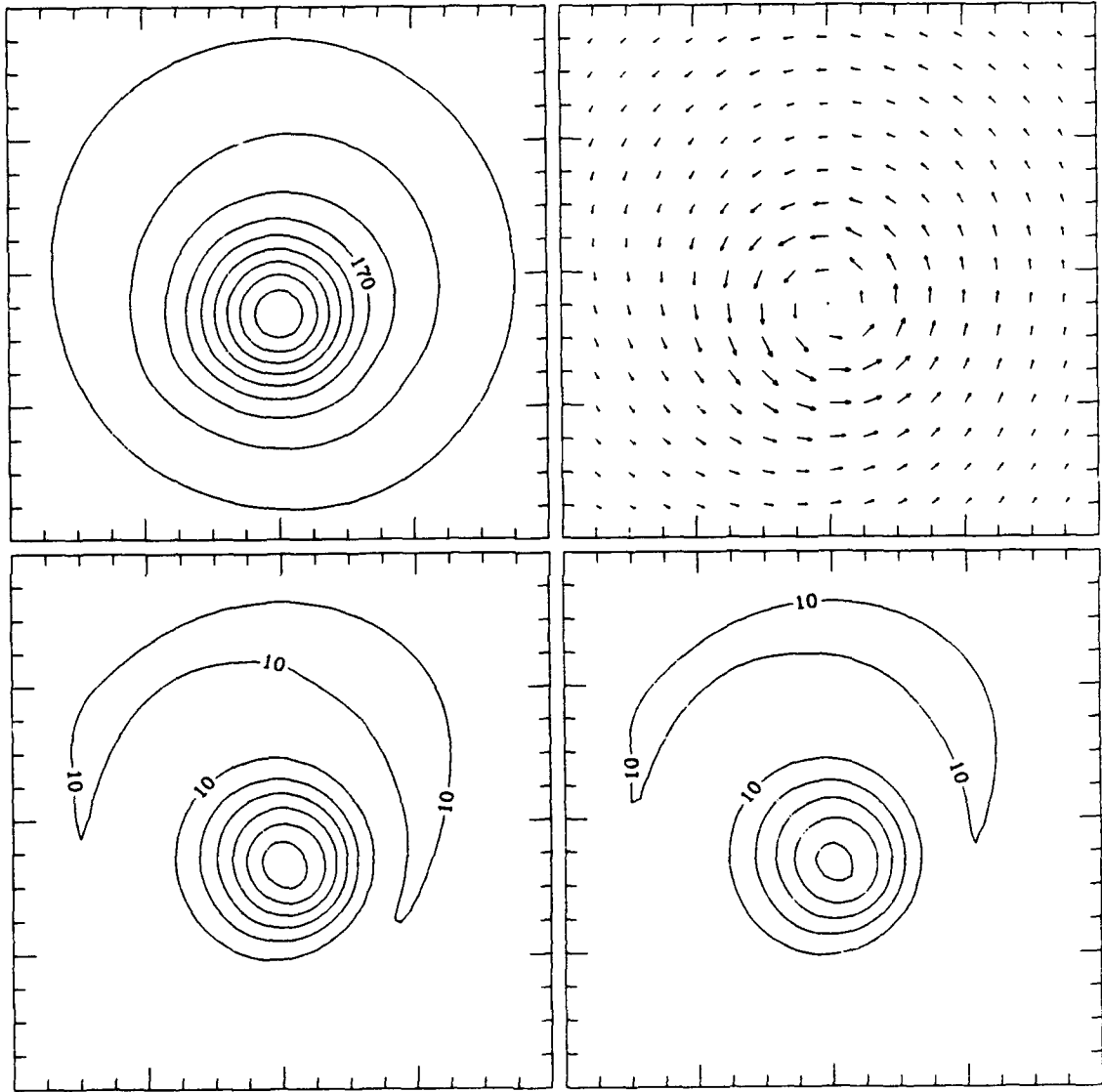


Figure 3.31: The same as Fig. 3.30 but for 36 hrs.

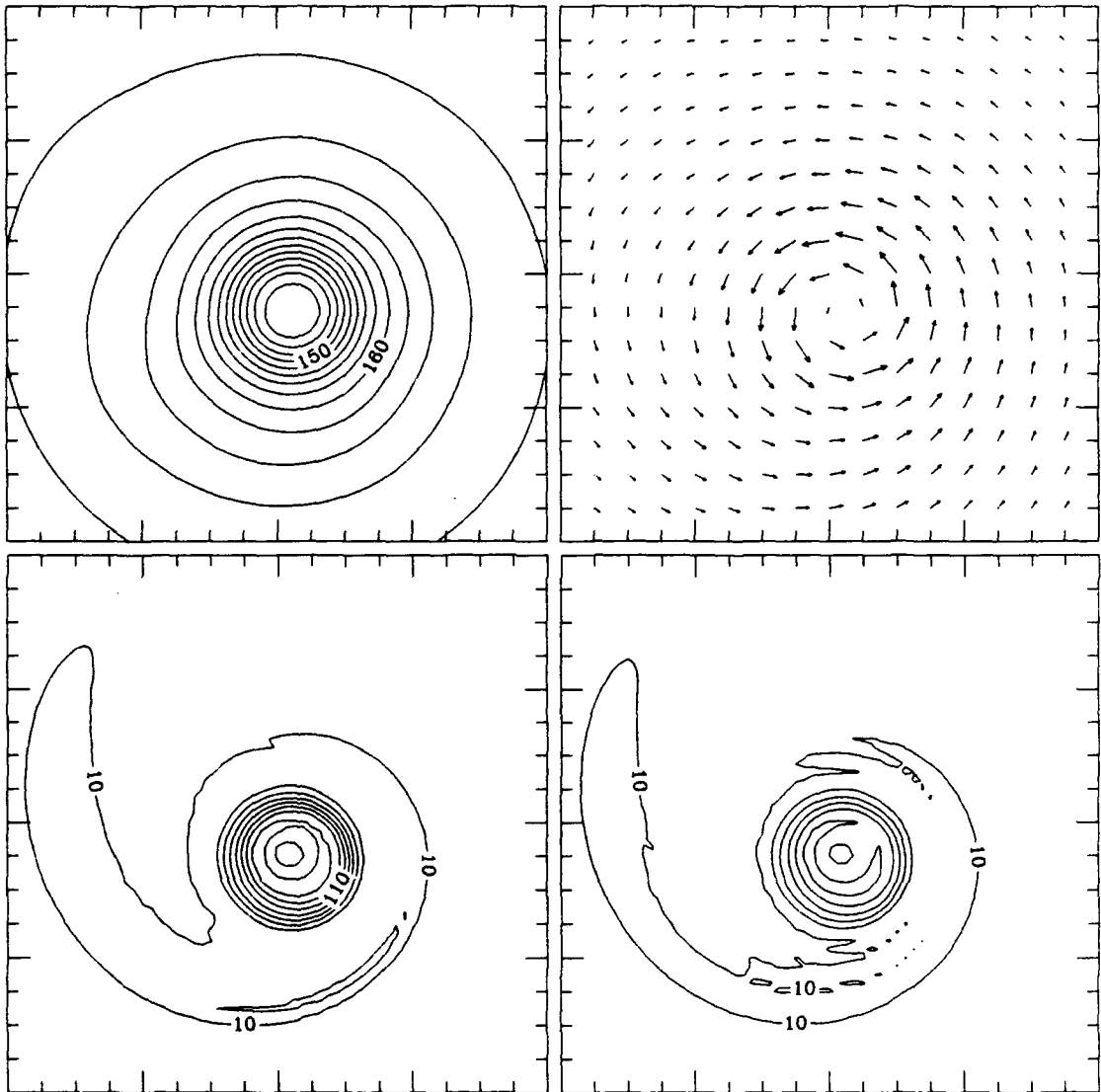


Figure 3.32: The same as Fig. 3.30 but for 48 hrs.

band suggesting the model is evolving on the diabatic slow manifold. The band is also found to correspond to the location of a secondary tangential wind maximum. Figure 3.33 shows the tangential wind speed for four radial arms which emanate from the vortex center at 90° angles starting from the positive x axis. The upper left panel shows clearly that the band is associated with an increase in the tangential wind. These secondary wind maxima are often found in nature (Willoughby *et al.*, 1982).

These results seem to indicate that banding process can be explained rather well using PV arguments. Other related results (not shown) indicate that asymmetric heating may also be responsible for the formation of concentric eyewalls which are observed occasionally in smaller intense tropical cyclones (Willoughby *et al.*, 1982). During a model simulation in which the heating was turned off slowly, thus simulating a vortex which comes in contact with an area of intense convection but slowly propagates away, the asymmetries in the PV field simply wrapped around the existing vortex, creating an annular region of PV. The fact that concentric eyewalls are only observed in the more intense hurricanes supports this idea. When coming in contact with an area of intense convection, the more intense hurricanes would allow the PV anomalies to simply wrap around the vortex before having time to interact with it. Observational studies would need to be done, however, to support this hypothesis.

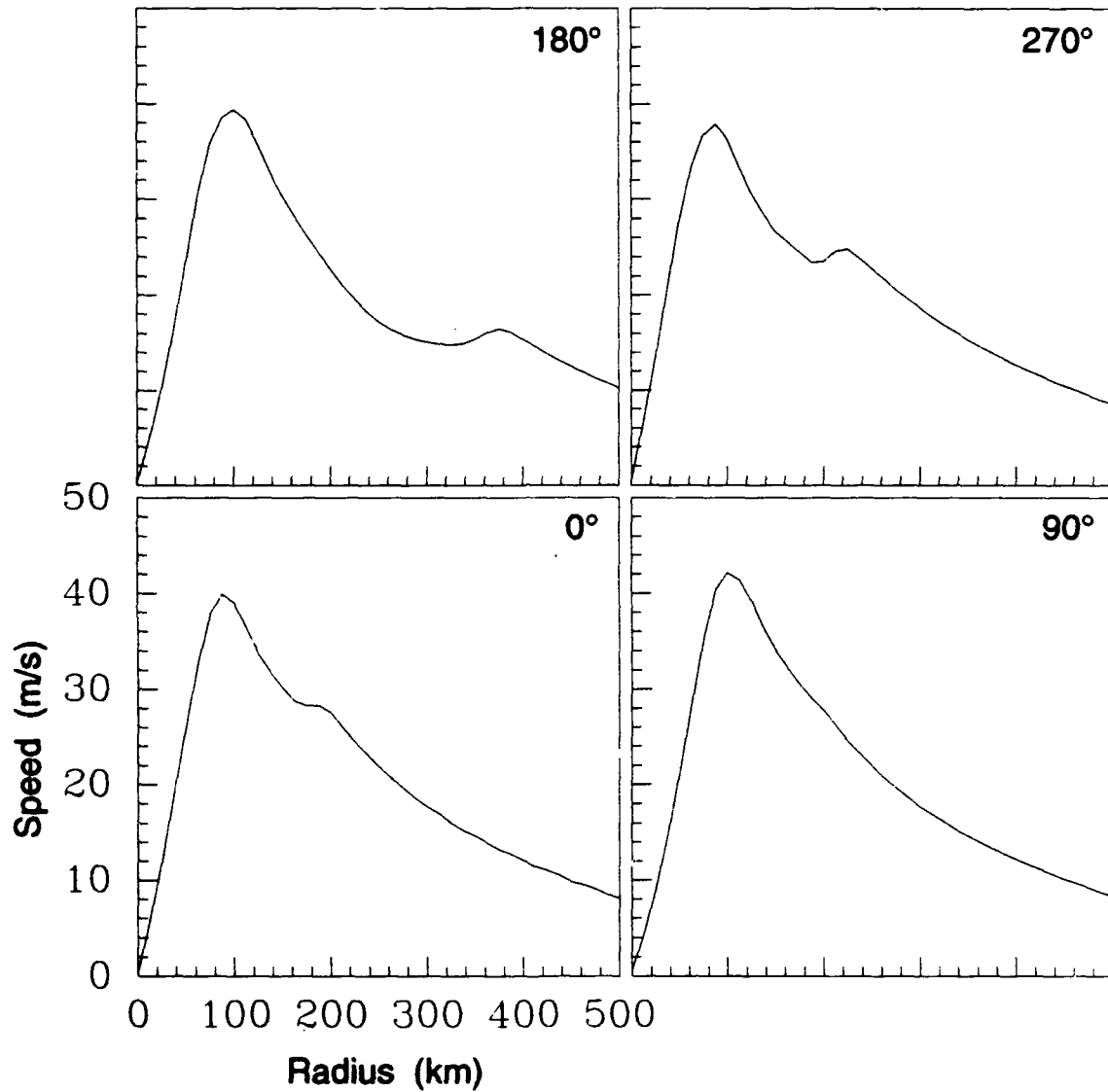


Figure 3.33: The tangential wind speed along four radial arms extending from the center of the vortex at 48 hrs (see Fig. 3.32). The radial arms are at 0° (lower left), 90° (lower right), 180° (upper left), and 270° (upper right) as measured from the positive x axis.

Chapter 4

OUTER BAND FORMATION THROUGH ITCZ BREAKDOWN

In this chapter we examine the formation of outer bands in tropical cyclones resulting from the breakdown of the intertropical convergence zone (ITCZ). We begin by first defining outer bands and presenting observational evidence for their existence. In section 4.2 we present a brief review of the applicable general stability theories which help us to understand the necessary conditions for barotropic instability. These theories provide a basis for understanding some of the fundamental dynamics of ITCZ breakdown. In the final section, we present both numerical analysis and model simulations of ITCZ breakdown and outer band formation. The numerical analysis makes use of linear normal mode theory which (although it is slightly less general than other stability theories) allows us to predict unstable patterns and growth rates. The normal mode stability analysis is then followed by five numerical experiments.

4.1 Observational Evidence for Outer Bands

Before presenting evidence for the existence of outer bands, it is first necessary to define exactly what is meant by outer bands. Outer hurricane bands are defined as bands of convection which are typically located farther than 500 km from the center of the vortex and owe their existence to the breakdown of the ITCZ. As an example, we present GOES IR satellite images of the tropical North Pacific during late July 1988 in Figs. 4.1-4.2.

On July 26, the ITCZ appears as a relatively uniform area of convection which varies between 5° and 9° latitude in width and nearly 40° latitude in length. By August 3rd, the ITCZ has broken down and five tropical disturbances remain. Between some of the disturbances there exist noticeable filaments of convection. These are the outer bands. By August 12th, the ITCZ has again begun to reform, and the process begins to repeat

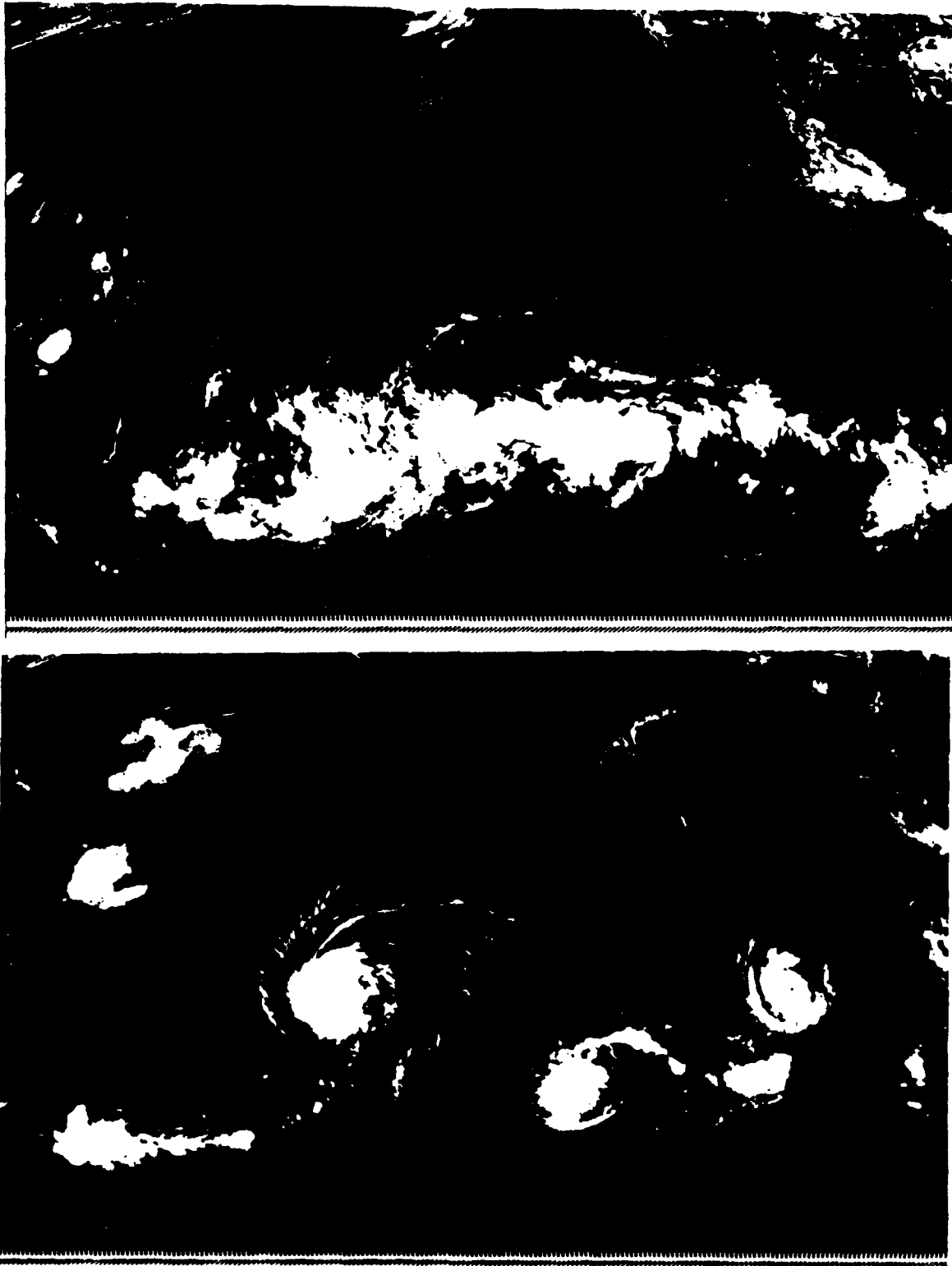


Figure 4.1: GOES IR images at 1646 UTC on 26 July (top) and 3 August (bottom), 1988. Outer bands are especially noticeable extending from the second vortex from the left in the bottom panel.



Figure 4.2: Same as Fig. 4.1 but for 12 August 1988.

itself. The basic dynamics of the ITCZ breakdown process and outer band formation can be explained through barotropic instability arguments. This is not to imply that moist physical processes and baroclinicity do not play a role. Certainly, they must. We are simply trying to isolate the fundamental aspects of the dynamics.

A relationship between the ITCZ and hurricane bands was first noted by Fletcher (1945). Fletcher hypothesized that spiral bands were formed by individual convergence lines from the ITCZ being “coiled” into the center of the tropical storms. Although his theory is flawed, the connection he drew between the ITCZ and hurricane bands may be valid.

In the following two sections, we will show that the breakdown of a strip of relatively high potential vorticity (PV) air takes on many of the same attributes of the observed ITCZ breakdown, if regions of higher PV are interpreted as regions of more intense convection. The breakdown of a PV strip is characterized by the “pooling” of PV in certain locations which causes other regions of PV to become extremely thin and eventually detach (Pratt and Pedlosky, 1991). The mechanism for this breakdown was best described by Hoskins

Table 4.1: Summary of linear and nonlinear stability theory for various types of dynamical systems. Question marks imply no known theory exists.

Dynamics	Linear	Nonlinear
Nondivergent	Rayleigh	1880
	Taylor	1915
	Fjørtoft	1950
Quasi-geostrophic	Charney-Stern	1962
Semi-geostrophic	Eliassen (f -plane)	1983
	Magnusdottir (β -plane)	1990
	Magnusdottir (sphere)	1991
Primitive Equation	Ripa (shallow water)	1983
	Ripa (multiple finite layers)	1991

et al. (1985) as the cooperative interaction of counter propagating Rossby waves, or more generally, PV waves. We begin our discussion by first familiarizing ourselves with the basic principles of barotropic stability theory.

4.2 A Review of Stability Theory

In this section, we review some of the fundamental barotropic stability theorems. These theorems offer insight to the understanding of ITCZ breakdown by providing the conditions necessary for barotropic instability. The present state of stability theory for various dynamical systems is summarized in Table 4.1. Currently, nonlinear stability theorems are restricted to highly balanced flows. Here we review the existing stability theorems for both the nondivergent barotropic equations and the shallow water (primitive) equations. We begin by reviewing Rayleigh's famous stability theorem for the linear nondivergent barotropic system. This discussion is followed by stability theorems for the nonlinear nondivergent system as derived by Arnol'd (1965,66) and the linearized shallow water system as derived by Ripa (1983).

4.2.1 Rayleigh's Theorem

The most elegant method of deriving Rayleigh's stability theorem was first presented by Taylor (1915). This method involves the use of the variable η which represents a particle displacement in the y -direction. We begin the derivation by considering the nondivergent

vorticity equation in Cartesian coordinates linearized about a basic state which has only a zonal component. The absolute vorticity (here defined as ζ) equation and particle displacement equations, take the form

$$\frac{D\zeta'}{Dt} + v' \frac{\partial \bar{\zeta}}{\partial y} = 0 \quad (4.1)$$

and

$$\frac{D\eta}{Dt} = v' \quad (4.2)$$

where $D/Dt = \partial/\partial t + \bar{u}\partial/\partial x$. The barred quantities represent zonal means whereas primed quantities denote small amplitude perturbations about the zonal mean. By combining (4.1) and (4.2) we obtain

$$\frac{D}{Dt} \left(\zeta' + \eta \frac{\partial \bar{\zeta}}{\partial y} \right) = 0. \quad (4.3)$$

If the quantity inside the parentheses in (4.3) vanishes at $t = 0$, then it vanishes for all time. Multiplying this quantity by $-v'$ and rearranging terms gives us the relationship

$$\frac{DA}{Dt} - v'\zeta' = 0, \quad (4.4)$$

where

$$A \equiv -\frac{1}{2}\eta^2 \frac{\partial \bar{\zeta}}{\partial y} \quad (4.5)$$

represents the wave activity for the nondivergent barotropic system. If we expand ζ' and use the continuity equation, (4.4) can be written in final form as

$$\frac{\partial A}{\partial t} + \frac{\partial[\bar{u}A + \frac{1}{2}(u'^2 - v'^2)]}{\partial x} + \frac{\partial(u'v')}{\partial y} = 0 \quad (4.6)$$

We note here the similarity between the linear wave-activity equation (4.6) and the non-linear shallow water form (3.39).

Rayleigh's stability theorem can now be obtained by integrating (4.6) over the entire domain (assuming a doubly periodic domain) to obtain

$$\frac{d}{dt} \iint A dx dy = 0. \quad (4.7)$$

From (4.5) and (4.7), we see that if the mean vorticity field is monotonic, η can grow only locally. If η is to grow in an overall sense, the mean vorticity gradient must reverse sign. This is Rayleigh's classic necessary condition for barotropic instability.

4.2.2 Arnol'd's Theorem

In the previous subsection we considered the linear nondivergent barotropic governing equations. We now wish to generalize Rayleigh's theorem to finite amplitude disturbances. This was first accomplished by Arnol'd (1965, 1966). In this subsection, we derive Arnol'd's theorem for the f -plane in Cartesian coordinates. The governing equations for this case can be written in the form

$$\frac{\partial}{\partial t}[u - f(y - y_c)] + \frac{\partial}{\partial x}[u(u - f(y - y_c)) + p/\rho] + \frac{\partial}{\partial y}[v(u - f(y - y_c))] = 0 \quad (4.8)$$

$$\frac{\partial v}{\partial t} + \frac{\partial(uv)}{\partial x} + \frac{\partial \frac{1}{2}(vv)}{\partial y}, + fu + \frac{1}{\rho} \frac{\partial p}{\partial y} \quad (4.9)$$

$$\frac{\partial u}{\partial x} + \frac{\partial v}{\partial y} = 0, \quad (4.10)$$

where y_c is a constant to be defined later. We regard (4.8)–(4.10) as a closed system in u , v and p , where the density, ρ , is constant. A consequence of (4.8)–(4.10) is the conservation of the absolute vorticity ζ . Since ζ is conserved, any function $C(\zeta)$ is also conserved. Thus, the Casimir function $C(\zeta)$ satisfies

$$\frac{\partial C}{\partial t} + \frac{\partial(uC)}{\partial x} + \frac{\partial(vC)}{\partial y} = 0. \quad (4.11)$$

Adding (4.8) and (4.11), we obtain

$$\frac{\partial[u - f(y - y_c) + C]}{\partial t} + \frac{\partial[u(u - f(y - y_c) + C) + p/\rho]}{\partial x} + \frac{\partial[v(u - f(y - y_c) + C)]}{\partial y} = 0. \quad (4.12)$$

Following McIntyre and Shepherd (1987) and Haynes (1988), we now wish to choose $C(\zeta)$ such that the disturbance part of $[u - f(y - y_c) + C]$ can be written as a divergence, plus a term which is explicitly second order in wave amplitude. The disturbance part of $[u - f(y - y_c) + C]$ is defined as $[u - f(y - y_c) + C]_e = u_e + C(\zeta) - C(\zeta_0)$. The subscript e is now used to represent the disturbance part of a field while a subscript 0 represents its basic state. This change in notation is to distinguish the finite amplitude disturbances discussed in this subsection from the small amplitude approximation of the previous subsection. After some manipulation, the above expression can be written

$$[u - f(y - y_c) + C]_e = A + \frac{\partial[C'(\zeta_0)v_e]}{\partial x} - \frac{\partial[C'(\zeta_0)u_e]}{\partial y} + u_e \left[1 + \frac{\partial C'(\zeta_0)}{\partial y} \right], \quad (4.13)$$

where

$$A = C(\zeta) - C(\zeta_0) - \zeta_c C'(\zeta_0)$$

is the wave-activity of the system and primed quantities now refer to derivatives with respect to the dependent variable. Through use of a Taylor series expansion, it is easy to verify that A is a second order quantity. In addition, the second term on the right hand side of (4.13) is the divergence of a flux. We now wish to choose $C(\zeta)$ in such a way that the last term in (4.13) vanishes. The choice

$$C(\zeta) = \int_{\zeta}^{\zeta_c} [y_0(\tilde{\zeta}) - y_c] d\tilde{\zeta}, \quad (4.14)$$

where $\zeta_c = \zeta_0(y_c)$ and $y_0(\zeta)$ is the inverse of $\zeta_0(y)$ (i.e. $y_0(\zeta_0(y)) = y$), makes the last term in the square brackets in (4.13) vanish, as can easily be verified.

Noting that the basic state is a steady solution of the governing equations and then substituting (4.13) into (4.12) we obtain

$$\begin{aligned} \frac{\partial A}{\partial t} + \frac{\partial}{\partial x} \left[u(u - f(y - y_c) + C) + p/\rho + C'(\zeta_0) \frac{\partial v_e}{\partial t} \right] \\ + \frac{\partial}{\partial y} \left[v(u - f(y - y_c) + C) + -C'(\zeta_0) \frac{\partial u_e}{\partial t} \right] = 0. \end{aligned} \quad (4.15)$$

Using the disturbance momentum equations

$$\frac{\partial u_e}{\partial t} - \zeta v_e + \frac{\partial(\frac{1}{2}u_e^2 + u_0 u_e + \frac{1}{2}v_e^2 + p_e/\rho)}{\partial x} = 0, \quad (4.16)$$

$$\frac{\partial v_e}{\partial t} + \zeta u - \zeta_0 u_0 + \frac{\partial(\frac{1}{2}u_e^2 + u_0 u_e + \frac{1}{2}v_e^2 + p_e/\rho)}{\partial y} = 0, \quad (4.17)$$

in (4.15) and defining y_c such that $u_0(y_c) = 0$, we obtain

$$\frac{\partial A}{\partial t} + \frac{\partial}{\partial x} [uA + \frac{1}{2}(u_e^2 - v_e^2)] + \frac{\partial}{\partial y} [v_e A + u_e v_e] = 0, \quad (4.18)$$

where the wave-activity can also be written as

$$A = - \int_0^{\zeta_c} [y_0(\zeta_0 + \tilde{\zeta}) - y_0(\zeta_0)] d\tilde{\zeta}. \quad (4.19)$$

To obtain the nonlinear stability condition we now integrate (4.18) over the entire domain (again assuming a doubly periodic domain) to obtain

$$\frac{d}{dt} \iint A dx dy = 0. \quad (4.20)$$

Although this looks identical to (4.7), we must keep in mind that the A in (4.20) is defined by (4.19) while the A in (4.7) is defined by (4.5). The results are consistent, however, since (4.19) reduces to (4.5) in the small amplitude limit. To see this, we consider the integrand in (4.19), i.e.

$$[y_0(\zeta_0 + \bar{\zeta}) - y_0(\zeta_0)] \quad (4.21)$$

A Taylor series expansion about ζ_0 of (4.21) yields $(dy_0(\zeta_0)/d\zeta)\bar{\zeta}$. Using this result to evaluate the integral in (4.19) yields

$$A = -\zeta_e^2 \frac{dy_0(\zeta_0)}{d\zeta}, \quad (4.22)$$

where $\zeta_e = \zeta'$ in the small amplitude limit. Using the relationship given by (4.3) to eliminate ζ' and noting that $dy_0/d\zeta = (d\zeta_0/dy)^{-1} = (d\bar{\zeta}/dr)^{-1}$ in the small amplitude limit, we arrive at the desired relationship. That is,

$$\lim_{\zeta_e \rightarrow \zeta'} \left\{ - \int_0^{\zeta_e} [y_0(\zeta_0 + \bar{\zeta}) - y_0(\zeta_0)] d\bar{\zeta} \right\} = -\frac{1}{2} \eta^2 \frac{\partial \bar{\zeta}}{\partial y}. \quad (4.23)$$

Thus, (4.19) is simply a finite amplitude generalization of the wave-activity obtained through Rayleigh's theorem.

We now note that since y_0 is a monotone function of $\bar{\zeta}$, the integrand in (4.19), is bounded by the lines $-\bar{\zeta}|dy_0/d\zeta|_{\max}$ and $-\bar{\zeta}|dy_0/d\zeta|_{\min}$. These lines represent the maximum and minimum slopes respectively of the integrand in (4.19) multiplied by the variable of integration, $\bar{\zeta}$. In addition, the monotonic nature of y_0 implies $A \leq 0$ for all values of ζ_e . This allows us to write

$$\zeta_e^2 |dy_0/d\zeta|_{\min} \leq 2|A(\zeta_0, \zeta_e)| \leq \zeta_e^2 |dy_0/d\zeta|_{\max}. \quad (4.24)$$

Together, (4.20) and (4.24) imply that

$$\begin{aligned} |dy_0/d\zeta|_{\min} \iint \zeta_e^2(x, y, t) dx dy &\leq \iint 2|A(\zeta_0, \zeta_e, t)| dx dy = \\ \iint 2|A(\zeta_0, \zeta_e, 0)| dx dy &\leq |dy_0/d\zeta|_{\max} \iint \zeta_e^2(x, y, 0) dx dy, \end{aligned}$$

which can also be written

$$\iint \zeta_e^2(x, y, t) dx dy \leq \frac{|dy_0/d\zeta|_{\max}}{|dy_0/d\zeta|_{\min}} \iint \zeta_e^2(x, y, 0) dx dy. \quad (4.25)$$

This is the form of Arnol'd's (1965, 1966) result derived by McIntyre and Shepherd (1987). The inequality (4.25) bounds the disturbance enstrophy at time t in terms of the initial disturbance enstrophy and the radial gradient of the basic state absolute vorticity. It rules out the possibility of instability for basic state flows with $d\zeta_0/dy > 0$ (or $d\zeta_0/dy < 0$) everywhere. Thus, Arnol'd's theorem provides a sufficient condition for stability, or conversely, a necessary condition for instability.

4.2.3 Ripa's Theorem

Until now, we have discussed stability with regard only to nondivergent flow. We now wish to relax this assumption of balance but retain the assumption of linearity. The case we consider is the linear shallow water equations on the f -plane. This theorem was first derived by Ripa (1983) on the β -plane and sphere for a single layer of fluid. Ripa (1991) later generalized his theorem to include multiple discrete incompressible layers (but not continuously stratified).

The shallow water equations linearized about a basic state which is in gradient balance can be written in cylindrical coordinates as

$$\frac{\partial u'}{\partial t} - \bar{\zeta}v' + \frac{\partial(\bar{u}u' + gh')}{\partial x} = 0, \quad (4.26)$$

$$\frac{\partial v'}{\partial t} + \zeta'\bar{u} + \bar{P}\bar{h}u' + \frac{\partial(\bar{u}u' + gh')}{\partial y} = 0, \quad (4.27)$$

$$\frac{\partial h'}{\partial t} + \frac{\partial(\bar{h}u' + \bar{u}h')}{\partial x} + \frac{\partial(v'\bar{h})}{\partial y} = 0, \quad (4.28)$$

where $\bar{P} \equiv \bar{\zeta}/\bar{h}$, $\bar{\zeta}$ being the zonally averaged absolute vorticity. To derive Ripa's theorem we need to combine (4.26)–(4.28) into equations for

$$E' = \frac{1}{2} [\bar{h}(u'^2 + v'^2) + 2\bar{u}u'h' + gh'^2], \quad (4.29)$$

$$M' = u'h', \quad (4.30)$$

and

$$P' = \frac{1}{\bar{h}} \left(\frac{\partial v'}{\partial x} - \frac{\partial u'}{\partial y} - \bar{P}h' \right). \quad (4.31)$$

To derive the equation for E' we form $(\bar{h}u' + h'\bar{u}) \cdot (4.26) + (\bar{h}v') \cdot (4.27) + (gh' + \bar{u}u') \cdot (4.28)$ to obtain

$$\frac{\partial E'}{\partial t} + \bar{h}^2 \bar{u} v' P' + \frac{\partial[(\bar{h}u' + \bar{u}h')(gh' + \bar{u}u')]}{\partial x} + \frac{\partial[\bar{h}v'(\bar{u}u' + gh')]}{\partial y} = 0. \quad (4.32)$$

To derive the equation for M' we form $h' \cdot (4.26) + u' \cdot (4.28)$ to obtain

$$\frac{\partial M'}{\partial t} + \bar{h}^2 u' P' + \frac{\partial[\bar{u}M' + \frac{1}{2}\bar{h}(u'^2 - v'^2) + \frac{1}{2}gh']}{\partial x} + \frac{\partial[u'v'\bar{h}]}{\partial y} = 0. \quad (4.33)$$

Combining the integrated forms of (4.32) minus u_0 times (4.33) we obtain

$$\iint \left(\frac{\partial(E' - u_0 M')}{\partial t} + \bar{h}^2 v' P' (\bar{u} - u_0) \right) dx dy = 0, \quad (4.34)$$

where u_0 is an arbitrary constant. The equation for P' is obtained by forming the vorticity equation from (4.26)–(4.27) and eliminating the divergence using (4.28). This equation takes the form

$$\frac{DP'}{Dt} + \frac{d\bar{P}}{dy} u' = 0, \quad (4.35)$$

where $D/Dt = \partial/\partial t + \bar{u}\partial/\partial x$. Defining the meridional particle displacement, η , by $D\eta/Dt = v'$ and assuming both P' and η vanish at some finite time, we obtain

$$P' + \frac{d\bar{P}}{dy} \eta = 0. \quad (4.36)$$

Multiplication of (4.36) by v' yields

$$v' P' + \frac{D}{Dt} \left(\frac{d\bar{P}}{dy} \frac{1}{2} \eta^2 \right) = 0. \quad (4.37)$$

Finally, using (4.37) in (4.34) for $v' P'$ we obtain

$$\frac{d}{dt} \iint \left(E' - u_0 M' - \bar{h}^2 \frac{d\bar{P}}{dy} \frac{1}{2} \eta^2 (\bar{u} - u_0) \right) dx dy = 0, \quad (4.38)$$

which is the divergent barotropic generalization of the nondivergent barotropic result (4.7).

We now argue that, if $E' - u_0 M' \geq 0$ and $(\bar{u} - u_0) d\bar{P}/dy \leq 0$, the constraint (4.38) does not allow η^2 to grow in an overall sense. We now note that the three rightmost terms (4.29) can be written in a quadratic form for h' and v' . The quadratic, and therefore E' , will be positive if the coefficients of the quadratic satisfy $\bar{h} \geq 0$ and $\bar{u}^2 \leq g\bar{h}$ (Strang, 1988,

p. 325). Since $\bar{h} \geq 0$ by assumption, then $E' \geq 0$ if $\bar{u}^2 \leq g\bar{h}$. By a similar argument, $E' - \omega_0 M' \geq 0$ if $[(\bar{u} - u_0)]^2 \leq g\bar{h}$. We can now state Ripa's shallow water generalization of the theorems of Rayleigh and Fjørtoft. *If there exists any value of u_0 such that*

$$(\bar{u} - u_0) \frac{d\bar{P}}{dy} \leq 0 \quad \text{and} \quad (\bar{u} - u_0)^2 \leq g\bar{h} \quad (4.39a, b)$$

for all r , then the flow is stable to infinitesimal perturbations. Ripa has also discussed several corollaries of (4.39), one of which is obtained by choosing $u_0 = \max[\bar{u}]$. This results in the following weaker sufficient condition for stability. *If*

$$\frac{d\bar{P}}{dy} \geq 0 \quad \text{and} \quad \max[\bar{u}] \leq \min[\bar{u} + (g\bar{h})^{1/2}] \quad (4.40a, b)$$

for all r , then the flow is stable to infinitesimal perturbations.

To recover the stability results for the nondivergent barotropic model from the stability results for the divergent barotropic model we consider the limit $g\bar{h} \rightarrow \infty$, in which case (4.39b) is satisfied for any finite u_0 . Then, there is no difference between vorticity and potential vorticity, and a choice of u_0 such that $\bar{u} - u_0 < 0$ everywhere leads to $d\bar{\zeta}/dy \geq 0$ everywhere as sufficient for stability, while a choice of u_0 such that $\bar{u} - u_0 > 0$ everywhere leads to $d\bar{\zeta}/dy \leq 0$ everywhere as sufficient for stability. Thus, a necessary condition for instability is that $d\bar{\zeta}/dy$ have both signs (Rayleigh's theorem). It is also of interest to note that, if $d\bar{\zeta}/dy = 0$ at $y = \hat{y}$, then the choice $u_0 = \bar{u}(\hat{y})$ leads from (4.39a) to $[\bar{u}(\hat{y}) - u_0]d\bar{\zeta}/dy < 0$ somewhere as a necessary condition for instability (Fjørtoft's theorem).

4.3 Numerical Analyses and Simulations

In the previous section, we saw that the common factor to all stability analyses was the need for a reversal in the PV gradient. They did not however indicate to what extent these disturbances could grow nor with what speed. In this section, we attempt to shed some light on this problem through both normal mode stability analysis and numerical simulations. This theory is then applied to the breakdown of the ITCZ and the formation of outer bands.

In the first subsection we present a linear normal mode stability analysis of a PV strip. This provides an estimate of both unstable patterns and growth rates. In subsection 4.3.2 we simulate the breakdown of the ITCZ and the formation of outer bands through five model integrations.

4.3.1 Normal Mode Stability Analysis

In the previous section we examined various general stability theories. Although these theories provide necessary conditions for stability, they tell us nothing about the rate at which these instabilities will grow or the favored patterns for instability. To determine these unknowns, we utilize the less general tool of normal mode stability analysis. This type of analysis is less general in the sense that it assumes wave form instabilities, i.e. stabilities which are proportional to $e^{i(kx+ly-\nu t)}$. The normal mode stability analysis of a PV strip was first presented by Rayleigh (1945, vol. 2, pp. 384-398) and is presented here as a review. Note that for the nondivergent, barotropic analysis, there is no difference between PV and absolute vorticity.

We begin the analysis by considering the linearized nondivergent barotropic dynamics of a PV field with the following basic state zonal flow

$$\bar{u}(y) = \begin{cases} -\zeta_0 y_0 & y_0 \leq y < \infty \\ -\zeta_0 y & -y_0 \leq y \leq y_0 \\ \zeta_0 y_0 & -\infty < y \leq -y_0 \end{cases} \quad (4.41)$$

The basic state absolute vorticity field corresponding to (4.41) is

$$\bar{\zeta}(y) = f - \frac{\partial \bar{u}}{\partial y} = \begin{cases} f & y_0 \leq y < \infty \\ f + \zeta_0 & -y_0 \leq y \leq y_0 \\ f & -\infty < y \leq -y_0 \end{cases} \quad (4.42)$$

Because the vorticity is constant everywhere except at the interfaces, the equation which the perturbation streamfunction must satisfy is simply

$$\frac{\partial^2 \psi'}{\partial x^2} + \frac{\partial^2 \psi'}{\partial y^2} = 0 \quad (4.43)$$

If we assume a normal mode solution which is proportional to $e^{i(kx-\nu t)}$, the solution to (4.43) can be written as

$$\psi'(x, y, t) = e^{i(kx-\nu t)} \left\{ \begin{array}{ll} \Psi_n e^{-k(y-y_0)} + \Psi_s^{-k(y+y_0)} & y_0 \leq y < \infty \\ \Psi_n e^{k(y-y_0)} + \Psi_s^{-k(y+y_0)} & -y_0 \leq y \leq y_0 \\ \Psi_n e^{k(y-y_0)} + \Psi_s^{k(y+y_0)} & -\infty < y \leq -y_0 \end{array} \right\} \quad (4.44)$$

It is easily confirmed by inspection that $\psi'(x, y, t)$ is continuous.

Now let us assume that the northern and southern interfaces of the PV strip are perturbed in a sinusoidal fashion by an amount $\eta_n = \hat{\eta}_n e^{i(kx-\nu t)}$ and $\eta_s = \hat{\eta}_s e^{i(kx-\nu t)}$, where η_n and η_s represent the distances the northern and southern interfaces are displaced from their original positions respectively. Since PV is materially conserved, η_n and η_s also represent particle displacements. The equations governing the displacement of the boundaries can be written

$$\frac{\partial \eta_n}{\partial t} + \bar{u} \frac{\partial \eta_n}{\partial x} = \nu' = \frac{\partial \psi'}{\partial x} \quad \text{and} \quad \frac{\partial \eta_s}{\partial t} + \bar{u} \frac{\partial \eta_s}{\partial x} = \frac{\partial \psi'}{\partial x}. \quad (4.45)$$

Our goal is to use (4.44) in (4.45) to determine under what conditions the particle displacement will grow unbounded. Before this can be done, however, we must first relate the complex streamfunction amplitudes (Ψ_n and Ψ_s) to the complex particle displacement amplitudes ($\hat{\eta}_n$ and $\hat{\eta}_s$). We do this by requiring the zonal component of the wind ($\bar{u} + u'$) to be continuous at the boundaries $y = y_0 + \eta_n$ and $y = -y_0 + \eta_s$, where the zonal wind is obtained from $u' = -\partial \psi' / \partial y$. In doing this, we obtain

$$k \Psi_n = \frac{1}{2} \zeta_o \hat{\eta}_n \quad \text{and} \quad k \Psi_s = -\frac{1}{2} \zeta_o \hat{\eta}_s. \quad (4.46)$$

Substituting (4.46) into (4.44) and using the result in (4.45) gives

$$\begin{pmatrix} \frac{1}{2} \zeta_o (1 - 2ky_0) & -\frac{1}{2} \zeta_o e^{-2ky_0} \\ \frac{1}{2} \zeta_o e^{-2ky_0} & -\frac{1}{2} \zeta_o (1 - 2ky_0) \end{pmatrix} \begin{pmatrix} \hat{\eta}_n \\ \hat{\eta}_s \end{pmatrix} = \nu \begin{pmatrix} \hat{\eta}_n \\ \hat{\eta}_s \end{pmatrix} \quad (4.47)$$

Equation (4.47) is a standard matrix eigenvalue problem which can be solved in the usual manner. The solutions for the eigenvalues/frequencies are

$$\nu_k = \pm \frac{1}{2} \zeta_o [(1 - 2ky_0)^2 - e^{-4ky_0}]^{\frac{1}{2}} \quad (4.48)$$

The solution for ν will be purely imaginary if ky_o lies between 0 and 0.6392. By differentiating (4.48) with respect to ky_o and setting the result to zero, the most unstable mode is found to occur when $ky_o = 0.3984$. Since $k \equiv 2\pi/L_x$ where L_x is the wavelength in the x -direction, we obtain the following relationship between the half-width of the disturbance and the wavelength of the most unstable mode,

$$2\pi y_o \approx 0.4L_x, \quad (4.49)$$

i.e., the wavelength of the most unstable mode is approximately eight times the width of the strip. Thus, in the absence of any adverse shear or variation of the earth's vorticity, we would expect the wavelength of the most unstable mode to be constant regardless of the intensity of vorticity strip.

The above analysis can be made slightly more general by including the effects of adverse shear, that is, the addition of a uniform anticyclonic shear layer (Dritschel, 1989). We include this effect partly because of generality but mainly out of necessity. The necessity of this analysis stems from the models periodic boundary conditions. Having periodic boundary conditions implies no mean vorticity field can exist since this would imply a mean circulation around the periphery of the model domain. A mean circulation, however, requires the wind to be moving in opposite directions at opposing boundaries. This clearly violates the models requirement of periodicity. As will be seen in the following section, the mean vorticity field can be removed by subtracting it from the initial vorticity field. Subtracting the mean positive vorticity is equivalent to adding a uniform region of negative vorticity. We denote the negative vorticity as being some fractional amount of ζ_o , namely $-\Lambda\zeta_o$ where Λ can be any number. The resulting mean wind and absolute vorticity profiles for this case take the form

$$\bar{u}(y) = \begin{cases} -\zeta_o(y_o - \Lambda y) & y_o \leq y < \infty \\ -\zeta_o y(1 - \Lambda) & -y_o \leq y \leq y_o \\ \zeta_o(y_o + \Lambda y) & -\infty < y \leq -y_o \end{cases}, \quad (4.50)$$

and

$$\bar{\zeta}_a(y) = f - \frac{\partial \bar{u}}{\partial y} = \begin{cases} f - \zeta_o \Lambda & y_o \leq y < \infty \\ f + \zeta_o(1 - \Lambda) & -y_o \leq y \leq y_o \\ f - \zeta_o \Lambda & -\infty < y \leq -y_o \end{cases}. \quad (4.51)$$

Because the vorticity is constant except near the boundaries, ψ' must still satisfy (4.44). In addition, (4.46) remains valid. The effect of adverse shear is felt only in the definition of $\bar{u}(y)$ and therefore only in the equations for η_n and η_s . Using this fact, we see that the new matrix eigenvalue problem takes the form

$$\begin{pmatrix} \frac{1}{2}\zeta_o[1 - 2ky_o(1 - \Lambda)] & -\frac{1}{2}\zeta_o e^{-2ky_o} \\ \frac{1}{2}\zeta_o e^{-2ky_o} & -\frac{1}{2}\zeta_o[1 - 2ky_o(1 - \Lambda)] \end{pmatrix} \begin{pmatrix} \hat{\eta}_n \\ \hat{\eta}_s \end{pmatrix} = \nu \begin{pmatrix} \hat{\eta}_n \\ \hat{\eta}_s \end{pmatrix}. \quad (4.52)$$

The corresponding solution to (4.52) is

$$\nu_k(\Lambda) = \pm \frac{1}{2}\zeta_o \{ [1 - 2ky_o(1 - \Lambda)]^2 - e^{-4ky_o} \}^{\frac{1}{2}}. \quad (4.53)$$

Clearly instabilities cannot exist if $\Lambda \geq 1$ since the radicand in (4.53) will be positive for all wavelengths. This will result in ν being strictly real. The effect of adverse shear is to decrease both the wavelength of the most unstable mode and its growth rate. Figure 4.3 shows the decrease in the maximum growth rate with increased adverse shear as well as the increase in the nondimensional wavenumber, ky_o , of the most unstable mode. These results agree with the β -plane analyses performed numerically by Kuo (1973) and analytically by Schubert *et al.* (1992). For the case of our present model, Λ will remain less than ~ 0.2 .

In the next subsection, we integrate the shallow water equations starting with various initial vorticity patterns which are meant to represent both the PV strips described above and the ITCZ.

4.3.2 Numerical Experiments

The breakdown of PV strips for nondivergent flows have been extensively studied using contour dynamical methods (Dritschel, 1989; Pratt and Pedlosky, 1991) in which the positions of boundaries between regions of piecewise constant PV are predicted. Although contour dynamics provides an elegant method for studying instabilities, it requires discontinuous vorticity patterns. In addition, the contour dynamical studies mentioned above were both balanced studies. In this subsection, we relax the assumption of balance and integrate the divergent barotropic (shallow water) equations for five different experiments.

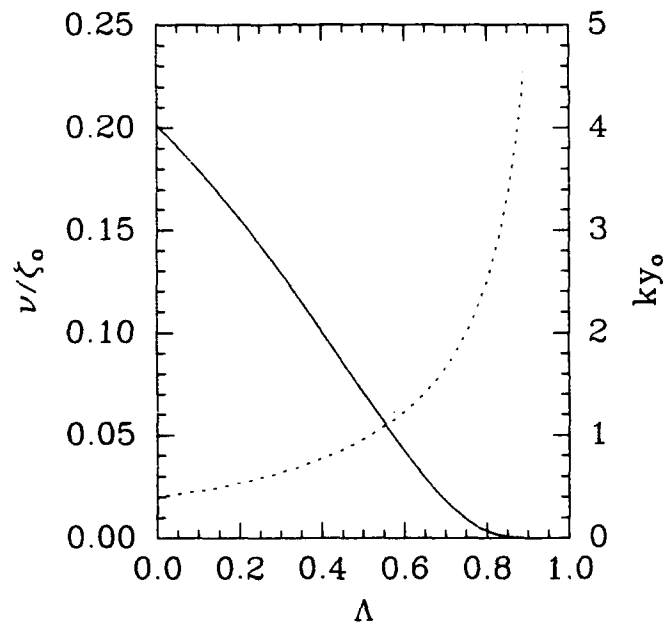


Figure 4.3: The change in normalized growth rates and nondimensional wavenumber with increased adverse shear. The solid line corresponds to normalized growth rates which are read on the left ordinate and the dashed line corresponds to the most unstable (nondimensional) wavenumbers which are read on the right ordinate.

Unlike contour dynamical models, our model uses spectral discretization. This means a discontinuous initial vorticity field is not permissible since that would require an infinite number of spectral coefficients to represent the jump. We therefore represent a strip of PV in two different ways. The first method defines the PV strip to be Gaussian in y (centered about the line $y = y_c$) and constant in x , i.e.

$$\zeta(y) = \hat{\zeta} \exp \left[- \left(\frac{(y - y_c)}{y_h} \right)^2 \right], \quad (4.54)$$

where y_h is the Gaussian half-width which defines the e -folding distance and $\hat{\zeta}$ is the maximum value of vorticity. The second vorticity pattern to be defined is also constant in x but rather than being Gaussian in y , we use the profile function (3.19) to describe the strip's variation in y . Once the vorticity pattern has been defined, the balanced wind and mass fields are determined by the nonlinear balance equation described in Chapter 2. Even though the initial vorticity pattern is unstable, instabilities will not grow unless the fluid is perturbed. To perturb the fluid without exciting large gravity waves, we add white noise to half the slow mode spectral coefficients and leave the fast modes undisturbed. The remaining half of the slow mode spectral coefficients are computed as the complex conjugates of the disturbed half. This ensures the physical fields will remain real.

As mentioned previously, the mean vorticity field must first be removed before it can be used. This can easily be done by transforming the vorticity field to spectral space, setting the spectral coefficient corresponding to $\hat{k} = \hat{l} = 0$ to zero, and transforming the field back to physical space.

Experiment one is intended to simulate a continuous ITCZ pattern which is centered at 10°N in the eastern Pacific Ocean. We start from an initial state which is defined by a PV strip extending across the entire width of the domain. The strip is Gaussian in y with a half-width of 235 km and a maximum vorticity of $6.25 \times 10^{-5} \text{ s}^{-1}(2.5f)$, which gives an adverse shear of ~ 0.065 . Figure 4.4 shows the height, wind, normalized PV, and absolute vorticity fields at the initial time. The PV is normalized by the mean depth H which is taken to be 300 m. This value of H provides a pure gravity wave speed of $\sim 54 \text{ ms}^{-1}$ and a Rossby radius of $\sim 1360 \text{ km}$ if f is calculated at 10°N . The absolute vorticity

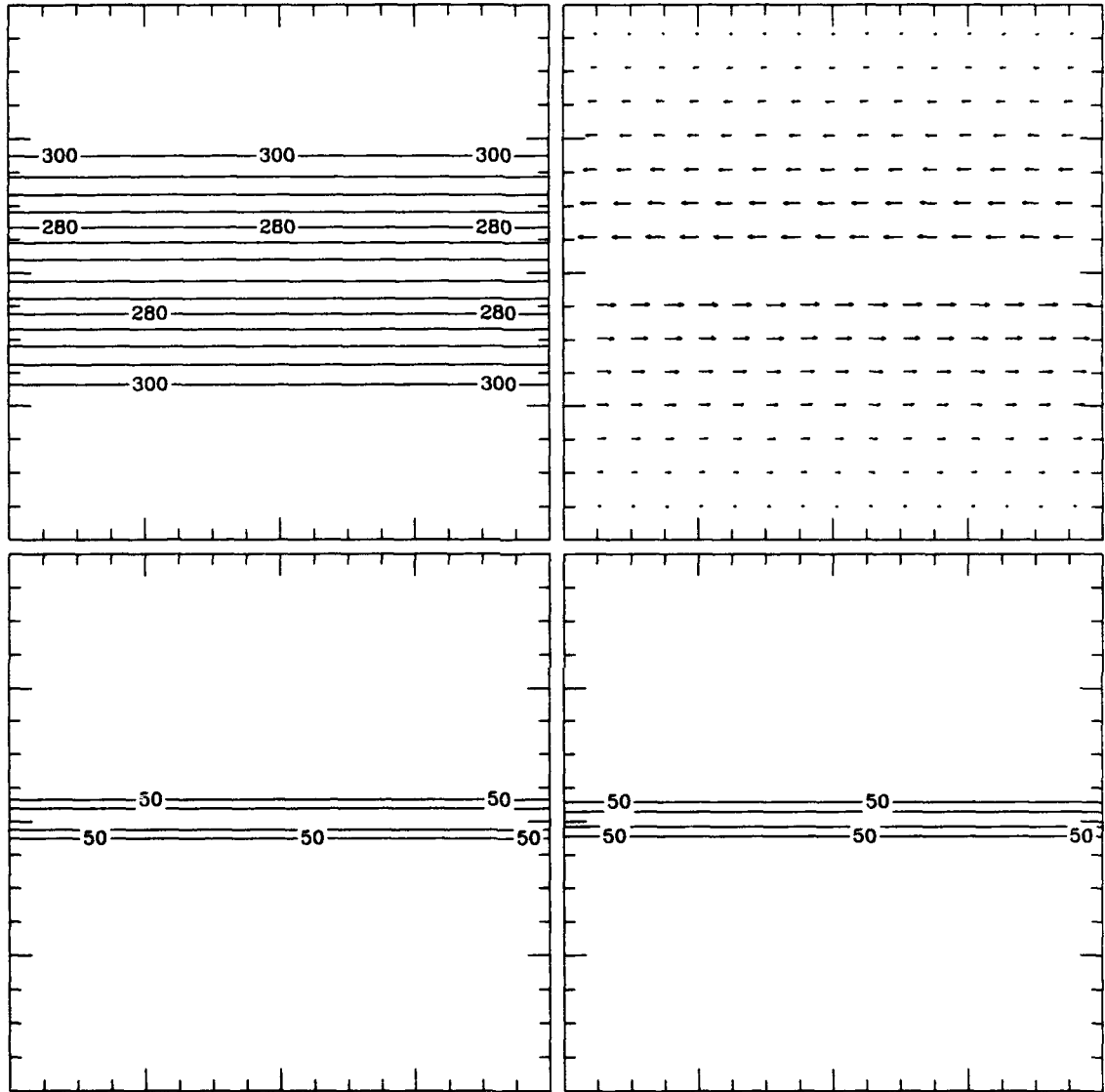


Figure 4.4: Dynamic fields at initial time for experiment one: height (upper left), winds (upper right), normalized PV (lower left), and absolute vorticity (lower right). The height field has a contour interval of 5 m. The maximum wind vector, defined as the length between two successive tick marks, is 20 ms^{-1} . The normalized PV and absolute vorticity have contour intervals of 25×10^{-6} and are in units of 10^{-6} s^{-1} . Tick marks are every 400 km.

(lower right) and normalized PV fields (lower left) have contour intervals of $2.5 \times 10^{-5} \text{ s}^{-1}$ or $1f$ starting at $2f$. These contours are scaled by 10^6 . The height field (upper right) has contour intervals of 5 m and the maximum wind vector length (as measured between two vectors without allowing overlap) is 20 ms^{-1} . The grid size is $6400 \text{ km} \times 6400 \text{ km}$ with 128×128 points on the transform grid, thus 42 waves are kept in both x and y . The initial wind varies from -11 ms^{-1} to 11 ms^{-1} giving a total wind shear across the ITCZ of 22 ms^{-1} . Figures 4.5–4.8 show the evolution of the vorticity and PV fields at intervals of two days starting at the eighth model day. All fields are shown for day fourteen in Fig. 4.9.

Prior to the eighth day, instabilities are not easily recognizable. After the eighth day, the disturbances grow quite rapidly. Especially interesting to note is the development of two disturbances placed relatively close to one another. As time proceeds, these disturbances undergo a merger process which appears to be complete by the fourteenth model day. The merger of geostrophic vortices in laboratory experiments has been well documented by Griffiths and Hopfinger (1987) who noted that vortices will merge if they are less than 3.3 ± 0.2 radii apart. This criterion appears to be satisfied in the model simulation. By day eleven (not shown), the two closest vortices have begun the merger process. By day fourteen, the process is complete and only two of the three original disturbances remain. The origin of the outer bands is especially noticeable on the twelfth day. On this day, the pooling process has created a rather thin filament of PV which connects the circular vortex to the merging vortex. This filament is precisely what we mean by an outer band. This band is still clearly visible in the PV field by the fourteenth day.

Before continuing, we note that the time scale of the model ITCZ breakdown appears slower than that observed in nature. The model took 14 days for the ITCZ to breakdown whereas in nature, the ITCZ generally breaks down in three to seven days. It must be made clear, however, that in nature the ITCZ is not perturbed with such small amplitude forcings. If one considers day eight as representative of a finitely perturbed ITCZ (i.e. letting day eight represent day one in nature) then the simulated ITCZ breakdown is very close to that in nature. Faster breakdowns can also be obtained simply by increasing the amplitude of the perturbations.

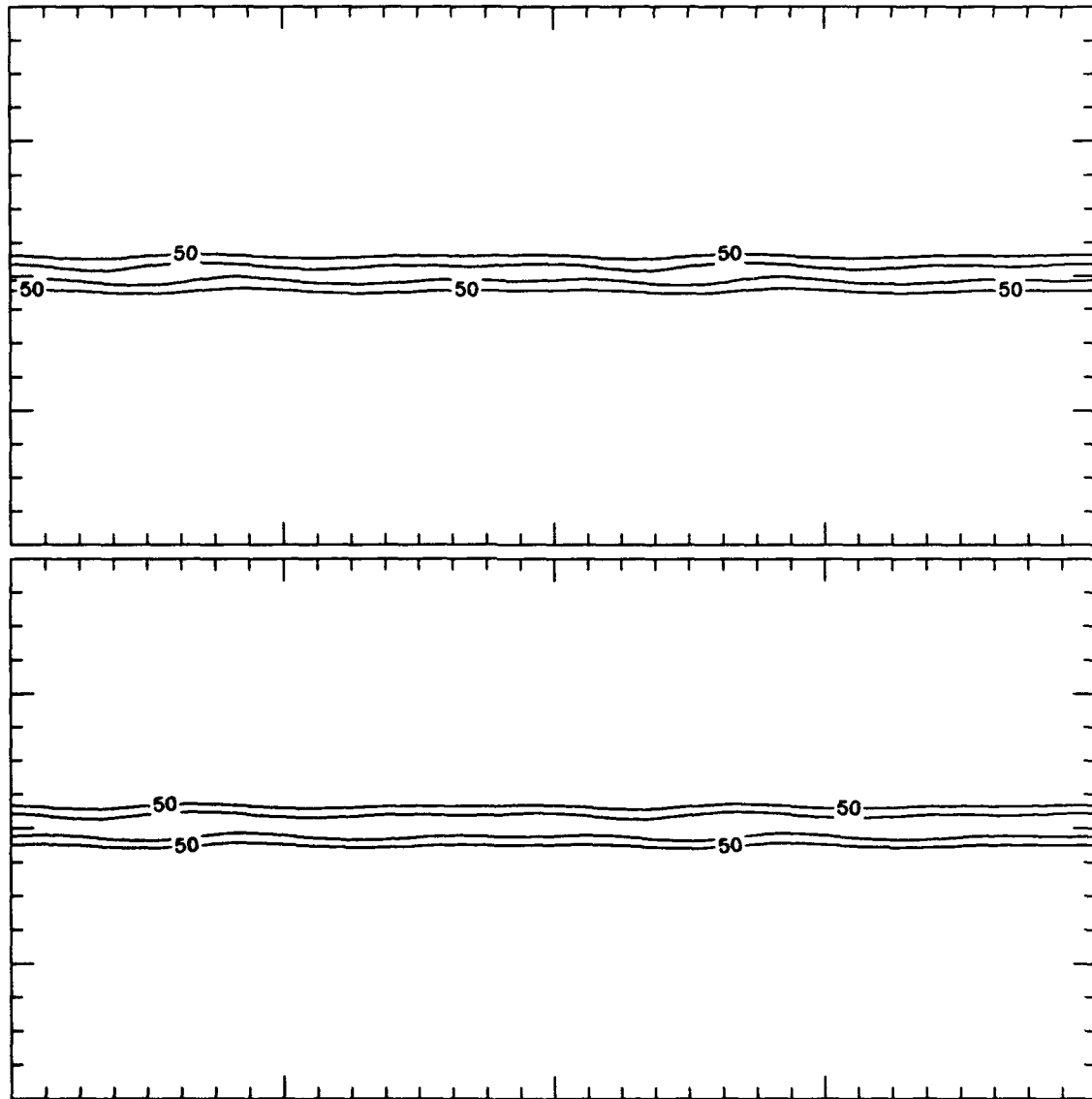


Figure 4.5: Vorticity (top) and $\bar{F}V$ (bottom) at day eight for experiment one. Two domain periods are shown. Units are 10^{-6} s^{-1} and contour intervals are 25×10^{-6} .

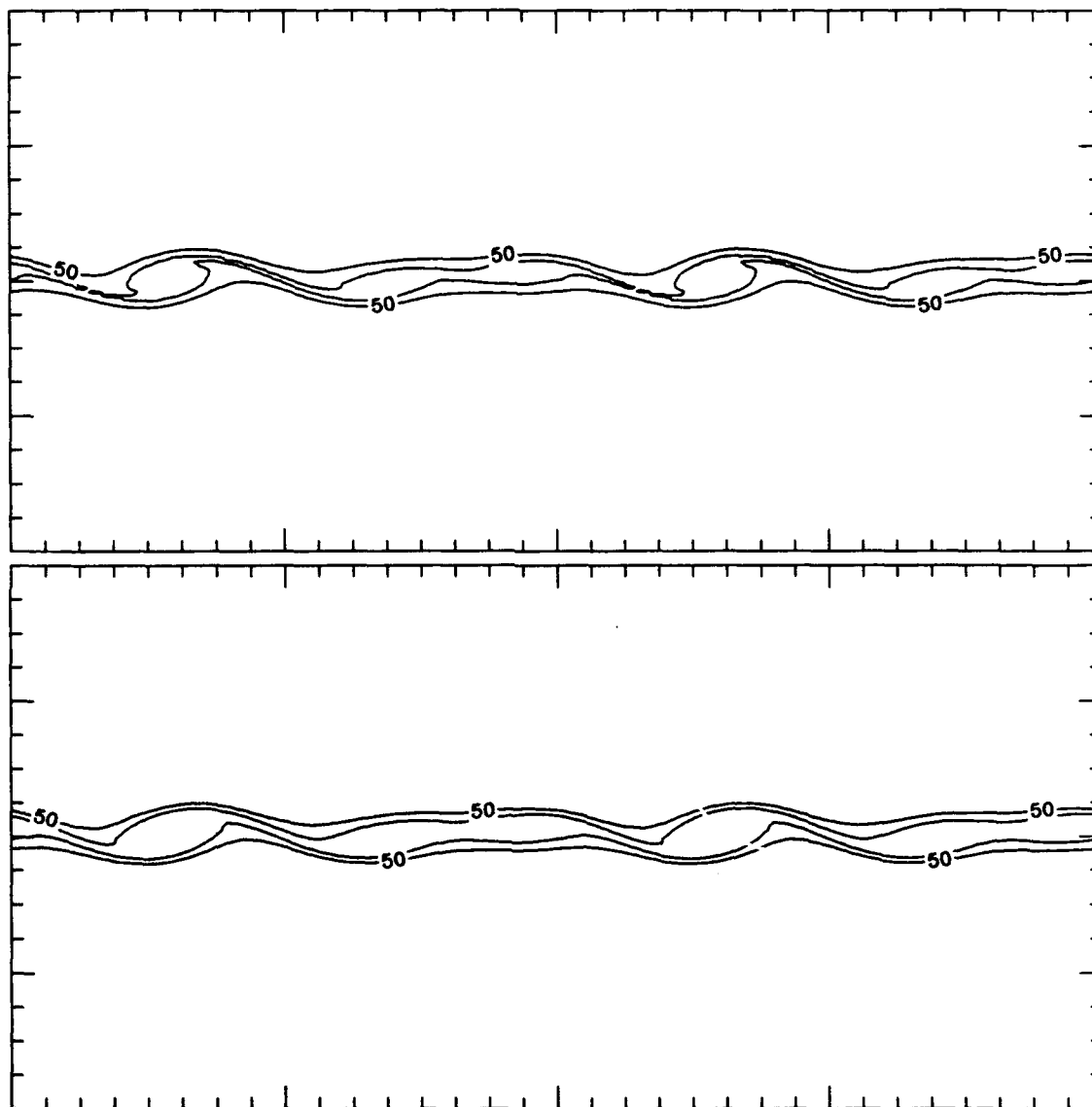


Figure 4.6: Same as for Fig. 4.5 but for day ten.

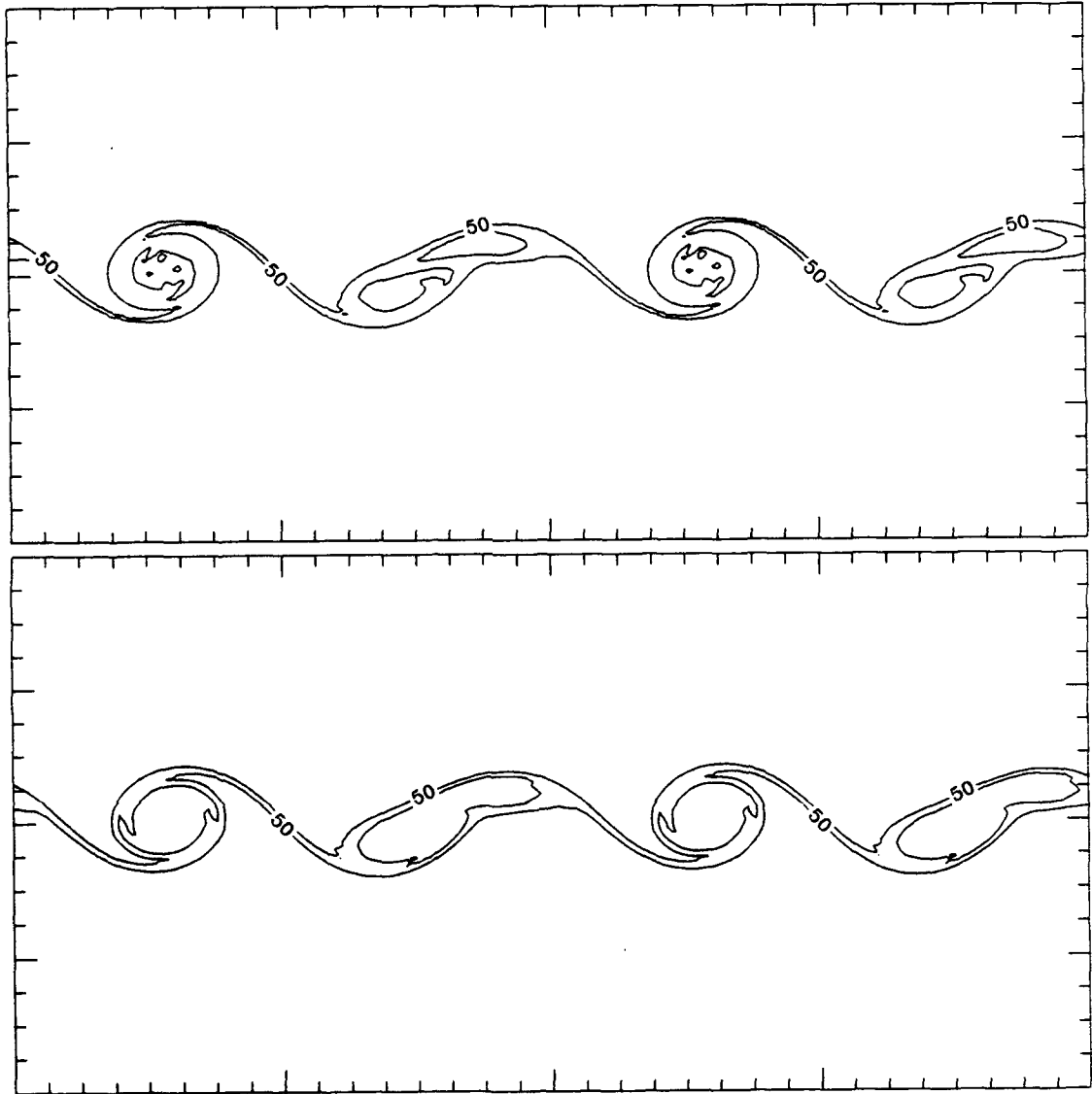


Figure 4.7: Same as for Fig. 4.5 but for day twelve.

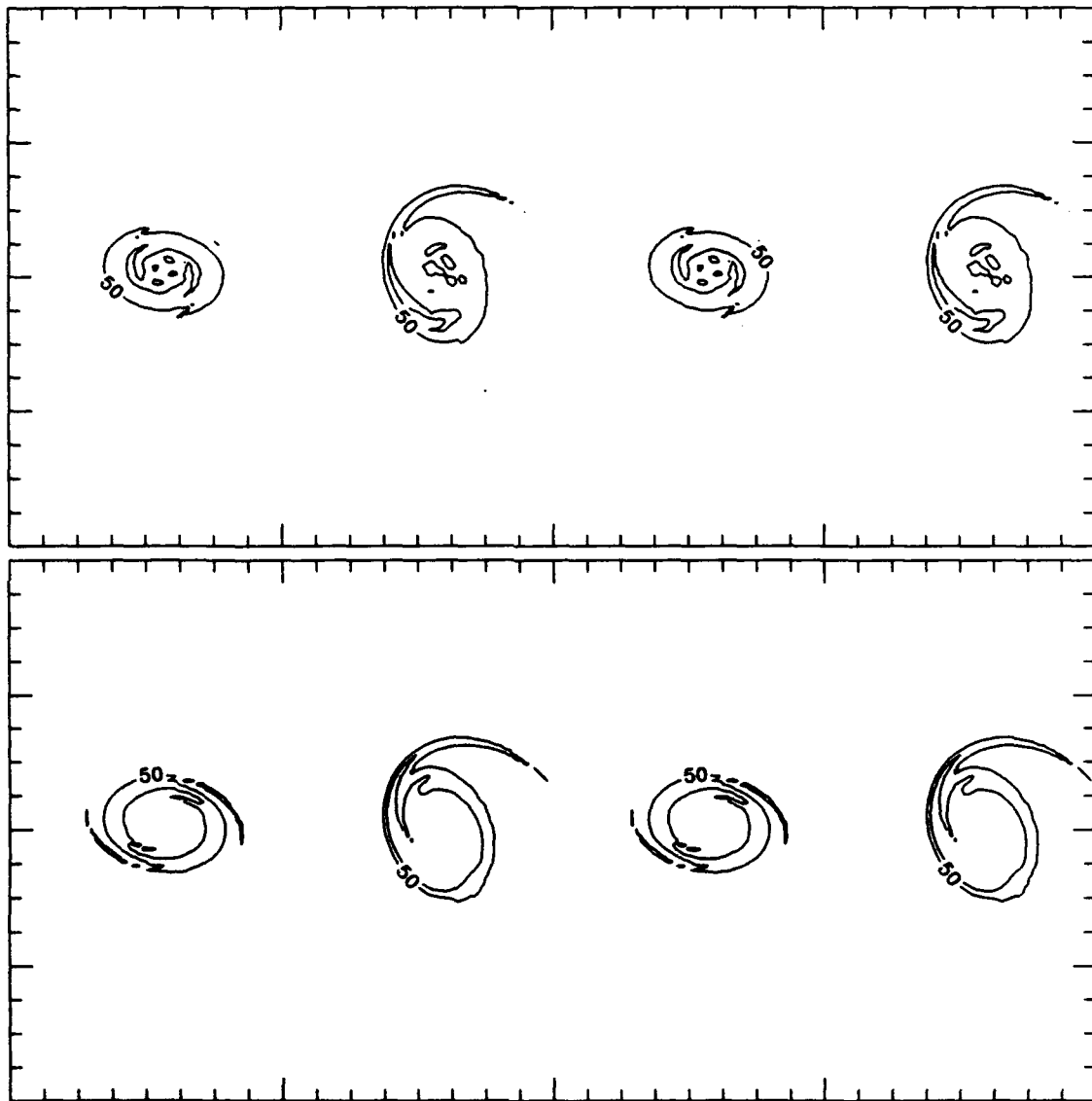


Figure 4.8: Same as for Fig. 4.5 but for day fourteen.

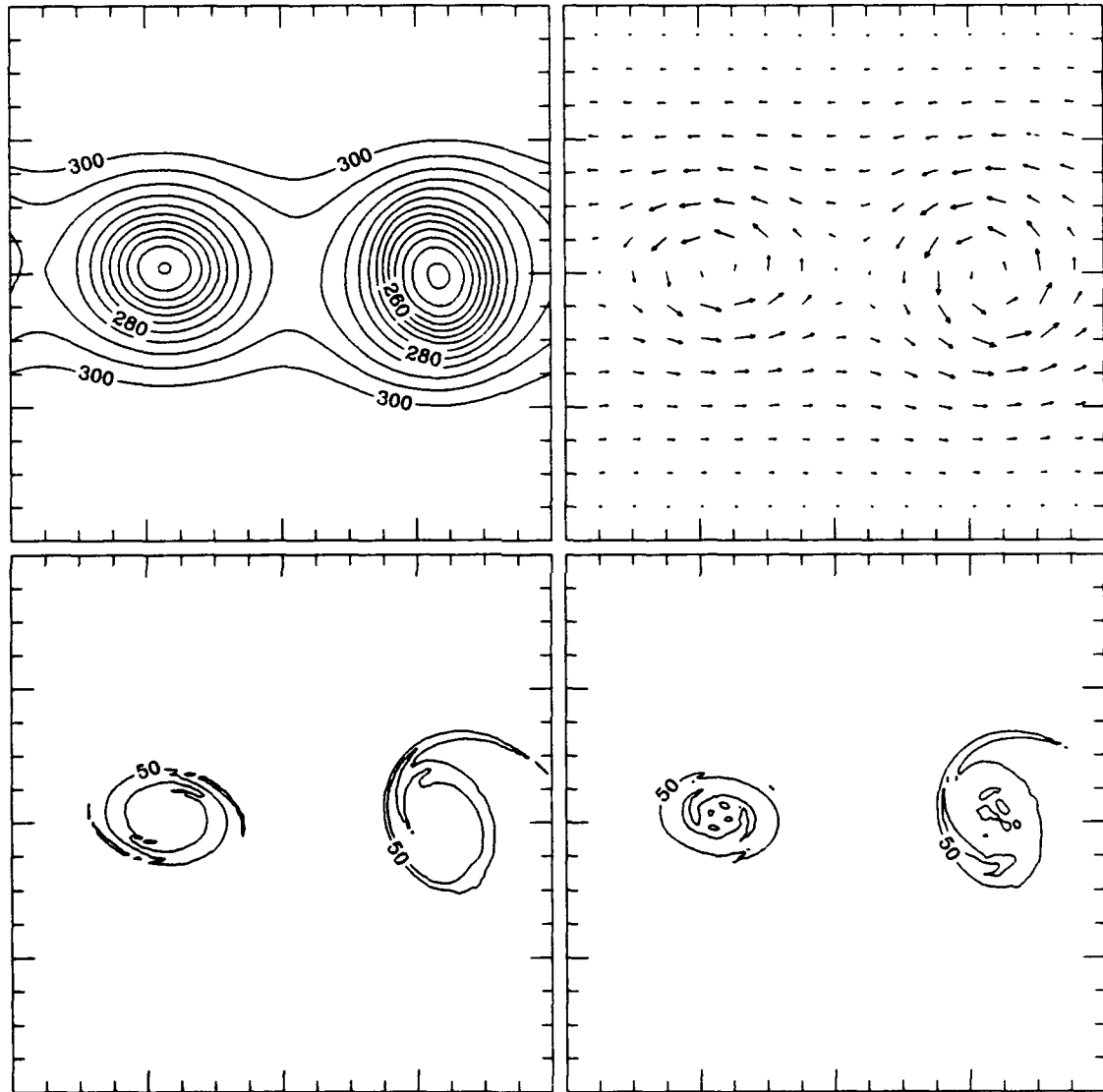


Figure 4.9: Same as for Fig. 4.4 but for day fourteen.

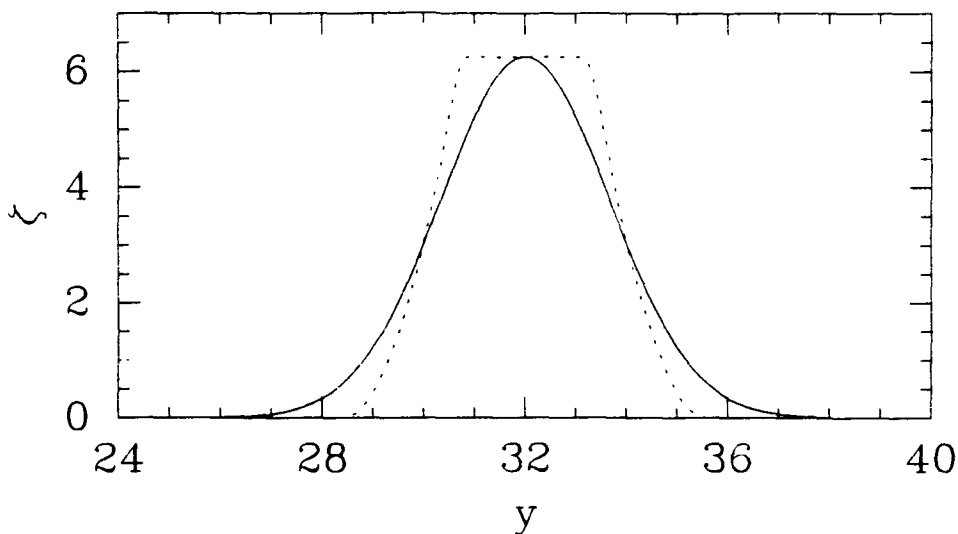


Figure 4.10: Initial relative vorticity profiles for experiments one through three. The smooth line is for Gaussian profile and dashed is for the Melander profile. The relative vorticity has units of s^{-1} and is scaled by 10^5 . The distance is measured in hundreds of kilometers.

For the second experiment, we consider the effect of changing the shape of the initial PV profile. We choose an initial vorticity field which makes use of the profile functions (3.19)–(3.20) (hereafter referred to as a Melander profile) and has the same average vorticity and initial winds as the previous Gaussian experiment. In order to use (3.19) in Cartesian coordinates, we simply replace r by $|y - y_c|$. The profile obtained by letting $R_i = 100$ km and $R_0 = 400$ km is shown in Fig. 4.10 along with the Gaussian curve used in experiment one. By examining Fig. 4.10, it is obvious that we are more closely approximating the uniform vorticity strips which were considered in the normal mode stability analysis.

As with experiment one, we again perturb the above vorticity distribution by adding white noise to the balanced modes. It is important to note that the same sequence of random numbers is used for both experiments one and two. The effect of changing this will be examined in the final experiment. Results from experiment two for days ten and fourteen are shown in Figs. 4.11–4.13. Both experiments show the same trend of ITCZ breakdown and the formation of outer bands. The primary difference between experiments one and two is the observed appearance of a third vortex. Although the third vortex did

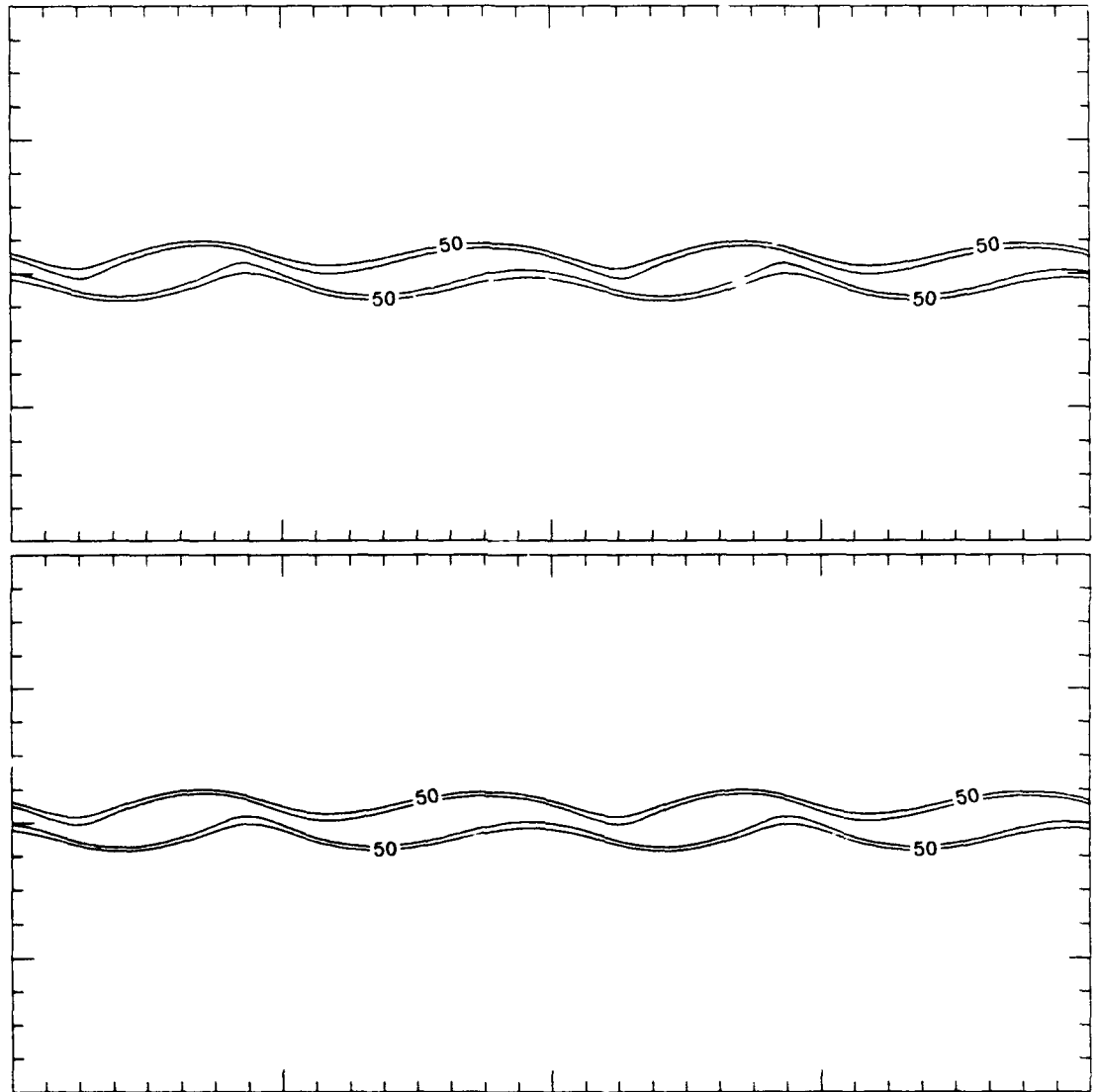


Figure 4.11: Vorticity (top) and PV (bottom) at 10 days for experiment two. Units and contour intervals are the same as for experiment one.

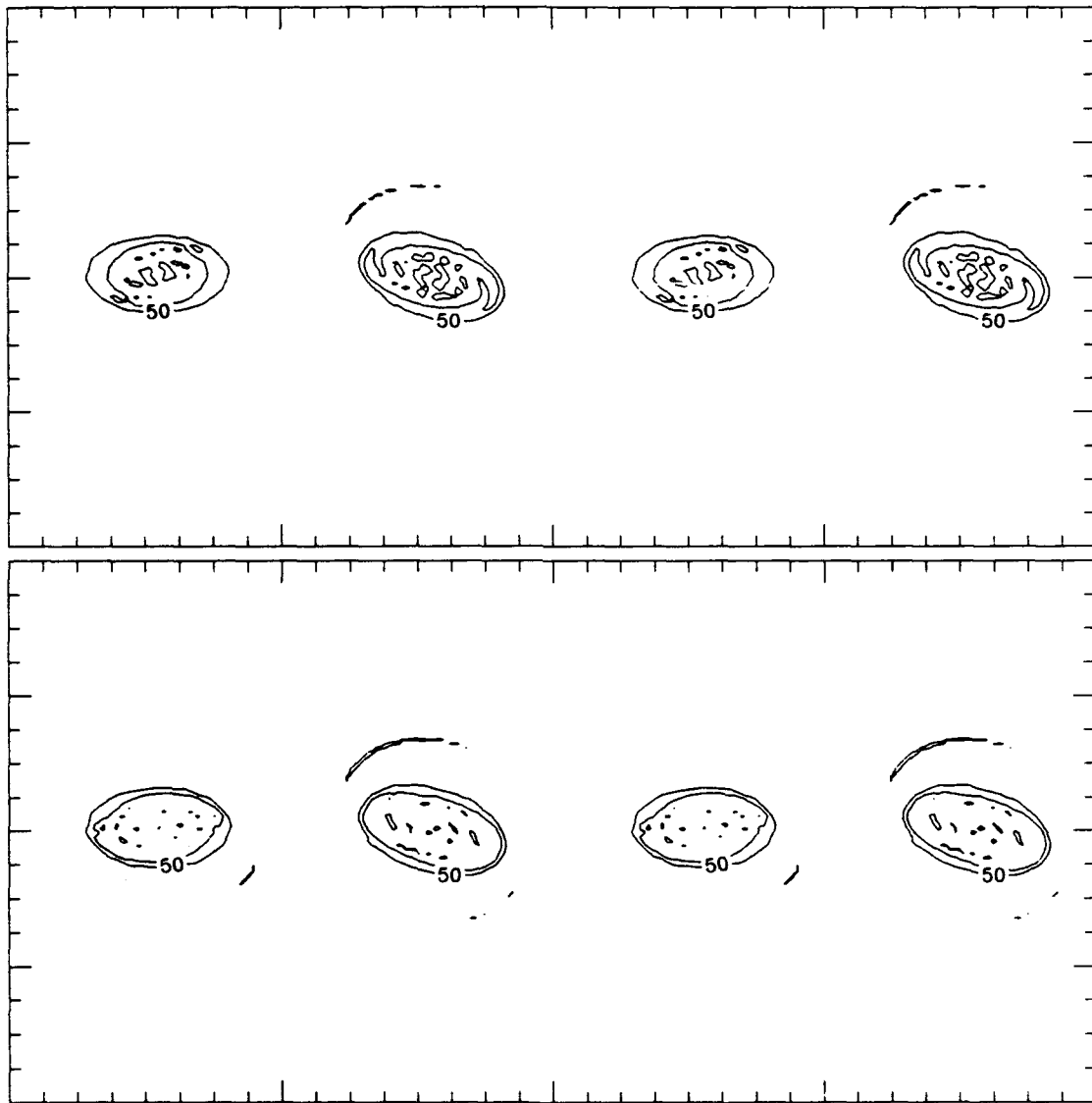


Figure 4.12: Same as Fig. 4.11 but for day fourteen.

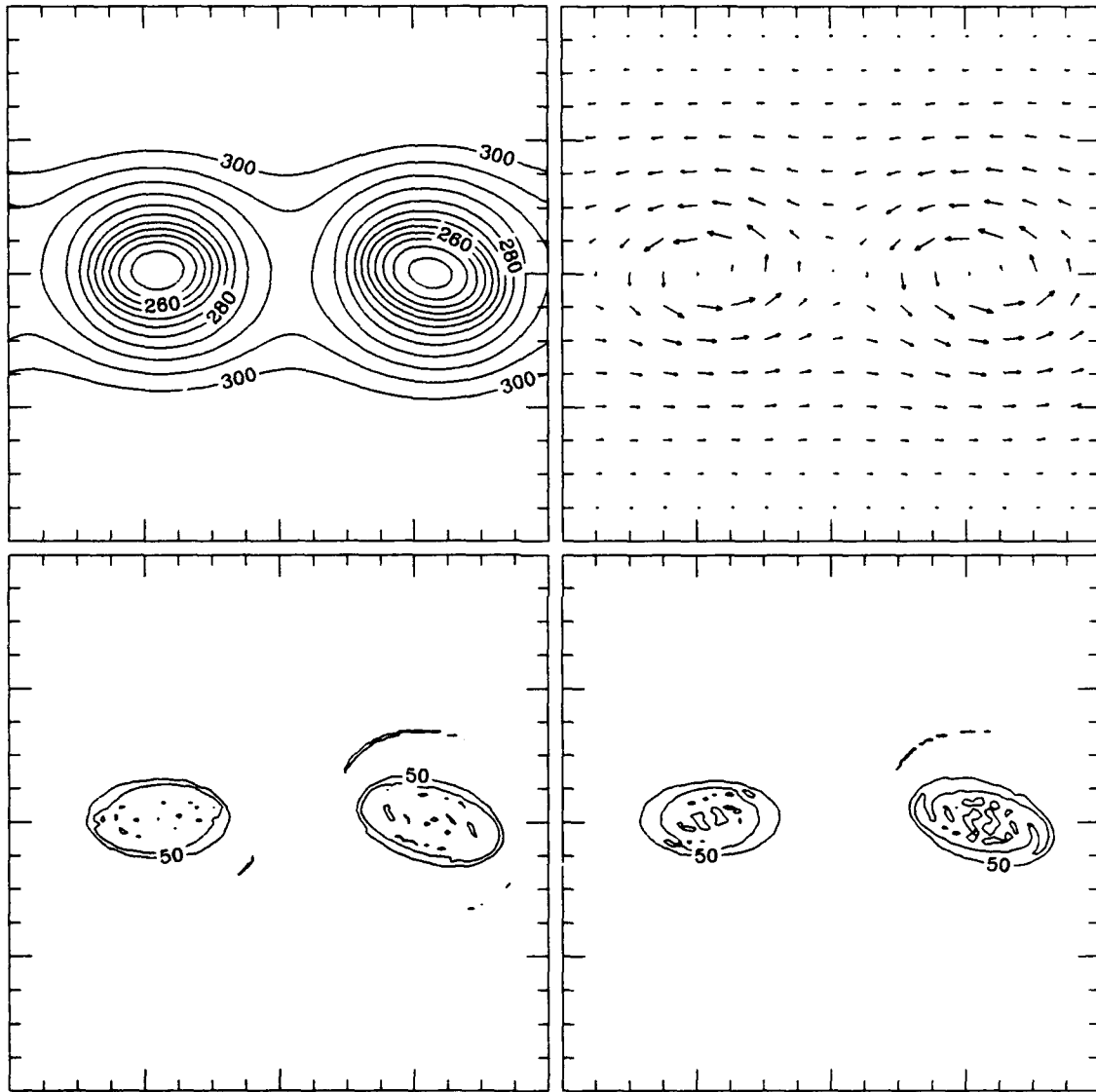


Figure 4.13: Dynamic fields for experiment two at fourteen days. Panels, units, and contour intervals are the same as in experiment one.

not appear in experiment two, it is interesting to note that the areal extent of the pooled vorticity is greater near the location where the two merging vortices formed in experiment one. It is also clear that outer bands form regardless of the initial shape of the vorticity field.

For the third experiment, we examine the effect of increasing the width of the PV strip on both the breakdown of the ITCZ and the formation of outer bands. The initial vorticity field for experiment three is given as a Gaussian distribution in y with a half-width of 300 km and a maximum vorticity, $\hat{\zeta}$, of $2f$. This value of $\hat{\zeta}$ again produces a maximum zonal wind of $\sim 11 \text{ ms}^{-1}$. Again, as in experiments one and two, we perturb the balanced modes with the same sequence of random numbers. The model results are shown in Figs. 4.14–4.16. As expected from linear theory, the weaker $\hat{\zeta}$ produces slower growth rates with experiment three taking sixteen model days for the vortices to fully detach as opposed to fourteen days for the earlier experiments. Again from linear theory, we should also expect wider vorticity distributions to produce greater disturbance wavelengths. Comparison with experiments one and two, however, shows no noticeable increase in the wavelengths of the disturbances. This may partially be explained by the model's boundary conditions which force periodicity. Additionally, the wavelength of the most unstable mode does not vary by a significant amount between experiments one and three. This can be seen in Fig. 4.17 which gives the nondimensional growth rate as a function of the zonal wavenumber s , where s is defined as the domain length in the x direction divided by the wavelength. Thus, s gives the maximum number of waves for a given wavelength that can fit in the model's x domain. Figure 4.17 shows that the most unstable wavenumber varies little between experiments one and three. It therefore seems reasonable that because the boundary condition forces periodicity, both the $y_h=235$ km and the $y_h=300$ km Gaussian strips could easily produce wavenumber two patterns. However, as the strips are made thinner, they are more inclined to produce wavenumber three type patterns. In making these statements, we must remember that comparison of nonlinear results with linear normal mode theory is highly subjective. The half-width of a Gaussian profile may not adequately approximate the half-width of a uniform vorticity profile.

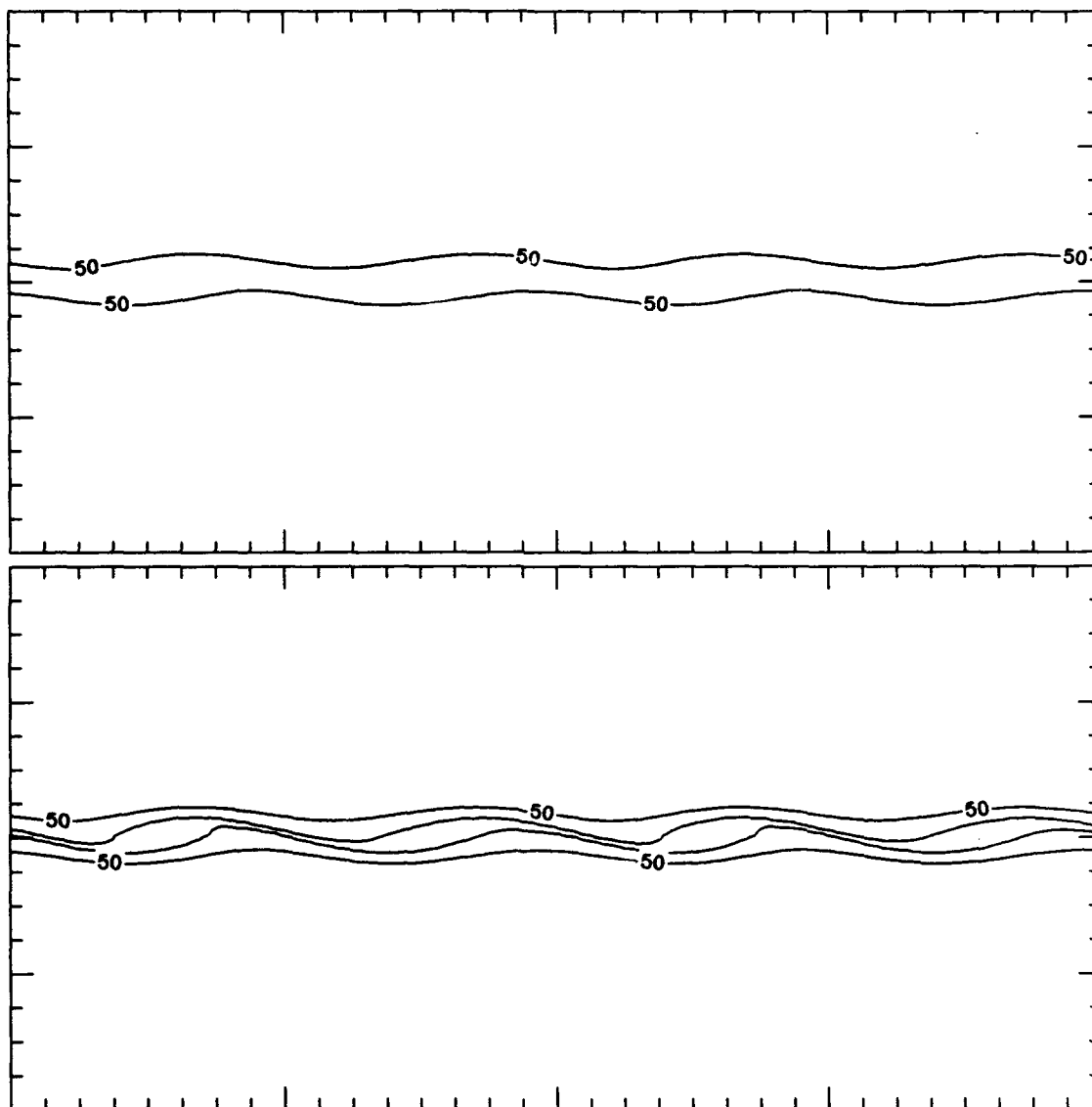


Figure 4.14: Vorticity (top) and PV (bottom) at twelve days for experiment three. Units and contour intervals are the same as for experiments one and two.

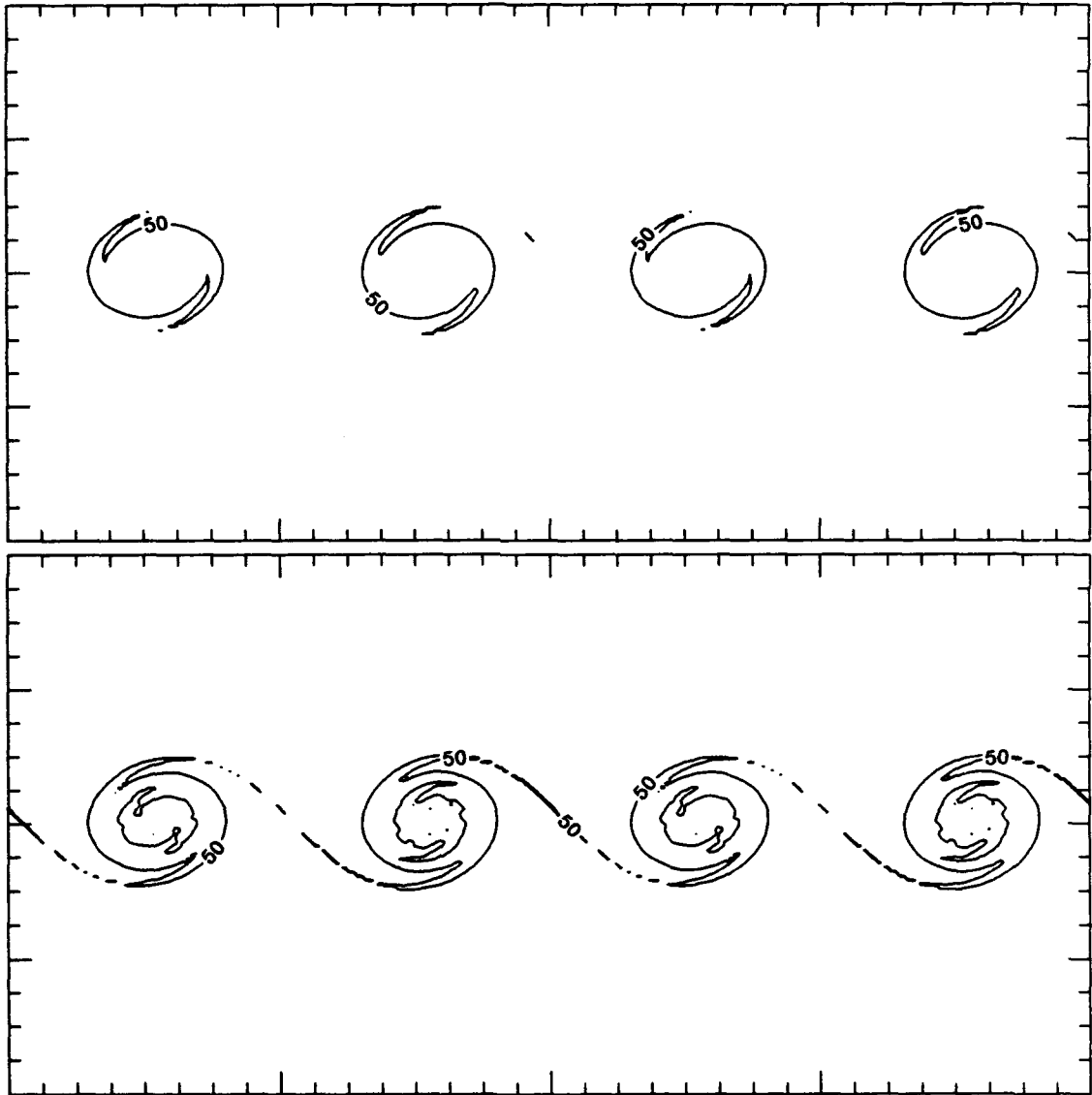


Figure 4.15: Same as Fig. 4.14 but for day sixteen.

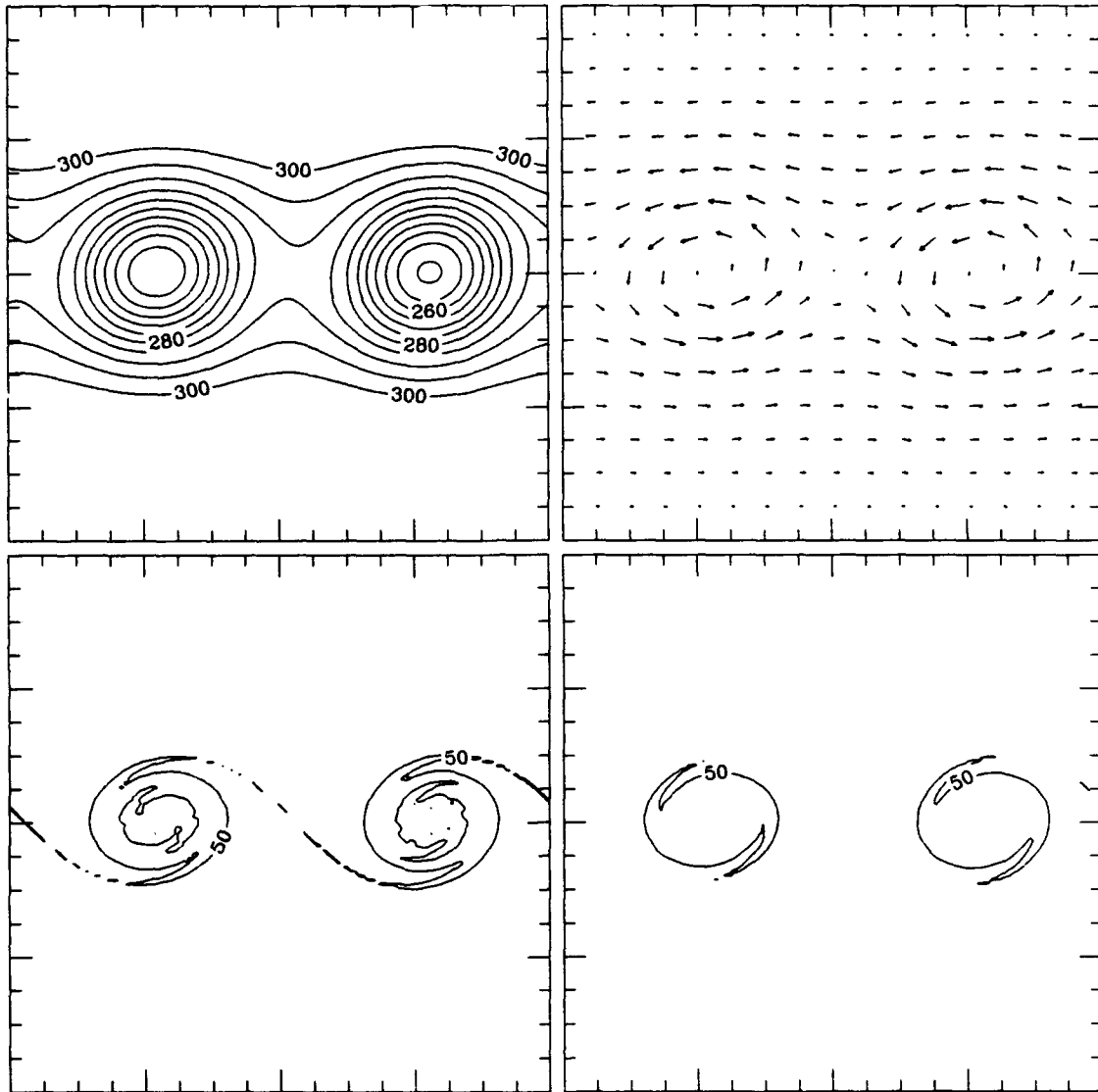


Figure 4.16: Dynamic fields for experiment three at sixteen days. Panels, units, and contour intervals are the same as in experiment one and two.

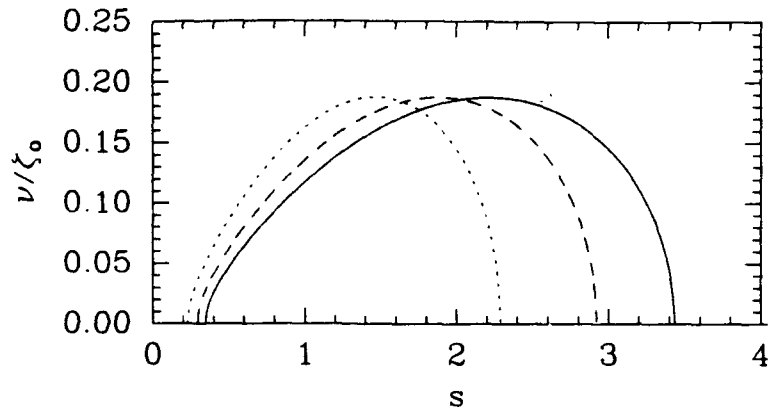


Figure 4.17: Nondimensional growth rate versus nondimensional zonal wavenumber s (see text for detail). Dotted line corresponds to $y_0 = 300$ km, dashed line corresponds to $y_0 = 235$ km, and solid line corresponds to $y_0 = 200$.

In experiment four we test the sensitivity of experiment one's results to the initial condition. We do this by simply changing the seed of the random number generator, thus producing a new sequence of random numbers, and integrating the model as before. The results of this experiment for days ten and fourteen are presented in Fig. 4.18 and Fig. 4.19. These results demonstrate the tremendous sensitivity of the model to the initial condition. The linear analysis can again help us to understand these results. As we noted in experiment one, Fig. 4.17 shows that growth rates between two wavenumbers vary little, especially for thinner strips. Thus, if the perturbation excites wavenumber two slightly more than wave number three, a wave number two pattern would be expected and vice versa. Figure 4.17 also suggests that using the Gaussian half-width as an approximation to a uniform vorticity fields half-width may not be accurate. Results from the nonlinear integration suggest that a width considerably shorter than the Gaussian half-width may provide a better approximation.

In the previous experiments we assumed the ITCZ was a continuous disturbance across the entire domain of the model. We now wish to consider the effects of a localized ITCZ. Therefore, for the fifth experiment, we consider an initial vorticity field which is Gaussian in y (with $y_h = 235$ km) but confined in x . To accomplish this, we again make use of the Melander profile equations. We now specify the profile function to be function of $|x - x_c|$ and let $R_0 = 1600$ km and $R_i = 2000$ km. This produces a disturbance which

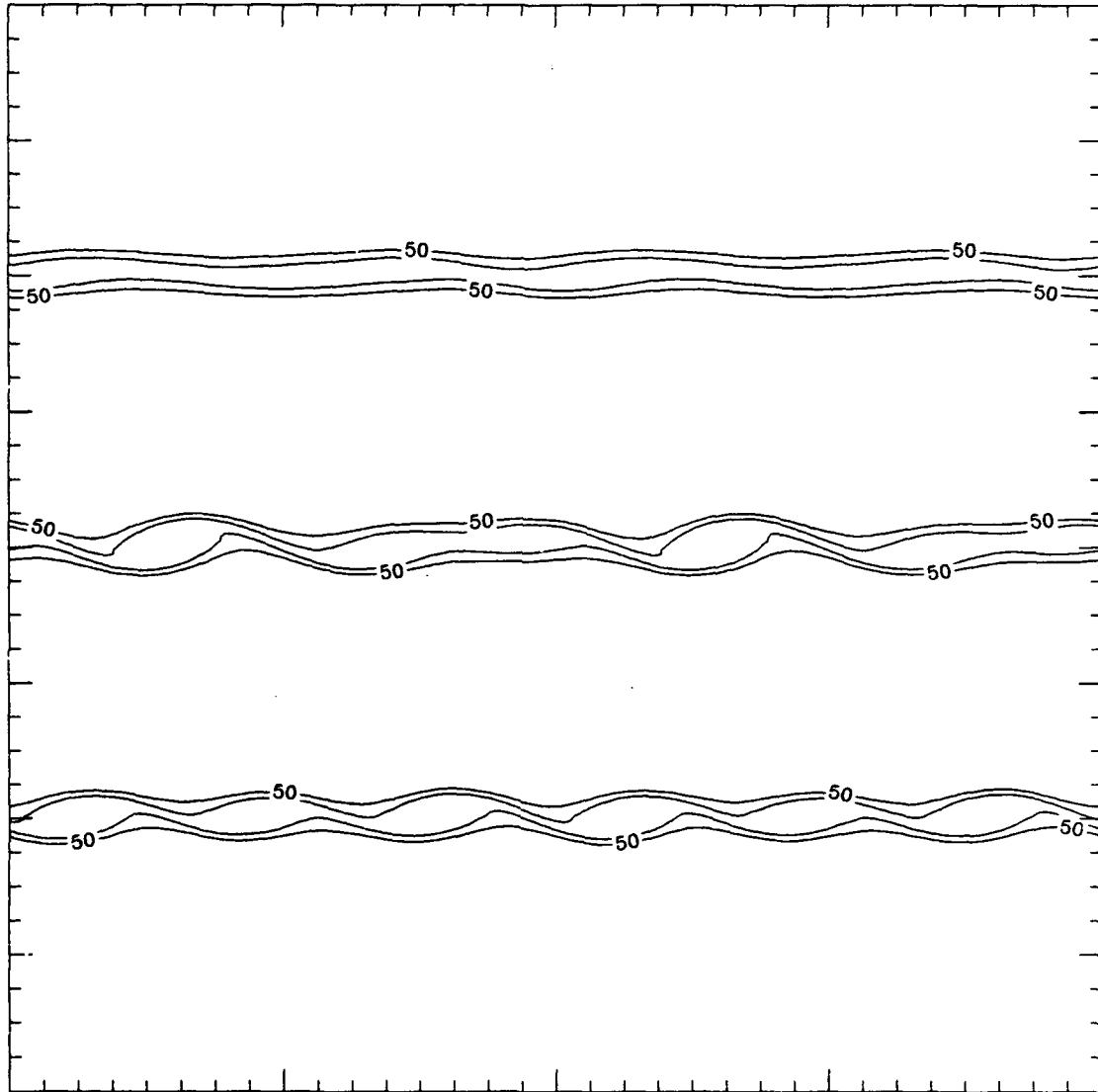


Figure 4.18: PV fields for experiment four at 10 days. The three PV strips were each generated using the same initial vorticity field, but each were perturbed using different sequences of random numbers with identical ranges in magnitude. The middle PV strip corresponds to experiment one. The domain is plotted twice. Units and contour intervals are the same as for experiment one.

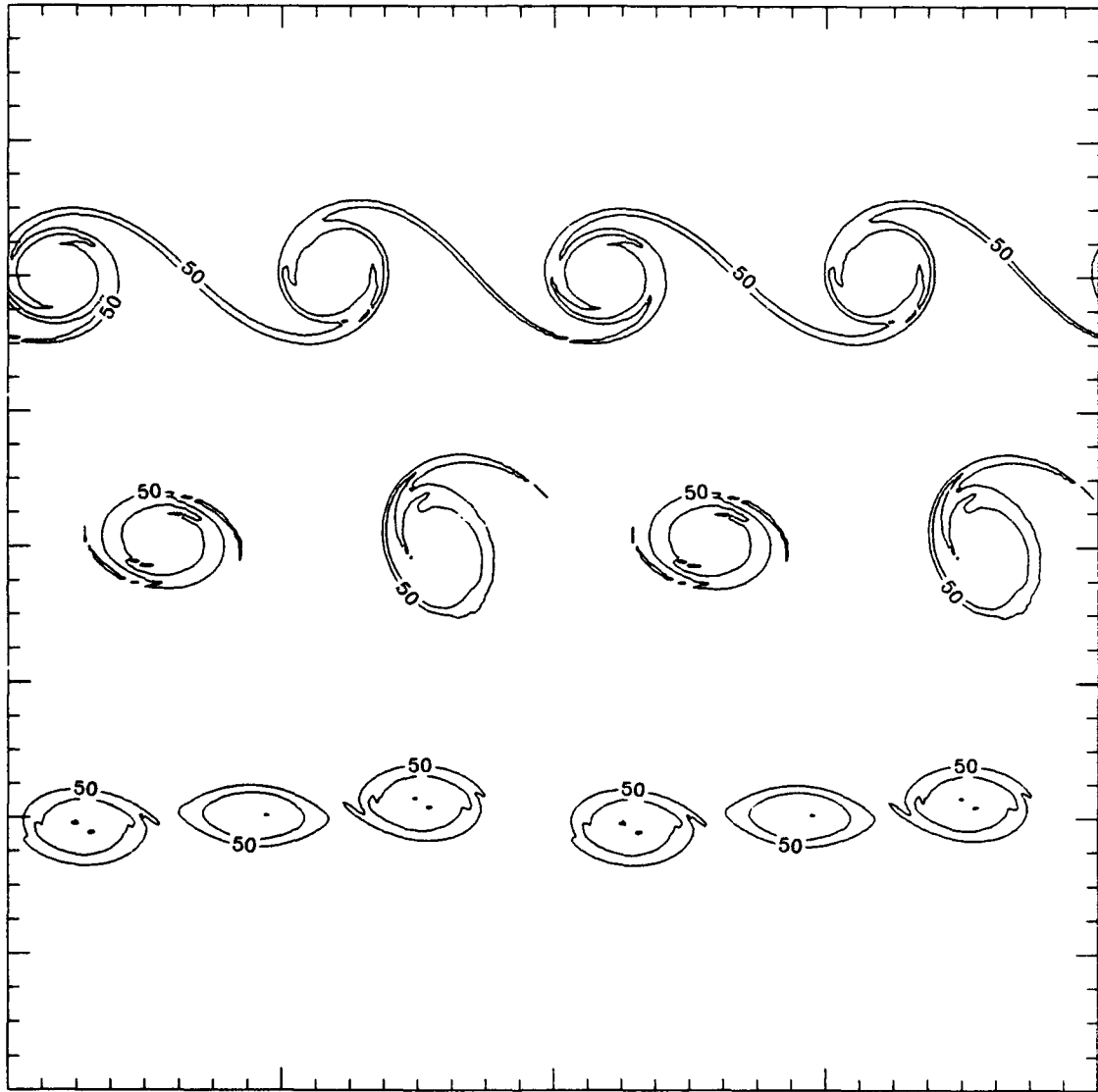


Figure 4.19: Same as Fig. 4.18 but at fourteen days.

is approximately one half of the domain length. The maximum value of vorticity is again chosen to be $2.5f$. The model is run for a period of four days by which time the strip has broken down into two separate vortices. The results of the four day calculation are shown in Figs. 4.20–4.23. Again, as in experiments one through four, the ITCZ breaks down and thin bands of PV form between the incipient vortices. By day four, all fields indicate the existence of two separate vortices. This is roughly four times faster than the experiments with a continuous disturbance. This is not surprising, however, since wave breaking at large x is aiding the ITCZ breakdown process by providing rather large perturbations in the PV field. Another noticeable difference between experiments five and the others is the motion of the disturbances. Clearly, the circulation of each incipient vortex is influencing the other's motion; thus, the two vortices simply rotate around one another (the Fujiwhara effect). This same feature appears to be evident in the satellite images shown in Figs. 4.1–4.2 (although, admittedly, spherical effects are also largely responsible for the vortex positions).

To summarize our results, PV dynamics and barotropic instability theory provide useful tools for examining both the breakdown of the ITCZ and the formation of outer bands. This in no way implies other concepts, such as moist dynamical processes and baroclinic effects, are not important. Clearly, they must be. We have simply isolated a fundamental part of the dynamics and have demonstrated its usefulness in understanding the complex processes of ITCZ breakdown and outer band formation.

In the next chapter, we consider the stability of spiral bands after their formation.

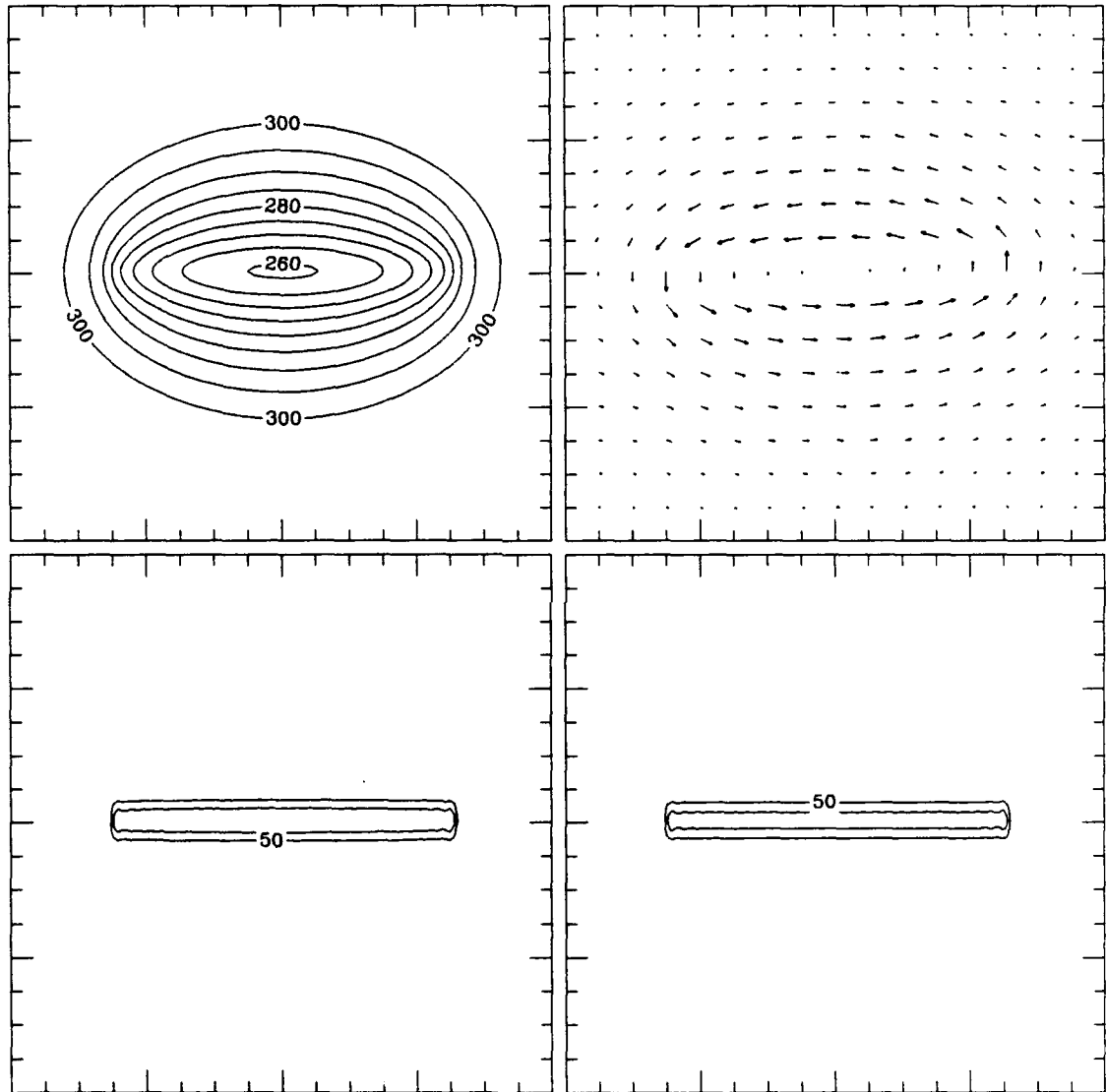


Figure 4.20: Dynamic fields at initial time for experiment five. Panels, units, and contours are identical to experiments one through four.

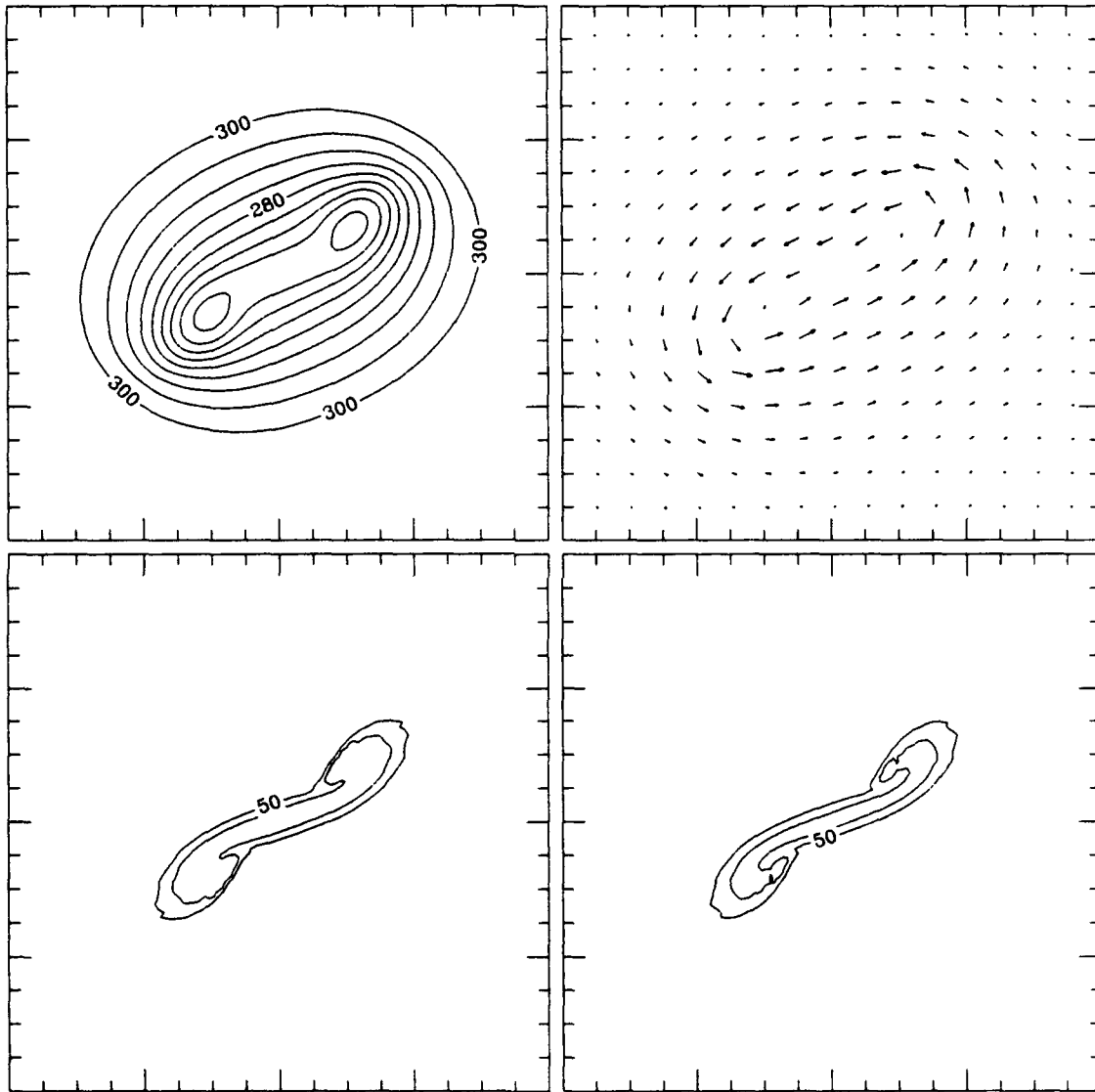


Figure 4.21: Same as figure 4.20 but for day two.

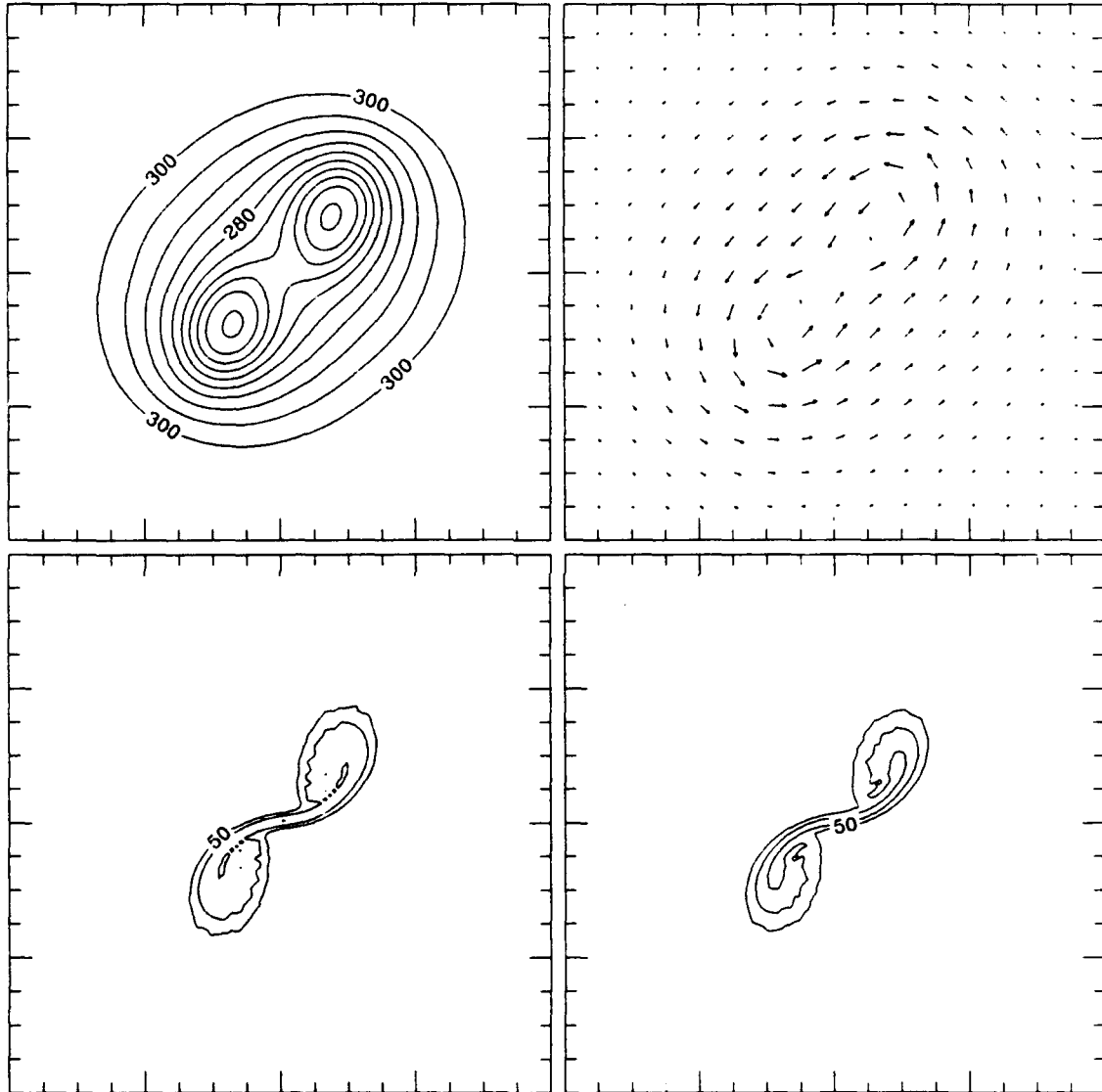


Figure 4.22: Same as figure 4.20 but for day three.

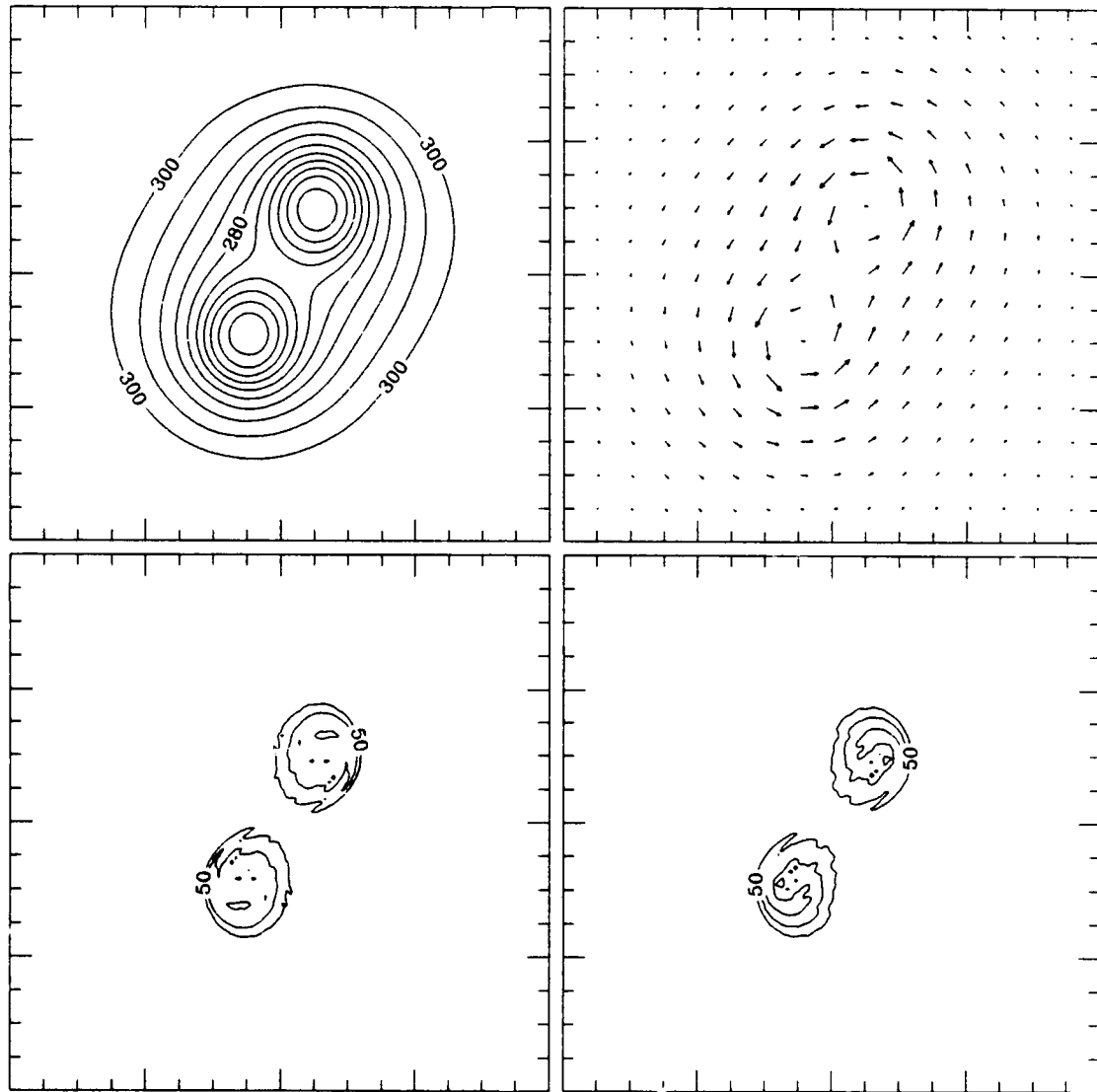


Figure 4.23: Same as figure 4.20 but for day four.

Chapter 5

ON THE STABILITY OF SPIRAL BANDS

In Chapter 3 we described the evolution of spiral bands in tropical cyclones and noted the ejection of PV tongues into areas of relatively low PV. In Chapter 4, we noted that reversed PV gradients satisfied the necessary condition for barotropic instability and helped explain the breakdown of the ITCZ into pools of PV. This raises the the following question. Why are spiral bands are never observed to be unstable even though they, themselves, are most probably areas of reversed PV gradients. In this chapter we attempt to shed some light on the this problem by examining the stability of PV rings surrounding a main vortex. We attempt to show that the main vortex of the tropical cyclone provides enough adverse shear to resist the "rolling up" of spiral bands. We also examine the stability of annular regions of high PV in the absence of any main vortex. This will help shed some light on such observed features as hurricane meso-vortices and polygonal eyewalls.

We begin by considering the normal mode stability analysis of multiple concentric annular regions of PV. In section 5.2 we consider the specific case of three regions of different PV. This case involves a center region of irrotational air, a ring of high PV air, and a surrounding region of irrotational air as r goes to infinity. We use this case to examine the stability of bands without the presence of a main vortex. This case also has dynamic links to eyewall instabilities and polygonal eyewalls. In the final section, we consider a four region model. The fourth region is the addition of a high PV region in the center of the vortex. We use this to test the effects of intense adverse shear on the growth rates of instabilities.

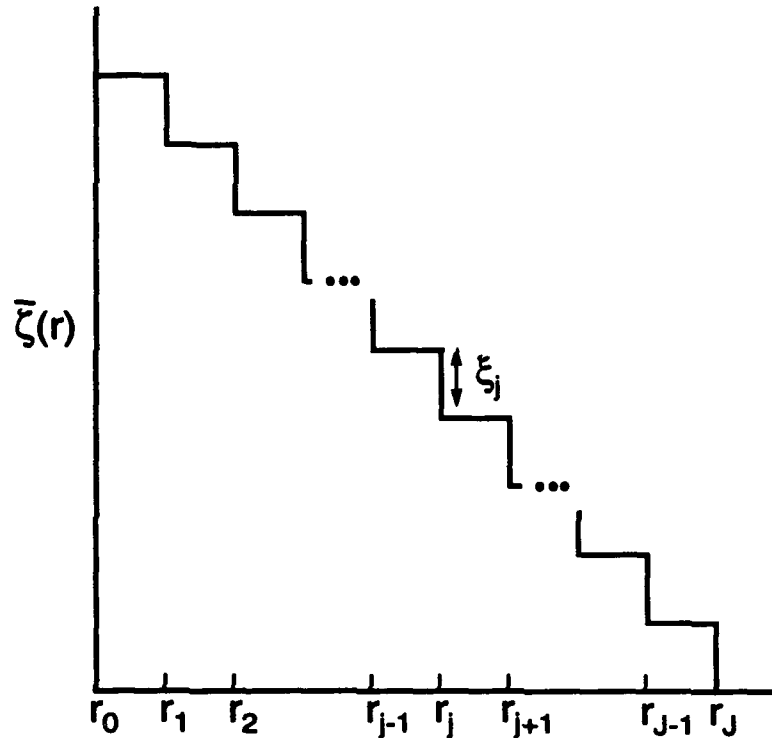


Figure 5.1: The piecewise continuous mean vorticity distribution as a function of r . As one proceeds radially inwards, the vorticity jumps in increments of ξ_j .

5.1 Normal Mode Stability Analysis

In this section we derive a method for determining the normal mode stability of annular PV strips to small amplitude disturbances. We consider the basic state axisymmetric vorticity distribution shown in Fig. 5.1. At $r = r_j$ ($j = 0, 1, 2, \dots, J$) the vorticity jumps by an amount ξ_j as one proceeds radially inward, where ξ_j can be either positive or negative. The basic state streamfunction corresponding to this vorticity distribution is given by

$$\bar{\psi}(r) = \sum_{j'=1}^j \frac{1}{2} \xi_{j'} r_{j'}^2 \ln(r/r_{j'}) + \sum_{j'=j+1}^J \frac{1}{4} \xi_{j'} (r^2 - r_{j'}^2) \quad \text{for } r_j \leq r \leq r_{j+1}, \quad (5.1)$$

which can be confirmed by two differentiations, the first of which yields

$$r\bar{v}(r) = \sum_{j'=1}^j \frac{1}{2} \xi_{j'} r_{j'}^2 + \sum_{j'=j+1}^J \frac{1}{2} \xi_{j'} r^2 \quad \text{for } r_j \leq r \leq r_{j+1}, \quad (5.2)$$

and the second of which yields

$$\bar{\zeta}(r) = \sum_{j'=j+1}^J \xi_{j'} \quad \text{for } r_j \leq r \leq r_{j+1}. \quad (5.3)$$

Since (5.3) corresponds to the staircase vorticity pattern shown in Fig. 5.1, and since $\bar{\psi}(r)$ and $\bar{v}(r)$ are continuous, (5.1) is the solution of the axisymmetric barotropic invertibility principle $d/r dr(r d\bar{\psi}/dr) = \bar{\zeta}$.

Now suppose that each interface is perturbed by an amount $\eta_j(\varphi, t)$ in the sinusoidal fashion $\eta_j(\varphi, t) = \hat{\eta}_j e^{i(m\varphi - \nu t)}$. The solution for the perturbation streamfunction is

$$\psi'(r, \varphi, t) = \left[\sum_{j'=1}^j A_{j'} (r_{j'}/r)^m + \sum_{j'=j+1}^J A_{j'} (r/r_{j'})^m \right] e^{i(m\varphi - \nu t)} \quad r_j \leq r \leq r_{j+1}. \quad (5.4)$$

It can easily be confirmed that ψ' is continuous. Continuity of v at $r_j + \eta_j$ yields $m A_j = -\frac{1}{2}\xi_j r_j \hat{\eta}_j$. Using this in (5.4), and the resulting expression in

$$\frac{\partial \eta_j}{\partial t} + \bar{\omega}_j \frac{\partial \eta_j}{\partial \varphi} = -\frac{im}{r_j} \psi'(r_j), \quad (5.6)$$

we obtain

$$(\nu - m\bar{\omega}_j) \hat{\eta}_j + \sum_{j'=1}^J \frac{1}{2} \xi_{j'} I_{jj'}^{(m)} \hat{\eta}_{j'} = 0, \quad (5.7)$$

where

$$I_{jj'}^{(m)} = \begin{cases} (r_{j'}/r_j)^{m+1} & j' \leq j \\ (r_j/r_{j'})^{m-1} & j' \geq j, \end{cases}$$

and $\bar{\omega}_j \equiv \bar{v}/r_j$. This form of the eigenvalue/eigenvector problem is identical to that presented by Dritschel (1989).

If all the $\xi_{j'}$ vanish except the one for $j' = j$, we obtain

$$\frac{\nu}{m} = \bar{\omega}_j - \frac{\xi_j}{2m} = \frac{1}{2} \xi_j \left(1 - \frac{1}{m} \right),$$

which is the special case found in our discussion of PV waves in Chapter 3.

5.2 The Stability of Annular Potential Vorticity Regions

We now consider the specific case of a single annular region of PV (i.e. $J = 2$), there are two interfaces for this case as shown in Fig. 5.2. The eigenvalue problem for this simplified case reduces to

$$\begin{pmatrix} m\bar{\omega}_1 - \frac{1}{2}\xi_1 & -\frac{1}{2}\xi_2(r_1/r_2)^{m-1} \\ -\frac{1}{2}\xi_1(r_1/r_2)^{m+1} & m\bar{\omega}_2 - \frac{1}{2}\xi_2 \end{pmatrix} \begin{pmatrix} \eta_1 \\ \eta_2 \end{pmatrix} = \nu \begin{pmatrix} \eta_1 \\ \eta_2 \end{pmatrix}. \quad (5.8)$$

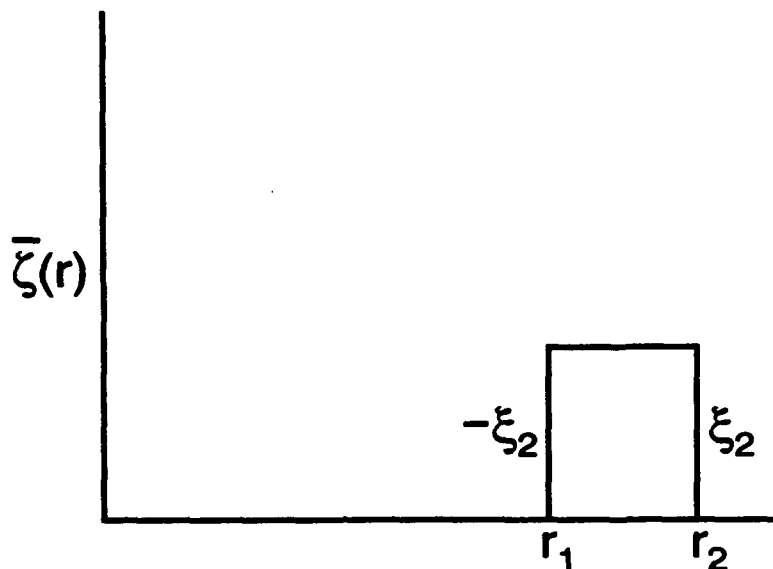


Figure 5.2: The assumed vorticity profile for $J = 2$.

If we note that $\bar{\omega}_1 = 0$, $\bar{\omega}_2 = \frac{1}{2}[(r_1/r_2)^2 - 1]$, and $\xi_1 = -\xi_2$ for this special case, it can easily be verified that ν will be pure real for $m = 0, 1$, or 2 . This implies the vorticity field will remain stable to these disturbance patterns. The remaining wavenumbers can, however, produce frequencies with imaginary components. Figure 5.3 shows the normalized growth rates ν_i/ξ_2 as a function of the nondimensional width of the annular region, r_1/r_2 . Clearly, thinner annular regions should produce the highest growth rates but at much higher wavenumbers. The nonlinear normal mode analysis also provides information on the amplitude and phase of the most unstable modes. Fig. 5.4 shows the most unstable amplitude and phase of a wave number four pattern with $r_1 = 200$ km and $r_2 = 250$ km.

To test our results numerically for the divergent barotropic case, we initialize our model with an annular region which is Gaussian in r . Unlike in Chapter 4, however, we cannot simply perturb the model with white noise. The reason for this is that experience shows that the influence of the doubly periodic boundary condition will always force the growth of a wavenumber four pattern. To overcome this problem, we instead perturb the model with a weak forcing of the wavenumber desired. The wavenumber of the forcing is chosen to be the most unstable wavenumber based on linear theory while using the the Gaussian half-width to represent the width of the ring. Although, we cannot say for

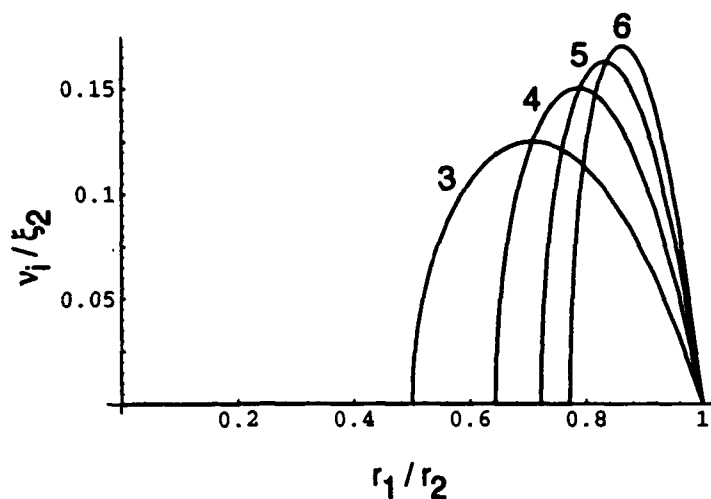


Figure 5.3: The normalized growth rates as a function of the width of the annular region for wavenumber 3, 4, 5, and 6 disturbances.

certain that the chosen wavenumber is necessarily the most unstable for the nonlinear divergent case, it does allow us to view the evolution of various unstable patterns.

To demonstrate the growth of instabilities within an annular region, we integrate the model starting from an initial state has zero vorticity everywhere except within an annular region. Within the annular region, the vorticity is Gaussian in r with a half-width of 35 km and a maximum value of $2.5 \times 10^{-4} \text{ s}^{-1}$. The center of Gaussian profile is located at a radius of 225 km. If the Gaussian half-width is taken to be representative of the half-width a uniform annular region, then the most unstable wavenumber for this case should be four, i.e. $r_1/r_2 = 0.73$. For this simulation and all others in the chapter, we used 128^2 points on the transform grid and kept 42 waves. The initial fields for this experiment are shown in Fig. 5.5 to demonstrate the amplitude of the initial forcing. The results from this experiment are shown in Figs. 5.6–5.8 for 24, 36 and 48 hrs respectively. By 24 hours the growing instabilities are clearly visible in both the PV and vorticity fields. The patterns in both these fields bear remarkable similarity to the pattern predicted by linear theory (Fig. 5.4). By 36 hours, four distinct circulation patterns have clearly developed as evidenced by all fields. These four vortices are completely detached by 48 hours.

Similar results were also found for wavenumber three and five perturbations. These results are shown in Figs. 5.8–5.11. For the wavenumber three perturbation, we used a

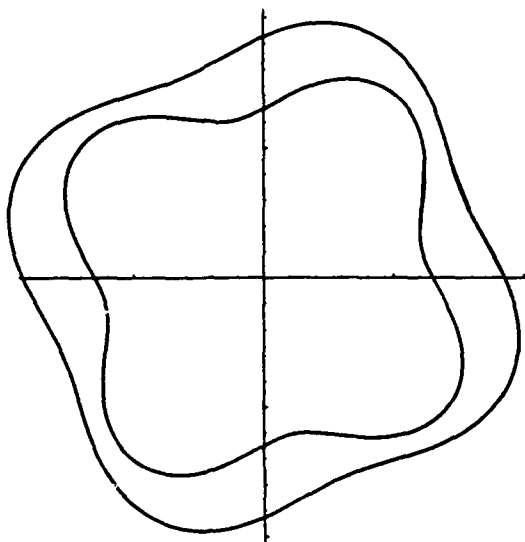


Figure 5.4: The amplitude and phase relationship for a wavenumber four disturbance in which $r_1 = 200$ km and $r_2 = 250$ km. The amplitudes of the disturbances are known only to within an arbitrary constant.

Gaussian half-width of 50 km centered at a radius of 225 km. Again if assume the Gaussian half-width is representative of the half-width of a uniform annular region, then we obtain a ratio of $r_1/r_2 = 0.63$, which is most unstable for wavenumber three disturbances. The wavenumber five perturbation used a Gaussian half-width of 20 km centered at 225 km which gives a ratio of $r_1/r_2 = 0.83$. The effect of increasing the width of the disturbance follows linear theory well. As the width of the disturbance is increased the growth rates of the instabilities decrease. This is easily confirmed by comparing Fig. 5.9 with Fig. 5.11, and Fig. 5.10 with Fig. 5.12. Clearly, the thinner strip evolved faster.

Although we have been examining the stability of these annular regions with regards to spiral bands, the results may also have applications to the eyewall of a tropical cyclone. The vorticity field for the eyewall of a tropical cyclone is similar in shape to the above annular regions of vorticity in that the peak vorticity is not observed in the center of the vortex (as we have assumed in the previous chapters) but at some small distance away from the center. It is therefore possible for instabilities of the type discussed above to be found near the eyewall. There are two types of observations which support such a theory. The first is the observed phenomena of meso-vortices in some tropical cyclone eyewalls

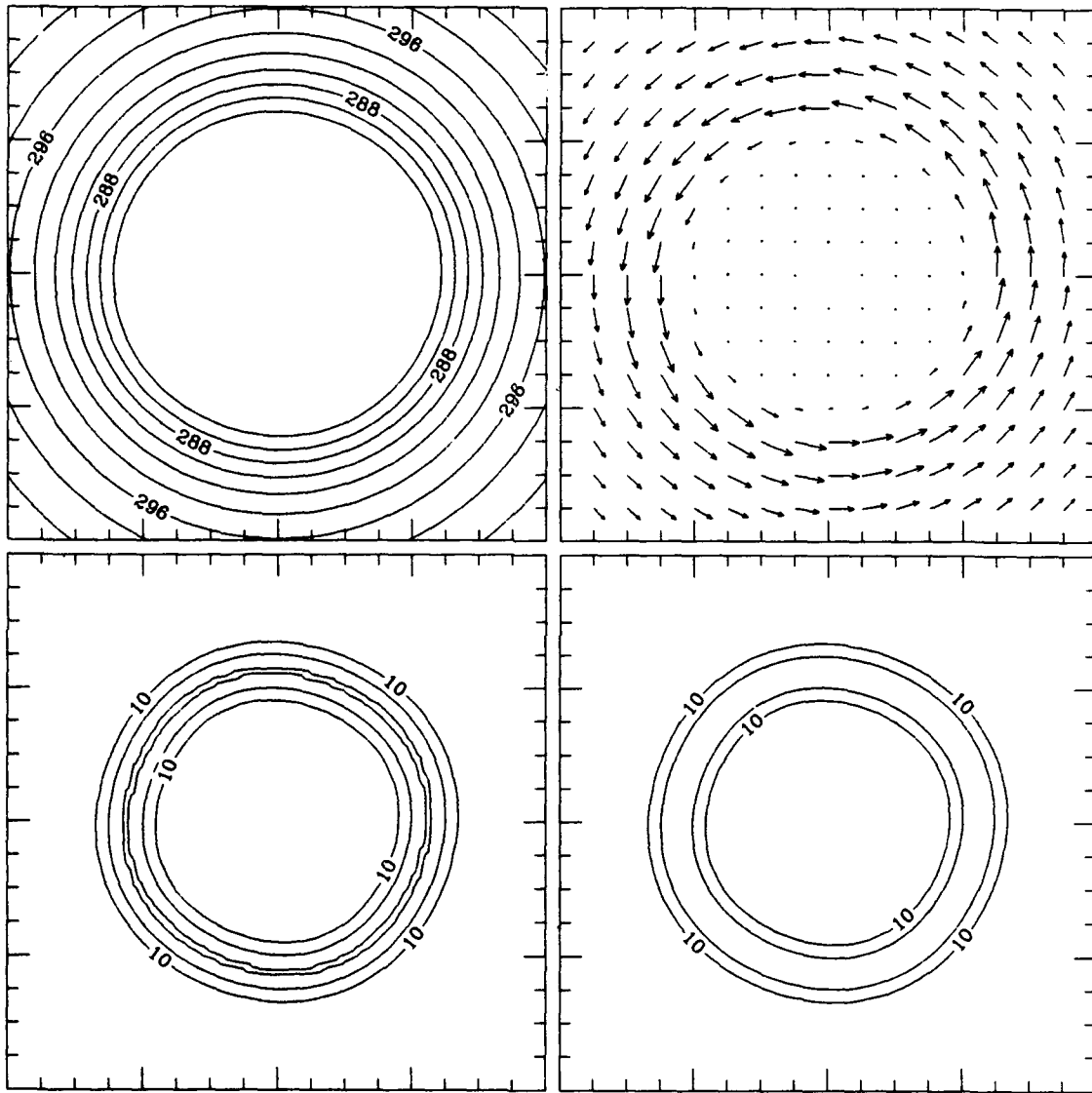


Figure 5.5: The initial wind and mass fields for the wavenumber four perturbed case. The height field (upper left) has contour intervals of 2 m. The wind field (upper right) has a maximum wind vector of 12ms^{-1} . The normalized PV (lower left) and absolute vorticity (lower right) are in units of 10^{-5} s^{-1} and have contour intervals of 1.0×10^{-4} .

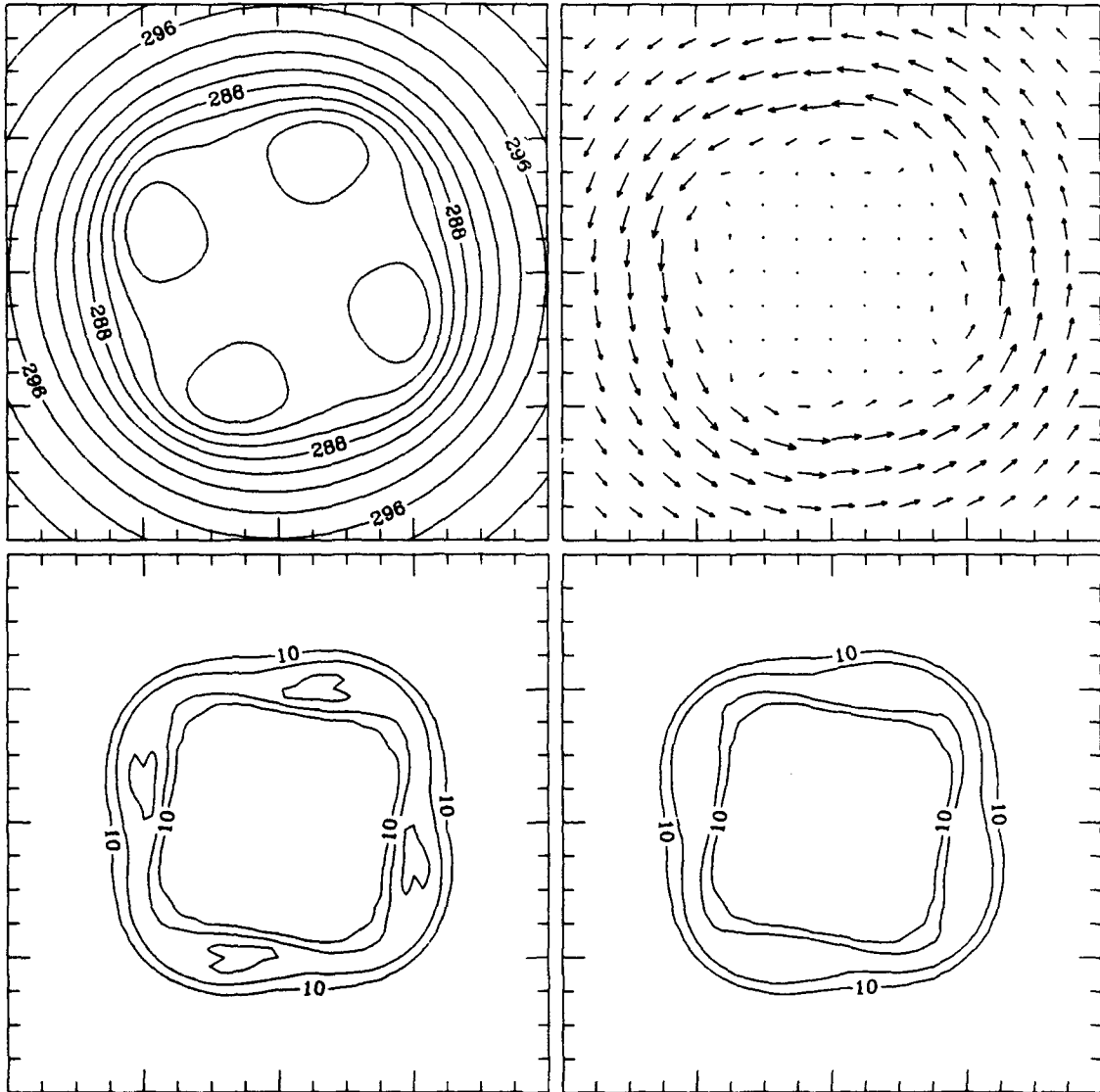


Figure 5.6: The same as Fig. 5.5 but for 24 hours.

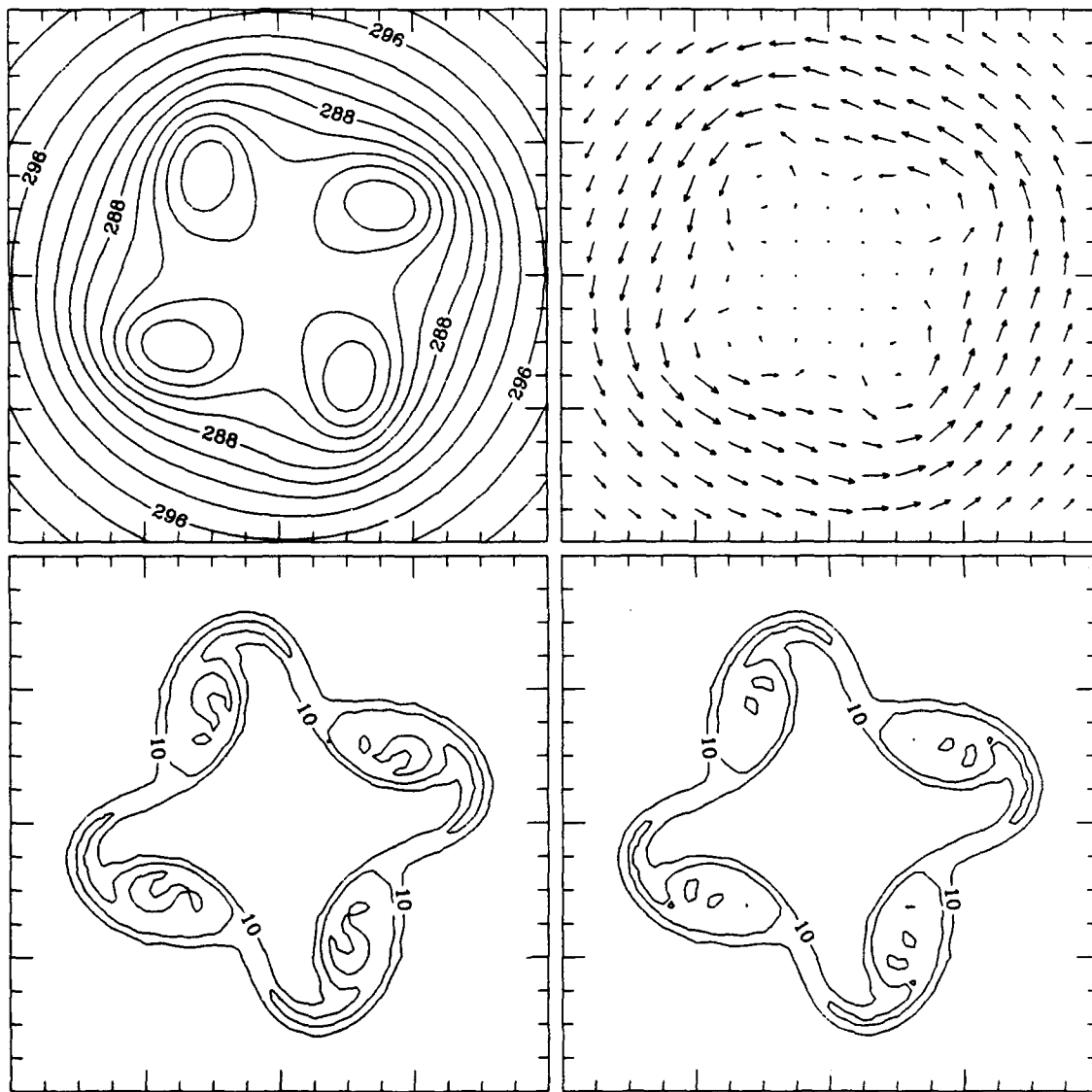


Figure 5.7: The same as Fig. 5.5 but for 36 hours.

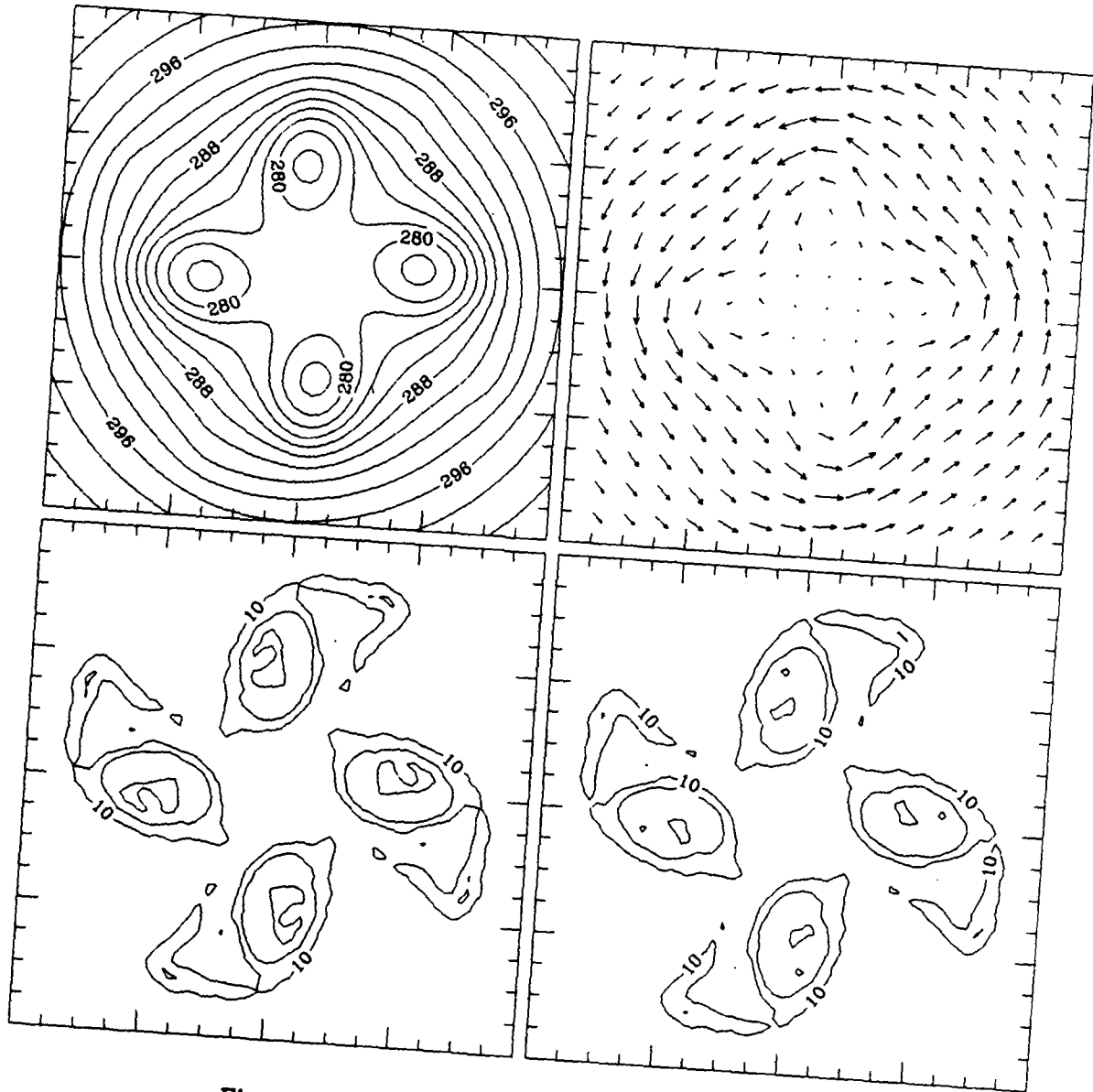


Figure 5.8: The same as Fig. 5.5 but for 48 hours.

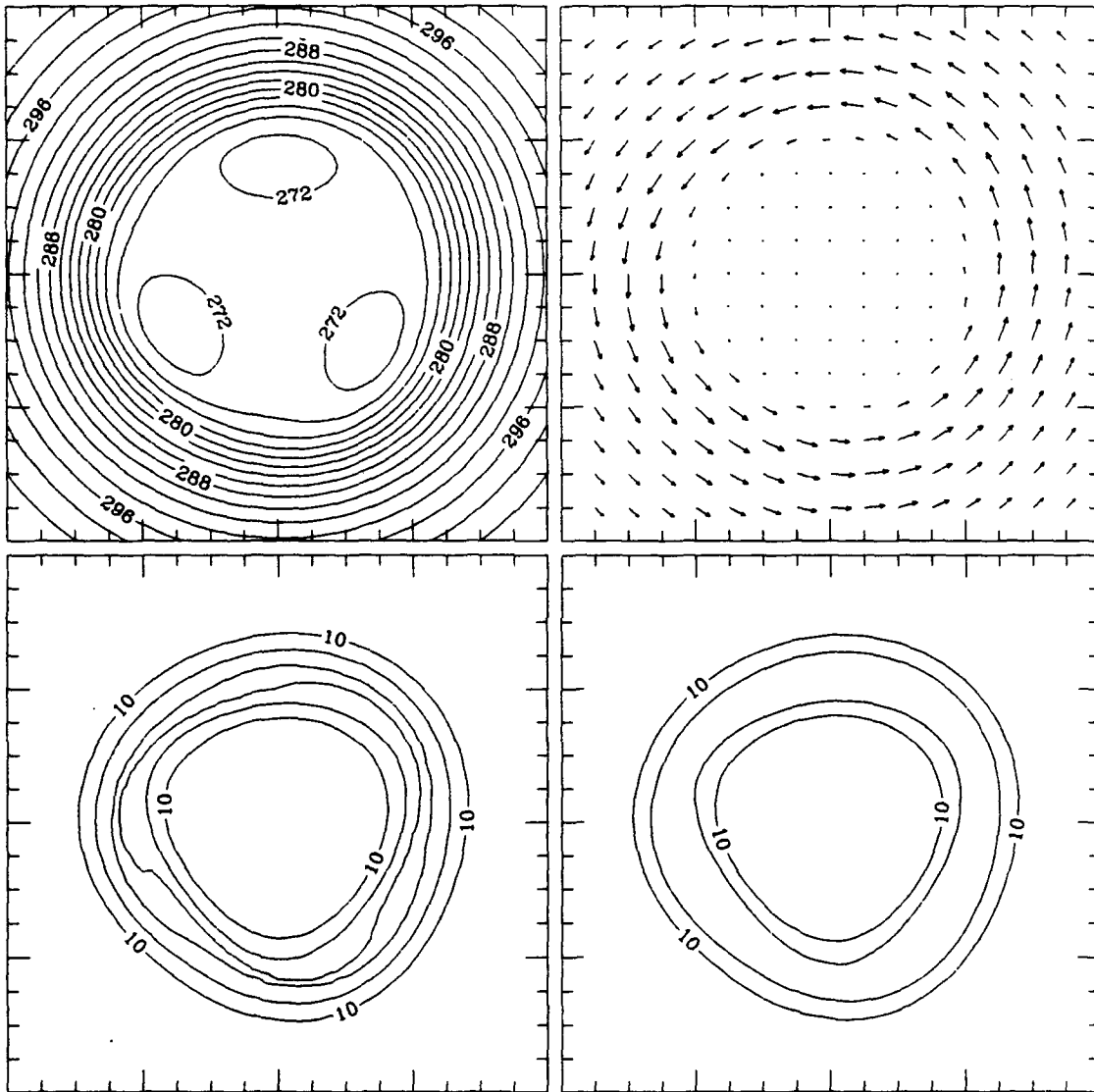


Figure 5.9: The wind and mass fields for the wavenumber three perturbed case at 24 hrs. The maximum wind vector is 15 ms^{-1} . Panels, units and contour intervals are the same as for Fig. 5.5.

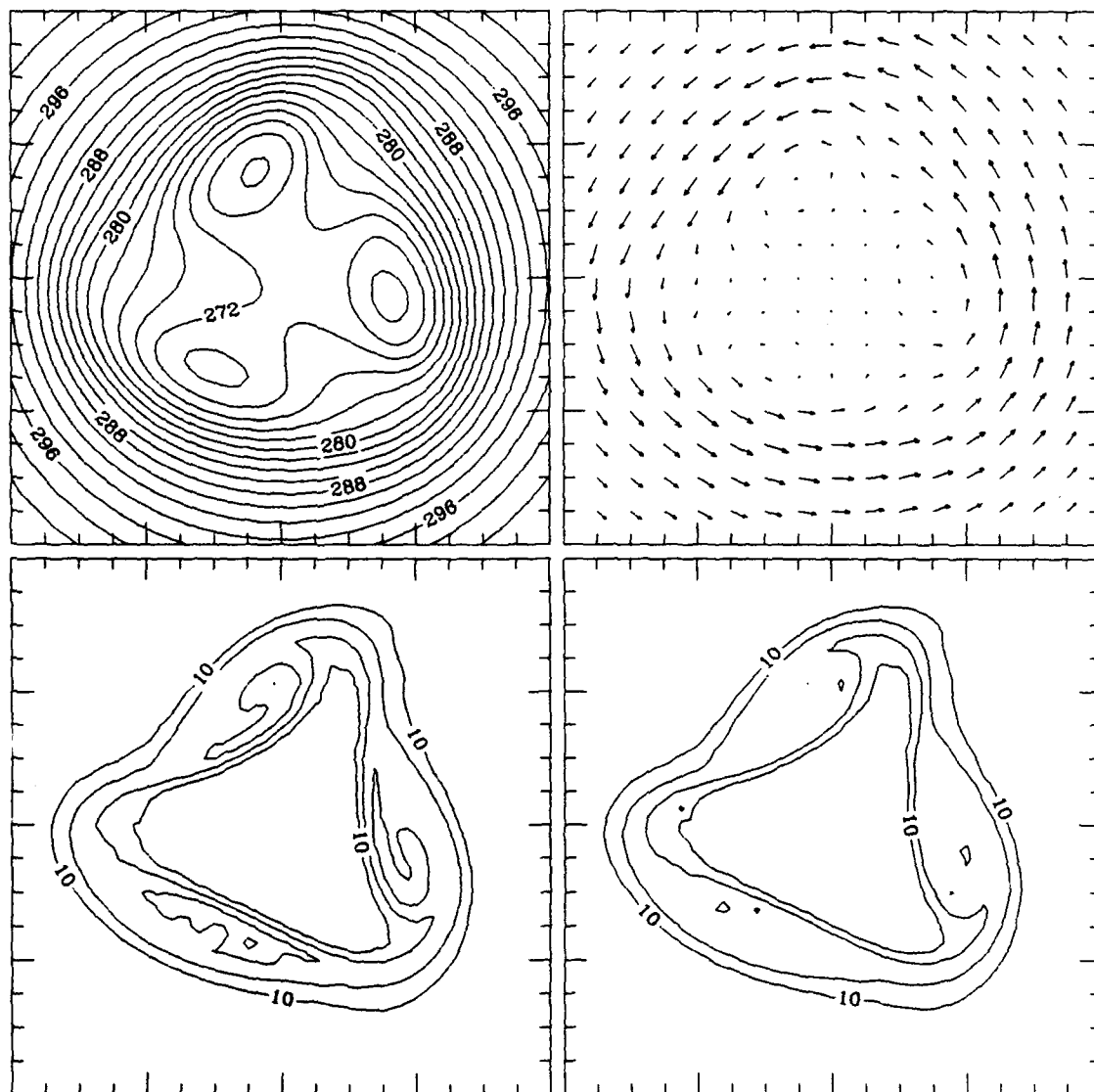


Figure 5.10: The same as Fig. 5.9 but for 48 hours.

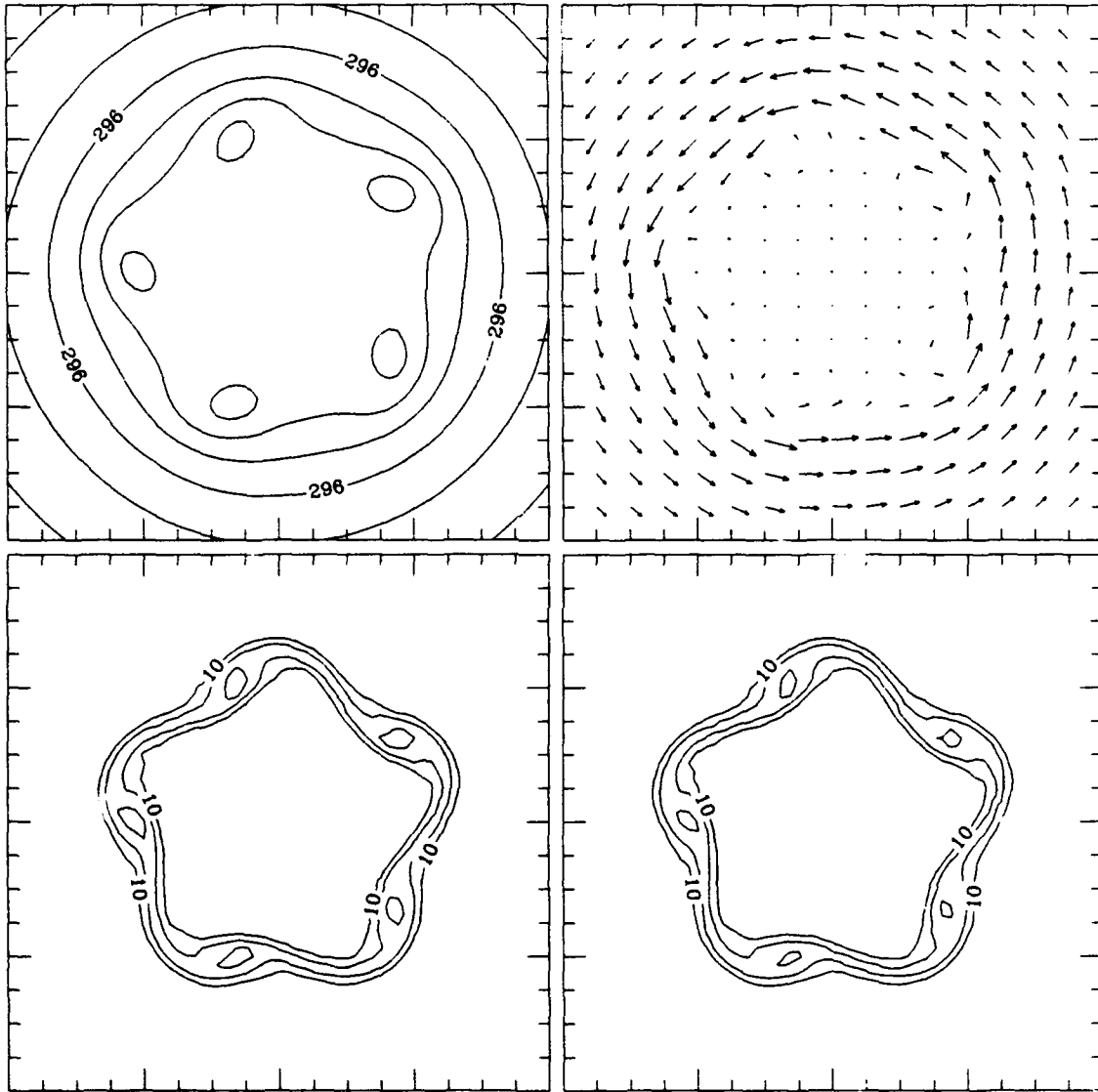


Figure 5.11: The wind and mass fields for the wavenumber five perturbed case at 24 hrs. The maximum wind vector is 8 ms^{-1} . Panels, units, and contour intervals are the same as for Fig. 5.5.

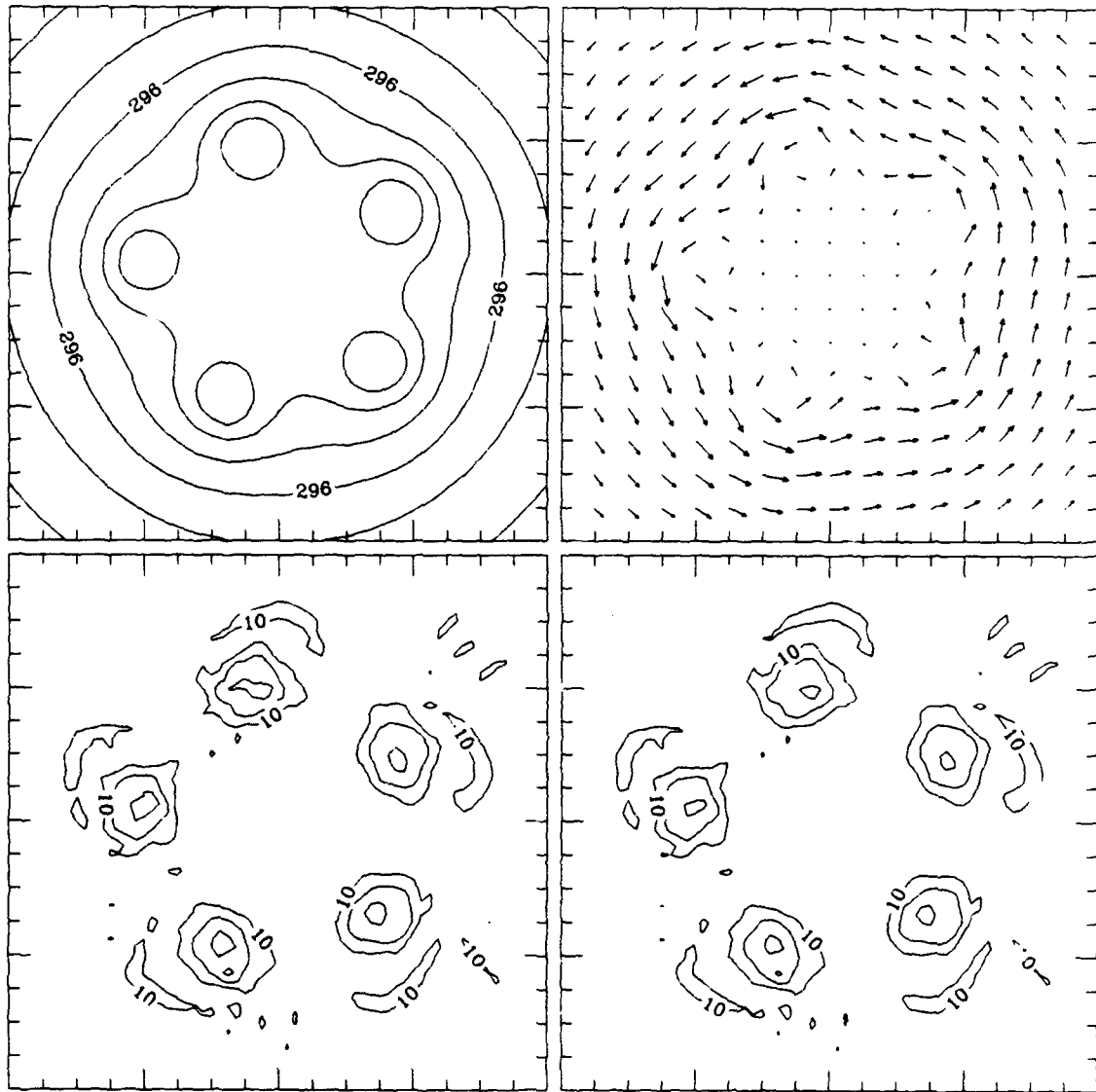


Figure 5.12: The same as Fig. 5.11 but for 48 hours.

(Black and Marks, 1991). The second is the polygonal eyewall shapes observed in some tropical cyclones (Lewis and Hawkins, 1982; Muramatsu, 1986).

Black and Marks (1991) observed a meso-vortex in hurricane Hugo (1989) during what was intended to be a routine penetration at 450 m. The vortex had wind and pressure perturbations of $\sim 30\text{ms}^{-1}$ and 12 mb, respectively. The perturbation winds were roughly a factor of three smaller than those in the eyewall. The perturbation vorticity, however, was observed to be about one order of magnitude greater and nearly equivalent to that of a tornado. The above model results also indicate similar trends. That is, the vorticity is highest in the model vortices even though the winds are not significantly greater and the geopotential is also clearly less in the vortices. Although the dynamics of a true meso-vortex are considerably more complicated than our simple model can handle, the similarities are curious.

Support for our instability theory also comes from the observed phenomena of polygonal eyewalls. As evidenced in the above simulations, an annular region of PV can evolve into polygonal patterns. Lewis and Hawkins (1982) showed there to be distinct polygonal patterns in the eyewalls of several hurricanes. Figure 5.13 shows an example of two such polygonal eyewall features of Hurricane Betsy (1965) as seen by WSR-57 radar. Polygonal patterns were also found in Hurricane Anita (1977), Hurricane Debbie (1969) and Hurricane Frederic (1979). To prove these polygonal features were not simply artifacts of the radar, Lewis and Hawkins (1982) were able to obtain simultaneous data from both the National Weather Service's linear receiver radar and the RFC airborne digital log receiver radar system for Hurricane Anita. Both systems showed similar pentagon eye patterns. In addition, Lewis and Hawkins showed that the polygonal patterns also appeared in the time-integrated radar rainfall estimates of Hurricane Frederic, again suggesting that these polygonal eyewall patterns are real physical features and not simply artifacts of the observing system.

The dynamical theory put forth by Lewis and Hawkins was that these patterns were due to the modulation of convection by horizontally propagating internal gravity waves. They proposed that interference patterns due to the superposition of differing wavenumbers and periods would tend to produce polygonal eyes. Their model results, however,

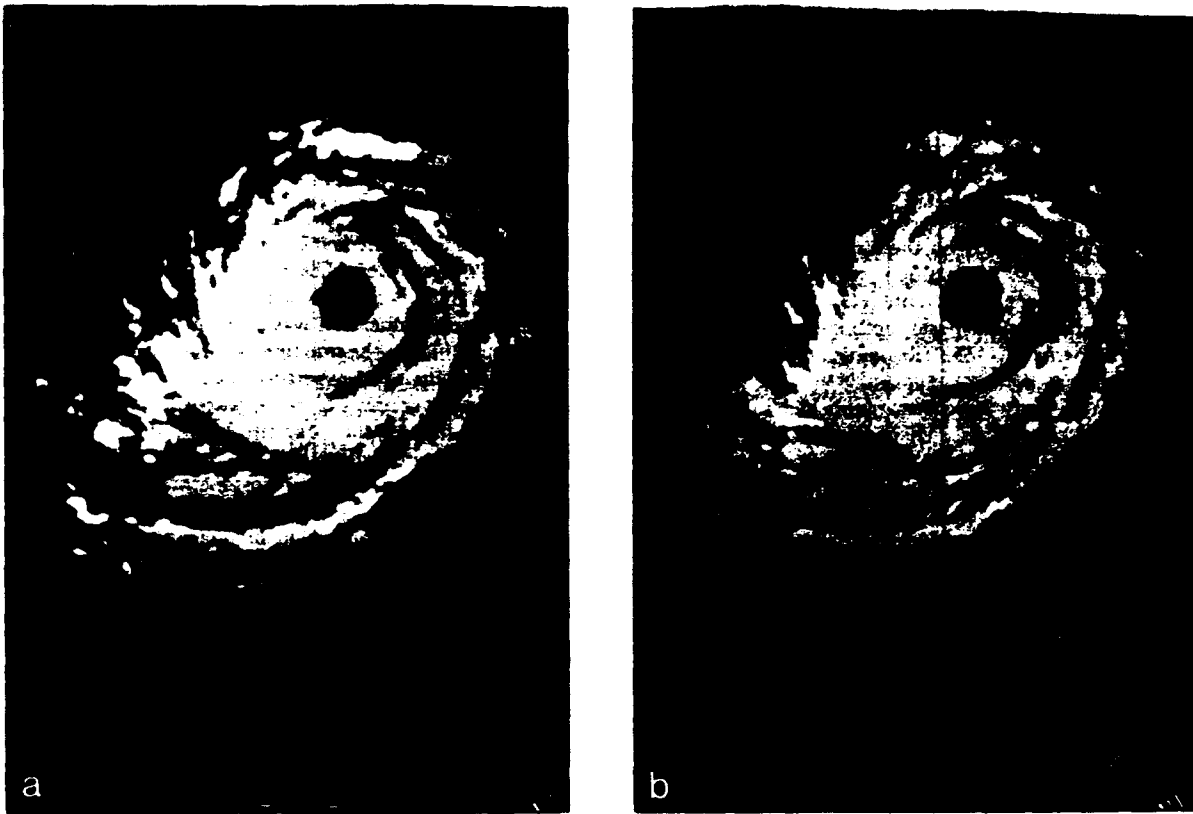


Figure 5.13: Two examples of polygonal eyewall features of Hurricane Betsy as seen by WSR-57 radar. (From Lewis and Hawkins, 1982.)

suggest that if this were the case, polygonal features should also be equally prominent in spiral bands as well. Their observational studies, however, show only one such case where this was observed (Caroline, 1975).

In a similar study, Muramatsu (1986) performed an extensive analysis of the polygonal eyewall patterns in typhoon 8019 WYNNE (1960). Muramatsu also performed an in-depth comparison of several hurricanes and typhoons which exhibited polygonal eyewall features, the results of which are shown in Table 5.1. Muramatsu determined the most common characteristics displayed by these tropical cyclones were: 1) concentric eyes in the developed tropical cyclone stage, 2) central pressures ranging from 920–950 mb, and 3) square to hexagonal shapes occurred in highest frequency (pentagon was observed most frequently and persisted the longest). These observations lend support to the instability theory presented above. Concentric eyewalls suggest definite peaks in the PV field, thus more closely resembling annular PV regions. Secondly, the more intense tropical cyclones, as determined by central pressure, would be expected to have higher PV values

Table 5.1: Summary of tropical cyclone characteristics and features of polygonal eyes. (From Muramatsu, 1986).

Cyclone names	Feature	Eye diameter		Concentric double eye	Central pressure
		inner	outer		
DONNA 1960	5	23 km	90 km	yes	940 mb
BETSY 1965	6	40	120	yes	950
	4	40	100	yes	950
DEBBIE 1969	5	20	36	yes	950
ANITA 1977	4	33	72	yes	926
	5	33	67	yes	926
FREDERIC 1979	4	30	100	yes	950
ALLEN 1980	6	24	130	yes	920
Typhoon 8019 WYNNE	4-6	30	260	yes	920-935
Typhoon 6118	4-5	26-35	150	yes	920

and therefore be more susceptible to instabilities. Lastly, the smaller number polygons should be observed most frequently because of the ratio of the inner to outer distance of the eyewalls. However, why pentagons should be favored is not yet understood. A weakness of our theory is that Muramatsu did not observe any tendency of the outer eyewalls to also show polygonal features, although Lewis and Hawkins (1982) did show one such case (Hurricane Debbie, 1969). The numerical experiments we performed indicated that the vorticity field contained minimal gravity-wave activity. This suggests that the theory of interfering gravity waves seems less plausible than our present theory. In addition, our present theory does not require the spiral bands, themselves, to be polygonal shaped.

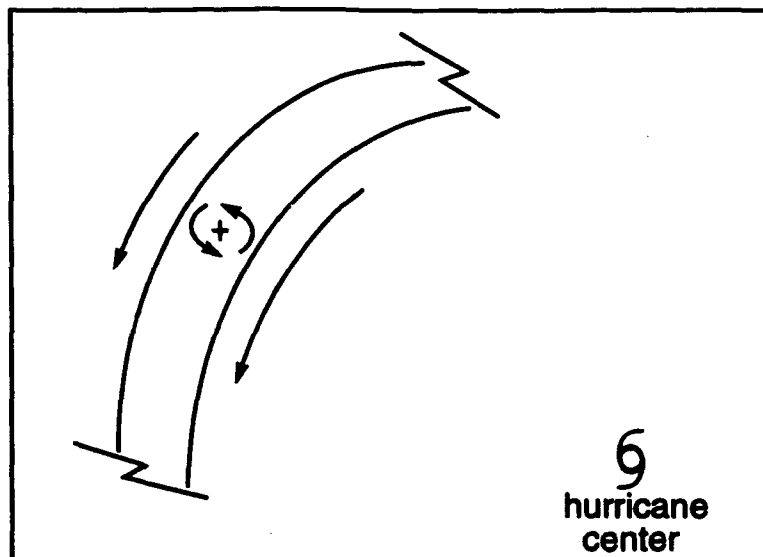


Figure 5.14: A schematic representation of adverse shear. The shear of the vortex created by the decrease in tangential wind speed with radius clearly opposes the circulation induced by the PV anomaly.

5.3 The Effect of Adverse Shear on Stability

In the previous section, we considered the growth of instabilities for an annular band which was free of influence from any other circulations. Chapter 4 indicated that under these situations, the PV field is unstable and thus instabilities should freely grow. Indeed, this was the case. In nature, however, the spiral bands are influenced greatly by circulation of the main vortex. Since the tangential winds of the main vortex decrease with radius (beyond the radius of maximum winds), they introduce a shear which opposes the cyclonic circulation induced by the PV anomaly of the spiral band. This situation is shown schematically in Fig. 5.14. When the shear environment opposes the anomaly, we refer to this as adverse shear (Dritschel, 1989). We will demonstrate in this section that the tendency for instabilities to grow in spiral bands is severely hampered by adverse shear of the vortex. Our discussion begins again with a look at normal mode stability analysis and is followed by a numerical simulation.

5.3.1 Normal Mode Stability Analysis

We simulate the effect of a main vortex on a spiral band by considering an annular region of vorticity (as before) with another region of higher vorticity located at the center

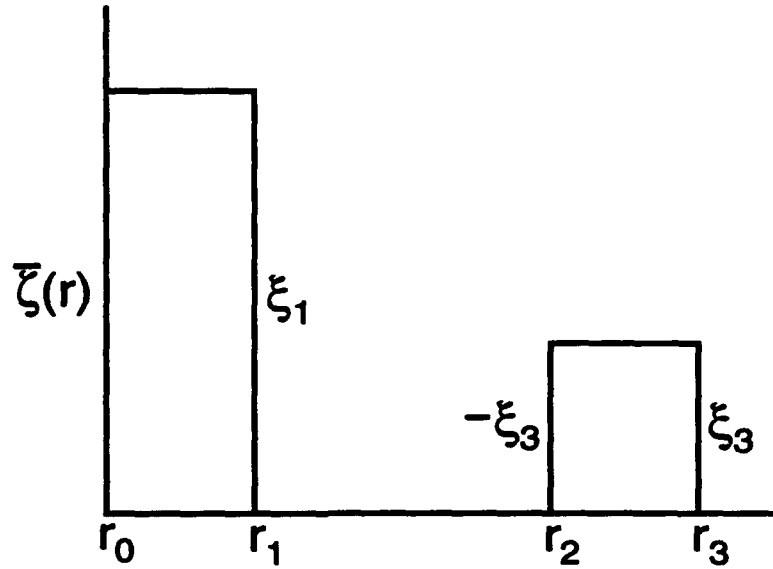


Figure 5.15: An example of the vorticity profile for $J = 3$.

of the annulus (see Fig. 5.15). This is done by considering the case of $J = 3$ in (5.7), for which the matrix eigenvalue problem can be written

$$\begin{pmatrix} m\bar{\omega}_1 - \frac{1}{2}\xi_1 & -\frac{1}{2}\xi_2(r_1/r_2)^{m-1} & -\frac{1}{2}\xi_3(r_1/r_3)^{m-1} \\ -\frac{1}{2}\xi_1(r_1/r_2)^{m+1} & m\bar{\omega}_2 - \frac{1}{2}\xi_2 & -\frac{1}{2}\xi_3(r_2/r_3)^{m-1} \\ -\frac{1}{2}\xi_1(r_1/r_3)^{m+1} & -\frac{1}{2}\xi_2(r_2/r_3)^{m+1} & m\bar{\omega}_3 - \frac{1}{2}\xi_3 \end{pmatrix} \begin{pmatrix} \hat{\eta}_1 \\ \hat{\eta}_2 \\ \hat{\eta}_3 \end{pmatrix} = \nu \begin{pmatrix} \hat{\eta}_1 \\ \hat{\eta}_2 \\ \hat{\eta}_3 \end{pmatrix}. \quad (5.9)$$

We now consider the specific case of $r_1 = 50$ km, $r_2 = 200$ km, $r_3 = 250$ km, $\xi_2 = -\xi_3 = 2.5 \times 10^{-4} \text{ s}^{-1}$, and ξ_1 is allowed to vary from 0.0 to $15.0 \times 10^{-4} \text{ s}^{-1}$. The frequencies and corresponding e -folding times of the most unstable modes as a function ξ_1 are shown in Fig. 5.16. When $\xi_1 = 0.0$, the results are identical to case of $J = 2$ for the same values of r_1 and r_2 . As the vorticity of the main vortex increases, the adverse shear also increases. Clearly, the growth rates of the most unstable modes decrease as the adverse shear generated by the main vortex increases. Also of importance is the trend for the wavenumber of the most unstable mode to increase as the adverse shear increases. The implications of this result is that the growth rates of instabilities in spiral bands should be expected to decrease dramatically as the strength of the main vortex increases and the wavenumber of the disturbance should increase. The fact that the PV in spiral bands is never observed to “pool” supports this result.

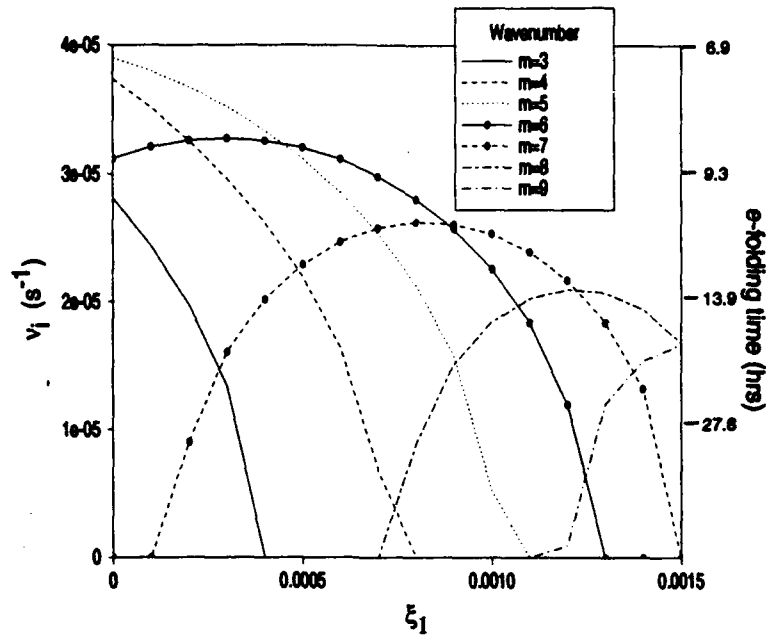


Figure 5.16: The growth rates (ν) of the most unstable modes for wavenumbers $m=3-9$ as a function of ξ_1 . Constant values include $r_1 = 50$ km, $r_2=200$ km, $r_3 = 250$ km, and $\xi_2 = -\xi_3 = 2.5 \times 10^{-4}$.

5.3.2 Numerical Simulation of Adverse Shear

To demonstrate the effects of adverse shear on a spiral band, we have integrated the wavenumber four case of the previous subsection but with the addition of an initial central vorticity region which again takes the form of the Melander profile. The Melander profile for this case is defined by $R_i = 50$ km, $R_0 = 100$ km, $\kappa = 2.56$, and $\hat{\zeta} = 5.0 \times 10^{-4}$. Thus, the vorticity within the main vortex is only twice that of the band. To keep comparisons with the results of the previous section fair, we have also given the model band a wavenumber four perturbation initially. Figure 5.17 shows the initial fields from this experiment. The results at 64 and 120 hrs are shown in Figs. 5.18 and 5.19. Prior to 64 hours, instabilities in the band are not noticeable. Only at 64 hours and beyond are they clearly visible. When no main vortex was present, the wavenumber four pattern had completely detached by 48 hours. By 120 hours, individual pools of PV are clearly discernible and the band appears to display a wavenumber eight PV pattern. The trend predicted by linear normal mode theory is therefore correct. Not only did the instabilities

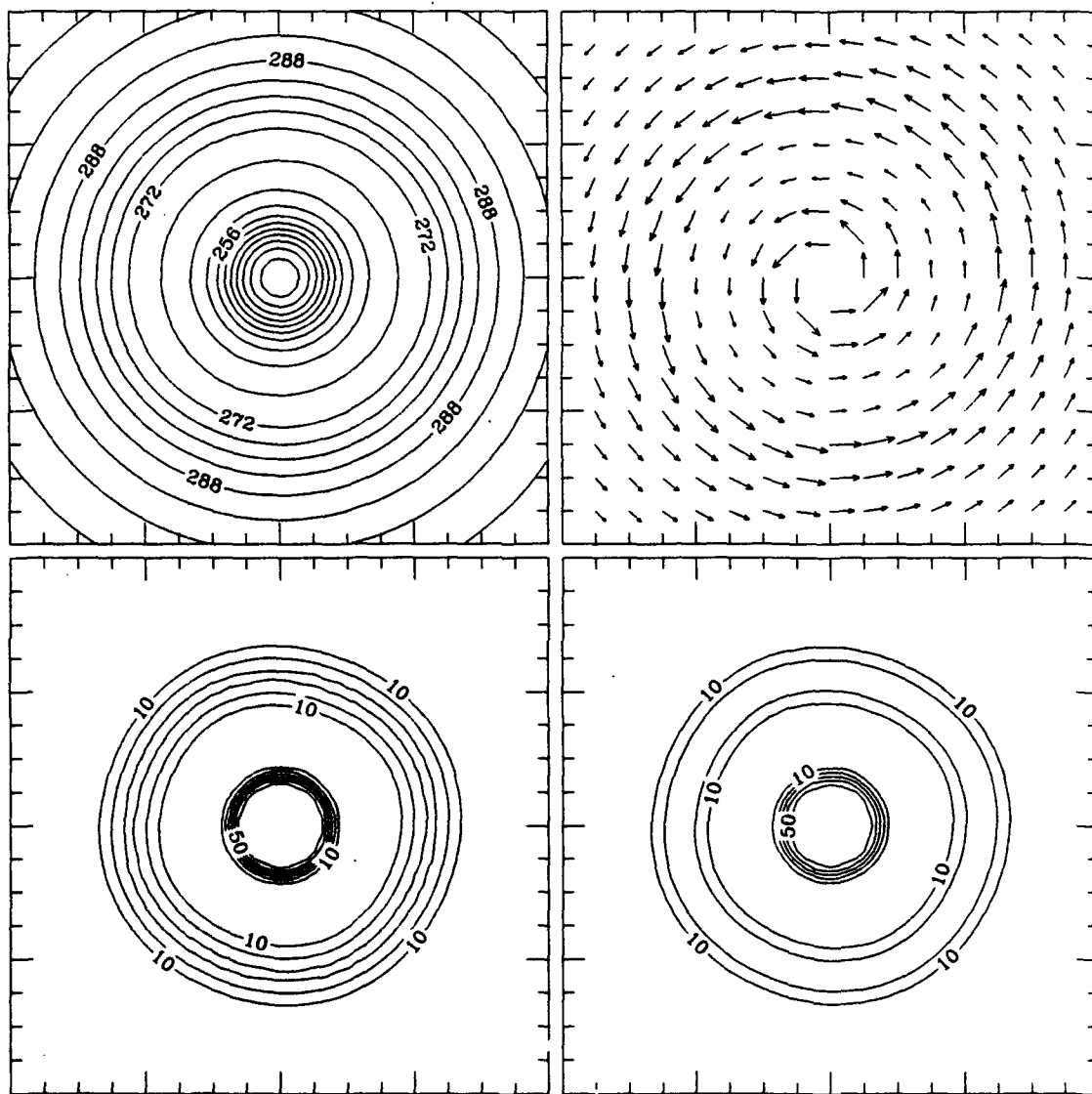


Figure 5.17: The initial wind and mass fields for the wavenumber four perturbed case with a main vortex. The height field (upper left) has contour intervals of 4 m. The wind field (upper right) has a maximum wind vector of 17ms^{-1} . The PV (lower left) and vorticity (lower right) are in units of 10^{-5} s^{-1} and have contour intervals of 1.0×10^{-4} .

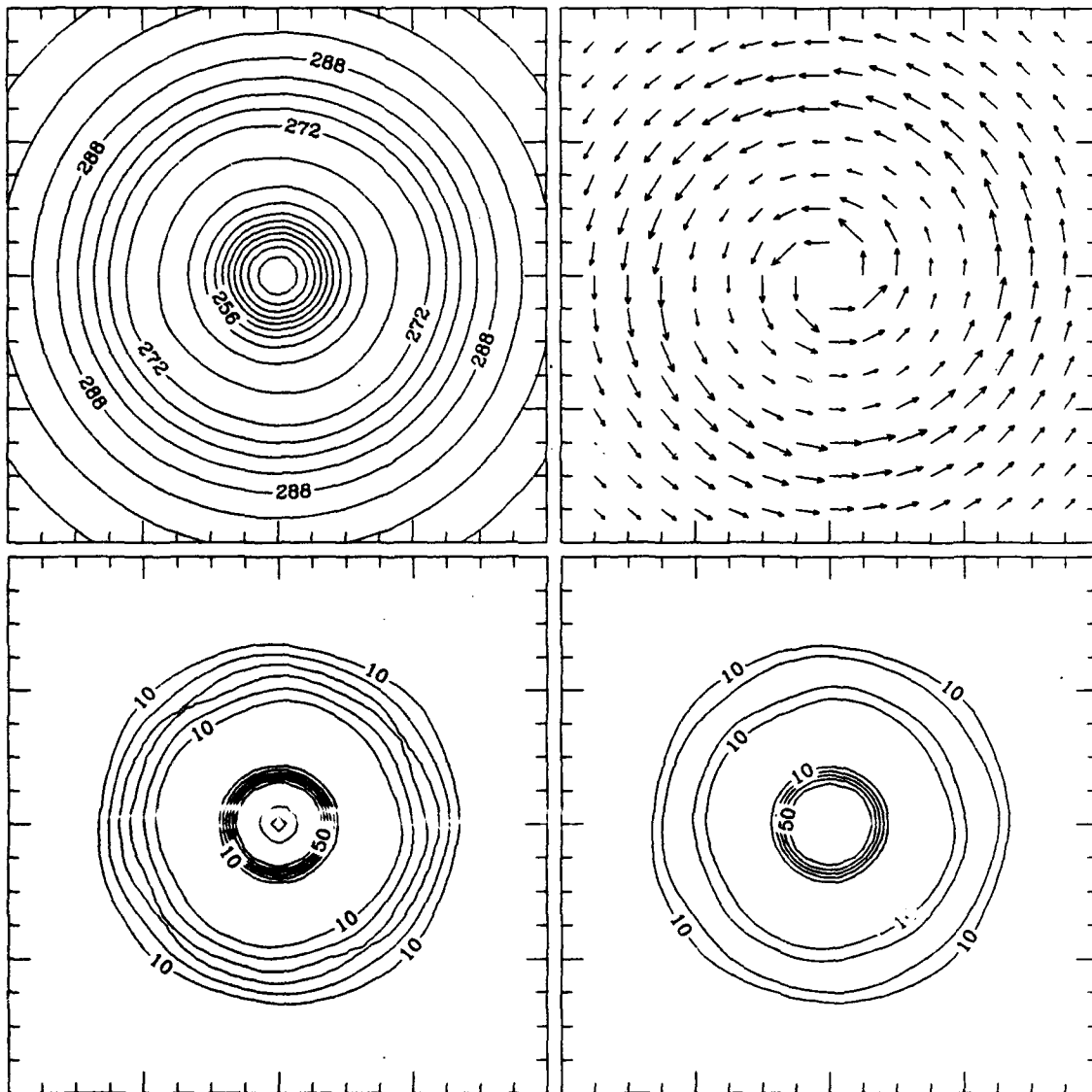


Figure 5.18: The same as Fig. 5.17 but for 64 hours.

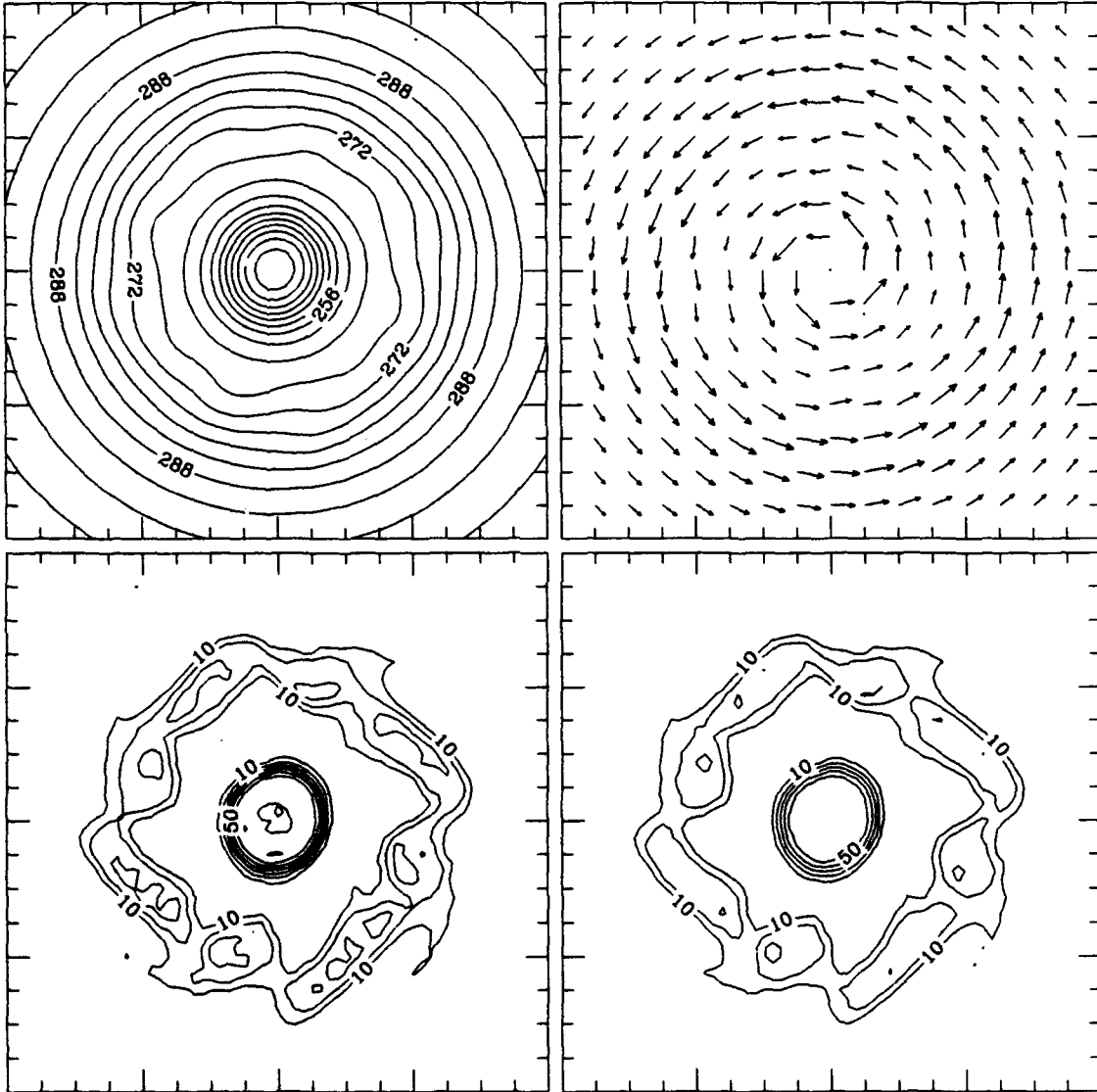


Figure 5.19: The same as Fig. 5.17 but for 120 hours.

take longer to amplify, but much higher wavenumbers were produced. In nature we should expect these results to be even more dramatic because of the extremely high vorticity associated with the main vortex of a tropical cyclone, which have been measured to be as high as $4.8 \times 10^{-3} \text{ s}^{-1}$ (Hawkins and Imbembo, 1976). Although numerous calculations of vorticity within spiral bands are not available, results from Powell (1990) and Ryan *et al.* (1992) suggest the vorticity in the bands can range from $1.5 \times 10^{-4} \text{ s}^{-1}$ to $2.5 \times 10^{-3} \text{ s}^{-1}$. If these values are assumed to representative of typical hurricane bands, the lifetime of the bands should be much less than the time required for instabilities to affect the spiral bands. Even if the vorticity in the main vortex is only twice that of the band, as in the above experiment, it is doubtful that a single band could persist in nature for 120 hours (5 days) as required by model results.

Chapter 6

SUMMARY AND CONCLUSIONS

We have presented several new theories concerning the formation and stability of both inner and outer hurricane spiral bands through use of a limited area, shallow water, normal mode spectral model. Because the basis functions of the model were the normal modes of the system, we were able to naturally partition the geostrophic (rotational) modes from the gravity-inertia modes. The bands were found to project almost entirely onto the rotational modes. These results indicate that the gravity wave theories conventionally accepted for hurricane bands (e.g. Tepper, 1958, Abdullah, 1966; Kurihara, 1976; Willoughby, 1978) may not be entirely appropriate. Evidence was supplied to suggest that spiral bands should more appropriately be classified as slow manifold phenomena (Leith, 1980; Daley, 1991) which project onto both the rotational and gravatational modes in such a way that transient gravity waves are minimized.

In Chapter 3 we considered the formation of inner bands, which we defined as bands that typically form less than 500 km from the center of the vortex and owe their existence to asymmetries in the PV field. We demonstrated that the concept of PV wave breaking, which has been found to be useful when examining stratospheric data (McIntyre and Palmer, 1984; Jukes and McIntyre, 1987; Polvani and Plumb, 1992), also appears to be useful for explaining the formation of inner hurricane bands. Simulations of this process were performed by assuming convective heating had generated an asymmetric PV field and letting the model evolve unforced. From these experiments, we found that the PV contours underwent a rapid and irreversible deformation which acted to eject filaments of high PV air from the center of the vortex to large radii, thus forming bands. Additionally, the PV field also underwent a continual axisymmetrization process which acted

to restore the PV field to a more circular shape. These results corresponded well to the nondivergent barotropic results found by Melander *et al.* (1987b). The effect of the wave breaking and axisymmetrization process was to cause both an outward shift in the radius of maximum winds and an increase in the maximum wind speed. Outside the radius of maximum winds, but inside the spiral bands, the effect of symmetrization was to decrease the tangentially averaged wind speed. Near the banded regions, a slight increase in the tangentially averaged wind speed was noticed.

To better understand the wave breaking process, passive tracer integrations and wave activity/wave activity flux diagnostics were performed. The passive tracer experiments showed that the PV field behaved in a nearly identical fashion to a passive tracer, even though it is the inversion of PV which determines the wind and mass fields for balanced systems. We also used the passive tracer technique to perform Lagrangian studies of the wave breaking process, by combining two passive tracers, one which initially varied only in y and one which initially varied only in x . Since the intersection of any two contours uniquely defined a particle, we could trace the trajectory of a particle simply by following the path of the proper contour intersection. This study allowed us to verify that the particles which appeared in the banded regions, originated near the lobes of the elliptical shaped PV patterns.

The second tool used to study the wave breaking process was wave activity and wave activity flux diagnostics. The exact form of wave activity, as derived by Haynes (1988), was used. Wave activity provides a conservative measure of wave amplitude, and confirms that banded regions are also regions of large wave amplitude. The implications of this, however, are unclear since the form of wave activity used is incomplete in the sense that its flux cannot be directly related to changes of the mean wind (as with quasi-geostrophic theory). We therefore cannot accurately determine how the waves and mean flows will interact. The wave activity experiments done in this study were of the simplest form; that is, there was no external forcing involved and the basic state was both axisymmetric and constant in time. It is expected that the use of wave activity with a more physically complete model would prove to be more useful. In the case of external forcings, the wave

activity would not be conserved in diabatically or frictionally forced regions. This would allow one to view the effects of external forcings on wave amplitude. The wave activity studies considered here were merely a step towards this goal.

The formation of bands by vortex merger was also studied. Five model simulations were presented to examine the banding process. The first four simulations considered the merger of a symmetric vortex with pre-existing PV regions of different sizes and intensities. In all cases spiral bands were readily formed. In the fifth simulation we considered a symmetric vortex which was located near a mass sink (PV source). The mass sink was intended to represent a convective heat source in nature. The mass sink (heat source) was turned on in a gradual manner to avoid the generation of transient gravity waves, thus ensuring the model evolved along the diabatic slow manifold. As the heating intensified, PV anomalies were induced and the initial vortex propagated towards the heat source. The effect of the heat source was to generate a region of high PV air which was advected around and into the vortex. As the vortex moved closer to the heat source, vortex merger occurred and a spiral band formed. Unlike the unforced experiments, the bands associated with the forced experiments appeared to exhibit deviations from axisymmetry in the height fields. These results relate more closely to observed studies (e.g., Ryan *et al.*, 1992; Powell, 1990) and suggest that hurricane bands evolve along the diabatic slow manifold (or more precisely, the diabatic frictional slow manifold) in nature.

Results from Chapter 3 suggest that more work is needed to fully understand hurricane band formation by wave breaking and vortex merger processes. At the observational level, PV maps of tropical cyclones are desperately needed. This is not an easy task, however, since the calculation of Rossby Ertel PV (which can be approximated by $-g\zeta(\partial\theta/\partial p)$) involves the calculation of both horizontal and vertical derivatives. Any errors in the wind, are multiplied when their derivatives are calculated. In addition, obtaining a sufficiently dense data set to resolve spiral bands (~ 30 km wide) is difficult for obvious reasons. The use of aircraft Doppler radar in recent years, however, has shown promise by providing a relatively accurate and dense source of wind data. Work to compute PV fields in hurricanes is currently being attempted at the Hurricane Research Division of NOAA.

Aside from observational studies, more work in the area of modeling is also needed. The results presented in Chapter 3 were for the simplest case possible. Although this allowed us to isolate the fundamental dynamics, other factors related to tropical cyclones may play a key role. The foremost factor is friction. Since the model used in this paper was a shallow water model, frictional forces could not be represented in any true physical sense. That is, we could add a surface friction term in the form of a bulk aerodynamic formula, but its effects would be to simply damp the winds with time – no feedback into a cumulus parameterization scheme is possible. This suggests that a layered normal mode model would also be useful since frictional effects could then be fed back into the heating fields. An incompressible, three layer (fixed boundary layer, inflow region, and outflow region) normal mode model of this type was accomplished by DeMaria and Schubert (1984) and was used to study tropical cyclone motion. A similar, but more useful normal mode model, which uses three isentropic layers was developed by DeMaria and Pickle (1988) and was used by Shapiro (1992) to investigate the effect of asymmetries and the β -effect on hurricane motion. Preliminary results towards this goal have been attempted in this study through use of a three layer extension of the present model. The three layers represented the boundary layer, inflow (cyclonic) layer, and outflow (anticyclonic) layer of a tropical cyclone. In contrast to DeMaria and Schubert (1984), the boundary layer was of variable depth. When the model was run unforced with an initial elliptical shaped PV pattern, results were similar to those obtained for the shallow water case. Additional work in this area is still needed to add a workable cumulus parameterization scheme.

In Chapter 4, we considered the formation of outer spiral bands. These bands were defined as those which typically form 500 km from the vortex center, and owe their existence to the breakdown of the ITCZ. Several general stability theorems, both linear and nonlinear, were reviewed. These theorems all indicated that a reversal in the PV gradient is a necessary condition for barotropic instability. Although the general stability theorems provided conditions for instability, they offered no information concerning growth rates or unstable patterns. In order to predict such features, we utilized the less general technique of linear normal mode stability analysis. This analysis technique is less general

because it assumes the instabilities grow with spatial structure e^{ikx} . Results from the normal mode stability analysis showed that as the width of a PV anomaly decreased, the growth rates of the instabilities increased and the wavenumber of the most unstable mode also increased. To test the results of the normal mode stability analysis, numerous numerical model integrations were performed by initializing the model with various shapes and sizes of PV strips. These strips were continuous in x but confined in y except for the final experiment. In the final experiment, the initial PV field was confined in both x and y . Results from the numerical simulations displayed similar trends to those predicted by linear theory. That is, instabilities grew faster for the thinner strips and showed a tendency for higher wavenumbers. In addition, these results bore remarkable resemblance to the natural breakdown of the ITCZ over the eastern Pacific Ocean. One implication of these results is that the analysis of easterly wave formation in the North African region performed by Burpee (1972) is not unique to that region. As Schubert *et al.* (1991) demonstrated, ITCZ convection alone can lead to PV anomalies. These PV anomalies, in turn, satisfy the necessary condition for unstable flows, resulting in breakdowns in the ITCZ similar to those presented in Chapter 4.

The resulting patterns from initially similar PV strips appears to be highly sensitive to the initial condition. This sensitivity was tested by making three separate model integrations starting from identically specified wind and mass fields. In each case, the fields were perturbed using different sequences of random numbers (but of equal magnitude). In all three cases the ITCZ broke down and pools of high PV air were formed. The difference, however, was in the number of pools which formed. The three runs resulted in one wavenumber three pattern and two wavenumber two patterns. This suggests that predicting the locations of incipient hurricanes based on ITCZ patterns would be difficult because of the inherent nonlinearity of the problem.

One possible extension of the previous study is to include spherical effects. Some work in this area has been performed by Dritschel (1992) using a nondivergent barotropic model on a sphere. He concluded that barotropic flows on a sphere have an even more pronounced tendency to produce small short lived vortices, especially in equatorial and

mid-latitude regions. Work is currently being done at C.S.U. to extend Dritschel's work to the shallow water system using the recently developed NCAR global shallow water spectral model (Hack and Jakob, 1992).

In Chapter 5, we investigated the stability of spiral bands. This investigation followed logically from Chapters 3 and 4, the reason being that in Chapter 3 we saw how the banding process created strips of relatively high PV (and therefore reversals in the PV gradient), and in Chapter 4 we saw that regions of PV gradient reversals satisfied the necessary condition for barotropic instability.

The stability analysis was done both analytically and numerically. The analytic study again made use of nonlinear normal mode analysis. An eigenvalue/eigenvector problem was formed by considering the boundary displacement of multiple concentric annular regions of uniform vorticity. To simulate an isolated spiral band, we considered the case of a single annular region of PV located at an arbitrary distance from the center of the domain. The stability analysis produced similar results to that of Chapter 4. As the band was made narrower, both the growth rates and wavenumbers of the most unstable mode increased. These results were also verified through numerical integrations.

The above mentioned numerical simulations lead to a somewhat unexpected finding. As the annular regions of PV broke down in the above experiments, they began to form polygonal shapes. Similar polygonal shapes have also been found in the eyewalls of intense hurricanes (Lewis and Hawkins, 1982; Muramatsu, 1986). If we approximate hurricane eyewalls by annular regions of high PV air, then it seems reasonable to assume that barotropic instabilities should also be observed, especially in more intense hurricanes. As a result, these barotropic instabilities could act to form polygonal shapes in hurricane eyewalls. As further observational evidence of eyewall instabilities, Black and Marks (1991) noted the presence of a meso-vortex in Hurricane Hugo (1989). This may be due to the PV pooling process which occurs as instabilities grow. Numerical simulations demonstrated well the breakdown of an annular PV region and subsequent formation of smaller scale circulations. On a much finer scale, the instabilities of annular high PV regions may also have some relevance to the observed phenomenon of tornado suction spots. These

suction spots are secondary vortices which rotate around the parent vortex (Fujita *et al.*, 1972). Linear normal mode analysis of this phenomena has been performed by Snow (1978), and bear some resemblance to our present results. Although these two phenomena may be closely related, tornado suction spots are obviously a nonhydrostatic process and therefore not representable by a shallow water model such as the one used in the present study.

In the final section of Chapter 5, we offered an explanation as to why spiral bands are not observed to undergo unstable growth even though they satisfy the necessary condition for instability. The explanation appears to be related to the adverse shear generated by the main vortex. Physically, the adverse shear of the main vortex opposes the circulation which the PV anomaly tries to generate. Results which demonstrate this effect in a two-dimensional fluid have been presented both numerically and analytically by Dritschel (1989). In the present study, we also used both linear normal mode analysis and numerical simulations to study the problem. The linear analysis examined the stability of a 50 km wide annular region of PV centered at 225 km from the cylindrical coordinate center. At the coordinate center was a uniform vorticity region of 50 km radius. The vorticity of the center region was allowed to vary, thus providing different intensities of adverse shear. Results showed that as the adverse shear increased, the growth rate of the most unstable mode decreased, while the wavenumber increased. A similar case to that used for the linear analysis was simulated using the model. In the case of the model simulation, the vorticity in the main vortex was twice that of the band. Results from the simulation confirmed those suggested by the linear analysis. The complete breakdown of the annular region took approximately three times longer and the wavenumber of the most unstable mode doubled.

A problem that persisted throughout the Chapter 5 experiments was the tendency for the annular PV regions to be perturbed in a wavenumber four pattern. This tendency occurred because of doubly periodic boundary conditions. To overcome this problem, it may be useful to integrate the cylindrical coordinate model presented in Appendix A. This would allow random perturbations in the initial fields to be used for determining the

true most unstable mode. Two drawbacks, however, are that the basis functions of the cylindrical model have poor convergence properties, and no fast transform exists in the radial direction. For simple studies, such as those suggested above, these problems may be surmountable.

REFERENCES

- Abdullah, A.J., 1966: The spiral bands of a hurricane: A possible explanation. *J. Atmos. Sci.*, **23**, 367-375.
- Abramowitz, M., and I. Stegun, 1964: *Handbook of Mathematical Functions*. Dover edition, 1972, Dover, New York, 1046pp. [ISBN 0-486-61272-4]
- Andrews, D.G., and M.E. McIntyre, 1978a: An exact theory of nonlinear waves on a Lagrangian-mean flow. *J. Fluid Mech.*, **89**, 609-646. Corrigendum, **95**, 796.
- , and ———, 1978b: On wave-action and its relatives. *J. Fluid Mech.*, **89**, 647-644.
- Anthes, R.A., 1982: *Tropical Cyclones: Their Evolution, Structure and Effects*. Amer. Met. Soc. [ISBN 0-933876-54-8]
- Arnol'd, V.I., 1965: Conditions for nonlinear stability of stationary plane curvilinear flows of an ideal fluid. *Dokl. Akad. Nauk. SSSR*, **162**, 975-978. (English translation: *Soviet Math.*, **6**, 773-777).
- , 1966: On an a priori estimate in the theory of hydrodynamical instability. *Izv. Vyssh. Uchibn. Zaved. Matematika*, **54**, no. 5, 3-5. (English translation: *American Math Soc. Transl., Series 2*, **79**, 267-269).
- Black, P.G., and F.D. Marks, 1991: The structure of an eyewall meso-vortex in Hurricane Hugo (1989). *Preprints from the 19th Conference on Hurricanes and Tropical Meteorology*, Amer. Met. Soc., 579-582.
- Brigham, E.O., 1988: *The Fast Fourier Transform and its Applications.*, Prentice-Hall, Inc., Englewood Cliffs, New Jersey, 448pp. [ISBN 0-13-307505-2]
- Burpee, R.W., 1972: The origin and structure of easterly waves in the lower troposphere of North Africa. *J. Atmos. Sci.*, **29**, 77-90.
- Charney, J.G., and M.E. Stern, 1962: On the stability of internal baroclinic jets in a rotating atmosphere. *J. Atmos. Sci.*, **19**, 159-172.

- Conte, S.D., and C. de Boor, 1980: *Elementary Numerical Analysis: An Algorithmic Approach*. 3rd ed., MacGraw Hill, 432pp. [ISBN 0-07-012447-7]
- Daley, R., 1991: *Atmospheric Data Analysis*, Cambridge University Press, 457pp. [ISBN 0-521-38215-7]
- DeMaria, M., and W.H. Schubert, 1984: Experiments with a spectral tropical cyclone model. *J. Atmos. Sci.*, **41**, 901-924.
- , and J.D. Pickle, 1988: A simplified system of equations for simulation of tropical cyclones. *J. Atmos. Sci.* **45**, 1542-1554.
- Dritschel, D.G., 1986: The nonlinear evolution of rotating configurations of uniform vorticity. *J. Fluid Mech.*, **172**, 157-182.
- , 1989: On the stabilization of a two-dimensional vortex strip by adverse shear. *J. Fluid Mech.*, **206**, 193-221.
- , 1992: The roll-up of vorticity strips on the surface of sphere. *J. Fluid Mech.*, **234**, 47-69.
- Eliassen, E., B. Machenhauer, and E. Rasmussen, 1970: On a numerical method for integration of the hydrodynamical equations with a spectral representation of the horizontal fields. Report No. 2, Kobenhavns Universitet, Institut for teoretisk meteorolgi, 35pp.
- Eliassen, A., and E. Palm, 1960: On the transfer of energy in stationary mountain waves. *Geophysica Norvegica*, **22**, 1-23.
- , 1983: The Charney-Stern theorem on barotropic-baroclinic instability. *Pure Appl. Geophys.*, **121**, 563-572.
- Evans, J.L., and G.J. Holland, 1991: Interactions between a barotropic vortex and an idealized subtropical ridge. Part I: Vortex motion. *J. Atmos. Sci.*, **48**, 301-314.
- Faller, A.J., 1961: An experimental analogy to and proposed explanation of hurricane spiral bands. *Proceedings of the Second Technical Conference on Hurricanes, Part II*. Amer. Met. Soc. 307-313.
- Fjørtoft, R., 1950: Application of integral theorems in deriving criteria of stability for laminar flows and for the baroclinic circular vortex. *Geofis. Publ.*, **17**, No. 6, 52pp.

- Fletcher, R.D., 1945: The general circulation of the tropical and equatorial atmosphere. *J. Meteor.*, **2**, 167-174.
- Fujita, T.T., K. Watanabe, K. Tsuchiya, and M. Shimada, 1972: Typhoon-associated tornadoes in Japan and new evidence of suction vortices in a tornado near Tokyo. *J. Meteor. Soc. Japan*, **50**, 431-453.
- Fujiwhara, S., 1923: On the growth and decay of vortical systems. *Q. J. R. Met. Soc.*, **49**, 75-104.
- Fung, I.Y., 1977: The organization of spiral bands in a hurricane. Ph.D. Dissertation, Massachusetts Institute of Technology, 139pp.
- Gottlieb D., and S.A. Orzag, 1977: *Numerical Analysis of Spectral Methods: Theory and Applications.*, Regional conference series in applied mathematics, No. 26, Society for Industrial and Applied Mathematics, Philadelphia, 177pp.
- Gray, W.M., 1964: On the scales of motion and internal stress of the hurricane. Ph.D. Dissertation, University of Chicago, 203pp.
- Griffiths, R.W., and E.J. Hopfinger, 1987: Coalescing of geostrophic vortices. *J. Fluid Mech.*, **178**, 73-97.
- Hack, J.J., and R. Jakob, 1992: Description of a global shallow water model based on the transform method. NCAR Technical Note (NCAR/TN-343+STR), Climate and Global Dynamics Division, NCAR, Boulder, CO, 39pp.
- Hawkins, H.F., and S.M. Imbembo, 1976: The structure of a small, intense hurricane (Inez 1966). *Mon. Wea. Rev.*, **104**, 418-442.
- Haynes, P.H., 1988: Forced, dissipative, generalizations of finite amplitude wave-activity conservation relations for zonal and nonzonal basic flows. *J. Atmos. Sci.*, **45**, 2352-2362.
- Holland, G.J., and J.L. Evans, 1992: Interactions between a barotropic vortex and an idealized subtropical ridge. Part II: Structure changes. *J. Atmos. Sci.*, in press.
- , and M. Lander, 1992: On the meandering motion of tropical cyclones. Submitted to *Mon. Wea. Rev.*

- , and G. Dietachmayer, 1992: On the interaction of tropical cyclone scale vortices. Part III: Continuous barotropic vortices. Submitted to *Q. J. R. Met. Soc.*
- Hoskins, B.J., M.E. McIntyre, and A.W. Robertson, 1985: On the use and significance of isentropic potential vorticity maps. *Q. J. R. Met. Soc.*, **111**, 877–946.
- Juckes, M.N., and M.E. McIntyre, 1987: A high-resolution one-layer model of breaking planetary waves in the stratosphere. *Nature*, **328**, 590–596.
- Krylov, V.I., 1962: *Approximate Calculation of Integrals*. The Macmillan Company, New York, 357pp.
- Kuo, H.L., 1973: Dynamics of quasigeostrophic flows and instability theory. *Adv. Appl. Mech.*, **13**, 247–330.
- Kurihara, Y., 1976: On the development of spiral bands in a tropical cyclone. *J. Atmos. Sci.*, **33**, 940–958.
- Lamb, H., 1945: *Hydrodynamics, 6th ed.*, Dover Publications, N.Y., 738 pp. [ISBN 0-486-60256-7]
- Lander, M., and G.J. Holland, 1992: On the interaction of tropical cyclone scale vortices. Part I: Observations. Submitted to *Q. J. R. Met. Soc.*
- Leith, C.E., 1980: Nonlinear normal mode initialization and quasi-geostrophic theory. *J. Atmos. Sci.*, **37**, 958–968.
- Lewis, B.M., and H.F. Hawkins, 1982: Polygonal eye walls and rainbands in hurricanes. *Bull. Amer. Met. Soc.*, **63**, 1294–1300.
- Ligda, M.G.H., 1955: Hurricane squall lines. *Bull. Amer. Met. Soc.*, **36**, 340–342.
- MacDonald, N.J., 1968: The evidence for the existence of Rossby-like waves in the hurricane. *Tellus*, **20**, 138–149.
- Magnusdottir, G., and W.H. Schubert, 1990: On the generalization of semi-geostrophic theory to the β -plane. *J. Atmos. Sci.*, **47**, 1714–1720.
- , and ———, 1991: Semigeostrophic theory on the hemisphere. *J. Atmos. Sci.*, **48**, 1449–1456.

- Maynard, R.H., 1945: Radar and weather. *J. Meteor.*, **2**, 214-226.
- McIntyre, M.E., and T.N. Palmer, 1983: Breaking planetary waves in the stratosphere. *Nature*, **305**, 593-600.
- , and ———, 1984: The surf zone in the stratosphere. *J. Atmos. and Terrest. Phys.*, **46**, 825-849.
- , and ———, 1985: A note on the general concept of wave breaking for Rossby and gravity waves. *Pure Appl. Geophys.*, **123**, 964-975.
- , and T.G. Shepherd, 1987: An exact local conservation theorem for finite amplitude disturbances to non-parallel shear flows with remarks on Hamiltonian structure and on Arnol'd's stability theorems. *J. Fluid Mech.*, **181**, 527-565.
- McWilliams, J.C., 1984: The emergence of isolated coherent vortices in turbulent flow. *J. Fluid Mech.*, **146**, 21-43.
- Melander, M.V., N.J. Zabusky, and J.C. McWilliams, 1987a: Asymmetric vortex merger in two dimensions: Which vortex is "victorious"? *Phys. Fluids*, **30**, 2610-2612.
- , J.C. McWilliams, and N.J. Zabusky, 1987b: Axisymmetrization and vorticity-gradient intensification of an isolated two-dimensional vortex through filamentation. *J. Fluid Mech.*, **178**, 137-159.
- , N.J. Zabusky, and J.C. McWilliams, 1988: Symmetric vortex merger in two dimensions: Causes and conditions. *J. Fluid Mech.*, **195**, 303-340.
- Merrill, R.T., 1984: A comparison of large and small tropical cyclones. *Mon. Wea. Rev.*, **112**, 1408-1418.
- Muramatsu, T., 1986: The structure of polygonal eye of a typhoon. *J. Met. Soc. Japan*, **64**, 913-921.
- Orzag, S.A., 1970: Transform method for the calculation of vector-coupled sums: Application to the spectral form of the vorticity equation. *J. Atmos. Sci.*, **27**, 890-895.
- Phillips, N.A., 1959: An example of non-linear computational instability. *The Atmosphere and Sea in Motion*, Rossby Memorial Volume, New York, Rockefeller Instit. press, 501-504.

- Platzman, G.W., 1968: The Rossby wave. *Q. J. R. Met. Soc.*, **94**, 225-248.
- Polvani, L.M., and R.A. Plumb, 1992: Rossby wave breaking, microbreaking, filamentation, and secondary vortex formation: The dynamics of a perturbed vortex. *J. Atmos. Sci.*, **49**, 462-476.
- Powell, M.D., 1990: Boundary layer structure and dynamics in outer hurricane rainbands. Part I: Mesoscale rainfall and kinematic structure. *Mon. Wea. Rev.*, **118**, 891-917.
- Pratt, L.J. and J. Pedlosky, 1991: Linear and nonlinear barotropic instability of the geostrophic shear layers. *J. Fluid Mech.*, **224**, 49-76.
- Randall, D.A., 1989: An introduction to atmospheric modeling. Chapt. 3, Ordinary differential equations of first order. Unpublished notes.
- Rayleigh, J.W.S., 1945: *The Theory of Sound*, vol. 2, Dover Publications, Inc., New York, 504 pp. [ISBN 0-486-60293-1]
- Ripa, P., 1983: General stability conditions for zonal flow in a one-layer model on the β -plane or the sphere. *J. Fluid Mech.*, **126**, 463-489.
- , 1991: General stability conditions for a multi-layer model. *J. Fluid Mech.*, **222**, 119-137.
- Ritchie, E., and G.J. Holland, 1992: On the interaction of tropical cyclone scale vortices. Part II: Discrete vortex patches. Submitted to *Q. J. R. Met. Soc.*
- Rossby, C.-G., 1939: Relation between variations in the intensity of the zonal circulation of the atmosphere and the displacements of the semi-permanent centers of action. *J. Marine Res.*, **2**, 38-55.
- Ryan, B.F., G.M. Barnes, and E.J. Zipser, 1992: A wide rainband in a developing tropical cyclone. *Mon. Wea. Rev.*, **120**, 431-447.
- Schubert, W.H., J.J. Hack, P.L. Silva Dias, and S.R. Fulton, 1980: Geostrophic adjustment in an axisymmetric vortex. *J. Atmos. Sci.*, **37**, 1464-1484.
- , and M. DeMaria, 1985: Axisymmetric, primitive equation, spectral tropical cyclone model. Part I: Formulation. *J. Atmos. Sci.*, **42**, 1213-1224.

- , and B.T. Alworth, 1987: Evolution of potential vorticity in tropical cyclones. *Q. J. R. Met. Soc.*, **113**, 147–162.
- , P.E. Ciesielski, D.E. Stevens, and H. Kuo, 1991: Potential vorticity modeling of the ITCZ and the Hadley Circulation. *J. Atmos. Sci.*, **48**, 1493–1509.
- , P.E. Ciesielski, and K.W. Harding, 1992: Dynamics of the Australian summer monsoon. Submitted to the *Q. J. R. Met. Soc.*
- Shapiro, L.J., 1992: Hurricane vortex motion and evolution in a three-layer model. *J. Atmos. Sci.*, **49**, 140–153.
- Shepherd, T.G., 1988: Nonlinear saturation of baroclinic instability. Part I: The two-layer model. *J. Atmos. Sci.*, **45**, 2014–2025.
- Snow, J.T., 1978: On inertial instability as related to the multiple-vortex phenomenon. *J. Atmos. Sci.*, **35**, 1660–1677.
- Strang, G., 1988: *Linear Algebra and Its Applications*. 3rd ed., Harcourt, Brace, Jovanovich, Inc., 505pp. [ISBN 0-15-551005-3]
- Tatehira, R., 1961: A mesosynoptic and radar analysis of typhoon rain band (case study of typhoon "Hellen," 1958). *Proc. Second Tech. Conf. Hurricanes*, Miami, Amer. Met. Soc., 115–126.
- Taylor, G.I., 1915: Eddy motions in the atmosphere. *Philos. Trans. R. Soc. Lond. A*, **115**, 1–26.
- Temperton, C., 1983a: Self-sorting mixed-radix fast Fourier transforms. *J. Comp. Physics*, **52**, 1–23.
- , 1983b: Fast mixed-radix real Fourier transforms. *J. Comp. Physics*, **52**, 340–350.
- Tepper, M., 1958: A theoretical model for hurricane radar bands. *Proc. Seventh Radar Conf.*, Amer. Met. Soc., K56–K65.
- Toomre, A., 1977: Theories of spiral structure. *Ann. Rev. Astron. Astrophys.*, **15**, 437–478.
- Turner, J.S., 1973: *Buoyancy Effects in Fluids*. Cambridge University Press, 367pp. [ISBN 0-521-08623]

- Welander, P., 1955: Studies on the general development of motion in a two-dimensional, ideal fluid. *Tellus*, **7**, 141-156.
- Wexler, H., 1947: Structure of hurricanes as determined by radar. *Annal N.Y. Acad. Sci.*, **48**, 821-844.
- Willoughby, H.E., 1978: A possible mechanism for the formation of hurricane rainbands. *J. Atmos. Sci.*, **35**, 838-848.
- , J.A. Clos, and M.G. Shoreibah, 1982: Concentric eyewalls, secondary wind maxima, and the evolution of the hurricane vortex. *J. Atmos. Sci.*, **39**, 395-411.

Appendix A

THE NORMAL MODE MODEL IN CYLINDRICAL COORDINATES

In this chapter we present the normal mode transform in cylindrical coordinate. Although this version of the model was not used in the numerical integrations it is none the less useful to see the similarities to the Cartesian coordinate model. It is of interest to note that all normal mode models reduce to the oscillation equation (2.18) regardless of geometry or vertical structure.

A.1 The Governing Equations in Cylindrical Coordinates

The shallow water equations in cylindrical coordinates can be written in rotational form as

$$\frac{\partial u}{\partial t} - f(v + A) + \frac{\partial}{\partial r}(\Phi + K) = F \quad (\text{A.1})$$

$$\frac{\partial v}{\partial t} + f(U + B) + \frac{\partial}{r \partial \varphi}(\phi + K) = G \quad (\text{A.2})$$

$$\frac{\partial \phi}{\partial t} + c^2 \left(\frac{\partial r(u + C)}{r \partial r} + \frac{\partial(v + D)}{r \partial \varphi} \right) = S, \quad (\text{A.3})$$

where u is now the radial component of velocity, v is the tangential component, and

$$A = \frac{\zeta v}{f}, \quad B = \frac{\zeta u}{f}, \quad \zeta = \frac{\partial(rv)}{r \partial r} - \frac{\partial u}{r \partial \varphi}$$

$$K = \frac{1}{2}(u^2 + v^2)$$

$$C = \frac{u\phi}{H}, \quad D = \frac{v\phi}{H},$$

and F , G , and S are the frictional and diabatic effects. Using these equations we can now complete the tangential transform

A.2 The Tangential Transform and Lateral Boundary Condition

If we define the tangential finite Fourier transform of $u(r, \varphi, t)$ as $u_n(r, t)$, the tangential transform pair can be written as

$$u_n(r, t) = \frac{1}{2\pi} \int_0^{2\pi} u(r, \varphi, t) e^{-in\varphi} d\varphi \quad (\text{A.4})$$

$$u(r, \varphi, t) = \sum_{n=-\infty}^{\infty} u_n(r, t) e^{in\varphi} \quad (\text{A.5})$$

where n represents the wavenumber in the tangential direction. By using similar definitions for the tangential wind component and geopotential, (A.1)–(A.3) can be transformed to obtain

$$\frac{\partial u_n}{\partial t} - f(v_n + A_n) + \frac{\partial}{\partial r}(\phi_n + K_n) = F_n \quad (\text{A.6})$$

$$\frac{\partial v}{\partial t} + f(u_n + B_n) + \frac{in}{r}(\Phi_n + K_n) = G_n \quad (\text{A.7})$$

$$\frac{\partial \phi_n}{\partial t} + c_n^2 \left[\frac{\partial}{r \partial r} r(u_n + C_n) + \frac{in}{r}(v_n + D_n) \right] = S_n, \quad (\text{A.8})$$

Having completed the tangential transform, we are now far enough into spectral space to define our lateral boundary condition. Since there is no natural physical boundary condition, we will choose the simplest computational boundary condition. We consider the perturbation geopotential, ϕ , to vanish at $r = a$ for all time (where a is the radial boundary). If we also assume that the nonlinear and forcing terms vanish for large r , then from (A.3) the divergence must also vanish at the boundary. Thus, our boundary condition is nearly equivalent to a zero divergence boundary condition.

Before considering the problem of radially transforming our governing equations, it will again prove convenient to express our tangentially transformed equations in vector form. We can accomplish this as we did in chapter three by defining $\mathbf{W}_n = [u_n, v_n, \phi_n/c]^T$. Again these vectors have been chosen to ensure consistency in units. Using these definitions we can write

$$\frac{\partial \mathbf{W}_n}{\partial t} + \mathcal{L}_n \mathbf{W}_n = \mathbf{F}_n + \mathbf{N}_n, \quad (\text{A.9})$$

where the nonlinear terms \mathbf{N}_n are given as

$$\mathbf{N}_n = \left[fA_n - \frac{\partial}{\partial r} K_n, -fB_n - \frac{in}{r} K_n, -c \left(\frac{\partial r C_n}{r \partial r} + \frac{in}{r} D_n \right) \right]^T \quad (\text{A.10})$$

and the Forcing terms, \mathbf{F}_n , are given as

$$\mathbf{F}_n = [F_n, G_n, S_n/c]^T. \quad (\text{A.11})$$

The matrix operator is defined as

$$\mathcal{L}_n = \begin{pmatrix} 0 & -f & c \frac{\partial}{\partial r} \\ f & 0 & c \frac{in}{r} \\ c \frac{\partial r(\cdot)}{r \partial r} & c \frac{in}{r} & 0 \end{pmatrix}. \quad (\text{A.12})$$

Using these definitions, we are now prepared to complete the radial transform of (A.9).

A.3 The Radial Transform

We begin the radial transform by defining the complex inner product to be

$$(\mathbf{x}, \mathbf{y}) = \frac{2}{a^2} \int_0^a (x_0 y_0^* + x_1 y_1^* + x_2 y_2^*) r dr, \quad (\text{A.13})$$

where \mathbf{x} and \mathbf{y} are three component complex vectors which satisfy the boundary condition and the asterisk denotes the complex conjugate. As discussed in Appendix B, \mathcal{L}_n is skew-Hermitian with respect to the inner product (A.13), meaning $\mathcal{L}_n^\dagger = -\mathcal{L}_n$. Since it is well known that the eigenvalues of skew-Hermitian operators are pure imaginary, we can write

$$\mathcal{L}_n \mathbf{K}_{npq} = i\nu_{npq} \mathbf{K}_{npq}, \quad (\text{A.14})$$

where ν_{npq} are the eigenvalues and \mathbf{K}_{npq} are the corresponding vector eigenfunctions (or transformation kernels). These subscripts will become clearly defined shortly. One can easily solve for these eigenvalues and eigenfunctions by substituting our definition of \mathcal{L}_n into (A.14) and reducing the system of three equations down to one equation in one unknown. The equation obtained by solving for the third component of \mathbf{K}_{npq} is the order n Bessel equation and the corresponding solution is chosen to be the order n Bessel function of the first kind, $J_n(k_{np}r)$, where $k_{np}^2 \equiv (\nu_{npq}^2 - f^2)/c^2$. It should be noted that

we chose Bessel functions of the first kind to ensure our solutions remain bounded at the origin. The other two components are then obtained through direct substitution.

One other possible solution for \mathbf{K}_{npq} can also be obtained. This corresponds to the case when $\nu_{npq} = 0$. We will again refer to this as the geostrophic case since the equations which are obtained by substituting $\nu_{npq} = 0$ into our definition of \mathcal{L}_n are simply the geostrophic balance equations. It is important to note that any function can be chosen for the third component of the kernel and it will satisfy the geostrophic relation. We again choose the Bessel function of the first kind to remain consistent with our previous solutions. This case will be denoted with the subscript $q = 0$.

Finally, we can write the transformation kernel as

$$\mathbf{K}_{npq}(r) = A_{npq} \left\{ \begin{array}{l} \left(\begin{array}{l} -\frac{icn}{fr} J_n(k_{np}r) \\ \frac{c}{f} \frac{\partial J_n(k_{np}r)}{\partial r} \\ J_n(k_{np}r) \end{array} \right) \quad q = 0 \\ \left(\begin{array}{l} \frac{in}{k_{np}r} J_n(k_{np}r) - \frac{i\nu_{npq}}{fk_{np}} \frac{\partial J_n(k_{np}r)}{\partial r} \\ \frac{n}{r} \frac{\nu_{npq}}{fk_{np}} J_n(k_{np}r) - \frac{\partial J_n(k_{np}r)}{k_{np} \partial r} \\ \frac{ck_{np}}{f} J_n(k_{np}r) \end{array} \right) \quad q = 1, 2 \end{array} \right\} \quad (\text{A.15})$$

where A_{npq} is the normalization factor given by

$$A_{npq} = f \left\{ (\nu_{npq}^2 + f^2 + c^2 k_{np}^2) J_{n+1}^2(k_{np}a) \right\}^{-\frac{1}{2}}. \quad (\text{A.16})$$

J_n is the order n Bessel function of the first kind and k_{np} ($p = 1, 2, 3, \dots$) are the discrete wave numbers satisfying the boundary condition

$$J_n(k_{np}a) = 0, \quad (\text{A.17})$$

with

$$\nu_{npq} = \left\{ \begin{array}{ll} 0 & q = 0 \quad (\text{geostrophic modes}) \\ -(f^2 + c^2 k_{np}^2)^{\frac{1}{2}} & q = 1 \quad (\text{gravity - inertia mode}) \\ (f^2 + c^2 k_{np}^2)^{\frac{1}{2}} & q = 2 \quad (\text{gravity - inertia mode}) \end{array} \right\}. \quad (\text{A.18})$$

Equation (A.17) is derived by setting the third component of \mathbf{K}_{npq} equal to zero at the boundary in order to satisfy the boundary condition that ϕ must vanish at $r = a$. Since f , c , and k are all non-zero, the only possible solution is for $J_n(k_{np}a)$ to be zero for both the geostrophic and gravity-inertia modes.

It should now be clear just exactly what the subscripts n , p , and q represent. The n obviously refers to the tangential mode, the p indexes the radial modes, and the q gives the mode type corresponding to the three possible solutions for the frequency.

Before we discuss the orthonormality of our basis functions, we must first consider how they behave at the origin. We know that our kernel must be bounded at the origin (because we chose Bessel functions of the first kind), but we do not know what values the kernels take at the origin. In order to examine this, we use the limiting form of Bessel functions of the first kind for small arguments (Abramowitz and Stegun, eqn. 9.1.7), that is,

$$J_n(k_{np}r) \sim \frac{k_{np}^n r^n}{2^n n!}, \text{ as } r \rightarrow 0. \quad (\text{A.19})$$

By using (A.19) along with Hopital's rule we can express the vector kernel, $\mathbf{K}_{npq}(r)$ at $r = 0$ as

$$\mathbf{K}_{npq}(0) = \begin{cases} \begin{matrix} n = 0 & n = 1 & n > 2 \\ \begin{pmatrix} 0 \\ 0 \\ 1 \end{pmatrix} & \begin{pmatrix} -\frac{ic}{2f} k_{1p} \\ \frac{c}{2f} k_{1p} \\ 0 \end{pmatrix} & \begin{pmatrix} 0 \\ 0 \\ 0 \end{pmatrix} \end{matrix} & q = 0 \\ \begin{matrix} \begin{pmatrix} 0 \\ 0 \\ \frac{ck_{0p}}{f} \end{pmatrix} & \begin{pmatrix} \frac{i}{2} \left(1 - \frac{\nu_{1ps}}{f}\right) \\ -\frac{1}{2} \left(1 - \frac{\nu_{1ps}}{f}\right) \\ 0 \end{pmatrix} & \begin{pmatrix} 0 \\ 0 \\ 0 \end{pmatrix} \end{matrix} & q = 1, 2 \end{cases} \quad (\text{A.20})$$

As discussed in Appendix C, the transformation kernels (A.15) are orthonormal with respect to the inner product (A.13) even for the degenerate (geostrophic) modes, that is

$$(\mathbf{K}_{npq}, \mathbf{K}_{np'q'}) = \begin{cases} 1 & p' = p \text{ and } q' = q \\ 0 & \text{otherwise} \end{cases}. \quad (\text{A.21})$$

Using this orthonormality, it is possible to write our radial transform pair as

$$\mathbf{W}_n(r, t) = \sum_{p=1}^{\infty} \sum_{q=0}^2 W_{npq}(t) \mathbf{K}_{npq}(r), \quad (\text{A.22})$$

$$W_{npq}(t) = (\mathbf{W}_n(r, t), \mathbf{K}_{npq}(r)), \quad (\text{A.23})$$

where $W_{npq}(t)$ is a complex, scalar function of time having units of ms^{-1} . Equation (A.23) is the transform from radial physical space to spectral space and (A.22) is the inverse transform.

To derive the spectral equations (i.e. equations involving W_{npq}), we take the inner product of (A.9) with $\mathbf{K}_{npq}(r)$ to obtain

$$\frac{\partial}{\partial t}(\mathbf{W}_n, \mathbf{K}_{npq}) + (\mathcal{L}_n \mathbf{W}_n, \mathbf{K}_{npq}) = (\mathbf{F}_n, \mathbf{K}_{npq}) + (\mathbf{N}_n, \mathbf{K}_{npq}). \quad (\text{A.24})$$

Since $\mathcal{L}_n^\dagger = -\mathcal{L}_n$ with respect to the inner product, (A.13) we can use (A.12) to rewrite the second term in (A.24) as

$$(\mathcal{L}_n \mathbf{W}_n, \mathbf{K}_{npq}) = -(\mathbf{W}_n, \mathcal{L}_n \mathbf{K}_{npq}) = -i\nu_{npq}(\mathbf{W}_n, \mathbf{K}_{npq}). \quad (\text{A.25})$$

Using (A.24) we see that (A.25) can be written as

$$\frac{dW_{npq}}{dt} + i\nu_{npq}W_{npq} = F_{npq} + N_{npq}. \quad (\text{A.26})$$

Equation (A.26) completes our transformation from our original governing equations in physical space to normal mode spectral space. It is of interest to note that any normal model spectral model (regardless of the equations, geometry, etc.) leads to an equation of this form.

A.4 Computational Procedures

This section discusses some the complications which arise when integrating the cylindrical coordinate model. Included are discussions of the horizontal transforms and the calculation of derivatives and nonlinear terms.

A.4.1 The Horizontal Transforms

The tangential transform can be easily accomplished with any real FFT routine in a similar fashion to the transforms discussed in chapter three. Since FFTs are well documented in academic texts (e.g. Brigham, 1988), the tangential transform will not be discussed further here. The radial transform, however, does require some discussion.

Unlike the Cartesian coordinate model, our transformation kernel (A.15) does not consist of periodic functions. Because of this, there is no hope of computing the radial transform (A.11) exactly with a finite number of points. Aliasing error is therefore unavoidable.

Another difficulty with the radial transform is that there exists no fast transform for Bessel functions. We are therefore forced to evaluate the integral in (A.13) using the full number of operations required by the chosen quadrature method.

In the present study, we computed the integral in (A.13) using $3P+1$ points using both trapezoidal and Simpson's quadrature, where P represents the subscript of the highest radial wave number. We chose $3P+1$ points in order to be consistent with the Cartesian coordinate model. Results from linear model integrations indicated that with this number of points, Simpson's quadrature produced the best results.

Finally, it should be noted that Bessel series have a relatively slow rate of convergence which is on the order of $1/N$ where N is the number of terms in the series (Gottlieb and Orzag, 1977). Fourier series on the other hand converge on the order of $1/N^2$ (Gottlieb and Orzag, 1977). This implies that more waves would be required for the Bessel series to have the same accuracy as the Fourier series for the same function.

A.4.2 Calculation of Derivatives and Nonlinear Terms

It can easily be shown from (A.22) that r -derivatives can be calculated by summing the spectral coefficients W_{npq} with the r -derivatives of the transformation kernel. Since derivatives of Bessel functions are known exactly (see B.9), derivatives of the transformation kernel are known exactly. This indicates that derivatives of the dependent variables can be computed exactly to within the truncation limits of the model. One drawback however is that the transformation kernels are not eigenfunctions of the $\partial/\partial r$ operator. Thus, derivatives of the transformation kernels must be calculated at each time step or the derivative of the transformation kernel must be stored in an array. The choice of course depends on the amount of available computer storage. To demonstrate the amount of storage required for transformation kernels, consider the case where we use 128 points in the r direction to evaluate the transformation kernel, if we keep 42 waves in both the radial and tangential directions then roughly 5.4 megabytes of storage are required (assuming a complex variable is stored as two four byte words). If we choose to double this resolution, the amount of required storage increases by a factor of eight to 43.3 megabytes. One can easily see that as the resolution improves, the model quickly becomes cost prohibitive.

Nonlinear terms would require enormous computational expense in cylindrical coordinates. The reason being that not only would a transform to and from normal mode spectral space be required at each time step, but derivatives of the transformation kernel would need to be stored or calculated.

Appendix B

THE SKEW-HERMITIAN PROPERTIES OF THE LINEAR OPERATORS

In this appendix we will prove the skew-Hermitian property of the matrix operators (2.5) and (A.12) with respect to the inner products (2.8) and (A.13) respectively. Our first step is to define what is meant by skew-Hermitian. A linear operator is said to be skew-Hermitian with respect to an inner product if its adjoint is the same operator with the opposite sign. We define the adjoint operator, \mathcal{L}^\dagger , to be the operator which satisfies

$$(\mathcal{L}\mathbf{p}, \mathbf{q}) = (\mathbf{p}, \mathcal{L}^\dagger\mathbf{q}), \quad (\text{B.1})$$

where \mathbf{p} and \mathbf{q} in (B.1) represent complex vectors which satisfy the conditions of the inner product. Therefore, if an operator is skew-Hermitian with respect to an inner product, then

$$(\mathcal{L}\mathbf{p}, \mathbf{q}) = (\mathbf{p}, -\mathcal{L}\mathbf{q}). \quad (\text{B.2})$$

B.1 The Cartesian Coordinate System

Consider \mathbf{p} and \mathbf{q} to be the complex, three component vectors which are periodic in both x and y with period L_x and L_y respectively. Using (2.5) and (2.8) we can write

$$\begin{aligned} (\mathcal{L}\mathbf{p}, \mathbf{q}) = \frac{1}{L_x L_y} \int_0^{L_x} \int_0^{L_y} \left\{ \left(-fp_1 + c \frac{\partial p_2}{\partial x} \right) q_0^* + \left(fp_0 + c \frac{\partial p_2}{\partial y} \right) q_1^* \right. \\ \left. + \left(c \frac{\partial p_0}{\partial x} + c \frac{\partial p_1}{\partial y} \right) q_2^* \right\} dx dy \end{aligned} \quad (\text{B.3})$$

If (B.3) is integrated by parts and terms are rearranged, it can be rewritten as

$$\begin{aligned} (\mathcal{L}\mathbf{p}, \mathbf{q}) = \frac{1}{L_x L_y} \int_0^{L_x} \int_0^{L_y} \left\{ p_0 \left(fq_1^* - c \frac{\partial q_2^*}{\partial x} \right) + p_1 \left(-fq_0^* - c \frac{\partial q_2^*}{\partial y} \right) + \right. \\ \left. p_2 \left(-c \frac{\partial q_0^*}{\partial x} - c \frac{\partial q_1^*}{\partial y} \right) + c \left(\frac{\partial}{\partial x} (p_2 q_0^*) + \frac{\partial}{\partial y} (p_2 q_1^*) + \frac{\partial}{\partial x} (p_0 q_2^*) + \frac{\partial}{\partial y} (p_1 q_2^*) \right) \right\} dx dy \end{aligned} \quad (\text{B.4})$$

Because both \mathbf{p} and \mathbf{q} periodic in x and y , the last term in (B.4) must be identically zero. By factoring the complex conjugate operator from terms in parentheses, we see that (B.4) reduces to

$$(\mathcal{L}\mathbf{p}, \mathbf{q}) = (\mathbf{p}, -\mathcal{L}\mathbf{q}). \quad (\text{B.5})$$

Since $\mathcal{L}_m^\dagger = -\mathcal{L}$, we conclude that \mathcal{L} is skew-Hermitian with respect to (2.8).

B.2 The Cylindrical Coordinate System

Now consider \mathbf{p} and \mathbf{q} to be the complex, three component vectors whose third components vanish at $r = a$. Using (A.12) and (A.13) we can write

$$\begin{aligned} (\mathcal{L}_n\mathbf{p}, \mathbf{q}) = & \frac{2}{a^2} \int_0^a \left\{ \left(-fp_1 + c \frac{\partial p_2}{\partial r} \right) q_0^* + \left(fp_0 + c \frac{in}{r} p_2 \right) q_1^* \right. \\ & \left. + \left(\frac{\partial(rp_0)}{r\partial r} + c \frac{in}{r} p_1 \right) q_2^* \right\} r dr. \end{aligned} \quad (\text{B.6})$$

If we integrate by parts the terms involving derivatives with respect to r and rearrange terms we get

$$\begin{aligned} (\mathcal{L}_n\mathbf{p}, \mathbf{q}) = & \frac{2}{a^2} \int_0^a \left\{ p_0 \left(fq_1^* - c \frac{\partial q_2^*}{\partial r} \right) + p_1 \left(-fq_0^* + c \frac{in}{r} q_2^* \right) \right. \\ & \left. + p_2 \left(-\frac{\partial(rq_0^*)}{r\partial r} + c \frac{in}{r} q_1^* \right) \right\} r dr + [ap_0q_2^* + ap_2q_0^*]_{r=a}. \end{aligned} \quad (\text{B.7})$$

We know from our boundary condition, however, that p_2 and q_2 are zero at $r = a$ therefore the boundary terms in (B.7) must vanish. In addition, if we factor out the complex conjugate operator from the terms in parentheses, (B.7) can be written as

$$(\mathcal{L}_n\mathbf{p}, \mathbf{q}) = (\mathbf{p}, -\mathcal{L}_n\mathbf{q}). \quad (\text{B.8})$$

Since $\mathcal{L}_n^\dagger = -\mathcal{L}_n$, we again conclude that \mathcal{L}_n is skew-Hermitian with respect to the inner product (A.13).

Appendix C

THE ORTHONORMALITY OF THE BASIS FUNCTIONS

In this appendix we prove the statement of orthonormality of our basis functions (2.13) and (A.15) with respect to the inner products (2.8) and A.13) respectively. The proof will be done first in Cartesian coordinates and then in cylindrical coordinates.

C.1 Orthonormality of Cartesian Coordinate Basis Functions

The proof of orthonormality in Cartesian coordinates is straightforward. Since the x and y dependency of the basis functions is periodic, it is easily verified that if $k \neq k'$ and/or $l \neq l'$, the integral in (2.8) will be identically zero. If the $k = k'$ and $l = l'$ it is easily verified that the x and y dependency will integrate to exactly one, leaving only a vector multiplication left to evaluate. Because of this, if we wish to show that the eigenfunctions are orthonormal, we need only to show that the x and y independent parts of (2.13) are orthonormal. One can easily prove this to be true by computing the vector products of the as defined in (2.8) for the x and y independent parts of (2.13) for each mode type, q .

C.2 Orthonormality of Cylindrical Coordinate Basis Functions

The proof of orthonormality in cylindrical coordinates is considerably less straightforward. Our first step is to prove the orthogonality of \mathbf{K}_{npq} with $\mathbf{K}_{np'q'}$ where $p \neq p'$, $q = 1$ or 2 , and $q' = 0, 1$, or 2 . We do this by adding the inner product of $\mathcal{L}_n \mathbf{K}_{npq} = i\nu_{npq} \mathbf{K}_{npq}$ with $\mathbf{K}_{np'q'}$ to the inner product of \mathbf{K}_{npq} with $\mathcal{L}_n \mathbf{K}_{np'q'} = i\nu_{np'q'} \mathbf{K}_{np'q'}$ to obtain

$$\begin{aligned} & (\mathcal{L}_n \mathbf{K}_{npq}, \mathbf{K}_{np'q'}) + (\mathbf{K}_{npq}, \mathcal{L}_n \mathbf{K}_{np'q'}) = \\ & (i\nu_{npq} \mathbf{K}_{npq}, \mathbf{K}_{np'q'}) + (\mathbf{K}_{npq}, i\nu_{np'q'} \mathbf{K}_{np'q'}). \end{aligned} \tag{C.1}$$

Because of the skew-Hermitian property of \mathcal{L}_n (as discussed in appendix A), the left hand side of (C.1) vanishes. We can therefore rewrite (C.1) as

$$(\nu_{npq} - \nu_{np'q'}) (\mathbf{K}_{npq}, \mathbf{K}_{np'q'}) = 0. \quad (\text{C.2})$$

Since the eigenvalues for the gravity-inertia modes are distinct, the corresponding eigenfunctions must be orthogonal to satisfy (C.2). In addition, since the eigenvalues for the gravity-inertia modes are non-zero, the inner product of an eigenfunction from the geostrophic mode set must be orthogonal to an eigenfunction from the gravity-inertia mode set to satisfy (C.2).

Now we wish to prove the orthogonality of the degenerate (geostrophic) modes. Consider the case where $p \neq p'$ and $q = q' = 0$. The inner product of these eigenfunctions is

$$\begin{aligned} (\mathbf{K}_{np0}, \mathbf{K}_{np'0}) = & \frac{2}{a^2} A_{np0} A_{np'0} \int_0^a \left\{ \frac{c_m^2 n^2}{f^2 r^2} J_n(k_{np} r) J_n(k_{np'} r) + \right. \\ & \left. \frac{c_m^2}{f^2} \frac{\partial J_n(k_{np} r)}{\partial r} \frac{\partial J_n(k_{np'} r)}{\partial r} + J_n(k_{np} r) J_n(k_{np'} r) \right\} r dr. \end{aligned} \quad (\text{C.3})$$

If we integrate the second term on the right hand side by parts, we can shift the r derivative off $J_n(k_{np} r)$ and rewrite (C.3) as

$$\begin{aligned} (\mathbf{K}_{np0}, \mathbf{K}_{np'0}) = & A_{np0} A_{np'0} \frac{2}{a^2} \int_0^a \left\{ \frac{c_m^2 n^2}{f^2 r^2} J_n(k_{np} r) J_n(k_{np'} r) \right. \\ & \left. - \frac{c_m^2}{f^2} J_n(k_{np} r) \frac{\partial}{\partial r} \left[r \frac{\partial J_n(k_{np'} r)}{\partial r} \right] + J_n(k_{np} r) J_n(k_{np'} r) \right\} r dr + \\ & \left[a \frac{c_m^2}{f^2} J_n(k_{np} a) \frac{\partial J_n(k_{np'} r)}{\partial r} \right]_{r=a}. \end{aligned} \quad (\text{C.4})$$

Equation (C.4) can be simplified further by first recognizing that the boundary term vanishes because of (A.17). Secondly, we may eliminate the derivative in the second term on the right by using the equation that $J_n(k_{np'} r)$ satisfies (i.e. Bessel's equation) divided by r^2 . This equation can be written as

$$\frac{\partial}{\partial r} \left[r \frac{\partial J_n(k_{np'} r)}{\partial r} \right] + (k_{np'}^2 - \frac{n^2}{r^2}) J_n(k_{np'} r) = 0. \quad (\text{C.5})$$

By substituting (C.5) into (C.4) we obtain

$$(\mathbf{K}_{np0}, \mathbf{K}_{n'p'0}) = A_{np0} A_{n'p'0} \frac{1}{f^2} (\nu_{np0}^2 + f^2 + c_m^2 k_{np}^2) \frac{2}{a^2} \int_0^a J_n(k_{np}r) J_n(k_{n'p'}r) r dr, \quad (\text{C.6})$$

where ν_{np0} is identically zero but was added for consistency in notation. From Abramowitz and Stegun (1964, page 485, eqn. 11.4.5), the integral in (C.6) is evaluated as

$$\int_0^a J_n(k_{np}r) J_n(k_{n'p'}r) r dr = \begin{cases} 0 & p \neq p' \\ \frac{a^2}{2} \left[\left(1 - \frac{n^2}{k_{np}^2 a^2}\right) J_n^2(k_{np}a) + \left(\frac{\partial J_n(k_{np}r)}{\partial(k_{np}r)}\right)^2 \right]_{r=a} & p = p' \end{cases} \quad (\text{C.7})$$

However, this can be simplified to

$$\int_0^a J_n(k_{np}r) J_n(k_{n'p'}r) r dr = \begin{cases} 0 & p \neq p' \\ \frac{a^2}{2} J_{n+1}^2(k_{np}a) & p = p' \end{cases} \quad (\text{C.8})$$

through use of our boundary condition (2.22) and the derivative relation (Abramowitz and Stegun, 1964, page 361, eqn. 9.1.30)

$$\frac{\partial J_n(kr)}{\partial r} = \frac{n}{r} J_n(kr) - k J_{n+1}(kr). \quad (\text{C.9})$$

Finally, by substituting (C.8) into (C.6) while using the (A.16), we can write

$$(\mathbf{K}_{np0}, \mathbf{K}_{n'p'0}) = \begin{cases} 0 & p \neq p' \\ 1 & p = p' \end{cases} \quad (\text{C.10})$$

Thus, our eigenfunctions are orthonormal even for the degenerate (geostrophic) case.

Our final task is to show that eigenfunctions within the gravity-inertia mode sets are orthonormal. To do this, consider the case where $p = p'$ and $q = q' = 1$ or 2 . Our inner product can then be written as

$$(\mathbf{K}_{npq}, \mathbf{K}_{npq}) = A_{npq}^2 \frac{2}{a^2} \int_0^a \left\{ \frac{n^2}{k_{np}^2 r^2} J_n^2(k_{np}r) + \frac{\nu_{npq}^2}{f^2 k_{np}^2} \left(\frac{\partial J_n(k_{np}r)}{\partial r} \right)^2 + \frac{\nu_{npq}^2 n^2}{f^2 r^2} J_n^2(k_{np}r) + \frac{1}{k_{np}^2} \left(\frac{\partial J_n(k_{np}r)}{\partial r} \right)^2 - 2 \frac{n \nu_{npq}}{f k_{np}^2} \frac{\partial J_n^2(k_{np}r)}{r \partial r} + \frac{c^2 k_{np}^2}{f^2} J_n^2(k_{np}r) \right\} r dr \quad (\text{C.11})$$

The fifth term on the right hand side of (C.11) must vanish at the upper boundary because of (A.17) and also at the lower boundary because $J_n(0) = 0$ for all $n > 0$. We can also simplify (C.11) as we did for the geostrophic modes by integrating the by parts the terms

involving derivatives and using the equation which $J_n(k_{np}r)$ satisfies. By doing this and again using (A.17), we can rewrite (C.11) as

$$(\mathbf{K}_{npq}, \mathbf{K}_{npq}) = A_{npq}^2 \frac{1}{f^2} (\nu_{npq}^2 + f^2 + c_m^2 k_{np}^2) \frac{2}{a^2} \int_0^a J_n^2(k_{np}r) r dr \quad (\text{C.12})$$

Using (C.8) and (A.16), (C.12) can be written in final form as

$$(\mathbf{K}_{npq}, \mathbf{K}_{npq}) = 1. \quad (\text{C.13})$$

We have therefore proven that our eigen functions are indeed orthonormal for both the gravity-inertia modes and the geostrophic modes.

Appendix D

ON THE USE OF TEMPERTON'S CFFT ROUTINES

In this appendix the complex fast Fourier Transform (CFFT) routines which were used in the Cartesian coordinate model are discussed.

The CFFT routines used in the model were developed by Clive Temperton (1983a,b) and can be obtained through NCAR's public domain software library. The CFFT package is called `cfft99f.f` and was written to perform a number of simultaneous complex periodic Fourier transforms. The code was written to run efficiently on a Cray computer through use of parallel processing techniques. It is, however, portable to other machines.

Although FFT and CFFT routines are well documented in the literature, the storage of the spectral coefficients is explained here to aid in understanding the model code. The `cfft99f.f` routine takes a complex array of data of length I (0 to $I - 1$, where I has no prime factor greater than five) and returns a complex array of equal length containing the spectral coefficients of original data (the inverse can also be done). What is important to note is the order with which the spectral coefficients are returned. The first zero through $I/2$ storage locations in the array contain the zero through $I/2$ spectral coefficients. The last half of the array ($I/2 + 1$ to $I - 1$) contains the $i - I$ spectral coefficients. That is, $C_{-k} = C_{I-k}$, where C represents any spectral coefficient. As mentioned in chapters three and four, we cannot use all returned wavenumber if we wish to eliminate aliasing error. If we choose to keep $-K$ to K wavenumbers, the middle portion of the returned array must be neglected.

In the present model, we must perform a CFFT in two dimensions, both x and y . This results in a two dimensional array of data. The storage of the returned spectral coefficients follows those explained above in both dimensions. In two dimensions, we must

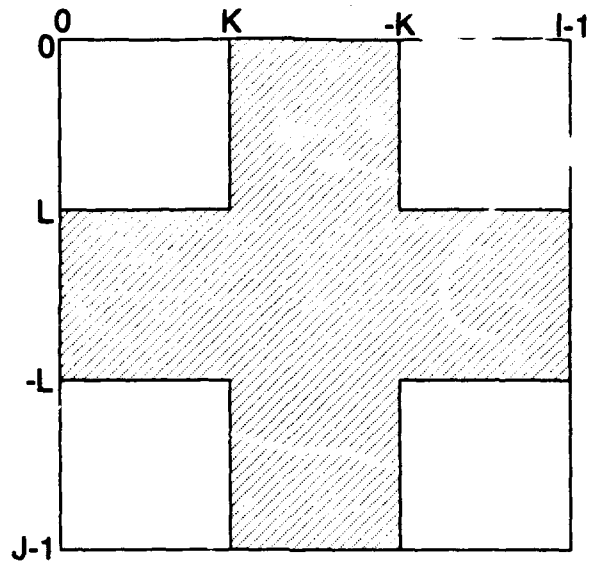


Figure D.1: The storage of the spectral coefficients in the Cartesian coordinate model code. The shaded area represents data which is neglected to prevent aliasing error.

neglect a cross shaped pattern in the returned array (see Fig. D.1) to prevent aliasing error.

To make the returned arrays more convenient for usage, we rewrite the needed data to a two dimensional array of length $(-K:K,-L:L)$. When we perform the inverse transform, we then simply zero out the wavenumbers greater than $|K|$ and $|L|$, rewrite the array in a form identical to the original array, and call `cfft99f.f` to perform the inverse transform.

It is important to note that although the original data field is real, we write the data to a complex array to perform the transform. This is done so `cfft99f.f` can be used in both x and y , thus ensuring compatibility by avoiding the use of a real FFT routine in one direction and a CFFT in the other.

END